

NASA CONTRACTOR REPORT 182278

PROPFAN TEST ASSESSMENT (PTA) FLIGHT TEST REPORT

B. H. Little, H. W. Bartel, N. N. Reddy,
G. Swift, and C. C. Withers
Lockheed Aeronautical Systems Company
Marietta, Georgia

P. C. Brown
Hamilton Standard Division
United Technologies Corporation
Windsor Locks, Connecticut

April 1989

Prepared for
Lewis Research Center
Under Contract NAS3-24339

NASA

National Aeronautics and
Space Administration

(NASA-CR-182278) PROPFAN TEST ASSESSMENT
(PTA): FLIGHT TEST REPORT (Lockheed
Aeronautical Systems Co.) 274 5 0001 21F

NPO-11738

unclas
65/07 0255895





FOREWORD

Under the leadership of the Lockheed Aeronautical Systems Company, an industry team including Allison Gas Turbine Division of General Motors, Hamilton Standard Division of United Technologies, Gulfstream Aerospace Corporation, and Rohr, Inc., developed and flew the Propfan Test Assessment (PTA) aircraft in a highly successful program of full-scale propfan research. This program was directed by the Advanced Turboprop Project Office of the NASA Lewis Research Center under contract NAS3-24339.

This report, describing and discussing the flight tests and their results, is submitted to satisfy the contractual requirements of DRD 220-09. It is also identified as Lockheed Report No. LG89ER0026.

PRECEDING PAGE BLANK NOT FILMED



TABLE OF CONTENTS

<u>Section</u>	<u>Title</u>	<u>Page</u>
	FOREWORD	iii
	TABLE OF CONTENTS	v
	LIST OF FIGURES	vii
	LIST OF SYMBOLS AND ABBREVIATIONS	xvii
1.0	SUMMARY	1
2.0	INTRODUCTION	3
	2.1 Background	3
	2.2 Objectives and Scope	4
	2.3 Significance of the PTA Flight Research Program	5
3.0	TEST HARDWARE	7
	3.1 Large-Scale Advanced Propfan (LAP) Description	7
	3.2 PTA Aircraft	7
4.0	INSTRUMENTATION	9
	4.1 Propfan Instrumentation	9
	4.2 Aircraft Surface Pressure and Flight Condition Instrumentation	10
	4.3 Airborne Acoustics and Vibration Instrumentation	11
	4.4 Acoustics Ground Instrumentation	11
	4.5 Aircraft Space Positioning Measurements	12
	4.6 Meteorological Instrumentation	12
5.0	TEST TECHNIQUES AND PROCEDURES	13
	5.1 Ground Tests	13
	5.1.1 LAP Structural Integrity Evaluation	13
	5.1.2 Baseline Acoustics and Vibration Tests	13
	5.2 Flight Research Tests	13
	5.2.1 Low Altitude Tests	14
	5.2.2 High Altitude Tests	15
6.0	DATA ANALYSIS AND PREDICTION METHODS	17
	6.1 Propfan Blade Response	17
	6.1.1 Propfan Test Data	17
	6.1.2 Propfan Response Prediction	17
	6.2 Acoustic Data	18
	6.2.1 Acoustic Data Processing	18
	6.2.2 Processed Data Output Format	19



TABLE OF CONTENTS (CONT'D)

<u>Section</u>	<u>Title</u>	<u>Page</u>
7.0	RESULTS AND DISCUSSION	21
7.1	Propfan Blade Structural Test Results	21
7.1.1	Blade Vibratory Response	21
7.1.2	Propfan Aerodynamic Performance	25
7.1.3	Conclusions - Propfan Structural Response	25
7.2	Acoustics Test Results	26
7.2.1	Far-Field Noise	26
7.2.2	Near-Field Noise - Sound Pressures	33
7.2.3	Near-Field Noise - Fluctuating Pressures	43
7.2.4	Cabin Noise	50
8.0	CONCLUDING REMARKS	63
APPENDIX A	PROPFAN BLADE EXCITATION FACTOR	65
APPENDIX B	LOCATIONS OF MICROPHONES, ACCELEROMETERS, AND STRAIN GAGES ON PTA AIRCRAFT	73
	REFERENCES	101
	FIGURES	103



LIST OF FIGURES

<u>Figure</u>	<u>Title</u>	<u>Page</u>
1	Large-Scale Advanced Propfan (LAP)	104
2	PTA Flight Test Envelope	105
3	Features of the SR-7L Blade Construction	106
4	PTA Testbed Aircraft	107
5	Propfan Electronic Data Acquisition System Schematic	108
6	SR-7L Propfan Strain Gage Locations	109
7	SR-7L Blade Strain Gage Locations	110
8	SR-7L Blade Strain Gage Locations	111
9	SR-7L Shank Strain Gage Locations	112
10	NASA Propfan Data System	113
11	Wing Surface Static Pressures	114
12	Typical Wing Static Pressure Tap Distribution	115
13	PTA Nacelle Pressure Instrumentation	116
14	Distribution of Acoustic and Vibration Transducers	117
15	Ground Instrumentation for Low-Altitude Tests	118
16	Ground-Based Microphone Arrangement	121
17	Crosswind Testing Using a C-130 as a "Blower" Aircraft	122
18	Acoustic Horn and Shaker Input Plate for Baseline Acoustics and Vibration Tests	123
19	Maps of Excitation Factor	124
20	Propfan Installed Low-Altitude Test Conditions	125
21	Low-Altitude Test Procedure With Propfan Removed	126
22	Low-Altitude Flight Paths at NASA Wallops Flight Facility	127
23	-1° Nacelle Tilt Test Conditions, Propfan On	128

LIST OF FIGURES (CONT'D)

<u>Figure</u>	<u>Title</u>	<u>Page</u>
24	-3° and +2° Nacelle Tilt Test Conditions, Propfan On	129
25	Cabin Noise Survey (TRAM) Test Conditions (-1° Nacelle Tilt)	130
26	Yaw Angle Test Conditions, Propfan On	131
27	Propfan-Off Test Conditions	132
28	Typical Strip Chart Record	133
29	Sample of Tabular Listing of Operational Parameters	134
30	Sample of Computerized Presentation of Narrow-Band Spectral Data	135
31	Sample of Computerized Tabulation of Spectrum Amplitude and Frequency at Orders of Blade Passage Frequency	136
32	Sample of Computerized Presentation of Flyover Noise Time History Data	137
33	Sample of Computerized Presentation of 1/3 Octave Band Spectral Data	138
34	Sample of Computerized Tabulation of Far-Field Noise Time History and Metrics Data	139
35	Sample Parametric Plot of Near-Field Noise Data	140
36	Sample Parametric Plot of Far-Field Noise Data	141
37	Flight Conditions for Propfan Structural Tests	142
38	Inboard Bending Vibratory Strain Over the -3° Nacelle Tilt Flight Envelope	143
39	Inboard Bending Vibratory Strain Over the -1° Nacelle Tilt Flight Envelope	144
40	Inboard Bending Vibratory Strain Over the +2° Nacelle Tilt Flight Envelope	145
41	Typical Frequency Spectrum for an Inboard Bending Strain Gage	146



LIST OF FIGURES (CONT'D)

<u>Figure</u>	<u>Title</u>	<u>Page</u>
42	Radial Distribution of Calculated and Measured 1P and 2P Strain at -3° Nacelle Tilt	147
43	Radial Distribution of Calculated and Measured 1P and 2P Strain at -1° Nacelle Tilt	148
44	Radial Distribution of Calculated and Measured 1P and 2P Strain at $+2^\circ$ Nacelle Tilt	149
45	Radial Distribution of Calculated and Measured 3P and 4P Strain at -1° Nacelle Tilt	150
46	SR-7L Blade Natural Frequencies	151
47	Effect of Equivalent Airspeed on Propfan Response at Low Altitude	152
48	Effect of Equivalent Airspeed on Propfan Response at High Altitude	153
49	Propfan Relative Excitation Factor	154
50	Effect of Nacelle Tilt on Propfan Response at Low Speed	155
51	Effect of Nacelle Tilt on Propfan Response at High Speed	156
52	Effect of Torque on Propfan Response	157
53	Calculated Camber Change with Torque	158
54	Effect of Rotational Speed on Propfan 1P and 2P Shank Flatwise Response at Low-Speed Conditions	159
55	Effect of Rotational Speed on Propfan 1P and 2P Response at High-Speed Conditions	160
56	Effect of Rotational Speed on Propfan 3P and 4P Shank Edgewise Response	161
57	Effect of Mach Number on Propfan Response at a Constant Airspeed of 126 m/sec (250 KEAS)	162
58	Comparison of Measured and Predicted Performance, Mach 0.8, $J = 3.07$	163
59	Comparison of Measured and Predicted Performance, Mach 0.7, $J = 2.75$	164



LIST OF FIGURES (CONT'D)

<u>Figure</u>	<u>Title</u>	<u>Page</u>
60	Comparison of Measured and Predicted Performance, Mach 0.5, J = 2.70	165
61	Planned Nominal Low-Altitude Test Conditions, Propfan Removed	166
62	Illustration of Nacelle Tilt, Angle of Attack, and Sideslip Angle	167
63	Coordinates for Normalized Lossless Data	168
64	Illustration of Anomalous High Frequency Noise	169
65	Effect of Spey Engine Thrust on Far-Field Noise - Propfan Blades Removed; Flyover Position at 305m (1000 ft) Radius	170
66	Noise Spectra With Propfan Blades Removed; Free Field Lossless Data at 305m (1000 ft) Radius	171
67	Comparison of 305m (1000 ft) Flyover Noise for Propfan Blades On and Off	172
68	Lossless SPL Azimuthal Directivity at Blade Passing Frequency	173
69	Lossless SPL Polar Directivity at Blade Passing Frequency	174
70	Variation of Noise With Propfan Power	175
71	Effect of Power and Helical Tip Mach Number on Peak OASPL	176
72	Effects of Power and Nacelle Tilt on Peak OASPL	179
73	Effect of Sideslip on Peak OASPL	181
74	Comparison of Predicted and Measured Peak OASPLs	182
75	Comparisons of Predictions With Measurements	183
76	Comparison of Predicted and Measured Time Histories	186
77	Typical Comparison of Predicted and Measured Noise Spectra	187



LIST OF FIGURES (CONT'D)

<u>Figure</u>	<u>Title</u>	<u>Page</u>
78	Effect of Shaft Horsepower on Predicted and Measured Noise, at Nominal Conditions	188
79	Effect of Propfan Tip Mach Number on Predicted and Measured Noise, at Nominal Conditions	190
80	Effects of Nacelle Tilt On Predicted and Measured Noise	192
81	Calculation Procedure for Lateral Noise Attenuation	193
82	Lateral Attenuation as a Function of Elevation Angle - Port Side (160, 200, 250, and 315 Hz Bandwidths Integrated)	194
83	Lateral Attenuation as a Function of Elevation Angle - Starboard Side (160, 200, 250, 315 Hz Bandwidths Integrated)	195
84	Lateral Attenuation of PTA Aircraft - Summary	196
85	PTA Acoustic Geometry	197
86	PTA Propfan and Wing Geometry	198
87	Fuselage Surface Microphone Locations	199
88	Effects of Near-Side Spey Engine on Fuselage Noise - Prop Off	200
89	Effects of Near-Side Spey Engine on Fuselage Noise - Prop On	201
90	Wing Boom Acoustic Data - Prop Off	202
91	Wing Boom Acoustic Data - Prop On	202
92	Sound Pressure Time Histories at 0.25 Propfan Diameter Aft of Propfan Plane	203
93	Sound Pressure Spectra at 0.25 Propfan Diameter Aft of Propfan Plane	204
94	Fuselage Axial Distribution of Measured Sound Pressure Level Along WL 70	205
95	Fuselage Circumferential Distribution of Measured SPL in Propfan Plane	206

LIST OF FIGURES (CONT'D)

<u>Figure</u>	<u>Title</u>	<u>Page</u>
96	Fuselage Surface Measured SPL	207
97	Wing Boom Axial Distribution of Measured SPL	208
98	Comparison of Measured SPLs on Fuselage Water Line 94 and on Wing Boom	209
99	Fuselage Measured SPL Dependence on Propfan Tip Speed and Power	210
100	Fuselage Measured SPL Dependence on Propfan Thrust and Tip Speed	212
101	Fuselage Measured SPL Dependence Upon Propfan Advance Ratio and Power Coefficient	212
102	Wing Boom Measured SPL Dependence on Propfan Tip Speed and Power	213
103	Fuselage Measured SPL Variation Over Flight Envelope	214
104	Effect of Propfan Helical Tip Mach Number on Fuselage SPL	215
105	Test Cases for Altitude Scaling Validation	216
106	Results from Altitude Scaling Validation Tests	216
107	Effect of Nacelle Tilt on Propfan Inflow Angle	217
108	Expected Influence of Propfan Inflow Angle and Direction of Rotation on Near-Field Noise	217
109	Effect of Nacelle Tilt on Fuselage and Wing Boom Measured SPLs	218
110	Effect of Nacelle Tilt on Fuselage SPLs	218
111	Fuselage Measured BPF1 SPL Variation Over Flight Envelope, NT = -3°	219
112	Fuselage Measured BPF1 SPL Variation Over Flight Envelope, NT = +2°	219
113	Effect of Nacelle Tilt on Fuselage Measured SPLs Within Flight Envelope	220



LIST OF FIGURES (CONT'D)

<u>Figure</u>	<u>Title</u>	<u>Page</u>
114	Effect of Nacelle Tilt on Wing Boom Measured SPLs Within Flight Envelope	220
115	Effect of Nacelle Tilt on Fuselage and Wing Boom Measured SPLs	221
116	Effect of Sideslip on Fuselage and Wing Boom Measured SPLs	221
117	Propfan Near-Field Acoustic Prediction Methodology	222
118	Summary of Fuselage Predicted and Measured SPLs	222
119	Summary of Predicted and Measured SPL Maxima Locations on Fuselage	223
120	Fuselage Axial Distribution of Measured and Predicted SPL	223
121	Fuselage Surface Predicted SPL	224
122	Comparison of Predicted and Measured Spectra on Fuselage	224
123	Predicted and Measured Fuselage SPL Dependence on Propfan Tip Speed and Power	225
124	Variation of Predicted and Measured Fuselage SPL With Tip Speed	225
125	Fuselage Surface Predicted SPL Over Flight Envelope	226
126	Fuselage Surface (Predicted Minus Measured) SPL Over Flight Envelope	226
127	Predicted and Measured Effect of Nacelle Tilt Upon Fuselage SPLs	227
128	Summary of Predicted and Measured SPLs at the Wing Acoustic Boom	227
129	Wing Lower Surface Acoustic Data - Prop Off	228
130	Wing Lower Surface Acoustic Data - Prop On	228
131	Wing Upper Surface Acoustic Data - Prop Off	229



LIST OF FIGURES (CONT'D)

<u>Figure</u>	<u>Title</u>	<u>Page</u>
132	Wing Upper Surface Acoustic Data - Prop On	229
133	Slipstream/Wing Impingement; Fluctuating Pressure Time Histories	230
134	Slipstream/Wing Impingement; Narrow Band Spectra of Fluctuating Pressures	231
135	Wing Lower Surface Measured FPL Distribution	232
136	Wing Lower Surface Distribution of Measured FPLs Along Leading Edge	232
137	Wing Upper Surface Measured FPL Distribution	233
138	Wing Upper Surface Distribution of Measured FPLs Along Leading Edge	233
139	Chordwise Distribution of Measured FPLs Over Wing Inboard Section	234
140	Wing Inboard Surface Measured FPL Dependence on Propfan Tip Speed and Power	235
141	Wing Outboard Surface Measured FPL Dependence on Propfan Tip Speed and Power	235
142	Wing Lower Inboard Measured FPLM Variation Over Flight Envelope	236
143	Wing Upper Inboard Measured FPLM Variation Over Flight Envelope	236
144	Wing Upper Outboard Measured FPLM Variation Over Flight Envelope	237
145	Wing Lower Outboard Measured FPLM Variation Over Flight Envelope	237
146	Relation Between Wing FPLM and Fuselage SPLM	238
147	Effect of Nacelle Tilt on Wing Surface Measured FPLs by Quadrant	238
148	Effect of Nacelle Tilt on Wing Surface Measured FPLs Within Flight Envelope - Lower Inboard	239



LIST OF FIGURES (CONT'D)

<u>Figure</u>	<u>Title</u>	<u>Page</u>
149	Effect of Nacelle Tilt on Wing Surface Measured FPLs Within Flight Envelope - Lower Outboard	239
150	Correlation of Nacelle Tilt Effect on Wing FPLs and Fuselage SPLs	240
151	Slipstream Impingement Fluctuating Pressure Prediction Methodology	241
152	Summary of Wing Predicted and Measured FPLs	241
153	Wing Lower Surface Measured and Predicted FPLs	242
154	Wing Lower Surface Predicted and Measured FPL	242
155	Predicted and Measured Wing FPL Dependence on Propfan Power and Tip Speed	243
156	Cabin Floor Plan	243
157	Illustration of Cabin Interior Surface Conditions	244
158	Identifications and Positions of Cabin Microphones	245
159	Identifications and Positions of Selected Exterior Microphones	246
160	Identifications and Positions of Selected Fuselage and Wing Accelerometers	247
161	Cabin Noise Spectral Character and Comparison With Exterior	248
162	Lateral and Axial Variation of Cabin Noise	249
163	Circumferential Variation of Cabin Noise	250
164	Spatial Variation of Cabin Noise in Propfan Plane, Blade Passage Frequency	250
165	Cabin Noise Variation Fore and Aft in Four Buttress Planes	251
166	Effect of Fuselage Pressurization on Cabin Noise	252
167	Effect of Cruise Flight Condition on Cabin Noise	252

LIST OF FIGURES (CONT'D)

<u>Figure</u>	<u>Title</u>	<u>Page</u>
168	Effect of Propfan Power and Tip Speed on Cabin Noise	253
169	Acoustic Diagnostic Testing	254
170	Comparative Response at 225 Hertz, at Wing and Fuselage Accelerometers, with Shaker Force Applied at Front Spar Outboard of Drive Engine	255
171	Typical Vibratory Force Spectrum Applied to Wing for Structureborne Noise Diagnosis	256
172	Vibratory Response at the Location of the Applied Force, for the Force Spectrum Above (Figure 174)	256
173	Relation Between Normalized Average Wing Tonal Vibration Level and Applied Force Level	257
174	Relation Between Normalized Average Fuselage Tonal Vibration Level and Applied Force Level	258
175	Relation Between Normalized Average Cabin Tonal Noise Level and Applied Force Level	259
176	Comparisons of Predicted Structureborne Noise and Measured Total Noise in the Cabin, for High- and Low-Altitude Cruise	260
177	Comparison of Oscillatory Pressure Levels on the Wing and Fuselage Surfaces, for a Cruise Flight Condition	261
178	Noise Reduction at the First Three Orders of BPF, for a Range of Cruise Conditions, Showing No Evidence of Structureborne Noise	262
179	BPF Noise Reduction for a Range of Tip Speeds/BPFs and Cruise Conditions, Showing a Possible Structureborne Contribution	262
180	Illustration of Noise Reduction Required at Blade Order Tones in Order to Achieve a Cabin Level of 80 dBA	263

LIST OF SYMBOLS AND ABBREVIATIONS

AGL	Above ground level
AL	Acceleration level
BL	Buttress Line
BPF	Blade passage frequency
c	Speed of sound
C	Centigrade
CBFM	Constant bandwidth frequency modulation
CG	Center of gravity
C_L	Lift coefficient
cm	Centimeters
C_p	Propfan power coefficient
dB	Decibels
dBA	"A"-weighted noise
dBOA	Overall noise
DC	Direct current
D_p	Propfan diameter
D_F	Fuselage diameter
DSA	Data sample average
EF	Excitation factor
EF_{eq}	Equivalent excitation factor
EPNL	Effective perceived noise level
F	Fahrenheit
FFT	Fast Fourier transform
FL	Input force level
FM	Frequency modulation

LIST OF SYMBOLS AND ABBREVIATIONS (CONT'D)

FPL	Fluctuating pressure level
FPLM	Maximum FPL in an area
fps	Feet per second
FS	Fuselage station
ft	Feet
H	Altitude
hp	Horsepower
Hz	Frequency, Hertz
IL	Insertion loss
in.	Inches
IRIG	Intermediate range instrumentation group
IRP	Infrequently repeating peak
J	Propfan advance ratio
KCAS	Knots, calibrated air speed
KEAS	Knots, equivalent airspeed
kHz	KiloHertz
km	Kilometers
kts	Knots
kw	Kilowatts
m	Meters
M	Mach number
mm	Millimeters
mps	Meters per second
M_{ROT}	Propfan rotational Mach number
M_{TH}	Propfan tip helical Mach number

LIST OF SYMBOLS AND ABBREVIATIONS (CONT'D)

N	Newtons
NR	Noise reduction
NT	Nacelle tilt angle
OASPL	Overall sound pressure level
P	Per revolution (as in 1P)
PCM	Pulse code modulation
PNdB	Perceived noise level
PNLT	Tone-corrected perceived noise levels
PSHP	Propeller shaft horsepower
psi	Pounds per square inch
PTH	Pressure time histories
q	Freestream dynamic pressure
QEC	Quick engine change
rpm	Revolutions per minute
RSS	Root sum squared
sec	Seconds
shp	Shaft horsepower
SPL	Sound pressure level
SPLM	Maximum SPL in an area
t	Time
TRAM	Cabin traversing microphone boom
V_{ROT}	Propfan rotational velocity
WL	Water line

LIST OF SYMBOLS AND ABBREVIATIONS (CONT'D)

Greek Symbols:

α, α_A	Aircraft angle of attack
β	Propeller blade angle
β_A	Aircraft sideslip angle
ϵ	Upwash angle
ρ	Freestream air density
ϕ	Azimuthal angle
θ	Polar angle
ψ	Propeller inflow angle

1.0 SUMMARY

Flight tests were performed to evaluate structural integrity and noise characteristics of a large-scale, advanced, single-rotation propfan designed for cruise flight at Mach 0.8, 10,668m (35,000 ft). This 2.74m (9 ft) diameter propfan comprised eight, thin, swept, variable-pitch blades mounted on an aerodynamically contoured spinner. The testbed aircraft was a modified Gulfstream II business jet with the propfan drive system mounted on the left wing. The flight test program included or simulated the full range of flight conditions (takeoff, climb-out, cruise, descent, and landing) anticipated for propfan powered aircraft.

The propfan was well-behaved structurally over the entire flight envelope with blade response dominated by once-per-revolution (1P) loads. The measured vibratory response showed expected trends with airspeed, power, rpm, and flight Mach number. Vibratory response variation with airspeed and nacelle tilt angle was directly proportional to excitation factor, as expected. The effect of inflow angle was strong.

Over a broad range of flight conditions, near-field noise and low-altitude, far-field noise were dominated by tones at first blade-passing frequency (BPF), but tones at higher harmonics were often distinguishable. At the design cruise condition, a large area of the fuselage was exposed to sound pressure levels (SPL) greater than 130 dB at first order BPF.

Cabin noise data also were dominated by blade order tones. For untreated cabin walls, the interior noise spectra were similar to exterior spectra with tone levels reduced by 25 to 30 dB. At the cabin noise levels measured, structureborne noise was not a significant fraction of total noise.

Fluctuating pressure levels (FPLs) were high on the wing surfaces immediately behind the propfan tips, and a significant area of the wing was exposed to FPL values greater than 140 dB.

Noise predictions generally underestimated ground SPL values and significantly underestimated FPL values in the propfan slipstream. For SPL values on the fuselage, the methods tended to underpredict noise for high power climb conditions and overpredict for high-speed cruise conditions.



2.0 INTRODUCTION

2.1 BACKGROUND

In response to national emphases on fuel conservation, the Advanced Turboprop (ATP) Project Office was established at NASA Lewis Research Center in the mid-1970s. The major objective of this office was to extend the excellent low-speed propulsive efficiency of the propeller to high subsonic speeds.

Working with Hamilton Standard, the SR (single rotation) series of high-speed propellers were developed and were dubbed "propfans." Wind tunnel model tests, combined with aircraft mission analyses, indicated that the best of the propfans would permit fuel savings of greater than 20 percent relative to equivalent-technology turbofan-powered transport aircraft cruising at Mach numbers of 0.8. Furthermore, the wind tunnel tests showed the propfans to be much quieter than any high-speed propellers developed earlier. These advances in propeller technology resulted from the use of very thin blades that were swept back radically in the outboard region.

Prior to declaration that propfans were ready for application, NASA determined that two steps were necessary. First, there must be assurance that the propfan blades--representing a radical departure in geometry from earlier blades--could be produced with the infinite-fatigue-life properties necessary for commercial aircraft. Second, more knowledge was needed about the noise characteristics of propfans to determine if: (a) the cabin noise treatment weight penalties were acceptable, and (b) propfan-powered aircraft could meet community noise standards.

To answer these questions, NASA established the Large-Scale Advanced Propeller, or LAP, Program and the Propfan Test Assessment, or PTA, Program. In the LAP Program, Hamilton Standard designed and built a 2.74m (9 ft) diameter version of their SR-7 propfan; and in the PTA Program, the Lockheed Aeronautical Systems Company developed a flying test platform for the LAP and performed a series of flight research tests.

The LAP rotor, as shown in Figure 1, consisted of eight, thin, highly swept blades, with tips designed to operate at helical Mach numbers of almost 1.2 at the design flight speed of Mach 0.8 at 10,668m (35,000 ft). The PTA aircraft was a Gulfstream II business jet that was modified to mount the propfan propulsion system on the left-hand wing while retaining the aft-mounted Spey engines as the primary power source. The propfan was powered by an Allison 501-M78 turboshaft engine rated at 4475 kw (6000 hp). The aircraft was extensively arrayed with microphones, pressure transducers, and accelerometers, while the propfan blades were instrumented with strain gages for the measurement of the desired research data.

This report presents results from the flight test portion of the PTA Program.

2.2 OBJECTIVES AND SCOPE

The objectives of the PTA flight test program were to evaluate:

- o Propfan structural integrity
- o Propfan source noise
- o Associated propfan-related cabin noise and vibration
- o FAR-36 community noise

The flight test envelope for the major portion of the research tests is shown in Figure 2. It was required that tests cover the propfan design point of Mach 0.8 at 10,668m (35,000 ft), and it was desired that data be obtained to Mach 0.85 at 12,192m (40,000 ft).

It was specified that flight research tests include four altitudes above 1524m (5000 ft), selected to cover the normal flight envelope of Figure 2 and, if possible, the extended flight envelope. At each altitude, at least four Mach numbers were to be selected. It was also specified that low-altitude tests should be conducted at a minimum of two altitudes to define far-field, propfan-generated noise at stations consistent with the FAR Part 36 noise measurement locations.

It was required that the test program provide a range of propfan excitation factors from 2.0 to 4.0 (4.5 desired), and that the higher-order vibratory loads of the propfan be in the range of 12 to 30 percent of the total dynamic loads. Excitation factor (EF) is a parameter developed by Hamilton Standard as a measure of unsteady aerodynamic loads on propeller blades caused by flow nonuniformity and is discussed in more detail in Appendix A.

In the PTA Program, a range of 1P excitation was provided by changing the nacelle tilt angle in a vertical plane parallel to the fuselage centerline plane. In this test program, a nacelle tilt of -1 degree, relative to the fuselage reference plane, was the baseline configuration. Two other nacelle tilt angles (-3 and +2 degrees) were also tested. The desired higher order excitation content was obtained by positioning the engine inlet an appropriate distance behind the propfan plane.

Some ground tests are also described in this report. They were required to:

- o Evaluate the relationship between wing excitation and cabin noise
- o Assess cross wind effects on propfan blade vibratory loads
- o Screen for incipient propfan stall flutter in taxi tests

The airplane was extensively instrumented with 33 microphones inside the cabin, 45 on the fuselage exterior surface, and 44 on the wing in the regions washed by the propfan slipstream. Another 5 microphones were placed in a boom on the left wing at a distance outboard of the propfan equal to the distance of the propfan from the fuselage. Accelerometers



were located at a number of positions on the wing and fuselage to measure vibrations and to assess the significance of structureborne noise.

The propfan blades were instrumented with 30 strain gages distributed over 5 blades. Outputs from these gages were continuously monitored by Hamilton Standard personnel whenever the propfan was operated.

High-altitude flight research tests were flown from the Lockheed facility at Dobbins Air Force Base, Marietta, Georgia. The low-altitude flight research tests were flown from NASA's Wallops Flight Test Station, Wallops Island, Virginia. First flight of the PTA aircraft was in March 1987; flight research tests began in June 1987; and tests were completed in March 1988.

Two additional flight tests were performed that were not part of the original PTA Program. One involved noise measurements for a special acoustic wall treatment that was installed in the PTA cabin. This wall treatment was designed and built under a separate contract, NAS1-18036, from NASA-Langley, and results will be reported under that contract. The second flight test added was a high-altitude, en-route noise test performed in cooperation with the FAA, and results will be reported by that agency.

Predictions were made of propfan vibratory blade stress, near-field sound pressure levels on the surface of and inside the fuselage, fluctuating pressure levels on the wing surfaces washed by the propfan slipstream, and sound pressures on the ground for low-altitude flyovers. Comparisons of predictions with measured data were made for a representative array of test variables.

2.3 SIGNIFICANCE OF THE PTA FLIGHT RESEARCH PROGRAM

The PTA flight research program accomplished all of its technical objectives. It demonstrated that advanced technology, high-speed propellers can be developed that will operate safely through the entire operating range of high-speed subsonic commercial aircraft. It also provided near- and far-field noise data on a full-scale propfan that can be used to update predictions that earlier were based on small-scale wind tunnel tests.

Another accomplishment that may have great long-range significance was the acquisition of a large amount of high-quality noise data for which test parameters were systematically varied. The data analyses already performed have shown a good many areas where noise prediction methods are inadequate, and in some cases have pointed the way to needed improvements in analytical methods. It is expected that further analysis of this data base can be very beneficial in developing better noise prediction methods.

An example of new insight that has been gained is the recognition, on the basis of PTA data analysis, of the significance of inflow angularity not only on blade loads, but also on propeller noise. The prediction codes used did not adequately account for this variable; the PTA data will not only provide insight for improvement of the codes, but also provide the systematic data base against which improved codes can be evaluated.

3.0 TEST HARDWARE

3.1 LARGE-SCALE ADVANCED PROPFAN (LAP) DESCRIPTION

The large-scale advanced propfan, shown in Figure 1, was a 2.74m (9 ft) diameter, 8-bladed, tractor-type propeller designed for a disk power loading (power/ D_p^2) of 257 kw/m² (32 shp/ft²) at the Mach 0.80, 10,668m (35,000 ft) cruise condition. It had a hydraulically-actuated blade pitch change system and a hydromechanical pitch control that allowed the propfan to operate in a speed governing mode.

Features of the structural configuration of the LAP blades are shown in Figure 3. These include a central aluminum spar which forms the structural "backbone" of the blade, a multi-layered, glass-cloth-reinforced shell overhanging the leading and trailing edge of the spar, a nickel sheath which covers the leading edge of the outer two-thirds of the blade, and a non-operational integral de-icing heater in the inboard leading edge area. Though the scope of the LAP testing never included utilization of the blade heaters, they were installed to evaluate the structural response of a blade closely resembling that of a typical blade configuration. The remaining internal cavities were filled with low-density rigid foam. The outboard portion of the spar was intentionally moved forward toward the blade leading edge to increase stability by reducing overhung mass in the tip trailing edge, while at the same time increasing the integrity of the leading edge from the standpoint of resistance to foreign object damage.

The blade design made use of a NACA Series 16 airfoil outboard and a Series 65 circular arc airfoil inboard. Each blade had an activity factor of 227.3 with 45 degrees of blade leading edge sweep at the tip. The blades were designed with predeflection so that they would assume the desired aerodynamic shape at the cruise operating condition.

A more detailed description of the LAP blades can be found in Reference 1.

3.2 PTA AIRCRAFT

The PTA testbed aircraft is shown in Figure 4. The testbed was developed from a Gulfstream Aerospace GII business jet aircraft, with the PTA propulsion system installed on the left wing. The propfan was powered by an Allison 501-M78B drive system (modified Model 570 industrial gas turbine engine and a modified T56 reduction gearbox). The direction of propfan rotation was up inboard.

This drive system was mounted in a forward nacelle compartment, identified as the QEC or "quick-engine-change" assembly. The installation was designed so that the QEC could be tilted up or down to change the inflow angle to the propfan. As previously mentioned, this variation in nacelle tilt was required to obtain the desired range of propfan blade loading.

The propfan installation on the left wing required some modification of the wing structure to improve wing flutter stability. Further improvement



in flutter margin was obtained by installation of a dynamic balance boom on the wing tip. A microphone boom was also installed on the left wing outboard of the nacelle at the same distance from the propfan as the fuselage was on the inboard side of the nacelle. This boom contained five microphones at the same longitudinal stations as five fuselage microphones to assess the effect of propfan rotation direction on noise.

To partially offset the weight of the additions to the left wing, a static balance boom was placed on the tip of the right hand wing. A flight test instrumentation boom was located on the aircraft nose to measure velocity and flow incidence angles. Over 600 channels of test data were tape recorded on board the aircraft with approximately 250 of these channels telemetered to the ground.

4.0 INSTRUMENTATION

4.1 PROPFAN INSTRUMENTATION

The propfan FM electronic instrumentation system provided the capacity to transmit 33 channels of information from transducers on the rotating portion of the propfan to data collection and monitoring equipment in the stationary field. Electric power for the instrumentation system and signals from the transducers were transmitted across the rotating/stationary interface by a brush block and platter-type slip ring assembly. The configuration of the propfan allowed for only eight slip rings. The need to transmit 33 channels of information, therefore, necessitated the use of multiplexing. The DC signals from 32 of the transducers in the rotating field were divided into two groups of sixteen and converted to frequency modulated signals by voltage-controlled oscillators. Each group was then multiplexed by a mixer, allowing 32 channels to be transmitted through two slip rings. The groups of 16 channels were then detranslated in the stationary field to 4 groups of 4 multiplexed channels (IRIG Standard/A through 4A) for recording. Simultaneously, discriminators demodulated each channel for real time monitoring of data. One discriminator was tuned to the center frequency of each channel. A schematic of the electronic data acquisition system is presented in Figure 5.

The FM electronic instrumentation system provided inherent noise immunity for data transmission. The frequency response of the system was 0 to 1000 Hz. Overall accuracy of the system was ± 3 percent RSS. Time correlation between channels was ± 13.8 microseconds.

Transducers installed on the propfan included strain gages to measure vibratory strain in the blade structure, pressure transducers to measure the actuator high and low pitch pressures, a potentiometer to measure the blade pitch angle, and a 1P sensor for measuring the propfan rotational speed.

The instrumentation system allowed for up to 10 strain gages to be installed on each blade, though a maximum of 30 gages were active at any one time. Sixteen active gages could be selected from blades 1 through 4, and an additional 16 could be selected from blades 5 through 8. Selection of the desired combination of strain gages was accomplished using eight programmable connectors mounted on the propfan hub. Programming of the connectors required jumper wires to connect the sockets of patch boards in the connectors. A total of 60 gages were applied to the propfan blades for the PTA test program. The gages were located at points where high stresses were predicted to occur for the various modes of aeroelastic response; flatwise bending, edgewise bending, torsion, and additional points to establish stress distributions. Strain gages were installed at the same location on several different blades in order to provide redundancy in case of a strain gage malfunction. This redundancy also allowed phase relationships between blades to be established and provided verification that similar aeroelastic phenomena were occurring at the same locations on different blades.

The gage locations are shown in Figures 6 through 9, and the active gages are indicated. The inactive gages were positioned to be used as backups in the event of primary gage failure. The strain gage pairs on the blade shanks and "vee" shear pairs (Gages 65V and 66V in Figure 8 with their counterparts at right angles) on the blade aerodynamic surfaces were wired to act as one gage.

Data from the propfan instrumentation was recorded on a 14-track IRIG tape recorder. Real time monitoring of data was accomplished using two, 4-channel oscilloscopes and a spectrum analyzer. The oscilloscope provided a time domain display of eight channels simultaneously. The spectrum analyzer provided a frequency domain display of one channel at a time.

4.2 AIRCRAFT SURFACE PRESSURE AND FLIGHT CONDITION INSTRUMENTATION

The data acquisition system carried on board the aircraft is depicted in Figure 10. Two primary multiplexing methods, Pulse Code Modulation (PCM) and Constant Bandwidth Frequency Modulation (CBFM) were used to condition the data signals for recording on 28-track magnetic tape. PCM was used for low frequency signals and CBFM for the dynamic data with frequency response to 2 kHz. Proportional bandwidth FM/FM telemetry was used to transmit selected data channels to the ground station for real time monitoring.

Steady-state static pressures were measured on the wing and propfan nacelle. The locations of these measurements are shown in Figures 11 through 13. Pressures were referenced to the nose boom static pressure and were measured with electronic scanning modules located in the wing leading edge region. Pressures and temperatures were also measured inside the PTA nacelle compartments.

Instrumentation was carried on board the aircraft to measure freestream properties, flow incidence angles, aircraft pitch and bank angles, Spey engine conditions, and control surface deflections. The propfan drive system and its nacelle were instrumented so that engine and gearbox vibrations and nacelle environmental conditions could be carefully monitored.

In addition to the surface pressure and Spey engine condition measurements referred to above, the following propfan engine and flight condition parameters were also acquired:

- o Propfan rpm
- o Engine torque
- o Power lever position
- o Speed lever position
- o Sideslip angle
- o Pitch angle
- o Indicated airspeed
- o Mach number

- o Aircraft CG vertical acceleration
- o Ambient air temperature
- o Ambient air pressure

These parameters were measured and recorded using Lockheed-installed instrumentation and the Lockheed data acquisition system. Time correlation between the Lockheed and Hamilton Standard measured parameters was obtained by recording the Lockheed time code generator signal on the Hamilton Standard data tapes.

4.3 AIRBORNE ACOUSTICS AND VIBRATION INSTRUMENTATION

To record acoustics and vibration data on the aircraft, there were 127 microphones, 99 accelerometers, and 14 strain gages that were distributed as indicated in the table of Figure 14. Locations of this instrumentation are shown in detail in the figures and tables of Appendix B.

The microphones used inside the cabin were Bruel and Kjaer prepolarized condenser microphones that were accurate to 0.5 dB over the total frequency range of PTA testing and somewhat better in the frequency range of the propfan fundamental tone and first harmonic.

On the exterior surfaces of the fuselage and acoustic boom, Kulite microphones of 0.254 cm (0.1 in.) diameter were used. Slightly larger wafer-shaped microphones (also Kulites) were used on the wing to allow a flush installation without penetration of the wing surface. The estimated accuracy of measurements from flight to flight was usually within 1 dB.

The presence of these surface microphones on the wing and fuselage and their known sensitivity to moisture damage necessitated the restriction that the PTA aircraft operate only when there was no precipitation. On ferry flights and other occasions when there was danger of encountering precipitation, the exterior surface microphones were covered with a waterproof tape.

4.4 ACOUSTICS GROUND INSTRUMENTATION

Ground instrumentation for the far-field acoustics measurement was arrayed along the hard surface Runway 10-28 at NASA Wallops Flight Test Station as shown in Figure 15. All test flights were flown along paths at right angles to this instrument array. The inset of Figure 15(a) shows the relative positions of the two microphone installations used for these tests. Tripod microphones were mounted over grass at a distance of 2.44m (8 ft) from the edge of the hard runway surface while the inverted microphones were mounted on the runway at the same distance from the edge.

Details of the two microphone installations are shown in Figure 16. The diaphragms of the inverted microphones were positioned 6 mm (0.25 in.) above the hard surface. The other microphone of each pair was mounted on a tripod so that the microphone diaphragm was 1.2m (4 ft) above the grassy surface and inclined slightly to present a grazing incidence to the

propfan sound waves. These tripod microphones were also fitted with windscreens. Four-track FM tape recorders were located at each microphone station; two tracks to record the microphone signals, one for time codes, and voice data and the fourth for tape speed compensation signals.

For the lateral noise attenuation measurements, it was important to have microphones at large distances from the flyover path, so for these tests the aircraft was flown over the west end of Runway 10-28 as indicated in Figure 15(a). For the FAR 36 sideline noise tests, the aircraft was flown along a path towards the midpoint of that runway so that data could be recorded on both sides of the flight path at the same time.

4.5 AIRCRAFT SPACE POSITIONING MEASUREMENTS

For the low-altitude, far-field noise tests, a C-band transponder was installed on the aircraft so that the aircraft could be tracked by the Wallops Airborne Real-Time Radar Control system. This system provided aircraft position data in terms of longitudinal, lateral, and vertical distance from the reference station in real time. For backup, a video camera was installed at the ground reference station to record the flight of the aircraft as it passed overhead. Altitude over the reference station was also measured with the aircraft's flight instrumentation.

4.6 METEOROLOGICAL INSTRUMENTATION

Meteorological data during the far-field noise tests were obtained from the Wallops base weather station, a tethered balloon, and a free balloon. The base station provided conditions at 10m (33 ft) above ground level, updated at 20-second intervals, and displayed on TV screens. Post-test, these weather conditions were available in a printed five-minute-average format.

The tethered balloon permitted readings of temperature, pressure, relative humidity, wind speed, and wind direction at specified intervals from 10m (33 ft) to 457m (1500 ft) above ground level.

Free balloons were released prior to flight tests--primarily to determine if meteorological conditions were appropriate for testing. These were particularly helpful in identifying temperature inversions and in determining when the temperature gradients were within the allowable range.

5.0 TEST TECHNIQUES AND PROCEDURES

5.1 GROUND TESTS

5.1.1 LAP Structural Integrity Evaluation

Static and taxi tests were performed to measure propfan blade vibratory stresses and extend the operational envelope of the blades. The initial static tests were followed by taxi tests and then by crosswind tests. In order to establish controlled conditions for the crosswind tests, the propwash from a C-130 aircraft was blown across the propfan at several crosswind angles in the arrangement shown in Figure 17.

5.1.2 Baseline Acoustics and Vibration Tests

One of the objectives of the acoustics program was to establish the transmission paths for noise and vibration that entered the aircraft cabin during flight. In order to accomplish this, it was necessary to perform baseline ground tests. In these tests, the PTA aircraft was supported on its landing gear in a hangar and subjected to acoustic and vibratory signal inputs of known strength. For each input signal, accelerometer and cabin noise readings were recorded. The experimental setup for these tests is shown in Figure 18.

5.2 FLIGHT RESEARCH TESTS

In discussing test techniques and procedures, the flight research tests are best described in terms of "high-altitude" and "low-altitude" tests rather than in terms of test objectives--primarily because a given test was often used for more than one objective. Furthermore, the major differences in techniques and procedures were more a function of test altitude than other factors.

A general technique used in both high- and low-altitude tests dealt with the inclusion of nacelle tilt angle as a primary variable. The nacelle tilt provision was designed into the PTA aircraft to permit a wide range of dynamic loading environment for the propfan. The problems associated with attaining this range and the need for the nacelle tilt can be illustrated with Figure 19, using the parameter, equivalent excitation factor, or EF_{eq} . Excitation factor is discussed in detail in Appendix A.

Figure 19 shows the variation of EF_{eq} with altitude, Mach number, aircraft gross weight, and nacelle tilt angle. For a given nacelle tilt angle, say 2 degrees, it can be seen that all of the other variables allow EF_{eq} to range only from about 3.5 to 4.5. Only by varying the angle of the propfan rotor axis, or nacelle tilt, could the desired range of EF_{eq} be obtained. From the analysis shown in Figure 19, nacelle tilt angles of +2, -1, and -3 degrees were chosen for the PTA aircraft.

The requirement for higher order content in excitation factor was met for the PTA aircraft by the location of the propfan engine inlet. The

asymmetric disturbance produced by the scoop inlet behind the propfan distorted the flow sufficiently to produce the desired higher order excitation. Guidance for inlet location was obtained from the small-scale model tests reported in References 2 and 3.

In all of the flight tests, critical parameters relevant to the propfan propulsion system and to propfan blade stresses were monitored in real time aboard the aircraft.

5.2.1 Low-Altitude Tests

The low-altitude flight research tests were conducted at the NASA Wallops Flight Test Station in Virginia because of the relatively low background noise and favorable topography in that location. The test plan is shown in Figure 20. After initial trial flights, however, it was concluded that the lowest safe test altitude (with allowance for engine failure) was the 305m (1000 ft) level. Test altitudes, therefore, ranged from that level up to 488m (1600 ft) AGL. All tests were planned for an airspeed of 361 km/hr (195 KCAS) with landing gear and flaps retracted.

Atmospheric conditions specified for the tests were:

- o No precipitation
- o No obvious gusts in the test area
- o Wind speed 6.2 mps (12 kts) or less with crosswind component 3.1 mps (6 kts) or less at 10m (33 ft) above the ground
- o No temperature inversions or cloud layers within 914m (3000 ft) AGL
- o Ambient temperature between 4.4°C (40°F) and 38°C (100°F) at 10m (33 ft) AGL
- o Relative humidity less than 95 percent

Terrain conditions satisfied the following requirements:

- o The ground plane elevation of all microphones was within 6.1m (20 ft) of the ground reference point
- o Ground cover was predominantly grass mowed to a height of less than 15.2 cm (6 inches)
- o There was no standing water, dew, or frost within 30.5m (100 ft) of the lines through the ground level microphone stations

For all of the flights with propfan power on, the Spey engines were set at "soft idle" power.

Ground microphone data were measured by tape recorders at each ground station. Data records at these stations were synchronized with the aircraft on-board data and with the Wallops data recording system.

A special test technique was required for the propfan power-off data because it was desired that these data provide a baseline noise measurement with the GII's Spey engines at soft idle. Since the aircraft could not sustain level flight with these engine settings, the procedure depicted in Figure 21 was employed. For each of five test distances from the ground reference station, the aircraft started at an altitude higher than the test altitude, reduced power, and glided through the test point.

Flight paths are depicted in Figure 22. To obtain data on lateral noise attenuation, the aircraft was flown along Path A at the west end of the runway along which the microphones were arrayed. For the FAR 36 overhead and sideline noise data, the aircraft was flown along Path B so that ground data could be obtained on both sides of the aircraft simultaneously.

Aircraft performance data, propfan propulsion system data, meteorological data, and acoustics data were examined daily to insure that test conditions were within prescribed limits. Tests were rerun where necessary.

5.2.2 High-Altitude Tests

All of the high-altitude flight research tests were conducted from the Lockheed flight test facility at Dobbins Air Force Base in Georgia. The flight test envelope and the test parameter variations are shown in Figure 23 for the nacelle tilt angle of -1 degree and in Figure 24 for nacelle tilt angles of $+2$ and -3 degrees. Bare-wall cabin interior noise spatial surveys were made for the flight conditions shown in Figure 25. The effects of aircraft yaw angle on noise and blade stresses were assessed in the test program depicted in Figure 26.

The general test technique was to measure propfan blade stress and noise and vibration at each test point. Data were recorded for approximately 60 seconds after the aircraft was stabilized on a test point. The Spey engine on the left side of the aircraft was always operated at the lowest power setting required to maintain level flight so that the propfan noise signal would be as strong as possible relative to background noise. To evaluate background noise, the test points shown in Figure 27 were flown with the propfan blades removed.

As in the case of the low-altitude tests, data were examined after each day's flight to determine the need for retest.



6.0 DATA ANALYSIS AND PREDICTION METHODS

6.1 PROPFAN BLADE RESPONSE

6.1.1 Propfan Test Data

Data analysis for the large quantity of data collected during the test proceeded as follows. Initially, strip charts of total vibratory strain were made for key strain gage locations for all test conditions. These strip charts served as a pre-screening tool to assess the quality of the data and to examine transient conditions. Figure 28 shows a typical sample of the strip chart record. As shown by the strip chart, each data record consisted of a 30- to 60-second sample during stabilized flight. Any variation in vibratory amplitude over a record indicated that conditions were not stabilized for the data record.

After reviewing the strip charts, the data were statistically analyzed to obtain the data sample average (DSA), or average peak vibratory amplitude. All of the strain gages for all test conditions were reduced to values of DSA. This corresponds to over 20,000 data records for the test.

To further study the blade response, selected data records were reduced by Fast Fourier Transform (FFT) methods to obtain the frequency and amplitude of the vibratory response. The frequency and amplitude data was used for comparisons with predictions as well as evaluations of the way harmonic content varied with operating condition.

6.1.2 Propfan Response Prediction

The calculation technique used to predict blade vibratory response involved the following automated procedure. The prediction code used an iteration scheme which required four steps per iteration. The first step required the calculation of steady-state aerodynamic loads from the Hamilton Standard steady aerodynamic code using appropriate operating conditions and an initial guess of the blade deflected geometry. The second step distributed the aerodynamic loads on a finite element model of the blade in its undeflected (as manufactured) position; and in the third step, the blade deflection due to the applied aerodynamic load was calculated. The final step determined a new set of aerodynamic loads from the deflected blade geometry so that the iterative process could start again.

When the deflected blade geometry did not change from one iteration to the next, the iteration was terminated. This procedure assured that the blade deflections were consistent with the aerodynamic loads. At this point, the steady-state blade operating position was determined for the desired test conditions.

After the steady-state iteration was completed, the unsteady aerodynamic loads were calculated with the Hamilton Standard multi-azimuth unsteady aerodynamic deck. The calculation of unsteady aerodynamic loads required a flow field defined at the propfan plane of rotation. The flow fields

were supplied by Lockheed in the form of tables, one table for each nacelle tilt angle setting, in the axial and tangential directions with respect to the propfan plane of rotation. Given the measured aircraft operating conditions, this allowed interpolation of the flow field for any Mach number from 0.2 to 0.85 at each nacelle tilt angle (-3 degrees, -1 degree, and +2 degrees). The output unsteady aerodynamic loads were in the form of in-plane and out-of-plane harmonic loads for the first four harmonics of rotation or propfan speed.

Each harmonic load component was distributed separately on the finite element blade model, and a direct forced response calculation was performed for each of the first four harmonics of rotation to determine blade vibratory stressing. Steady-state blade deflections were assumed in calculating unsteady aerodynamic loads.

It should be pointed out that whenever calculations are compared to measurements, differences arise both from inaccuracy in measurements and limitation in analyses. To correlate with measured strain, the analysis required a full description of the flight operating conditions. Therefore, the calculated results contained the combined errors in measured airspeed, temperature, pressure, pitch angle, yaw angle, power, and rotational speed.

6.2 ACOUSTIC DATA

Acoustic data for the several types of measurements and tests required different analysis and prediction techniques. In this section, therefore, general data analysis methods are described, and in later sections additional detail is provided where appropriate to describe techniques specific to different kinds of tests.

6.2.1 Acoustic Data Processing

The acoustic data acquisition system on board the PTA aircraft is shown in the block diagram of Figure 10.

At the Lockheed ground facilities, the backbone of the acoustic data processing system was a Digital Equipment Corporation VAX-based computer system. The VAX facility consisted of a large VAX-11/780 computer connected via a DECnet communications interface to a VAX-11/750 computer. The VAX-11/750 was interfaced to analog-to-digital conversion equipment, a PCM decommutation station, and a group of acoustic FFT analyzers. The computers also shared a large disk storage system for test data storage, and each in addition had its own assortment of peripheral devices which included tape drives, disk drives, line printers, electrostatic plotters, and computer terminals.

The data processing work was accomplished primarily using the VAX-11/750 portion of the system. As noted previously, the acoustic and vibration data were recorded by frequency modulation (FM) subcarrier oscillators using constant-bandwidth frequency division multiplexing techniques. The performance and environmental data were recorded by pulse code modulation

(PCM) time-division techniques. Both types of data were recorded on the same 28-track magnetic tape time correlated by IRIG-B time code.

The acoustic and vibration magnetic tape data were replayed into a sub-carrier discriminator system, one 10-channel track at a time. From the discriminators, the data were processed by a bank of five dual-channel, 800-line, 5000 Hz real-time, digital FFT analyzers. These HP Model 3562 narrow-band analyzers were operated in a spectrum analysis mode using Hanning windowing, 40 or 50 averages with 50- to 60-percent overlap, and a frequency range of 0 to 2000 Hertz which resulted in an effective bandwidth of 3.75 Hertz. All five units were interfaced via an IEEE 488 interface to the VAX computer and the plotters. Under computer control, the digital FFT data were transferred to the VAX disk files. A separate 1/3-octave analyzer (BK Model 2131) connected to the IEEE bus was used for processing the far-field noise data, using 1/2-second integration at 1/2-second intervals, and a frequency range of 25 to 10,000 Hertz.

Digital spectral data were compiled in the aforescribed manner for all transducers for selected flight conditions and for selected transducers for the remaining flight conditions.

For the PCM-acquired data, a decommutation station interfaced to the VAX computer was used to input the demultiplexed data along with the time code. A Lockheed-developed software package was used to control and process the data. The engineering unit data, stored as time histories on disk files, were then transferred to report-quality printers. Tabular lists of the values of the important operational parameters were then made for every test run flown in the flight research program. An example is shown in Figure 29.

6.2.2 Processed Data Output Format

The principal medium of display of the near-field acoustic data was a machine plot of narrow-band sound pressure level versus frequency, with a companion tabulation of the values of the important operational parameters, as exemplified in Figure 30.

A computer code was written that read and compiled the amplitude and frequency of the blade-order peaks in the spectral data. Tabular listings of these "peak data" were generated for all transducers and all operating conditions for which data were processed and filed. An example is shown in Figure 31.

The principal medium of display of the far-field acoustic data was a machine plot of level versus time for "A" weighted sound pressure level (dBA), overall sound pressure level (dBOA), and tone-corrected perceived noise level (PNdB). An example is shown in Figure 32. Such plots were made for all ground microphones and all low-altitude test conditions.

From these time-history plots, time increments were selected at which 1/3-third octave band spectra were machine plotted. A companion tabulation of the values of the important operational parameters was printed

on the same plots. An example is shown in Figure 33. Plots of this type were made for selected microphones and conditions.

The far-field acoustic time history data and computed metrics quantities were also tabulated for all microphones and all flight conditions. An example is shown in Figure 34.

In order to study how noise was influenced by various operational parameters, a computer code was developed that compiled and plotted acoustic data as a function of any desired parameter and printed the values of the "non-varied" parameters on the same plots. An example of a near-field noise parametric plot is shown in Figure 35. A far-field (flyover) noise parametric plot is shown in Figure 36.

7.0 RESULTS AND DISCUSSION

7.1 PROPFAN BLADE STRUCTURAL TEST RESULTS

7.1.1 Blade Vibratory Response

The flight test matrix is shown in Figure 37. Each test condition shown in Figure 37 represents a data sample where stabilized flight was obtained at one or more variations of power, rotational speed, or nacelle tilt angle. The data were obtained so that parametric evaluations could be made to study the influence of Mach number, equivalent airspeed, power (torque), and rotational speed.

As mentioned previously, the strain gage data were reduced to obtain a "data sample average" (DSA) of the total vibratory strain at a stabilized flight condition. Figures 38 through 40 summarize the DSA strain data for the inboard bending gage (Gage 11) over the entire flight envelope for the three nacelle tilt angles. These data show that nacelle tilt has a large effect on the vibratory response of the propfan. Upcoming discussions will clarify the trends in the measured strains that are shown in these figures.

Figure 41 shows the typical frequency content of the measured vibratory response of the blade inboard bending strain gage during flight. The figure shows that the response was characterized by peaks at integer multiples of the rotational speed and that the first harmonic (1P) dominated the response. A comparison of measured and calculated mid-chord strain for the above and other conditions establishes the relative importance of the strain gage locations and the harmonic content of their response.

Figures 42 through 44 show calculated and measured 1P and 2P vibratory strain plotted versus non-dimensional blade radius for a 1.5 km (5000 ft) altitude, Mach 0.30 airspeed, maximum continuous power, 100-percent propfan speed, and nacelle tilt angles of -3, -1 and +2 degrees, respectively. As can be seen on all three figures, the measured 1P strain distribution exhibits a peak near the 42-percent radial station, and the strain decreased toward the blade tip until the outermost strain gage shows a slight upward trend in measured strain.

The calculated strain follows a similar distribution, but at a 15-percent higher level inboard on the blade, tapering to 5-percent higher in the mid-blade region, and showing lower strain at the blade tip. The calculation does not show the strain rise at the blade tip, indicating that the local tip loading is higher than predicted. This is possibly due to some three dimensional and/or vortex action, as evidenced in previous tests, that is not included in the current aerodynamic methodology.

The 2P correlation was good for the -3 degree and -1 degree nacelle tilt angles, but underpredicted the strain in the tip region of the blade at the +2 degree nacelle tilt angle. The +2 degree nacelle angle 2P results

are trivial, however, because of the low amplitude response of the 2P harmonic at that condition.

Figure 45 shows curves of the test and calculated 3P and 4P vibratory strain versus non-dimensional radius at the 1.5 km (5000 ft) altitude, Mach 0.30 airspeed, and -1 degree nacelle tilt condition. The strain scale of Figure 45 has been reduced to 100 micro-strain because of the low amplitude response of the third and fourth harmonics. The 3P harmonic was overpredicted and the 4P harmonic underpredicted. The majority of the predicted test points gave similar results for the 4P harmonic. Both calculated and test amplitudes, however, were at negligible levels.

The Campbell plot, Figure 46, obtained from PTA ground testing shows a 3P/first edgewise critical speed at 100-percent propfan speed. All of the test points chosen for predictions were at 100-percent propfan speed with the exception of the points selected to analyze the effect of propfan speed. As shown by Figure 45, the predictions at 100-percent speed overpredicted the strain values because of this critical speed. This overprediction arose from the lack of damping in the structural and aerodynamic model of the SR-7L blade used in the prediction code. The exact location of the 3P critical speed changed with each unique operating condition, and as a result, the degree of error at the 100-percent speed condition changed greatly from case to case. Since the test data showed that the primary vibratory blade strain was at the 1P frequency and that the highest strain occurred on the inboard portion of the blade, the remaining flight test discussion focusses on 1P inboard blade and shank response trends.

As discussed in Appendix A, the key parameters that influence blade 1P response are equivalent airspeed and nacelle tilt (inflow) angle. Other secondary parameters are power, Mach number (compressibility), and rotational speed. The effect that equivalent airspeed and nacelle tilt had on the blade response is shown in Figures 47 and 48 for a low-altitude climb condition and a high-altitude cruise condition. The general shape of the response curves with equivalent airspeed is similar for both altitudes. For the -3 degree tilt angle, the strain level initially decreased with airspeed and then began to increase rapidly as airspeed increased, while the -1 degree tilt curves show a relatively flat response with a slight decrease in strain at an intermediate airspeed. The +2 degree tilt angle shows a steady decrease in strain over the entire airspeed range. The importance of nacelle tilt is brought out when the design cruise altitude condition of 10,668m (35,000 ft) is examined in Figure 48. A 2 degree decrease in tilt from -1 degree to -3 degrees at the highest speed nearly doubled the blade response. Proper choice of tilt angle significantly affects the overall design of an installation.

To further clarify the relationship between excitation factor and blade response, the relative excitation factor for the three nacelle tilt angles is illustrated in Figure 49. Changes in the magnitude of vibratory response correspond to the absolute value of the excitation factor. The blade response reached a minimum when the EF passed through zero. The -3 degree nacelle tilt EF passed through zero at the lowest airspeed while

the +2 degree nacelle tilt EF never passed through zero. Comparing Figure 49 to Figures 47 and 48 leads to the conclusion that the trend of propfan response to changes in nacelle tilt angle was as expected.

The sensitivity of blade response to nacelle tilt is shown in Figures 50 and 51 along with a comparison to predicted values of strain. Figure 50 shows the 1P and 2P response variation with nacelle tilt for an initial climb condition of maximum continuous power at 1.5 km (5000 ft) altitude and Mach 0.3. The 1P strain increased with increasing tilt angle at a rate of approximately 25 micro-strain per degree of tilt.

Figure 51 shows the 1P and 2P response variation with nacelle tilt for a cruise condition of 10.7 km (35,000 ft) altitude and Mach 0.8. In this figure, the measured 1P strain forms a parabola around the -1 degree tilt angle with a strain increase of approximately 60 micro-strain per degree of tilt on either side of the minimum. The increased sensitivity at high speed is due to the high dynamic pressure at these conditions and can be related back to the EF which shows a linear increase with tilt but a quadratic increase with equivalent airspeed. In both figures, the 2P strain is low and relatively unaffected by the large nacelle tilt changes.

The correlation of predicted and measured 1P strain is better at the low-speed conditions in Figure 50 than at the high-speed conditions in Figure 51. To get a better understanding of why the measured and predicted values differ, the excitation factors resulting from the calculations were examined for a number of operating conditions. The computed excitation factors showed that for the calculations to better correlate with measurements, the assumed negative tilt angle would have to be increased. This suggests two areas in need of improvement that would ultimately improve the correlation. One is that the nacelle tilt used in the calculation of the flow fields could be improved, and secondly, the measurement of aircraft pitch and yaw angles could be improved. It should be noted that the aircraft pitch and yaw measurements, together with the nacelle tilt measurement, had an accuracy of plus or minus 0.5 degree, and these values were used directly to compute the flow fields needed for the 1P calculations. In terms of accuracy of the predictions, this puts an error band of plus or minus 15 micro-strain around the 1.5 km (5000 ft) calculations in Figure 50 and an error band of plus or minus 30 micro-strain around the 10.7 km (35,000 ft) calculations in Figure 51.

After equivalent airspeed and nacelle tilt, power had the greatest effect on blade 1P response. Power is a strong factor because the cyclic loads are influenced by the propfan induced flow. As power is raised, the induced flow increases causing the 1P loads to increase. At low-speed climb conditions, the loads increase approximately with the square root of the power ratio. As flight speed increases, induced flow becomes less important, and the rate of increase with power falls off. Figure 52 shows the effect that engine torque, which at constant rotational speed is synonymous with power, had on the low-speed and high-speed 1P response of the propfan. At low speed, the strain increased at approximately the square root of the power ratio, but at high speed, power had very little

effect on the response. Calculations that were performed for the low-speed conditions showed a similar, but not as strong, effect as that displayed by the test data. The differences between test and analysis became substantial at low power where the propfan was almost windmilling.

To gain an understanding of the importance of a calculation scheme that assures consistent blade deflection and loads, the maximum camber values were plotted versus nondimensional blade radius for the above torque conditions in Figure 53. There was a substantial increase in camber as torque was increased, especially at span locations below 75 percent. Since camber is a measure of the chordwise curvature, it is directly related to the chordwise bending deflections. This figure illustrates the importance of the calculation of the steady-state blade deflected position because of the impact the deflections have on camber and therefore on aerodynamic loading.

The 1P and 2P calculated flatwise shank moment amplitudes are plotted in Figure 54 along with test data versus percent propfan speed at an airspeed of Mach 0.3, 1.5 km (4922 ft) altitude, and maximum continuous power. Both test results and calculations show that rotational speed has little effect on the 1P response. Through some analytical steps, it can be shown that the change in 1P loading for a propfan blade is not directly related to the relative blade section velocity, which contains both freestream and rotational speed components, but is directly related to the freestream velocity as implied by the excitation factor and shown in the data.

The comparison in Figure 54 of 2P test data to calculated values correlates well at propfan speeds above 88 percent. At 78-percent speed, the calculated amplitude was substantially overpredicted. This result is due to the fact that the structural model of the SR-7L blade had no damping properties, and operating at 78-percent speed, the blades were near the 2P/first flatwise critical speed. The 2P test data did not show a large increase in amplitude as the propfan speed was decreased to 78-percent speed. The calculated 2P curve peak location suggests that the calculated 2P/first flatwise frequency was too high.

Figure 55 shows the 1P, 2P, and 3P flatwise shank moment test data plotted versus percent propfan speed at the design cruise point of Mach 0.8, 10.7 km (35,000 ft), and maximum continuous power. The high-speed conditions show similar amounts of 1P and 2P excitations for the -1 degree tilt angle, and also show negligible 3P excitation.

Figure 56 shows curves of 3P and 4P edgewise shank moment variation with propfan speed for the Mach 0.3, 1.5 km (4921 ft) altitude condition discussed above. The 3P amplitude was overpredicted at the 3P/first edgewise critical speed near 100-percent propfan speed but correlated well at speeds up to 94 percent. Again, as was the case with the 2P critical speed, the calculated 3P amplitudes were much higher than test values at resonance (critical speed) because of the lack of damping in the blade model. It also appears that the calculated 3P/first edgewise resonant frequency was too low, considering where the 3P amplitude peak is located from the test data.

The 4P calculations in Figure 56 are in reasonable agreement with test data although the amplitude levels were low compared to the first two harmonics of propfan speed.

The lack of influence of compressibility on 1P response is shown in Figure 57 where shank flatwise vibratory moment is plotted against Mach number for the same equivalent airspeed. The test and analysis conditions used to create this plot were all at 100-percent rotational speed, constant equivalent airspeed of 126 mps (250 KEAS), but at different altitudes so that the speed of sound changed. The only factor that was not held constant, although it would have been desirable, was power, which decreased with Mach number. The 2P amplitude decreased as the Mach number increased and torque decreased. At this equivalent airspeed, with a -3 degree nacelle tilt angle, the 1P excitation was near the minimum value at the tested altitudes. This low excitation factor resulted in low 1P amplitudes over the wide Mach number range tested.

7.1.2 Propfan Aerodynamic Performance

Power coefficients for the propfan are presented as functions of blade angle and are compared to predictions in Figures 58 through 60. A smooth variation of power coefficient with blade angle was observed. The discrepancy between the measured and predicted power coefficient distribution is attributed to inaccuracies in the measurement of blade angle and the measured parameters: torque, rpm, airspeed, and density ratio, which are used to compute power coefficient and advance ratio. Periodic checks of the blade angle calibration, which were conducted during the course of the test, indicated up to a ± 1 degree potential error in measured blade angle. A system accuracy analysis, which considered the individual errors in each of the measured quantities, indicated that a possible overall error of ± 0.09 was possible in power coefficient. In addition, the effect of blade deflections were neglected in aerodynamic performance calculations for these off-design operating cases.

7.1.3 Conclusions - Propfan Structural Response

The test results showed that the propfan was well behaved structurally over the entire flight operating envelope. The blade response was dominated by 1P, and in some cases 2P, loads while all other harmonics were negligible. The measured vibratory response showed expected trends with airspeed, nacelle tilt, power, rpm, and Mach number.

The propfan vibratory response variation with airspeed and nacelle tilt followed the trend expected by an examination of excitation factor. The greater the excitation factor the greater the blade response. The data confirmed the high sensitivity that response had to changes in the nacelle tilt angle. For this installation, a -1 degree tilt of the nacelle was near-optimum to reduce 1P response in the flight envelope.

The flight test results also showed the effect of power at low speed on the 1P response, and that the power effect diminished as the airspeed was increased. The rotational speed and Mach number were shown to have little effect on the response of the propfan.

The comparison of test data to predictions showed that the analysis predicted trends with airspeed, nacelle tilt, power, rpm, and Mach number very well, but the calculations tended to overpredict the inboard response by about 15 percent at low speed. The inaccuracy of the aircraft angle of attack measurement at high speed, coupled with a high sensitivity of blade strain to this angle, prevented a fair comparison of measurement to predictions. The predictions also showed that the blade tip response was underpredicted indicating that the loading distribution on the blade may not be adequately defined.

7.2 ACOUSTICS TEST RESULTS

7.2.1 Far-Field Noise

7.2.1.1 Data Analysis Techniques

The objective of the far-field noise tests was to measure and determine characteristics of propfan noise. Extracting propfan noise from other noise sources, however, required some special techniques in testing, data acquisition, and data analysis. These techniques are described in this section.

Flights were conducted in two phases: (1) propfan blades installed, and (2) propfan blades removed. The purpose of the second phase was to estimate the noise generated by components other than the propfan. The Wallops airport lent itself best to test flights from north to south, but some flights were flown in the opposite direction, and some flights were flown with rearranged microphone locations in order to study acoustic characteristics on both sides of the flight path. The table of Figure 61 together with the test outline of Figure 20 illustrate the test conditions for flights with propfan installed and with propfan blades removed, respectively.

Total Aircraft Noise - Ground acoustic data were obtained for 14 microphones at 7 microphone locations. The operating parameters were varied within the ranges shown below:

Propfan shaft power: 1790 kw (2400 hp) to 4474 kw (6000 hp)
Propfan helical tip Mach number: 0.631 to 0.819
Propfan rotational tip speed: 188 mps (616 fps) to 256 mps (841 fps)
Nacelle tilt angle: -3, -1, and +2 degrees
Sideslip angle: -4.82 degrees to +2.46 degrees
Angle of Attack: 3.80 degrees to 7.10 degrees
Altitude: 256m (840 ft) to 524m (1720 ft)

For data analysis purposes, the definition of nacelle tilt angle, angle of attack, and sideslip angle are illustrated in Figure 62. All flights were level flights with: (1) landing gear and flaps retracted, (2) flight Mach

number nearly constant at 0.31, and (3) Spey engines operating at "soft flight idle." A total of 157 test runs with varying parameters were flown with the propfan operating.

The measured acoustic data were reduced as 1/3-octave band spectra at every 1/2-second interval using 1/2-second linear integration for about 50 seconds (starting at 25 seconds before the aircraft arriving at the reference flyover microphone until 25 seconds after the aircraft passed the reference microphone). Using these spectra, time histories of OASPL, dBA, and tone-corrected perceived noise levels (PNLT) were computed. These data, along with 1/3-octave band spectra at selected times, were examined closely for all the 14 microphones to identify any anomalies in the test data. Typical time histories and 1/3-octave band spectra were shown in Figures 32 and 33.

The data of Figures 32 and 33 include the noise sources of airframe, Spey engines, and propfan drive engine, in addition to the propfan. The results indicate that peak noise was measured close to the overhead position at the time of sound emission. From the spectra, the propfan blade-passing-frequency tone (BPF) is clearly distinguishable from the other sources, and in many cases, the SPL at the second blade passing frequency is also distinguishable. Higher harmonics, however, are not identifiable from these data.

Non-Propfan Noise - The significance of aircraft noise other than from the propfan (airframe and Spey engines, for instance) was evaluated by conducting flight tests under conditions similar to those for total noise, but with propfan blades removed.

Level flight tests were first conducted by operating the Spey engines at the minimum power required. Then a series of flights were conducted with the Spey engines operating at "soft flight idle" power. This required the gliding flight technique discussed in Section 5.

For all these flight runs, acoustic data at seven microphone stations, radar data (to identify the aircraft position as a function of time), and aircraft performance data were obtained. The ground-measured acoustic data were reduced as 1/3-octave band spectra at every 1/2-second interval using the same procedures as for total aircraft acoustic data.

Propfan Noise Extraction - To compare the total aircraft acoustic data with the data from flights with propfan blades removed, the data were normalized to 304.8m (1000-ft) radius as free-field, lossless data. This required first determining the emission angle, the emission time, and the corresponding airplane coordinates from radar data. The acoustic data were then corrected for atmospheric attenuation and spherical divergence. To minimize the ground reflection effects as functions of frequency and incidence angle, only inverted ground microphone data were used. Ground reflections were assumed to be 6 dB and independent of frequency and incidence angle. The coordinate system for normalized data is illustrated in Figure 63.

The lossless data exhibited some unusually high sound pressure levels as shown in Figure 64. The 1/3-octave band spectra from the flyover microphone, at the emission time corresponding to the minimum distance, are compared with and without atmospheric corrections. It may be observed that the lossless spectra in the range from 500 Hz to 3150 Hz remain constant, and beyond 6300 Hz, the sound pressure levels actually increase. This phenomenon is not an expected characteristic of any noise sources from the airplane. After studying the data for several microphones and several flight conditions, it was concluded that the sound pressure levels in the range of frequencies greater than 1000 Hz were not generated by airplane sources. It is conjectured that this is ambient noise (including instrumentation noise). Therefore, the far-field acoustic data were studied only in the frequency ranges from 50 Hz to 1000 Hz.

Using the two Spey engine power conditions (soft flight idle and minimum power for level flights), the effect of the Spey engine power (with propfan blades removed) was determined by comparing normalized 1000-ft radius, free-field, lossless data at various polar angles. Figures 65(a) through (c) illustrate 1/3-octave band spectral comparisons in the flyover plane for three different polar angles. The differences are small in the forward quadrant but increase in the aft quadrant. While it was beyond the scope of this research to investigate Spey engine noise characteristics, these comparisons aid in evaluating whether the level flight data may be used in identifying propfan generated sound pressures. It can be seen in Figure 65 that the gliding flight data must be used. Close examination of these data shows evidence of tones near the frequencies of 80 Hz and 400 Hz.

To investigate these tones, the acoustic data from all seven ground microphone stations for the four runs were reduced as normalized 1000-ft radius, free-field, lossless, 1/3-octave band spectra as functions of polar and azimuthal angle. Doppler corrections were not applied to these data. Typical data are shown in Figure 66. These data are for the flyover plane (azimuthal angle $\phi = 90$ degrees) and polar angles approximately equal to 35 degrees and 90 degrees. The directivity in the flyover plane as a function of polar angle indicated that the frequency band of the tone level changed from 500 Hz in the forward quadrant to 400 Hz when the aircraft was overhead as expected from Doppler frequency shift effects for sound radiating from the airplane. Therefore, it was concluded that this tonal noise was generated at the airplane and propagated to the microphone. No further analysis was conducted to identify the characteristics of this particular source. In the propfan noise data analysis, however, one should use caution in evaluating the propfan noise at or near 400 Hz.

Relative Magnitude of Propfan Noise - The 1/3-octave band spectra of total aircraft noise with the propfan at maximum power, and $M_{TH} = 0.76$, were compared with those of measured noise with propfan blades removed. This was accomplished by selecting similar operating conditions and using the 1000-ft normalized acoustic data. Typical comparisons are shown in Figures 67(a) through (c) in the flyover plane ($\phi = 90$ degrees) for three polar angles. As discussed in the previous section, the sound pressure levels in the high frequency range appear to be contaminated by background

noise. The spectral comparisons in the forward quadrant (Figure 67(a)) indicate that the total aircraft noise in the frequency range of propfan blade passage frequency (200, 250, or 315 Hz) was about 10 dB higher than the noise levels without propfan blades. In other frequency bands, however, propfan-off noise was higher than that with propfan on. This may have resulted from sources like engine inlet cavity noise when the propfan engine was shut down. In comparisons at the polar angles near 90 degrees (where the noise levels are expected to be maximum), propfan-on noise was clearly higher than that with propfan-off in the frequency range greater than 100 Hz (see Figure 67(b)). The comparisons in the aft quadrant (Figure 67(c)) also show that the propfan-on noise was higher than that for propfan-off.

These comparisons indicate that in most cases, the peak OASPL of the total aircraft noise was dominated by a discrete tone sound pressure level at BPF. In certain cases, the discrete tone sound pressure level at twice BPF was also distinguishable from the other sources. Because of the background noise and other anomalies, it is not possible at this time to completely separate the propfan-alone noise throughout the frequency range of 50 Hz to 10,000 Hz. Therefore, the OASPL of total aircraft noise was used to study the variation and trends of propfan noise discrete tones.

7.2.1.2 Propfan Noise Characteristics

Directivity in the Azimuthal Plane - Noise directivity in the azimuthal plane was derived using the data from seven ground (inverted) microphones. The sound pressure levels (SPLs) used were obtained at the time of peak OASPL in the time history. The data were gathered from various flights where operating parameters fell within a specified narrow range. Curves are drawn through these data points using least square fits as shown in Figure 68. These data are for -1 degree nacelle tilt, maximum propfan power, and tip Mach number of 0.760. It may be observed that the sound pressure levels are higher by about 4 dB on the starboard side than on the port side. It is believed that this is primarily an inflow angle effect.

Directivity in the Polar Plane - The directivity in the polar plane was derived from the time history data. The data were reduced to 1000-ft radius as a function of polar angle using radar data. These data show that the noise levels are higher in the aft quadrant than that of the forward quadrant as shown in Figure 69. The maximum noise levels occurred close to 90-degree emission angle.

Effects of Operational Parameters - The PTA aircraft did not represent a realistic propfan-powered aircraft because of its single propfan propulsion system and other special features. However, the acoustic data from these flight tests and the corresponding operational and performance parameters provide an extensive data base. These data may be used in deriving noise characteristics of advanced propellers and to establish variational trends as a function of the important aircraft and propulsion parameters. In deriving the effect of various parameters, it was recognized that the broadband noise, particularly in the high frequency range (i.e., greater than 1000 Hz), was contaminated with background noise, and

therefore, it is not reasonable to use the subjective noise metrics (i.e., dBA, EPNL, etc.). The OASPL, however, represents the blade passing frequency tone level, and therefore, in these analyses the peak OASPLs (in the time histories) were used. The following parameters are recognized to be the important parameters: (a) propfan shaft power, (b) rotational tip speed, (c) nacelle tilt angle, (d) sideslip angle, and (e) angle of attack. The effect of angle of attack on flyby noise was not derived due to lack of sufficient data.

Data were selected from different flights by keeping all the variables except the one for which effects were sought within narrow bands. Then, a linear regression curve fit was applied to the resulting data points. This is illustrated in Figure 70, where the variation of peak OASPL with propfan shaft power is plotted. The other parameters were held within a narrow range.

Variations of peak OASPL with propfan power are studied for flyover, port sideline, and starboard sideline positions. At each position, two microphones (inverted ground microphone on the hard surface and 4-ft high microphone on the grassy surface) are considered. Results are shown in Figure 71. Figures 71(a) through (e) show the variations in OASPL with power for different tip Mach numbers. For M_{TH} in the 0.78 to 0.79 range, the OASPL increases by about 13 dB by increasing propfan power from 2300 hp to 5900 hp. It may also be noticed that at the lower propfan powers, the OASPL increases about 10 dB by increasing the helical tip Mach number from 0.63 to 0.81. Figures 72(a) through (d) show the peak OASPL variation with propfan power for various nacelle tilt angles. These data illustrate that as the nacelle tilt increases (from -3 degrees to +2 degrees) the OASPL increases at all three measurement positions (i.e., flyover, port sideline, and starboard sideline). These changes in nacelle tilt angle changed the OASPL by 3 to 4 dB. The range of other parameters during the tests are indicated on these figures.

Effect of Sideslip Angle - The effect of sideslip angle on peak OASPL is shown in Figures 73(a) through (c). These data indicate that there is very little change in OASPL as the sideslip angle changes. However, it is evident from Figure 73 that the available data are very limited. Therefore, it is not possible to draw broad conclusions about the effects of sideslip angle on peak OASPL.

7.2.1.3 Assessment of Predictions

Sound pressure levels were predicted by Hamilton Standard using a method that included steady and unsteady loading, thickness, and broadband noise components. The loading noise contributions were based on lifting line aerodynamic calculations. The broadband noise was based on Amiet's trailing edge noise theory (Reference 4). Atmospheric effects were computed using the measured temperature and relative humidity. Ground reflections for the inverted ground microphones were assumed to be 6 dB and independent of frequency and incident angle. For the 4-ft high microphones on the grassy surface, the ground reflections were computed as a function of frequency and incident angle using impedance as given in

Reference 5. The sound pressure calculations were made only for propfan-generated noise (i.e., propfan drive engine, Spey engines, and airframe noise sources were not included).

One-third octave band spectra, as a function of time, were computed for 28 operating conditions and 6 microphone positions. The 6 microphones consisted of an inverted "flush" microphone on asphalt and a 4-ft high microphone on the grassy surface for flyover, port sideline, and starboard sideline positions. The actual measured operating conditions were used in the predictions.

Predicted peak OASPLs are compared with the measured OASPLs in Figure 74 where the available data from the 28 flights and 6 microphones were used. The peak OASPL is the maximum value in the OASPL time history. It should be noted that the OASPLs represent the blade passing frequency tone levels. Using the data points, linear regression curves were drawn. It is clear from this figure that the sound pressure levels were generally underpredicted by 6 to 10 dB. Subsequent figures will illustrate the effects of operational variables and provide insight about where the predictions are better or worse than the average.

Figures 75(a) through (f) illustrate the difference between predictions and measurements for 6 microphones separately. The underpredictions are the same order of magnitude for all the microphones. Therefore, it may be inferred that the difference between the prediction and measurement was not due to the propagation effects (atmospheric attenuation and ground reflections) but due to the underprediction of source noise.

Predicted OASPL time histories (signatures) were compared with measurements for all the predicted test conditions. A typical time history comparison is shown in Figure 76. Though the shape of the predicted time history compares well with that of measured data, the magnitudes are underpredicted. It is not appropriate to compare peak noise times since the time references for the two curves are different. Spectral comparisons were made by examining the 1/3-octave band spectra at the time of peak OASPL. A typical spectral comparison is shown in Figure 77. In this figure, the predicted spectra at time, $t = 0$, are compared with the measured spectra at time, $t = 2.5$ seconds (Refer to Figure 76.). It may be observed that the sound pressure levels were underpredicted in all frequencies. As mentioned earlier, the predictions were made only for the propfan source, whereas the measured data include propfan drive engine, Spey engines, and airframe noise. Therefore, the measured broadband noise is not comparable, but the discrete tones are. It may be observed that the results are underpredicted by about 5 to 10 dB.

In Figures 78(a) through (d), the predicted peak OASPLs are compared with the measurements as a function of propfan shaft power for four microphones. These results indicate that the predictions are slightly better at high power conditions than at low power conditions. In Figures 79(a) through (d), the predictions are evaluated as functions of propfan tip Mach number for four microphones. These results indicate that at high tip Mach numbers, the predictions are closer to measured data.

Figures 80(a) and (b) illustrate the comparison of predictions with measurement as functions of nacelle tilt. The predictions appear to be independent of nacelle tilt for inverted ground microphone, whereas the measured data increased as the nacelle tilt increased. The 4-ft high microphone data show the same trend.

7.2.1.4 Lateral Noise Attenuation

Lateral attenuation is generally defined as the attenuation of the sound propagating to the side of the flight path by the factors that are not readily accounted for (see Reference 6). For the purpose of this report, lateral attenuation is defined as the difference between sound pressure levels under the flight path and the sideline sound pressure levels for the same propagation distances as illustrated in Figure 81.

The lateral attenuation was calculated by using the sound pressure levels from flyover and sideline inverted ground microphones at the time corresponding to peak OASPL in the time history. Only the inverted ground microphone data were used so that the differences in ground reflections were minimized. The calculations were made only for the first blade passing frequency (BPF) tone. Since the propfan rotational speed changed from one flight to the other, BPF varied within the range of four 1/3-octave bands (viz, 160, 200, 250, and 315). The sum of the sound pressures in these four bands represents the BPF tone since the BPF tone level is higher than the other three bands by about 10 dB. Therefore, the total sound pressure levels (sum in the four bands) were used to derive the lateral attenuation of BPF tone. The measured flyover sound pressure levels were extrapolated to the same propagation distances as that of the sideline microphone (both corresponding to the emission time). The emission coordinates and the extrapolations were derived using the measured radar, forward speed, and ambient condition data.

The lateral attenuation information derived from the measured data is plotted against elevation angle in Figures 82 and 83 for different nacelle tilt angles. These data were derived from different flights with different altitudes, propfan powers, and propfan tip speeds. Figures 82(a) through (c) show data for the port side and Figures 83(a) and (b) for the starboard side. It is evident from these figures that there is a great deal of data scatter. To derive the trends in the lateral attenuation variation, the data were fitted with least square linear curves.

All of the lateral attenuation data are summarized in Figure 84. It may be seen from these figures that on the port side the lateral attenuation was positive (i.e., noise attenuated), and on the starboard side the attenuation was negative (i.e., noise reinforced). In general, the lateral attenuation was increased as the nacelle tilt increased. From these data, it may be concluded that the lateral attenuation was primarily due to the directivity of the propfan source noise.

7.2.1.5 Conclusions - Far-Field Noise

The first blade passing frequency discrete tone level was significantly higher (order of 10 dB) than other sources, and in many cases, the second and third blade passing frequency tone levels were also distinguishable from other components. The directivity of propfan-generated sound was such that the levels in the aft quadrant were higher than in the forward quadrant. Also, the levels on the starboard side of the aircraft were higher than on the port side.

The noise levels increased with propfan power, tip rotational speed, and nacelle tilt angle. The prediction method, developed by Hamilton Standard and based on lifting line aerodynamics, underpredicted the noise levels by about 8 dB. Based on the behavior of these data, it is suspected that the prediction of loading noise needs improvement. The lateral attenuation of blade passing frequency tone of PTA aircraft reinforced noise on the starboard side and attenuated on the port side. Also, the lateral noise attenuation was a strong function of nacelle tilt angle.

7.2.2 Near-Field Noise - Sound Pressures

7.2.2.1 Test Techniques and Conditions

The acoustic data reported here were measured on the fuselage and on the boom mounted on the wing. The airplane acoustic configuration details are shown in Figures 85 and 86. The acoustic boom was 19 feet long and extended forward of the propfan plane; it was diametrically opposite the fuselage location defined by the closest point of approach to the propfan. The propfan rotated in an up-inboard direction and at the fuselage closest point of approach was 0.616 propfan diameters from the fuselage.

The PTA and SR-7L design cruise conditions are summarized as follows:

- o Altitude = 10,668m (35,000 ft), Mach Number = 0.80
- o Propfan Tip Rotational Speed, $V_{ROT} = 244$ mps (800 fps),
 $M_{ROT} = 0.822$, $M_{TH} = 1.147$, Advance Ratio, $J = 3.06$
- o PSHP = 1933 kw (2592 shp), $PSHP/D^2_p = 257$ kw/m² (32.0 hp/ft²),
Power Coefficient, $C_p = 1.45$
- o Baseline Nacelle Tilt, NT = -1 degree

The propfan blade pitch angle was 58.5 degrees, and the propfan generated a thrust of approximately 8230N (1850 lb). For the rotational tip speed of 244 mps (800 fps), the frequency of the propfan fundamental tone was 226.4 Hz.

During near-field data acquisition, in addition to the propfan generated thrust, Spey thrust was required to maintain the aircraft in level flight. Minimization of Spey noise contamination on the propfan side of the

aircraft was obtained by operating the right hand Spey at maximum power with supplemental power provided by the left hand Spey. Because of the unsymmetric thrust distribution, the aircraft flew with a small steady sideslip angle.

The array of fuselage surface microphones is shown in Figure 87. They were concentrated in the regions where the highest SPLs were expected. The closest spacing between microphones was approximately 0.6m (2 ft). In the propfan plane, microphones were located around the fuselage. The microphones were of the peizoelectric type, were cylindrical, and were 0.093 inch in diameter. The microphones were vented to provide static pressure equalization across the diaphragms.

Acoustic and airplane/propfan performance data were acquired simultaneously at 570 test points. These test points were specifically defined to determine near-field acoustic characteristics as a function of five parameters: altitude, flight Mach number, propfan rotational tip speed, propfan power, and nacelle tilt (or inflow angle). The test points are defined in more detail in Section 4.2. All the data were recorded on board the aircraft, processed in the laboratory, and computer-stored for subsequent analysis. The principal forms used for analysis were narrow-band spectral analysis plots, listing of individual tone SPLs, listings of maximum SPLs and their locations, and parametric plots.

While much of the acoustic data was evaluated up to the fifth harmonic, the results reported here are generally limited to the first harmonic. This is because the fundamental had the highest SPL under all conditions examined, and the higher harmonics tended to decrease in an orderly manner.

7.2.2.2 Derivation of Propfan-Alone Noise

The acoustic data acquired included contributions from:

- o Propfan (tones and broadband)
- o Propfan drive system - Allison engine (tones and broadband)
- o Spey engine (tones and broadband)
- o Boundary layer (broadband)
- o Any other sources

The relative contributions and rankings of these sources were dependent upon propfan power setting and aircraft operating conditions within the flight envelope. To establish the acoustic characteristics of the unwanted noises, a series of flight test measurements were made with the "propfan-off," and the results were compared to identical flight conditions with the propfan operating. Spectral data for the prop-off configuration are shown in Figures 88(a) through (c) for the design cruise condition. The equivalent "prop-on" spectrum is shown in Figure 89. Analysis of the propfan-off data showed that:

- o Broadband noise from 200 Hz to 2 kHz scaled with freestream dynamic pressure. This suggests that the boundary layer is the principal contributor to broadband noise.
- o Spey engine noise was not identifiable at most locations at the higher altitudes and speeds (all power settings).
- o A low frequency noise source existed which peaked at less than 100 Hz. This noise was not evident with the propfan on and operating, and the tone level was "q" dependent. The origin was most probably an aeroacoustic phenomena associated with the inlet or exhaust of the windmilling propfan drive engine.

It was concluded that definition of propfan tones was clearly achievable, but definition of propfan-alone broadband noise was not feasible. The latter, however, can be no greater than the measured broadband noise flow which, on a 3.75 Hz bandwidth analysis, was at least 30 dB down from the fundamental tone level (at noisy locations) and had a boundary layer noise characteristic. The propfan broadband noise was submerged in this noise and thus was at an even lower level.

A similar set of acoustic spectra for the wing boom is shown in Figures 90 and 91. Here the tones are again clearly discernible; however, the composition of the broadband background noise level is more complex.

7.2.2.3 Noise Characteristics at the Design Point

Acoustic pressure time histories (PTH), which are initial steps in a number of noise prediction methods, are shown in Figure 92 for fuselage and wing boom locations. The PTHs are for conditions very close to the design point and are for noisy locations, but are not exactly 180 degrees apart in the propeller plane. The time interval covered one revolution of the propfan. The PTHs are periodic on both fuselage and boom but have distinctly different character. This difference in character may result from the fact that the measurement points are not diametrically opposite. The measurements shown include all "source" effects, propagation effects, and reception effects (such as boundary layer refraction and surface scattering).

Additional PTHs derived for up to one minute duration show very stable characteristics.

Narrow-band spectra corresponding to the above PTHs are shown in Figure 93. These spectra, which are rich in harmonics, are typical of this propfan operating at supersonic tip speed conditions. The highest SPL occurs at the first order of BPF; generally decreasing SPLs are associated with the higher harmonics. Near-field acoustic data acquisition was limited to 2 kHz. The background noise of the fuselage spectrum came from the turbulent boundary layer. The background noise of the wing boom spectrum was dominated by lower level tones corresponding to propfan shaft orders. Broadband noise of propfan origin is not readily apparent.

Other measurements for this propfan show that subsonic spectra are typified by a very strong fundamental tone, with higher order tones diminishing more rapidly than for supersonic tip speeds.

For the reference test conditions, the distribution of fuselage SPLs along WL 70 for the first five propfan tones is shown in Figure 94. This particular waterline generally contains the maximum SPLs. It is below the "closest point of approach," which was along WL 92. The tones have peak SPLs either in the propfan plane or just aft. The tones decrease in level with increasing tone number in an orderly manner and have similar directional characteristics. Values of SPL within 10 dB of the maximum SPL exist over an axial distance slightly greater than the propfan diameter. Values within 20 dB of the maximum extend from approximately one diameter ahead of to one diameter aft of the propfan plane. These acoustic characteristics are for the baseline nacelle tilt of -1 degree.

The fuselage circumferential distribution of fundamental tone SPLs in the plane of the propfan is shown in Figure 95. The maximum SPL was located at a position lower than the "closest point of approach." In this plane, SPL values within 10 dB of the maximum existed over most of the visible side of the fuselage, but fall off rapidly on the blind side. Comparable trends at lower SPL values were apparent for higher harmonics.

For the same reference test conditions, the fundamental tone SPLs are mapped over the side of the fuselage (looking from the propfan) in Figure 96. These SPLs include the previous waterline and circumferential distributions. The maximum SPL was 147.1 dB located $1/4 D_p$ aft of the propfan plane and below the closest point of approach. This SPL is an example of what will later be referred to as an "area maximum SPL."

The distribution of wing boom SPLs for the first five propfan tones is shown in Figure 97. The data presented are "as measured" and are essentially free-field. The tones all have maximum SPLs in the plane of the propfan and decrease in level with increasing blade order in an orderly manner; they all have very similar directional characteristics.

A comparison between "opposite location" wing boom and fuselage SPLs for the fundamental tone is shown in Figure 98. In the ground tests, it was found that wave reflection effects increased fuselage SPL measurements by about 6 dB. Therefore, the boom data of Figure 98 include an increment of 6 dB to permit direct comparison with the fuselage SPLs. This comparison then shows similar levels, but the boom data indicate a slightly higher directionality. Comparisons were similar for the higher harmonics. This comparison is for a nacelle tilt of -1 degree. In later sections, it will be shown that different nacelle tilts radically affect these relationships and that no generalized SPL relationship between fuselage and boom exists.

7.2.2.4 Effects of Propulsion Parameters on Noise

The variation of propfan fundamental tone SPL with rotational tip speed and power on the fuselage at the design cruise condition is shown in Figure 99(a) for a nacelle tilt of -1 degree. The propfan helical tip

Mach number ranged from 1.02 to 1.16. The SPL shown is the maximum on the side of the fuselage. It increased with propfan power and tip speed, but with different sensitivities.

The data shown in Figure 99(a) is for "total" propeller noise, e.g., the sum of all loading and thickness noise components. Examination of the noise trends reveals important evidence concerning its contributing noise sources makeup. The acoustic sensitivity to power was greater at the lower tip speeds than at the higher tip speed. For the highest tip speed, a reduction of power from maximum to minimum resulted in a 4 dB SPL reduction. That particular curve shows a flattening of noise with reducing power--suggesting that at the low power, the noise was dominated by a thickness noise floor. This level of thickness noise was then reinforced by the increasing level of loading noise at the higher powers to produce the characteristic shown. For the lowest tip speed, a similar reduction of power resulted in an 8 dB SPL reduction. The slope of this curve with power suggests that it is dominated by loading noise.

At the higher tip speeds and higher powers, a reduction of noise with increasing tip speed is shown. Similar trends were observed for the higher harmonics.

The same data is presented in an alternate form in Figure 99(b). Here the abscissa scale is propfan tip rotational speed. If expressed in terms of propfan tip helical Mach number, this scale would range from 1.02 to 1.16. This figure shows that for any given tip speed, increasing power increased SPL at the first order BPF. This increase was reduced at higher tip speeds. However, the conclusion is that loading noise made a significant contribution to propfan noise at all the operating conditions shown.

In Figure 100 acoustic data are plotted against estimated propfan thrust. The general trend was that increasing thrust increased SPL for all tip speeds. However, at the higher thrusts, small reductions of SPL are shown for either increasing or decreasing tip rotation velocity away from 243 mps (797 fps).

An SR-7 propfan propulsion map relating power coefficient, C_p , advance ratio, J , and blade angle, β , for $M = 0.8$ is shown in Figure 101. Superimposed on this chart are lines of constant SPL for the propfan fundamental tone. This format shows directly the influence of the propfan nondimensional operating parameters on SPL. The SPL contours increased in level in an orderly manner with decreasing J and increasing C_p . There was no optimum design combination for minimum noise such as is apparent for propulsion efficiency curves plotted on the same map. The constant dB lines are almost normal to the β_A lines. Measured acoustic data from a 2/9-scale model SR-7 propfan (Reference 7) show similar sensitivities to C_p and J .

The variation of the propfan fundamental tone SPL at the wing boom for the same basic propulsion parameters is shown in Figure 102. At the higher tip speeds, the SPL was even less sensitive to power than was observed on the fuselage (Figure 99(a)).

7.2.2.5 Noise Variation Over the Flight Envelope

The variation of the measured fuselage SPL at first-order BPF over the entire aircraft flight envelope is shown in Figure 103(a). In this data set the propfan tip speed was constant at 244 mps (800 fps), the nacelle tilt was maintained at -1 degree, and the propfan was always operating at maximum power (4474 kw (6000 shp) at low altitude and speeds, 1491 kw (2000 shp) at the highest altitude and speeds). Since testing was conducted at nearly constant aircraft weight, there was a variation of aircraft angle of attack (and consequently propeller inflow angle) over the flight envelope. This effect is included in the data presented. The data trends are very orderly. Lower SPLs are evident at points typical of low-altitude climb (higher powers and subsonic tip speeds) with continually increasing levels to cruise conditions (lower powers and supersonic tip speeds). The highest SPLs occur in the region of highest "q" and highest propfan tip helical Mach number.

The corresponding "acoustic flight envelope" for the second harmonic, at the same conditions, is shown in Figure 103(b). It shows a greater range of SPL levels than for the fundamental. Also, the second harmonic is much stronger, relative to the fundamental, at the high-speed cruise conditions than at the low-speed, high angle of attack conditions, as shown in Figure 103(b).

This "acoustic flight envelope" has different SPL distributions and sensitivities for other nacelle tilts and propfan tip speeds.

The effect of increasing propfan tip helical Mach number, M_{TH} , (at constant rotational speed) on near-field noise is shown in Figure 104. The range of tip helical Mach number, M_{TH} , is from 0.8 to just under 1.2. All the curves (which are for different altitudes and powers) show a smooth increase in SPL with increasing M_{TH} . No abrupt increase in SPL is apparent as the tip Mach number goes from subsonic to supersonic. This characteristic is for BPF 1. For higher harmonics, the trends would be steeper, but no discontinuity at $M_{TH} = 1$ is expected.

7.2.2.6 Noise Scaling with Altitude

Many near-field acoustic prediction procedures normalize the effect of altitude on acoustic pressure through a " ρc^2 " factor, where ρ is the ambient atmospheric density and c is the local speed of sound. A ρc^2 ratio also corresponds to a static pressure ratio; use of such a factor is an element in the scaling procedure for deriving flight SPLs from measured wind tunnel SPLs. Test cases were planned to produce data that would enable an evaluation of the parameter ρc^2 for altitude scaling of acoustic pressures. The tables of Figure 105 show five pairs of test points--two for supersonic tip speeds and three for subsonic. In each of these five cases, data were obtained for two altitudes at common C_p and J values. The tables list for each case the difference in SPL measured at the two altitudes.

To define theoretical differences in SPL for different altitudes, the scaling theory uses the relationship:

$$\Delta \text{dB} = 20 \log \frac{\rho_2 c_2^2}{\rho_1 c_1^2}$$

This relationship was used to calculate the differences in SPL for the five pairs of test conditions shown in Figure 105. Figure 106 shows the measured SPL differences plotted against the theoretical values. These data indicate that the scaling parameter is moderately accurate--giving results within about 2 dB of measured values. The fact that better agreement of the theory was obtained for Cases 1 and 2 than for Cases 3 through 5 is probably more a function of the magnitude of altitude differences than of a subsonic-versus-supersonic relationship.

7.2.2.7 Effects of Inflow Angle on Noise

Aerodynamic inflow direction relative to the propfan plane was expected to be an important parameter in the generation of propfan noise. This inflow angle is dependent upon airplane angle of attack, upwash angle at the propfan, and nacelle tilt. These angles are defined schematically in Figure 107. An example of the estimated relationship between nacelle tilt and propfan inflow angle at the design cruise point is also shown.

The engineering rationale for the way propfan inflow angle and propfan direction of rotation are expected to affect the near-field noise characteristics is shown in Figure 108. For the "up-inboard" rotation, increasing nacelle tilt (which increases propfan inflow angle) is expected to decrease blade lift noise on the fuselage and increase lift noise on the wing boom.

The measured effects of nacelle tilt variation on fuselage and wing boom SPLs at BPF 1 are shown for the cruise condition as functions of tip speed in Figure 109. The results, for the fuselage, show that increasing nacelle tilt provided significant SPL reductions for all propfan tip speeds. The reductions were larger at the lower tip speeds. On average, the acoustic sensitivity was 1 dB/degree of nacelle tilt. On the other side of the propfan, increasing nacelle tilt provided significant SPL increases at the wing boom with similar sensitivities, but opposite sign. Similar effects occurred over the entire fuselage surface and also in the higher harmonics.

These trends suggest that for the high-speed cruise condition, cyclic aerodynamic loading on the propfan blades played an important role in defining the magnitude and directionality of propfan noise.

This sensitivity to nacelle tilt is shown in an alternate format in Figure 110. These data again show that the highest fuselage SPLs are generated with the nacelle tilt at -3 degrees; the lowest SPLs were obtained with a nacelle tilt of +2 degrees. The difference in absolute SPL must be related to the relative magnitude of the cyclic loading component. The different SPL sensitivities to propfan rotational tip

speed (at almost constant power) imply that the role of cyclic loading noise was more important at the lower tip speeds.

The variation of maximum SPL measured on the fuselage is shown for 17 points within the flight envelope for the nacelle tilt of -3 degrees in Figure 111. An increase in SPL relative to the equivalent nacelle tilt data of -1 degree is evident at every test point. The highest fuselage SPL at first-order BPF acquired during the PTA flight test program occurred under these test conditions. It is the 151.7 dB point at an altitude of 8,229m (27,000 ft) and a Mach number of 0.83.

The variation of SPLM, measured on the fuselage, within the flight envelope for the nacelle tilt of +2 degrees is shown in Figure 112. A decrease in SPL relative to the equivalent nacelle tilt data of -1 degree is evident at every test point.

The effect of the 5-degree increase in nacelle tilt on fuselage SPLs at first-order BPF was determined for 17 points within the flight envelope and is shown in Figure 113 for the defined conditions. A noise reduction is evident at every test point. The larger reductions occurred at the higher q's and the higher Mach numbers, and the smaller reductions occurred at the lower q's and the lower Mach numbers.

The effect of the 5-degree increase in nacelle tilt on wing boom SPLs at BPF 1 is shown in Figure 114. A noise increase is evident at every test point. The larger increases occurred at the higher q's and the higher propfan tip helical Mach numbers, and the smaller increases occurred at the lower q's and the lower propfan helical tip Mach numbers.

The effects of nacelle tilt on fuselage and wing boom SPLs at BPF 1 are shown for the flight test condition of low altitude ($H = 5000$ ft) and low speed ($M = 0.28$) in Figure 115. The trends are similar to the cruise case shown earlier; however, the effects are much less. The reduced sensitivity is probably related to the cyclic aerodynamic loading change produced by a 5-degree nacelle tilt change being a smaller percentage of the blade steady aerodynamic loading (associated with maximum power) at this condition than for the $H = 10,668$ m (35,000 ft) and $M = 0.8$ condition.

An inflow angularity is also created by airplane sideslip, so a series of tests were planned to quantify the sensitivity of fuselage SPL to sideslip. In these tests, the largest values of sideslip were achieved by flying the aircraft with maximum rudder deflections. The results, shown in Figure 116, show the sideslip influence on fuselage and wing boom SPLs to be very similar both in trend and magnitude to that of nacelle tilt, e.g., 1 dB/degree. This coincidence of results happens even though the two different inflows would be expected to produce cyclic loading changes in different parts of the propfan disc and thus have different directional characteristics.

Because of the asymmetry of the PTA aircraft, most of the data points in the flight test program were taken with some degree of sideslip. At higher powers, this was generally in the range ± 0.5 degree. Therefore,

although most of the test points have some acoustic contamination due to sideslip, these results indicate that the effect was probably less than ± 0.5 dB.

7.2.2.8 Comparisons of Predicted and Measured Noise

After the flight test acoustic data were processed, a comprehensive set of near-field acoustic predictions was made by Hamilton Standard. Forty-six test points were selected as prediction cases to cover a very wide range of propfan test parameters. Aircraft and flight parameters for these points were used as starting conditions for the predictions. Twelve of the test cases required predictions at many microphone locations. Thirty-six predictions were made at a single microphone location corresponding to the location of SPLM. The predictions were for the first five harmonics and covered both amplitude and relative phase. They were on a propeller "total" noise basis only, i.e., they incorporated: loading noise, cyclic loading noise, thickness noise, and transonic noise. The predictions also included all source effects, propagation effects, and reception effects (which cover boundary layer refraction and surface scattering effects). A summary of the Hamilton Standard prediction methodology is shown in Figure 117. The comparisons between predictions and measurements covered acoustic pressure amplitude only.

The correlation between predicted and measured fuselage surface SPLs for first-order BPF is shown in Figure 118. These cases covered a wide variety of test conditions, e.g., altitude, Mach number, rotational tip speed, power, and nacelle tilt. Generally, noise was overpredicted at the higher SPLs associated with cruise conditions. At the design point, the overprediction was 3 dB. Underpredictions occurred at the lower SPLs associated with climb conditions.

On the fuselage, the predicted SPLM always occurred on WL 94, which was the closest point of approach to the propfan. As shown in Figure 119, 36 of the predicted maxima occurred in the plane of the propfan while 10 occurred slightly aft of the propfan plane. In comparison, the majority of measured SPLM locations occurred aft of the plane of the propfan and at a waterline location below the closest point of approach.

Axial distributions of predicted and measured SPLs, for fuselage waterlines containing the maximum levels of BPF 1 and BPF 2, are shown in Figure 120. For both harmonics, measured maxima consistently occurred 24 inches lower than the predicted. All conditions shown maximized at $+0.25 D_p$ aft of the propeller plane. Both harmonic maxima were overpredicted by 3 dB. The measured axial distributions showed a broader, flatter characteristic and thus extended over a greater length of fuselage than did the predicted distributions.

Predicted SPLs for BPF 1 for all measurement locations over the fuselage side at the design cruise condition are shown in Figure 121. SPL contours have been developed. These "predicted" contours include a larger fuselage surface area than did the measured data contours shown earlier. The predicted and measured contour shapes also have different characteristics.

Similar comparison data developed for the second, third, fourth, and fifth harmonics generally showed similar trends.

A comparison of spectra for the first five tones corresponding to the fuselage predicted and measured maximum SPL at design cruise is shown in Figure 122. The relative levels for these supersonic spectra are in good agreement; the 3 dB overprediction generally applies to all the harmonics. This comparison is fairly representative of high-speed cruise and other noisy conditions.

Predicted and measured trends of SPL, BPF 1, propfan tip speed, and power at the design cruise condition are compared in Figure 123. For all conditions, there is an overprediction. The predicted SPL at the higher tip speeds are essentially independent of power and do not demonstrate the measured sensitivity. These trends suggest that the predictions were dominated by a high level of the thickness noise component.

The same data are presented in a different format in Figure 124. The predicted SPLs do not show any evidence of a peak in the noise characteristic with propfan tip rotational speed.

The variation of predicted SPL, BPF 1, over the flight envelope is shown in Figure 125 for the conditions of $V_{ROT} = 244$ mps (800 fps) and maximum available power. The highest predicted level was 154.2 dB and occurred at the highest q and tip helical Mach number.

The differences between predicted and measured fuselage maximum SPLs over the flight envelope for the reference conditions are shown in Figure 126. The Δ dB value at each point is equal to the predicted minus the measured value. It can be seen that overpredictions occurred at conditions typical of cruise, while underpredictions occurred at conditions typical of climb. Similar comparisons were made for the second harmonic, with generally similar conclusions.

Predicted and measured fuselage SPL, BPF 1, trends with nacelle tilt are shown in Figure 127. These comparisons are for design cruise conditions, a range of propfan rotational tip speeds, and maximum available power. The predictions were always higher than measured values. They show little sensitivity to nacelle tilt, whereas the measured data show a dramatic reduction of fuselage SPL with increase of nacelle tilt. These results suggest again that the predicted total noise levels were overly weighted by thickness noise.

For the wing boom, predictions showed a similar insensitivity of SPL to nacelle tilt—again in contrast to measured data.

The correlation between the twelve predicted and measured SPLs, BPF 1, at the wing boom is shown in Figure 128. Generally, overpredictions occurred at the higher SPLs associated with cruise conditions. The underpredictions occurred at the lower SPLs associated with climb conditions.

7.2.2.9 Conclusions - Near-Field Sound Pressure Levels

The following summarizes the principal findings of the near-field investigations.

- o A comprehensive set of high-quality acoustic data was acquired on the fuselage and the wing boom together with detail airplane performance and propfan operating parameters for a wide range of test parameters.
- o The acoustic spectra were dominated by the first order BPF tone with higher order tones at lower SPLs.
- o There was no evidence of propfan generated broadband noise.
- o SPLs increased smoothly with transition from subsonic to supersonic propfan tip speeds.
- o At the airplane/propfan design cruise point:
 - The SPLM, for BPF 1, was 147 dB.
 - A large area of fuselage was exposed to SPLs greater than 130 dB for the first-order BPF of 226 Hz.
 - Small changes in SPL were obtained by changes in propfan tip speed at higher thrusts.
 - SPLs were very sensitive to propfan inflow angle and to propfan direction of rotation; increases in nacelle tilt caused dramatic reductions in fuselage SPL, especially at lower tip speeds.
 - SPLs were lower than predicted; predictions showed an insensitivity to power input and inflow angularity, in contrast to measured data.
- o For low-altitude climb, SPLs were higher than predicted.

7.2.3 Near-Field Noise - Fluctuating Pressures

The most significant acoustic impact of the propfan on the aircraft other than the sound pressure levels produced on the fuselage was the production of fluctuating pressure in the region where the propfan slipstream impinged on the wing. The slipstream contains blade trailing edge wakes and blade tip vortices--both of which produce oscillating surface pressures.

The character of the oscillating pressure on the wing is more complex than those on the side of the fuselage. The fuselage oscillating pressures result from airborne sound pressures, while the wake-impacted oscillating pressures are more nearly hydrodynamic in nature.

7.2.3.1 Test Techniques and Conditions

In the PTA Program, 44 piezoelectric transducers were placed on the upper and lower surfaces of the wing in the slipstream wake region to measure these fluctuating pressure levels (FPLs). Their locations will become obvious in the plots of the data. They were, however, concentrated in the regions of the wing behind the blade tips. Measurements of FPL were made at the same time SPL was recorded.

In the following sections, these FPL data will be discussed and compared with predicted values.

7.2.3.2 Derivation of Propfan-Alone Fluctuating Pressures

As in the case of SPL data, the FPL data consisted of "total" noise, e.g, the measured data included contributions from all sources (as modified by the presence of the wing surface and its boundary layer) as follows:

- o Propfan (tones and broadband)
- o Propfan drive system - Allison engine (tones and broadband)
- o Spey engine (tones and broadband)
- o Boundary layer (broadband)
- o Any other sources

The relative contributions and rankings of these sources were dependent upon propfan power setting and aircraft operating conditions within the flight envelope. To establish the fluctuating pressure characteristics of the unwanted noises on the wing, data were used from the "propfan-off" tests.

Measured prop-off and prop-on spectral data at a microphone location on the wing lower surface are shown in Figures 129 and 130 for the design cruise condition. Analysis of these and other data showed that with the propfan off:

- o A low-frequency tone was present that is believed to be an "organ-piping" associated with either the inlet or exhaust system of the windmilling propfan engine. This can also be seen in the fuselage SPL data.
- o The broadband spectra were insensitive to Spey engine power setting, just as in the case of near-field noise.
- o The broadband levels were lower than on the fuselage but had much greater spatial variation, possibly caused by other wing flow phenomena, e.g., shocks, shock/turbulence interaction, and flow separation.
- o Propfan-off data interpretation on the wing was more difficult than on the fuselage.

A similar set of data is shown for the wing upper surface in Figures 131 and 132. Generally, similar conclusions apply; however, the prop-off spectra do show some sensitivity to Spey engine power setting at frequencies below 500 Hz.

Both lower and upper surface propfan-on spectra show that:

- o Strong tones exist at the fundamental and harmonic tones of the blade passage frequency which exceed the floor level by at least 20 dB.
- o The broadband levels are higher with propfan-on than with propfan-off; this appears to be due to a multitude of pure tones associated with propfan engine drive frequency.

It was concluded that:

- o Definition of propfan tones was clearly achievable.
- o Definition of propfan-alone broadband noise was not feasible. Its level, however, can be no greater than the measured broadband noise floor. On a 3.75 Hz bandwidth analysis, the measured broadband noise is at least 30 dB down from the fundamental tone level (at noisy locations). The propfan broadband noise was submerged in this noise and thus was at an even lower level.

7.2.3.3 FPL Characteristics at the Design Point

Examination of the measured wing FPL data was initially conducted on a lower and upper wing surface basis. However, it became apparent that this was an over simplification of the phenomena involved, and that because of zonal differences, wing FPL analysis became more meaningful if conducted on a "quadrant" basis. This no doubt derived to a large degree from the effect of wing sweep, from the fact that the slipstream centerline was above the wing, and from rotational directivity effects.

Fluctuating pressure time histories (PTH) on the wing surface in each of the four impingement zones are shown in Figure 133. These data are for design cruise conditions, with the reference nacelle tilt of -1 degree, and therefore with supersonic helical tip Mach numbers. The time span was 0.04 seconds, which corresponded to a single rotation of the propfan blade. The PTHs are for the microphones which have the highest FPLs. They all exhibit periodicity, but each quadrant has a different characteristic. The upper and lower inboard PTHs indicate an interesting inversion in amplitude characteristics.

The narrow-band spectra for each quadrant, corresponding to the previously shown PTHs, are displayed in Figure 134. The analysis effective bandwidth was 3.75 Hz. These supersonic spectra, at design cruise, are dominated by the FPL at BPF 1 and are all rich in harmonics. The noise floors are 30 to 40 dB below the BPF 1 level and show a multitude of tones at the propfan shaft order frequency. There appears to be no discernible FPL

broadband noise. With respect to the tonal content, the FPL supersonic spectra are generally similar to SPL supersonic spectra. (Examination of FPL spectra at subsonic conditions, however, shows that much of the spectral tonal richness is retained, whereas the SPL subsonic spectra showed rapid tonal decay.)

The distribution of FPLs for BPF 1 over the wing lower surface is shown for design cruise conditions in Figure 135. The dots indicate the locations of the 22 lower surface microphones. The maximum value of FPL was 148.2 dB at the wing leading edge, immediately behind the propfan tip. FPLs in excess of 140 dB were measured in other zones.

Wing surface distributions for the FPL higher harmonics showed generally similar trends, but at lower levels.

In much of the ensuing text and figures, the maximum value of FPL in any quadrant will be abbreviated as FPLM.

The FPL linear distribution near the leading edge of the wing lower surface is shown in Figure 136 for five harmonics. Both inboard and outboard profiles show maximum FPLs directly behind the propfan tip, and a very peaky spatial distribution, dropping off rapidly going out of the slipstream. This localized excitation exposed a 24-inch span of inboard wing to FPLs in excess of 140 dB. The FPL harmonics show similar shapes, while decreasing in level in an orderly manner. Overall, the inboard excitations were stronger than the outboard excitations.

The distribution of FPLs for BPF 1 over the wing upper surface at the design cruise conditions is shown in Figure 137. The dots indicate the location of the 22 upper surface microphones. The highest FPL at the leading edge was 140.5 dB; however, a higher level was measured in the mid-chord location. Generally, the inboard FPLs were higher than the outboard FPLs.

Distributions for the FPL higher harmonics showed similar trends but at lower levels.

The FPL linear distribution close to the leading edge of the wing upper surface for five harmonics is shown in Figure 138. Both inboard and outboard profiles show maximum FPLs very close behind the propfan tip. The inboard distributions are broader than the outboard distributions. This localized excitation exposed a 24-inch span of inboard wing to FPLs of the order of 140 dB. The FPL harmonics showed similar shapes, while decreasing in level in an orderly manner. Overall, the inboard excitations appeared to be stronger than the outboard excitations.

The chordwise distribution of FPL for BPF 1 for the wing upper and lower inboard section at the design cruise condition is shown in Figure 139. Both surfaces show FPLs at BPF 1 in excess of 140 dB for considerable chordwise distances.

7.2.3.4 Effects of Propulsion Parameters on FPL

The dependencies of wing inboard FPLM upon propfan tip speed and propeller shaft horsepower at cruise design conditions for BPF 1 are shown in Figure 140 for a nacelle tilt angle of -1 degree. The lower surface FPL was always 5 to 10 dB higher than the upper surface FPL. Both exhibited increasing levels with power, but reached plateau at the higher powers. Both displayed a small sensitivity to rotational tip speed. Generally, the FPLs showed a surprisingly small variation (7 to 8 dB) over the total power and tip speed range. There is some evidence that, at a given power, the highest FPLs were produced by the lowest propfan rotational tip speeds.

The wing outboard FPLM dependencies upon propfan tip speed and propeller shaft horsepower at cruise design conditions for BPF are shown in Figure 141. The lower surface FPL was higher than the upper surface FPL at the higher powers. The lower outboard surface consistently showed the characteristics of increasing FPL with reducing tip speed. This can be attributed to the lower-propfan-tip-speed operation requiring an increase in blade C_L (through blade angle of attack increase) to maintain performance. This increased the strength of the tip vortex and hence the vortex/wing interaction FPLs. The measured FPLs shown for the wing upper outboard quadrant exhibited a more irregular pattern than for the other three quadrants. For the outboard quadrants, the propfan tip vortex had a greater distance to travel (because of wing sweep effects) before wing impingement. Possibly at this upper wing location, the transducers were not positioned correctly to acquire the maximum levels of FPL.

7.2.3.5 FPL Variation Over the Flight Envelope

The variation of FPLM for BPF 1 for the wing lower inboard quadrant over the flight envelope is shown in Figure 142. For this 19-point data set, propfan tip speed was held constant, and power was held at the maximum attainable. Some of the levels shown on this figure are low and out of pattern, but for most of the points, the FPL is maintained at a level of 150 ± 3 dB. The trend was towards slightly higher FPLs at lower altitudes and speeds; the highest FPL was 153.5 dB and occurred at $H = 1524\text{m}$ (5000 ft) and $M = 0.28$.

The variation of FPLM for BPF 1 for the other three quadrants over the flight envelope is shown in Figures 143 through 145. These data also indicate higher FPLs at the lower altitudes and Mach numbers.

The relationship between wing FPLs and fuselage SPLs for BPF 1 is shown in Figure 146 on a dB basis over the flight envelope. The value of FPLM is taken to be that at the lower inboard surface at 10-percent chord. A positive sign indicates that the FPLM is greater than the SPLM. Generally, FPLM exceeded SPLM. The exceedance increased with reducing altitude and Mach number and reached a maximum of 17.6 dB at $H = 1524\text{m}$ (5000 ft) and $M = 0.28$.

For lower propfan rotational tip speeds, the comparative differences between FPLM and SPLM were even larger.

These differences may have important implications for the relative levels of structureborne and airborne sound within the cabin at different operating conditions. If structureborne noise in the cabin is a problem, it should be more evident at low-speed, low-altitude conditions than at high-speed cruise.

7.2.3.6 Effects of Inflow Angle on FPL

The effect of nacelle tilt (and inflow angle) on FPLs at BPF 1 in each of the four wing quadrants is shown in Figure 147 for a rotational tip speed of 243 mps (797 fps) and the design cruise condition. These data are from the leading edge microphones. For the inboard quadrants, both upper and lower surfaces showed a reduction of FPL with an increase of nacelle tilt; the sensitivity was approximately 1 dB/degree. This effect of nacelle tilt on wing inboard FPLs is very similar to the SPL trends measured on the fuselage. For the wing outboard surfaces, the overall trend showed an increase in FPL with nacelle tilt (although there were some inconsistent points); this effect is similar to the SPL trends measured on the wing boom.

The effect of nacelle tilt on wing lower inboard surface FPLMs for the conditions of 243 mps (797 fps) propfan rotational tip speed and maximum continuous power is shown over the flight envelope in Figure 148. The total nacelle tilt change is 5 degrees, from -3 degrees to +2 degrees. The resulting change, in FPLM Δ dB, was obtained by subtracting the FPLM at NT = +2 degrees from the FPLM at NT = -3 degrees. The data show, for the majority of points, that there was a reduction of FPL on the wing lower inboard surface with an increase of nacelle tilt. The corresponding analysis for the upper inboard surface showed similar results. These results have the same trend as those for the fuselage SPLs.

The effect of nacelle tilt on wing lower outboard surface FPLs for the same conditions is shown over the flight envelope in Figure 149. Again the total nacelle tilt change was 5 degrees. The data show that, in general, there was an increase of FPL on the wing outboard lower surface with an increase of nacelle tilt. The corresponding analysis for the upper outboard surface showed similar results. These results have the same trends as those for the wing boom SPLs.

It appears that wing surface FPLs were strongly influenced by propfan nacelle tilt--or inflow conditions. The combination of increasing nacelle tilt (which increases propfan inflow angle) and propfan direction of rotation produced similar effects for FPLs and SPLs as summarized in Figure 150. These sensitivities to propfan inflow angle no doubt are related to the cyclic variation of propfan blade loading and tip vortex strength as it rotated in a non-axial flow field.

7.2.3.7 Comparison of Predicted and Measured FPLs

After the flight test acoustic data had been processed, a comprehensive set of wing FPL predictions was made at the same 46 test points that were used for the SPL predictions. Twelve of the test cases required predictions at many microphone locations. Thirty-six predictions were made at single microphone locations corresponding to the location of FPLM. The predictions were for the first five harmonics and covered both amplitude and relative phase. A summary of the Hamilton Standard prediction methodology is shown in Figure 151. The comparisons between predictions and measurements covered pressure amplitude only.

The correlation between predicted and measured FPLs for BPF 1 on the wing lower inboard surface for all 46 cases is shown in Figure 152. These cases covered a wide variety of test conditions, e.g., altitude, Mach number, rotational tip speed, power, and nacelle tilt. The prediction methodology underestimated the measured levels by, on average, 30 dB.

The distribution of predicted FPLs over the wing lower surface at design cruise conditions is shown in Figure 153. The highest levels were at the wing inboard leading edge. They show a reduction with increasing chordwise location. Comparison with measured levels are shown in brackets in a dB form. Negative signs indicate an underprediction.

A comparison of predicted and measured FPL distributions at the wing lower surface leading edge transducers immediately aft of the propfan tips is shown in Figure 154. The comparison is for design cruise conditions and is for the first three harmonics of FPL. All harmonic levels were underpredicted. It would appear that the propfan tip vortices produced an intense localized loading on the wing which was not being predicted.

The predicted and measured dependence of FPLM on propfan power and tip speed at the design cruise conditions for wing lower inboard surface are shown in Figure 155. Generally, both sets of data show increasing FPL with power, although the measured trends are flatter. At constant power, the predicted FPLs increased with reducing propfan tip rotational speed. There is limited measured evidence to support that trend in this particular quadrant, but it was consistently identified in the lower outboard quadrant.

7.2.3.8 Conclusions - Fluctuating Pressure Levels

The following summarizes the principal findings of the wing FPL investigations.

- o The FPL spectra were dominated by the propfan first order BPF tone with higher order tones at decreasing levels.
- o Propfan-generated broadband FPL was not readily apparent.
- o High FPLs occurred on the wing surfaces immediately behind the propfan tips.

- o The wing surface area exposed to an FPL greater than 140 dB (for BPF 1) covered a spanwise width of about 0.6m (2 ft) over a considerable chordwise distance--in each quadrant.
- o FPLs at the noisy inboard quadrants showed little sensitivity to power and tip speed.
- o FPLs were high over most of flight envelope; the highest FPLMs were measured at the lowest altitudes and Mach numbers (at maximum power).
- o The wing FPLs exhibited sensitivity to nacelle tilt similar to adjacent fuselage or wing boom SPL sensitivities.
- o The measured FPLs were much higher than predicted.
- o Wing FPLMs were slightly higher than fuselage SPLMs at design cruise but were much higher at low-speed, low-altitude conditions.
- o A unique data base has been established which:
 - Documents large-scale propfan slipstream/wing impingement FPLs and system performance parameters
 - Provides new insight into previously little-explored phenomena

7.2.4 Cabin Noise

7.2.4.1 Test Techniques and Conditions

During the cabin noise tests, the general arrangement of the testbed airplane was unchanged from that of the other flight research tests. The configuration is described and illustrated in Section 4. The configurational aspects of particular relevance to cabin noise are: the Spey engine operation; the cabin heating, air conditioning, and pressurization system; and the interior trim and furnishings installations.

Spey Engine Operation - Cabin noise data were obtained with the propfan operating at a variety of power, tip speed, flight speed, and altitude conditions. During these tests, the airplane was always in level flight attitude. The thrust from the propfan was often not sufficient to maintain this level flight condition. When this was the case, the Spey engines were used to supply the additional thrust required. When Spey engine thrust was needed, it was obtained from the right-hand engine whenever possible, keeping the left-hand engine at flight idle. The left-hand Spey engine was only powered-up when the combined thrust of the right-hand Spey at maximum continuous power and the propfan at test power were not sufficient for level flight.

Cabin Heating/Cooling - The cabin was air conditioned for crew comfort with the standard GII air cycle system, supplied by the Spey engine compressor bleed air. All standard GII air distribution ducting in the passenger cabin was removed, however, and heating/cooling air was introduced in the aft end and in the flight station and discharged through the outflow valves in the flight station.

This installation, while not ideal, maintained cabin air temperatures in a range narrow enough to minimize concern for the temperature-induced changes in air density and speed of sound (ρc).

Cabin Pressurization - The cabin was pressurized via the standard GII pressure regulation system, which provides for sea level pressure at altitudes below about 6,096m (20,000 ft). At higher altitudes, cabin pressure decreased in accord with a constant differential pressure of about 55,160 N/m² (8 psi). Thus, at the highest test altitude of about 12,192m (40,000 ft), where outside static pressure is about 18,823 N/m² (2.73 psi), the cabin pressure was about 73,983 N/m² (10.73 psi), which is equivalent to a cabin pressure altitude of about 2591m (8500 ft).

Cabin pressure was regulated by modulating the outflow valve which was located behind the avionics equipment rack near the flight station bulk-head.

The effects of variable cabin pressure were measured in the test program and are discussed in Section 7.2.4.5.

Interior Trim and Furnishings - The testbed cabin was totally devoid of trim, thermal insulation, soundproofing, and carpeting. Seating was available in the forward and aft ends only, and there only for the test engineers and observers. The general arrangement of the interior floor plan is shown in Figure 156. The cabin area within about 5 feet forward to about 10 feet aft of the propfan plane was kept clear of obstructions and personnel during acoustic testing. The fuselage shell construction concept and the bare-cabin character are visible in Figure 157. In some skin bays, a light-toned surface is visible. This is a .64 cm (1/4 in.) foam damping sheet, with either a vinyl or a foil backing, that was bonded to the skin. This was standard hardware in the production GII and was not readily removable. It was thought to be of minor consequence in low-order propfan noise and was therefore left in place. Figure 157 also shows the placement and comparatively large size of the passenger windows. In all tests, the window panes were installed and unobstructed.

7.2.4.2 Instrumentation

The cabin noise analyses were based primarily on the noise data obtained from the 33 microphones within the cabin. Important use was also made of the 45 fuselage exterior surface microphones, the 44 wing microphones in the propfan slipstream, the 51 accelerometers on the fuselage shell and floor structure, and the 25 accelerometers on the wing lower surface. For more specifics on the complete instrumentation system, and on the transducer locations and installations, see Section 4.0.

The cabin microphone locations and designations are shown in Figures 158 and 159. Those identified as MAXX are microphones in an axial array along the left-hand side of the fuselage, about three inches from the skin surface at about seated-head height. Those identified as MCXX are in circumferential arrays around the left-hand side at the three indicated fuselage stations, also about three inches from the skin surface. Those identified as MBXX are located on the traversing microphone boom (TRAM), in the grid arrangement shown, so as to survey the cabin cross section at any fuselage station between FS 245 and FS 430. The normal position for the TRAM was FS 301, the plane of the propfan. For certain selected conditions, it was incrementally traversed from FS 245 to FS 430. The exterior microphone locations and designations are shown in Figure 159 for the fuselage and wing. The fuselage surface microphones were arranged in axial and circumferential arrays at the locations illustrated. The wing surface microphones were arranged in arrays situated in the expected path of the propfan tip vortex on both the upper and lower surfaces. Upper and lower surface microphones are identified as MUXX and MLXX, respectively.

The accelerometers on the fuselage and wing surface structure are shown in Figure 160. Here also, there were axial and circumferential arrays denoted with AAXX and ACXX identifications. There were five accelerometer locations on window panes, denoted AWWX. All wing accelerometers were on the lower surface and were denoted with AWXX identifications.

7.2.4.3 Test Envelope

The basic flight research test conditions were dictated primarily by requirements for blade stress and near-field noise testing. These requirements resulted in a large matrix of tests involving systematic variation of altitude, flight speed, propfan shaft horsepower and rotational speed, and nacelle tilt angle. The specific combinations of parameters flown are shown in Figures 23 and 24. Cabin noise data were obtained concurrently with these tests, so a wealth of data were recorded.

In addition to the basic cabin noise tests that were run concurrent with other tests, a few tests were dedicated specifically to cabin noise. These dedicated tests included: (1) ground diagnostic tests in which cabin resonance modes were surveyed, and tests in which mechanical and acoustic forces were applied to the structure to evaluate sound transmission paths and to quantify relationships between noise and vibration; (2) variation of cabin pressure during otherwise constant flight conditions, to ascertain the need, if any, to correct the basic cabin noise data for pressurization effects; and (3) spatial surveys of cabin noise level for selected operating conditions, using the microphone traverse.

The specific conditions existent during the conduct of various concurrent and dedicated tests are always noted in conjunction with the data presentation.

7.2.4.4 Noise Characteristics

The character of the noise in the bare cabin was one of highly distorted nonsymmetric sound pressure waves comprised of multiple tones standing well above a random noise floor. The process of "transmission" through the shell structure did not alter the fundamental character of the cabin noise. The time histories (wave shapes) of the cabin sound pressures were therefore similar to those of the exterior sound pressures, which are discussed in detail in Section 7.2.2.3.

Typical examples of cabin interior and exterior sound pressure level spectra are shown in Figure 161. These spectra are for microphones situated in the area of maximum noise. The analysis effective bandwidth is 3.75 Hertz.

At the baseline cruise condition noted, the cabin noise spectrum was dominated by the blade-order tones and is consistent with the exterior spectrum in all respects. No unexpected noise sources are evident; no propfan noise traits are absent. The blade-order tones are evident through the eighth order in both cases. Even higher-order tones would have been visible had the instrumentation system been designed to operate above 2000 Hertz.

The level of the first-order tone, 113.3 dB, was slightly lower than expected for this condition. The wall noise reduction, NR, on the basis of maximum interior and exterior levels, is seen to be 30 to 35 dB at the low orders and 40 to 45 dB at the high orders. In subsequent sections it will be seen that spatial NR values were always less than these numbers.

The interior noise spectrum for the case with the propfan removed is also shown in Figure 161 for the same location and flight condition. The results from these tests were inconclusive. At frequencies above about 600 Hertz, the broadband noise floor was slightly higher when the propfan was operating. This may indicate a propfan broadband noise contribution to the other sources, but not necessarily. The increase in broadband noise with the propfan operating may derive from the drive engine inlet, gearbox, or discharge, or from the higher velocity slipstream flow on the nacelle and wing surfaces. However, even if this additional broadband noise is assumed to originate at the propfan, there is some comfort in the fact that the level is low, in the same range as normal aerodynamic noise, and well below the tone maxima.

When the drive engine was not operating (propfan off), the engine intake and discharge ducting systems formed large cavities that responded to the flow excitation. These sources are suspected to be the cause of the higher noise at 80 and 500 Hertz.

The sound pressure levels at the blade-order tones varied significantly with location as may be seen in Figures 162 through 165. Highest levels did not necessarily occur nearest the propfan, nor did the lowest levels occur farthest from the propfan. The levels were clearly influenced by the dynamics of the shell structure and by the acoustic response of the cabin volume.

Noise level variation laterally across the cabin in the propfan plane (Fuselage Station 301) is shown in Figure 162 for an array of five microphones at seated-head height. Noise levels at any particular blade order varied from 10 to as much as 25 dB. Similar variations occurred in the fore and aft direction, as also seen in Figure 162, for a six-microphone array along the left hand sidewall. Noise level variation circumferentially was much the same, as shown in Figure 163, for an array of five microphones at FS 301.

Lines of constant noise level at the first-order blade passage frequency in the plane of the propfan (FS 301) are shown in Figure 164. Figure 165 shows a three-dimensional plot of the first-order noise at a constant height of about 4 feet above the floor for a range of fuselage stations and buttress lines. These data locations represent a fore/aft traverse of TRAM microphones MBO4 through MBO7.

In each case illustrated, the propfan tip speed was 243 mps (797 fps), which corresponds to a blade passage frequency of 226 Hertz. At other blade passage frequencies, the noise level spatial variation was similar, but highest levels occurred at other locations. This also resulted from the influence of the shell dynamics and the cabin volume modal response.

The aforescribed variability in noise level at individual microphone locations tends to obscure the effects of the less influential parameters, such as altitude, speed, power, pressurization, etc. In order to reveal these parameter effects, it was necessary to examine noise level averages for groups of microphones. Average curves for the three arrays of microphones (Figures 162 through 164) are also shown in those figures and reveal a smooth consistent trend of decreasing level with frequency. This orderly behavior persisted during variation of the various parameters; so hereafter, most of the cabin noise analysis results are presented and discussed in terms of such averaged quantities.

7.2.4.5 Cabin Pressurization Effects

The sensitivity of cabin noise level to cabin pressurization was examined in order to determine whether corrections should be applied to other data obtained under conditions of varying cabin pressure. It was concluded that cabin pressurization caused comparatively small effects, and the data could be used "as measured" for assessing other test parameters.

Pressurization effects were determined by recording cabin noise data with the cabin pressurized and unpressurized while flying the testbed aircraft at constant speed, power, altitude, gross weight, and nacelle tilt angle. Several propfan blade passage frequencies (tip speeds) were flown so as to assess pressurization effects under varying structural response conditions. The tests were conducted at 3,658m (12,000 ft), 0.60 Mach, maximum continuous power (3764 kw (5048 PSHP)), and nacelle tilt of 1 degree down (baseline configuration).

When pressurized at 3,658m (12,000 ft), the fuselage shell pressure differential was 40,000 N/m² (5.8 psi); when unpressurized it was 2,068 N/m²

(0.3 psi); a change of $37,932 \text{ N/m}^2$ (5.5 psi). For these two cases, fuselage exterior sound pressure levels were averaged for 22 surface microphones, and cabin interior levels were averaged for 32 lateral, axial, and circumferential microphones. The results are shown in Figure 166 for the first-order blade passage frequency. In Figure 166 it is clear that the average cabin noise level is 1 to 5 dB higher with pressurization. Among the four blade passage frequencies, the mean noise increase was about 3 dB. This noise change is attributed to stiffening of the shell (attended by a resonance frequency shift toward the driving frequency) and to increased cabin air density (attended by stronger pressures radiated from the wall surfaces). The $37,932 \text{ N/m}^2$ (5.5 psi) change in pressure produces a density increase of about 43 percent which translates into a noise increase of about 3.1 dB. Thus, the effects of shell resonance change with pressurization are negligible.

The effects of pressurization were also examined at the second and third orders of blade passage frequency. The results were much the same--the mean noise increase was about 3.5 dB, and there was a bit more scatter about the mean.

7.2.4.6 Effects of Operating Conditions

Cabin noise varied with operating conditions in the same manner as did the fuselage exterior noise. Therefore, the parameters discussed here are limited to altitude, flight speed, propfan shaft power, and tip speed. Fuselage noise sensitivity to these and other operating conditions is described in Section 7.2.2.5.

The effects of cruise altitude and speed are illustrated in Figure 167 for constant power and tip speed conditions.

The baseline cruise condition of 10,668m (35,000 ft) and 0.8 Mach is seen to produce nearly the highest noise. At low-altitude cruise, average cabin noise is down about 7 dB at the first order and 10 dB at the third. The flight speeds shown are the high-speed condition appropriate for each altitude.

It is noteworthy that the average interior noise trends consistently follow the average exterior noise trends at each of the first three blade-order frequencies (which are multiples of 226 Hertz). And for these first three orders, the cabin noise level decreases about 5 to 7 dB per blade order.

The difference between the two sets of data represents average cabin noise reduction (NR). The average NR is seen to be in the range of 25 dB for all conditions and all orders.

Interior and exterior noise at the blade-passage frequency are also seen to be consistent when varying propfan power and tip speed at constant cruise conditions. This is illustrated in Figure 168. The cabin average noise levels changed about 8 dB between minimum (187 mps (615 fps)) and maximum (254 mps (835 fps)) tip speed. Likewise, levels changed about

8 dB when decreasing power from maximum (2394 kw or 3211 shp at this altitude) to minimum (483 kw or 648 shp). It is noteworthy that at 483 kw (648 shp) thrust was near zero; hence, blade lift was low, lift noise was low, and the principal source was thickness noise. Despite these source changes and the corresponding changes in directivity and spatial variation, the exterior and interior noise trends and relationships were essentially unchanged.

The horizontal scale of Figure 168 is also shown in terms of blade-passage frequency. Within the range of 175 to 238 Hertz excitation, no significant influences of structural or acoustic resonance are evident. The average noise reduction was consistently in the range of 25 dB. Similar results were obtained at other altitudes and at the second and third order of blade passage frequency. However, the variation in tip speed (excitation frequencies) increased the scatter in noise reduction somewhat.

7.2.4.7 Structureborne Noise

The PTA cabin was unique in many respects, and this necessitated special considerations in regard to SBN. These background factors and definitions are therefore discussed prior to describing the PTA data results.

Herein, the term Structureborne Noise (SBN) refers to that noise that is radiated into an airplane cabin by vibrating structures whose vibratory motion arises from causes other than direct acoustic excitation. An example of this SBN is cabin noise that is radiated by a section of a floor or by a section of a fuselage shell which is attached or connected to a wing, whereby the floor or shell structure is set into motion by wing vibrations that arise from remotely located causes. It follows that in the absence of remotely-generated cabin structural vibration, there would be no SBN.

Airborne noise (ABN), on the other hand, is cabin noise that is radiated by vibrating structures whose vibratory motion arises from the direct impingement of oscillatory pressures (whether acoustic or hydrodynamic) on the outer surface of the subject structure.

Given these definitions, SBN and ABN could be radiated into an airplane cabin by the same structure, and they could also be radiated independently by separate structures.

In any specific airplane with the usual causes of vibration, the severity or significance of SBN will be influenced by the airframe general arrangement and the details of the cabin structural interconnections to the other airframe components. To a large extent, these factors govern how efficiently the remotely-generated vibrations are imparted to the cabin structure. The significance of SBN will also depend on the type and on the extent of the provisions included for cabin noise reduction. In some cases, provisions that reduce airborne noise would automatically reduce SBN as well. But in other cases, provisions that reduce ABN could have no beneficial effect whatever on SBN. In this latter case, comparatively weak SBN sources that are undetectable in a bare untreated

airplane might become dominant in a finished airplane and produce a "noise floor" that could only be reduced by specialized provisions tailored specifically to control individual SBN sources.

In view of the aforementioned dependencies and uncertainties, it would be advisable in most airplanes, to conduct the SBN assessments after the cabin is completely furnished in the configuration that is intended to provide the desired passenger environment.

In the case of the PTA airplane, it was not possible to conduct the SBN assessments in a finished cabin despite the previously noted advantages of that approach. The PTA airplane cabin was completely bare throughout the cabin test section. It was totally devoid of passenger furnishings, trim, floor covering, or thermal insulation. This configuration was consistent in all of the cabin noise data flights. Consequently, the PTA data that are available for SBN assessments are for circumstances where ABN levels were high--much higher than would be tolerable in a normal passenger environment.

However, the PTA airframe configuration and the cabin structure interconnections to the wing are conducive to efficient SBN transmission. And the bare cabin interior that gave rise to the high ABN levels might also, in some areas at least, have given rise to proportionately high SBN levels as well. Given this distinct possibility, it was considered prudent and worthwhile to assess SBN in the PTA cabin. It must be reemphasized that the results derived therefrom would be limited to, and valid only for, the PTA airplane. The ultimate goal of gaging the relative importance of SBN for a generalized, low-noise propfan airplane could not be addressed.

Accordingly, static tests and flight tests were conducted to diagnose the mechanisms of sound transmission into the PTA cabin. The static test setup and the acoustic and vibration test apparatus are illustrated in Figure 169. One of these tests involved application of discrete and random forces to the wing front and rear spars, using an electromagnetic vibrator to generate force. In these tests, the vibration excited in the wing lower surface, and the resultant noise in the cabin, which is totally structureborne noise, were measured and correlated. This correlation between wing vibration and cabin structureborne noise then served as a basis for predicting in-flight structureborne noise using in-flight wing vibration data.

The relative vibratory responses in the wing and fuselage structures are depicted in Figure 170 for the case of excitation at the wing front spar outboard of the drive engine. A strong vibratory response is evident along the chord line where the shaker is located. The average vibration among the remaining wing accelerometers inboard of the engine is comparatively low; in fact, lower than the average vibration in the fuselage near the propfan plane. Clearly, the fuselage shell responded readily to vibration in the wing.

Shaker excitation of the wing was evaluated in terms of vibratory and acoustic response level and response linearity for force application at

the front spar in the inboard and outboard regions of the propfan slipstream and at the rear spar in the inboard slipstream region. In the overall, the inboard front spar area was judged to be more influential on cabin response.

A typical spectrum of the force applied is provided in Figure 171, showing the multi-tone discrete/random force character. The three tones are consistent with the first three orders of blade passage frequency. The corresponding vibration spectrum resulting at the same inboard front spar location is shown in Figure 172. The vibration is seen to have increased with order number while the force decreased.

The blade-order acceleration and noise levels were averaged (using a power ensemble averaging technique) for each test case, and for convenience of comparison, were normalized to a reference unit per pound (4.446 Newton) force. Figure 173 shows normalized average wing vibration levels for the three tone frequencies and three excitation locations. These results show: (1) linear relationship between force and wing vibration at all frequencies and locations, and (2) equal or higher response at the inboard front spar location. (A horizontal line on the normalized noise/force scale indicates that noise changed in direct proportion to force.) Similarly, Figure 174 shows normalized average fuselage vibration levels. These results show a linear relation to force at the inboard front spar and a nonlinear relation at the other two locations. At high force levels, the fuselage vibratory response is again highest for the case of inboard front spar excitation. For this case, fuselage levels are well below wing levels. The normalized average noise levels from the TRAM microphones at a fuselage station (TRAM position) near the front spar are shown in Figure 175. Cabin noise is seen to be linearly related to inboard front spar excitation force.

From these tests and analyses, it is clear that a propfan-induced oscillatory force on the wing can produce readily observable vibration and cabin noise. Also, the average cabin noise can be related to average wing vibration via Figures 173 through 175. For example, from Figure 173, at an inboard front spar relative force level of 15 dB at 225 Hz:

$$\text{Wing } \langle \text{AL} \rangle - \text{FL} = 79 \text{ dB}$$

(where the brackets denote a spatial average). From Figure 175 it can be seen that:

$$\text{Cabin } \langle \text{SPL} \rangle - \text{FL} = 55 \text{ dB}$$

at the same shaker frequency. Thus Cabin $\langle \text{SPL} \rangle$ is related to wing acceleration levels by:

$$\text{Cabin } \langle \text{SPL} \rangle = \text{Wing } \langle \text{AL} \rangle - 24 \text{ dB}$$

Using such empirical relationships, wing average vibrations measured in flight were used to estimate structureborne cabin noise levels. Examples are shown in Figure 176 for two extremes of altitude/speed conditions.

Also shown are the measured average cabin noise levels. It can be seen that the predicted structureborne noise is significantly lower than the measured noise except at BPF 3 at the low-altitude, low-speed condition.

Since the structureborne noise levels predicted for the PTA bare cabin (and shown in Figure 176) are higher than the total noise desired for a passenger environment, a reduction of the airborne noise without a reduction of the structureborne noise would result in a significant predicted structureborne noise problem. As stated previously, however, whatever might be done to reduce cabin airborne noise might reduce cabin structureborne noise as well. Such outcomes were not predicted and remain unknown.

An empirical relationship between cabin structureborne noise and the wing vibration intensity data was developed. Predictions with this technique showed that for the acoustically untreated PTA configuration, structureborne would be much lower than airborne noise. If airborne noise were reduced to an acceptable level, however, a reduction of structureborne noise might then become necessary.

One source of structureborne noise in the PTA cabin is wing structural vibration that, in turn, causes fuselage structural vibration. A principal cause of wing vibration is the impingement of the propfan tip vortex and wake fluctuating pressures on the wing surfaces. Therefore, structureborne noise might be more evident (over and above the airborne noise) at the flight conditions where wing FPLs were highest relative to the fuselage SPLs--conditions where fuselage exterior noise was low and slipstream fluctuating pressures on the wing were high. There were conditions where this was the case.

Figure 177 shows that at high-altitude, high-speed cruise and at a tip speed of 244 mps (800 fps), the highest FPLs on the wing surface were about 3 dB greater than the highest SPLs on the fuselage surface. The 3 dB difference increased to about 8 dB at a tip speed of 189 mps (620 fps). At low-altitude and low-speed cruise and a tip speed of 244 mps (800 fps), the difference between these maximum FPLs and SPLs, as shown in Figure 146, increased to nearly 18 dB. At this condition a reduction of tip speed to 189 mps (620 fps) further increased the FPL-SPL difference to the range of 25 dB. Clearly, this is a condition where structureborne noise may be likely to occur.

Accordingly, the in-flight cabin noise data were further examined for evidence of a structureborne noise contribution, and in this exercise, average noise reduction (NR) was used. Average NR is defined as the difference between average exterior and average interior noise levels. NR is largely determined by sidewall suppression and interior absorption, and typically varies with cabin pressurization and frequency. However, if any other source such as systems noise or structureborne noise were introduced so as to increase the cabin noise relative to exterior noise, or to sustain cabin noise level while exterior noise decreased, then NR would decrease in accord with the contribution of the new source. In other words, a significant decrease in NR would suggest the appearance of a cabin noise source other than ABN. This process would be capable of detecting SBN,

however, only in those cases in which the SBN level is near or higher than the ABN level. Thus, this approach would be quite insensitive to SBN at BPF in the PTA cabin where the level in the untreated cabin is much higher than the level typical of an acoustically treated cabin.

Average NR at the first three orders of blade passage frequency is shown in Figure 178 for a range of cruise conditions and a constant power and tip speed/BPF condition. In this illustration it is seen that average NR is virtually unchanged between 10,668m (35,000 ft) and 1,524m (5,000 ft) where structureborne noise is most likely to be a factor. The small changes that are visible in the data are thought to be the result of normal data scatter. Therefore, ABN was still higher than SBN at these conditions.

Average NR was further examined for the first-order of the blade passage frequency over the full range of tip speeds. This varied the first-order frequency from 238 Hertz down to 175 Hertz and further decreased fuselage SPLs relative to wing FPLs. The results are shown in Figure 179 for a range of altitudes. These results reveal a mild deterioration in NR at a tip speed of 229 mps (750 fps), and also at the lowest tip speeds, and suggest the possible presence of non-airborne noise at these low-altitude, low-tip-speed conditions. Further analysis would be necessary to determine whether or not this apparent non-airborne noise is SBN.

This could be a noteworthy result. It suggests an approach to testing that might be fruitful. If soundproofing were temporarily added in such a way as to intentionally reduce ABN but not SBN, then clearer definition of SBN might be obtained. Transmission paths could then be investigated, and an empirical relationship between SBN and wing FPL could be developed and subsequently used to predict SBN at other conditions of interest (such as the design cruise condition). SBN levels predicted in this manner would provide a basis for estimating the amount of SBN reduction required, if any, to achieve an acceptable passenger environment.

As stated previously, all of the evidence, or lack of evidence of structureborne noise discussed in this section, is derived from tests of the unfurnished acoustically untreated PTA cabin. It remains unknown whether SBN would be significant in either a generic or a specific multi-engine low-noise propfan-powered airplane.

7.2.4.8 Cabin Noise Reduction

While the PTA Program did not include an effort to reduce cabin total noise to a specific objective, it may be useful to roughly quantify the extent of noise reduction required.

At the baseline cruise condition of 10,668m (35,000 ft), 0.8 Mach, the "A" weighted sound levels of the bare PTA cabin ranged from 106 dBA to 86 dBA over the first seven blade orders, as illustrated in Figure 180. These levels sum to an "A" weighted overall level of 110 dBA. A reasonable cabin noise target (discounting the presence of discrete tones), might be about 80 dBA. In order to reduce the 110 dBA level to an overall of about

80 dBA, a soundproofing insertion loss (IL) of at least 30 dB is required. This assumes a treatment that is equally effective at all orders. A production airplane with multiple propfans would probably require at least 35 dB of soundproofing IL. Allowing for the additional annoyance of pure tones, for design margins, and for contributions from other sources, an appropriate IL target might be 40 dB. Recognizing that the NR measured for the shell structure averaged about 25 dB (see Figure 178), the combined wall and soundproofing total IL required would be about 65 dB. This degree of noise reduction presents a substantial challenge to the soundproofing designer. However, noise control research now in progress (and independent of the PTA Program) indicates that such a target will be achievable.

7.2.4.9 Observations

In the evaluation and interpretation of the cabin noise data, the following was observed.

1. The cabin noise was dominated by blade-order tones.
2. The first and second blade-order tones were, on an "A" weighted basis, equally annoying.
3. Interior noise spectra were consistent with exterior noise spectra after 25 to 30 dB of noise reduction (NR).
4. The propfan broadband noise level was low--in the same range as the boundary layer noise.
5. The propfan tone noise varied with location by 15 to 20 dB at any blade-order frequency.
6. The effect of pressurization on cabin noise level was small. The most influential factor is the air density increase with pressurization.
7. The effects of power, tip speed, altitude, and flight speed were consistent between cabin noise and exterior noise, i.e., a decreasing tip speed and power decreased cabin noise and exterior noise similarly.
8. The PTA cabin SBN levels that were predicted using wing vibration correlation techniques indicated some levels above those desired for an acceptably quiet cabin.
9. The PTA bare cabin noise environment was dominated by airborne noise.
10. The noise reduction afforded by the bare cabin wall averaged about 25 dB at the first three blade orders.
11. An additional cabin wall insertion loss of at least 30 dB over and above that provided by the bare wall would be required to achieve an 80 dBA passenger environment in the PTA cabin.



8.0 CONCLUDING REMARKS

The Propfan Test Assessment Program produced a considerable amount of high-quality flight test data on the structural integrity of, and noise propagation from, a high performance, single rotation propfan.

Blade vibratory response data, which were dominated by 1P loads, showed the propfan to be well-behaved structurally over the entire operational envelope of the aircraft. Predicted 1P blade responses at low flight speeds were about 15-percent higher than measured at the critical inboard bending gage. At high speeds also, predicted 1P blade response was higher than measured, but good comparisons were precluded by the extreme sensitivity of the predictions to propfan inflow angle and insufficient precision in the aircraft angle of attack measurement system. Nevertheless, measured data for all tests showed blade design methodology to adequately predict all critical loading conditions.

Blade response data correlated well with the excitation factor, which is proportional to the mean inflow angle at the propeller plane and the mean inflow dynamic pressure. Excitation factor was varied over a range from -3 degrees to +2 degrees, relative to the fuselage reference plane, with a variable nacelle tilt feature designed into the aircraft. The -1 degree position appeared best for low blade vibratory response over the test envelope.

As expected, noise of the propfan was characterized by tones at blade passage frequency and higher harmonics. There was little or no evidence of significant propeller broadband noise. Noise directivity was relatively strong--not only fore and aft of the propeller plane, but also relative to the direction of rotation in the propeller plane. Low-altitude, far-field noise, for instance, was greater on the side of the aircraft away from the propfan than on the near side. Far-field noise levels were greater than predicted, but sensitivity of these noise levels to propfan tip speed and power provides the designer with optimization tools to attain desired community noise levels.

Radiated noise was also strongly affected by propeller inflow angle. One of the greater deficiencies of the noise predictions resulted from inadequate recognition of this effect. Generally, however, the prediction methods adequately dealt with the trends of power, airspeed, and tip speed effects, although absolute levels were often missed by amounts greater than 3 dB. For this up-inboard rotating propfan, increasing nacelle tilt (or inflow angle) reduced noise on the fuselage surface inboard and increased noise on the boom surface outboard. This suggests that nacelle tilt angle may be used to optimize noise radiation to the cabin, but, of course, the impact on blade vibratory stress must also be considered.

Prediction methods did very poorly in the area of fluctuating pressure levels in the propfan wake--underpredicting by amounts averaging about 30 dB. Obviously, there is a need for improved analysis in this area.

PRECEDING PAGE BLANK NOT FILMED



Cabin noise measurements showed the untreated cabin walls to reduce noise levels about 25 dB. With exterior noise levels at 145 to 150 dB, however, it is estimated that additional wall treatment with insertion loss of about 40 dB would be required for commercial application. The data showed little evidence of structureborne noise being significant, but there was some implication that it could become important as cabin noise levels are reduced.

APPENDIX A

PROPFAN BLADE EXCITATION FACTOR

Whenever a lifting rotor (propeller, propfan, etc.) operates in a uniform flow parallel to the rotor centerline, each blade is loaded uniformly at every point in the rotation cycle, and no vibratory loads are generated. If, however, the rotor is inclined at an angle ψ to the flow field, the local angle of attack which each blade experiences varies as the blade rotates around the propeller plane.

This may be illustrated by Figure A-1. For a propfan with its axis at positive angle of attack, the blade on the side moving down will have a lower angle of attack than on the side where it is moving up. Thus, angle of attack will vary cyclically in the manner shown in Figure A-2. Consequently, blade loading will also vary cyclically--giving rise to once-per-revolution (1P) loads. For a propeller mounted on an aircraft, flow angularity due to yaw may also exist, and ψ can be considered to be:

$$\psi = \sqrt{\alpha^2 + \beta^2}$$

If the flow in which the propeller is immersed is not uniform, higher order (nP) cyclic loading may exist. For instance, the presence of a wing or pylon behind the rotor may cause a perturbation in velocity to feed forward into the propeller plane to create a local disturbance. Similarly, the presence of an engine inlet may also create velocity perturbations in the propeller plane.

The relative magnitude of these vibratory loads has been quantified by Hamilton Standard using an empirically derived parameter called excitation factor, or EF. The 1P loading is directly related to the freestream dynamic pressure and the inflow angle by the equation:

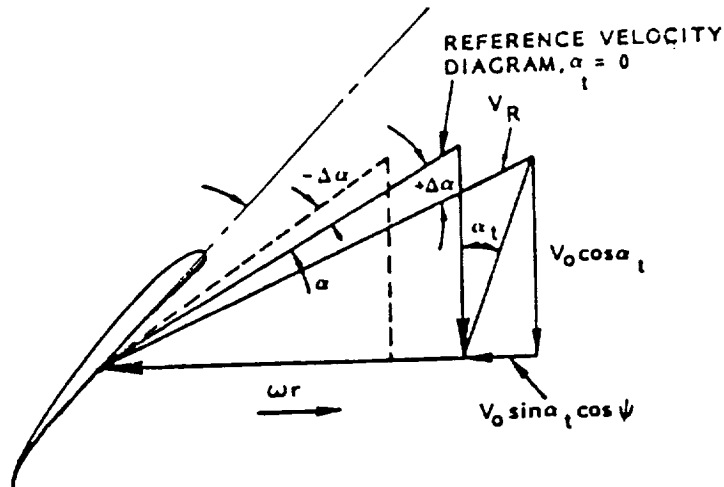
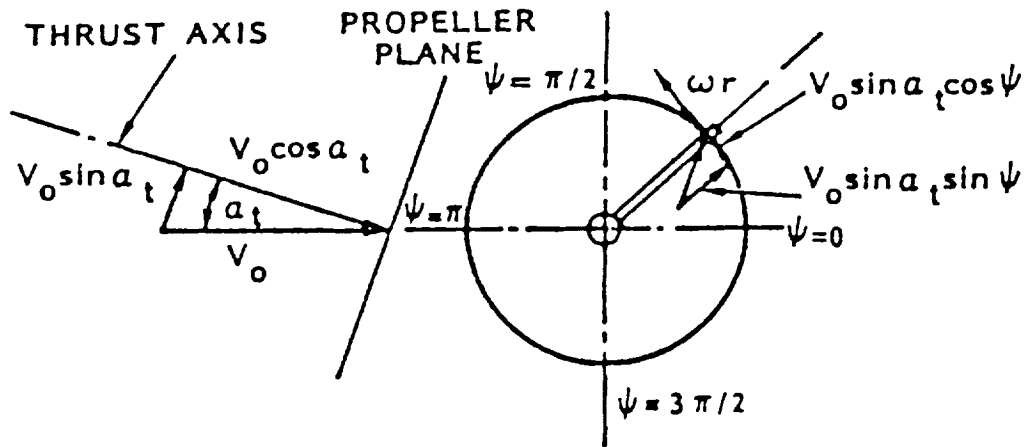
$$EF_{1P} = \psi \left(\frac{V_E}{179} \right)^2 \quad \text{for } V_E \text{ in mps}$$

$$\text{or } \psi \left(\frac{V_E}{348} \right)^2 \quad \text{for } V_E \text{ in kts}$$

Figure A-3 shows a plot of 1P EF as a function of angle of attack for the PTA configuration. It can be seen that there are two sets of curves--one for tilt of the nacelle in the vertical plane (where the nacelle tilt angle adds to the angle of attack effects), and a second for the effects of yaw angle (which is almost independent of angle in the vertical plane). When the effects of yaw and pitch angles are added, the results are as shown in Figure A-4. Here it can be seen that the effects of yaw are such that there is always an absolute value of EF greater than zero.



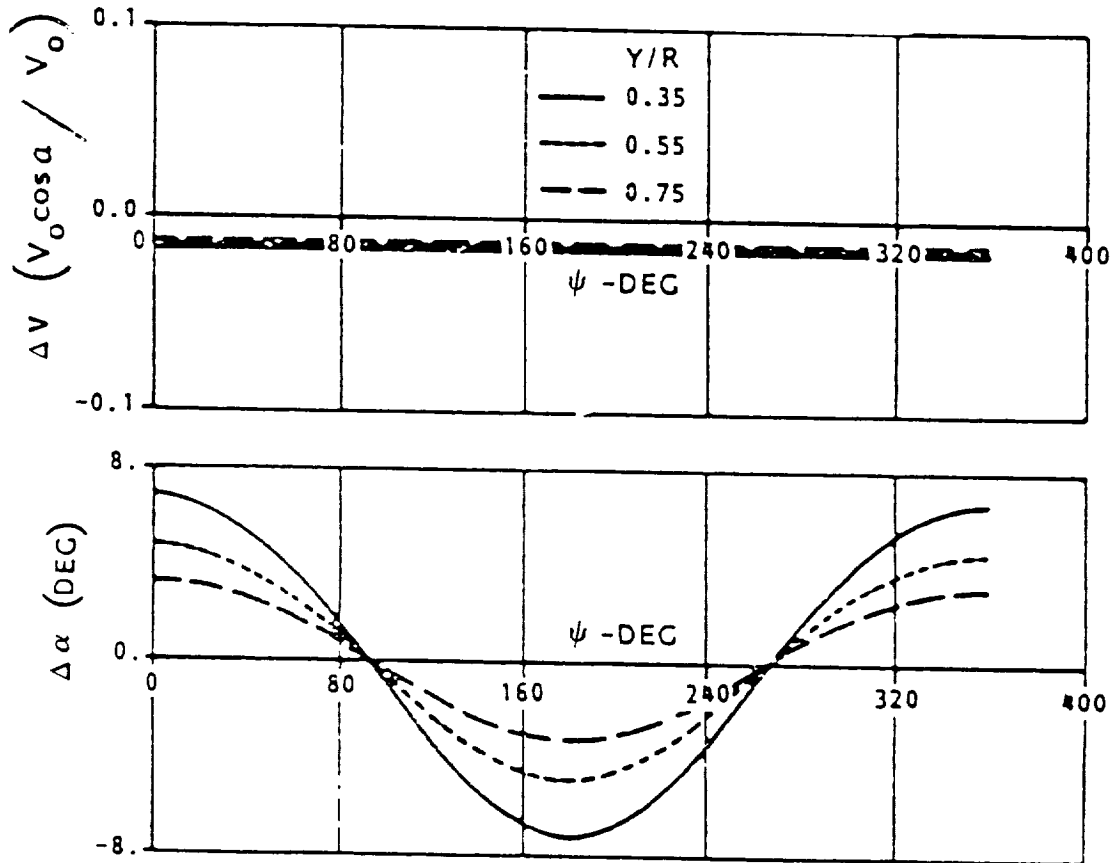
Finally, plots of equivalent EF for the PTA configuration are shown in Figure A-5. Equivalent EF includes higher order excitation due to those configurational aspects that are unique to the PTA. Values of EF were obtained by applying a magnification factor to the 1P EF values of Figure A-4. This magnification factor was determined by Hamilton Standard after the configuration was defined and preliminary predictions of the flow field in the plane of the propeller had been made.



- V_0 - FREESTREAM VELOCITY
- α_t - BLADE ANGLE OF ATTACK
- ω_r - ROTATIONAL VELOCITY
- ψ - AZIMUTH ANGLE

Figure A-1. Cyclical Variation of Propeller Blade Local Flow Field

SR-7L 1/9 SCALE PROPELLER



- V_0 - FREESTREAM VELOCITY
- V - PROPELLER AXIAL VELOCITY
- α_t - BLADE ANGLE OF ATTACK
- α - BLADE ELEMENT LOCAL ANGLE OF ATTACK
- Y - RADIAL LOCATION ALONG BLADE
- R - BLADE RADIUS
- ψ - AZIMUTH ANGLE

Figure A-2. Cyclical Variation of Propeller Blade Velocity and Angle of Attack

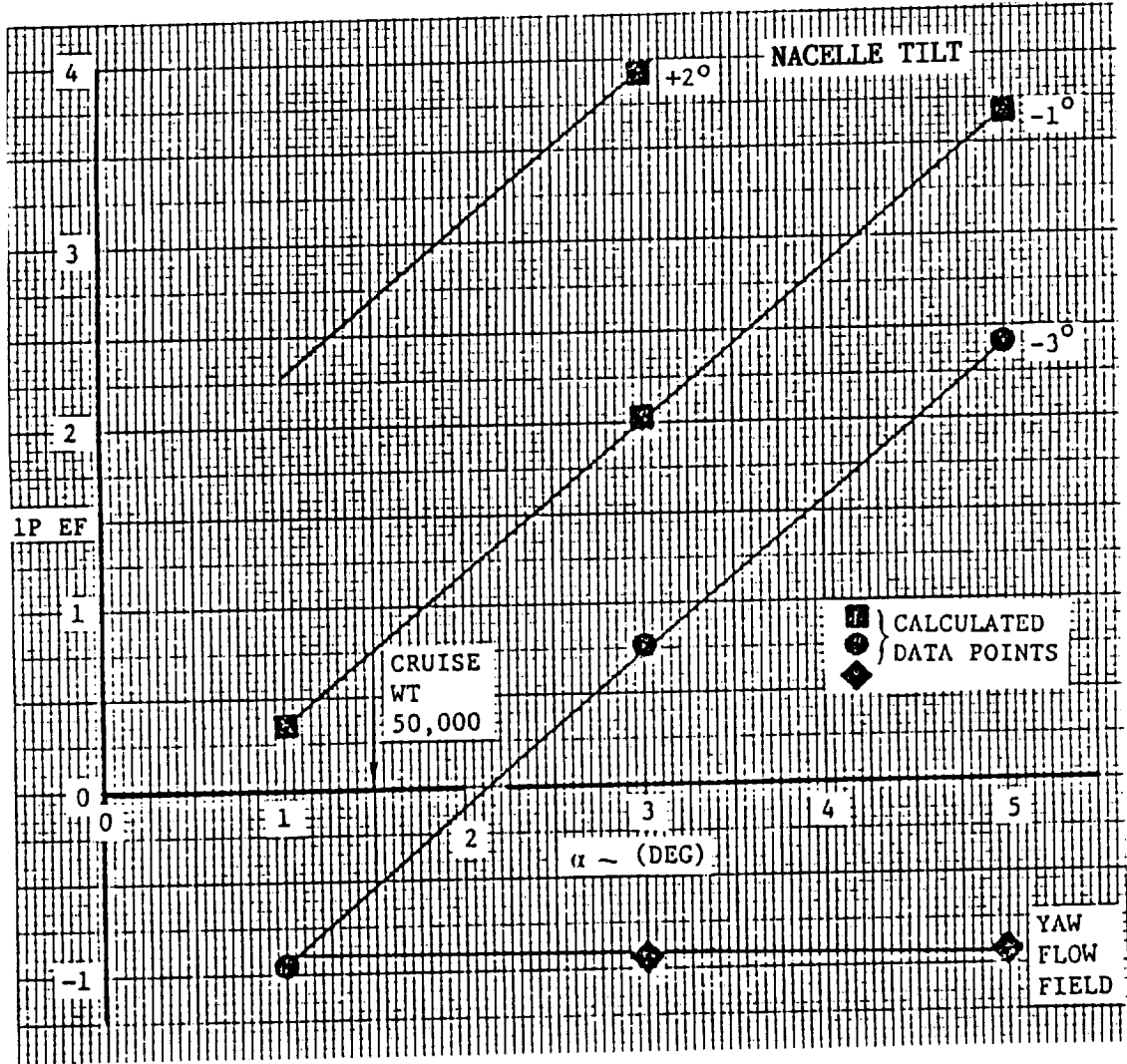


Figure A-3. PTA Propfan Excitation Factors Due to Pitch and Yaw

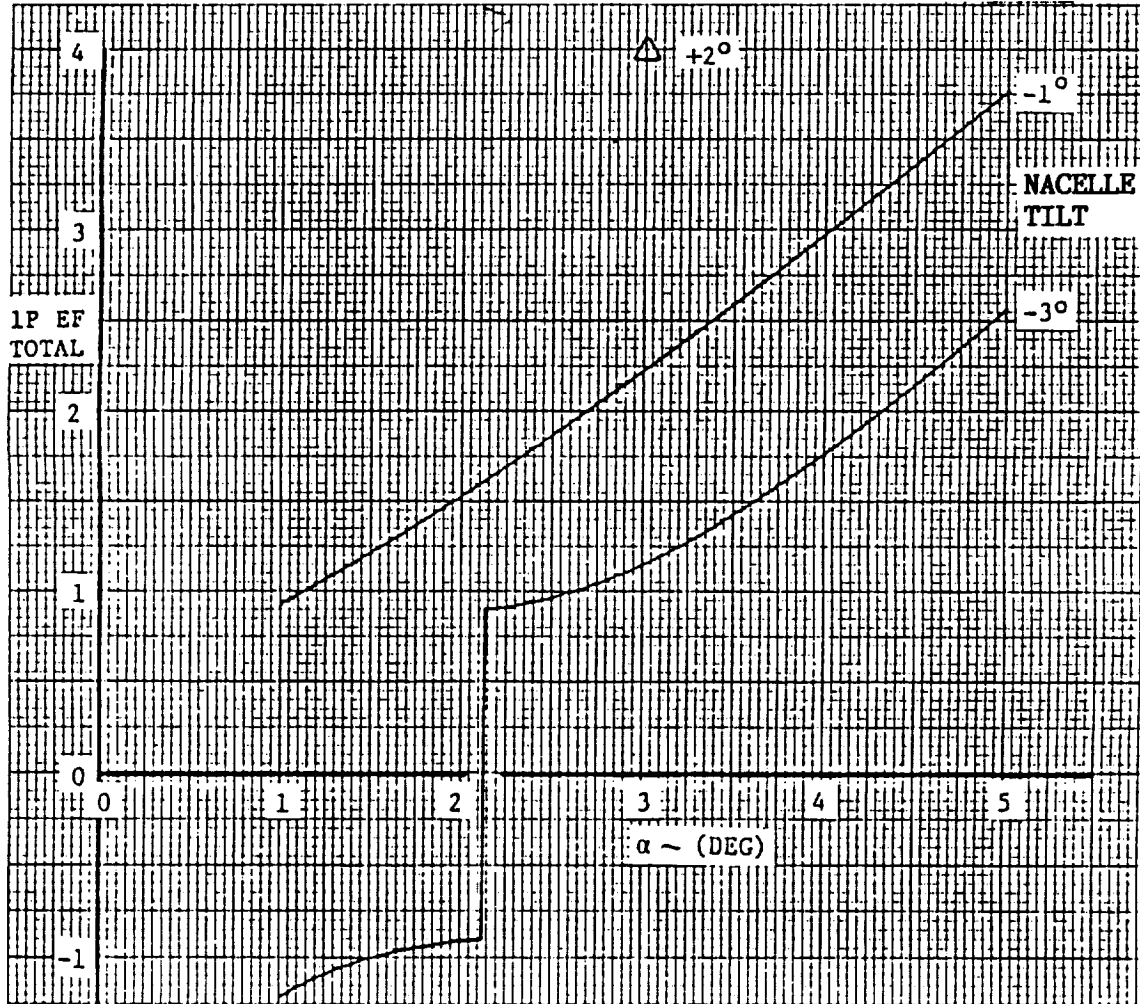


Figure A-4. PTA Propfan Total 1P Excitation Factors

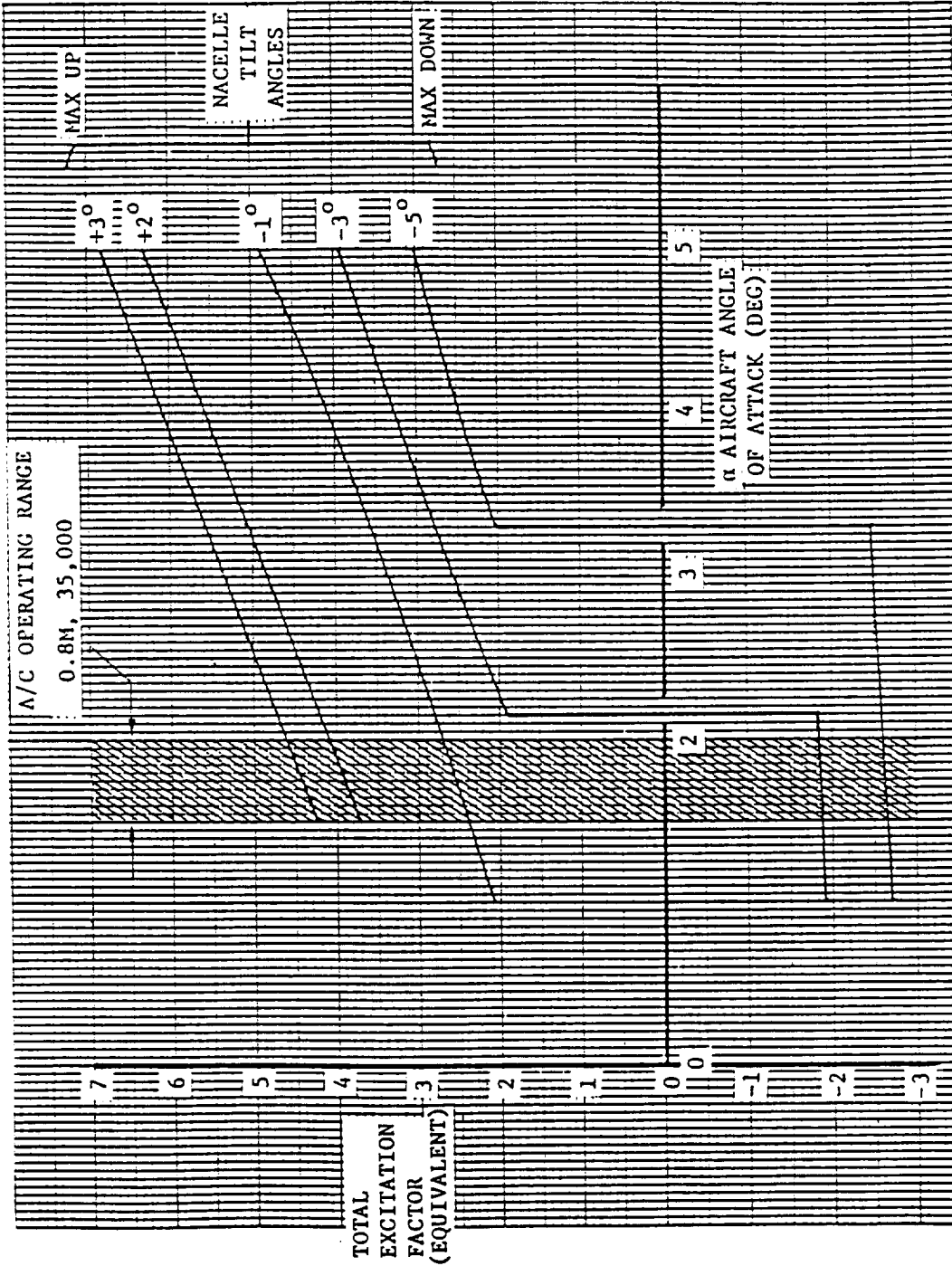


Figure A-5. PTA Propfan Equivalent Excitation Factors



APPENDIX B

LOCATION OF MICROPHONES, ACCELEROMETERS,
AND STRAIN GAGES ON PTA AIRCRAFT

List of Figures

<u>Figure</u>	<u>Title</u>	<u>Page</u>
B-1	Fuselage Surface Microphone Locations	75
B-2	Fuselage Surface Microphone Locations	76
B-3	Acoustic Boom Installation and Microphone Locations	78
B-4	Fuselage Internal Microphone Stations	79
B-5	Cabin Fixed Microphone Locations	80
B-6	Summary - Cabin Microphone Locations	82
B-7	Cabin Microphone TRAM Assembly	83
B-8	Microphone Locations Left Wing	85
B-9	Wing Lower Surface Microphone Locations	86
B-10	Wing Upper Surface Microphone Locations	87
B-11	Cabin Accelerometer Locations	90
B-12	Wing Accelerometer Locations	93
B-13	Acoustic Strain Gages Wing Upper Spar Cap	96
B-14	Acoustic Strain Gages Wing Lower Spar Cap	97
B-15	Accelerometer Locations, Nacelle/Wing	99
B-16	Propulsion System Accelerometer Locations	100

PREVIOUS PAGE BLANK NOT FILMED

APPENDIX B

List of Tables

<u>Table</u>	<u>Title</u>	<u>Page</u>
B-1	Fuselage Surface Microphone Locations	77
B-2	Cabin Fixed Microphone Locations	81
B-3	Cabin Moving Microphone Locations	84
B-4	Wing Lower Surface Microphone Locations	88
B-5	Wing Upper Surface Microphone Locations	89
B-6	Cabin Accelerometer Locations	91
B-7	Wing Accelerometer Locations	94
B-8	Left Wing Strain Gage Locations	98

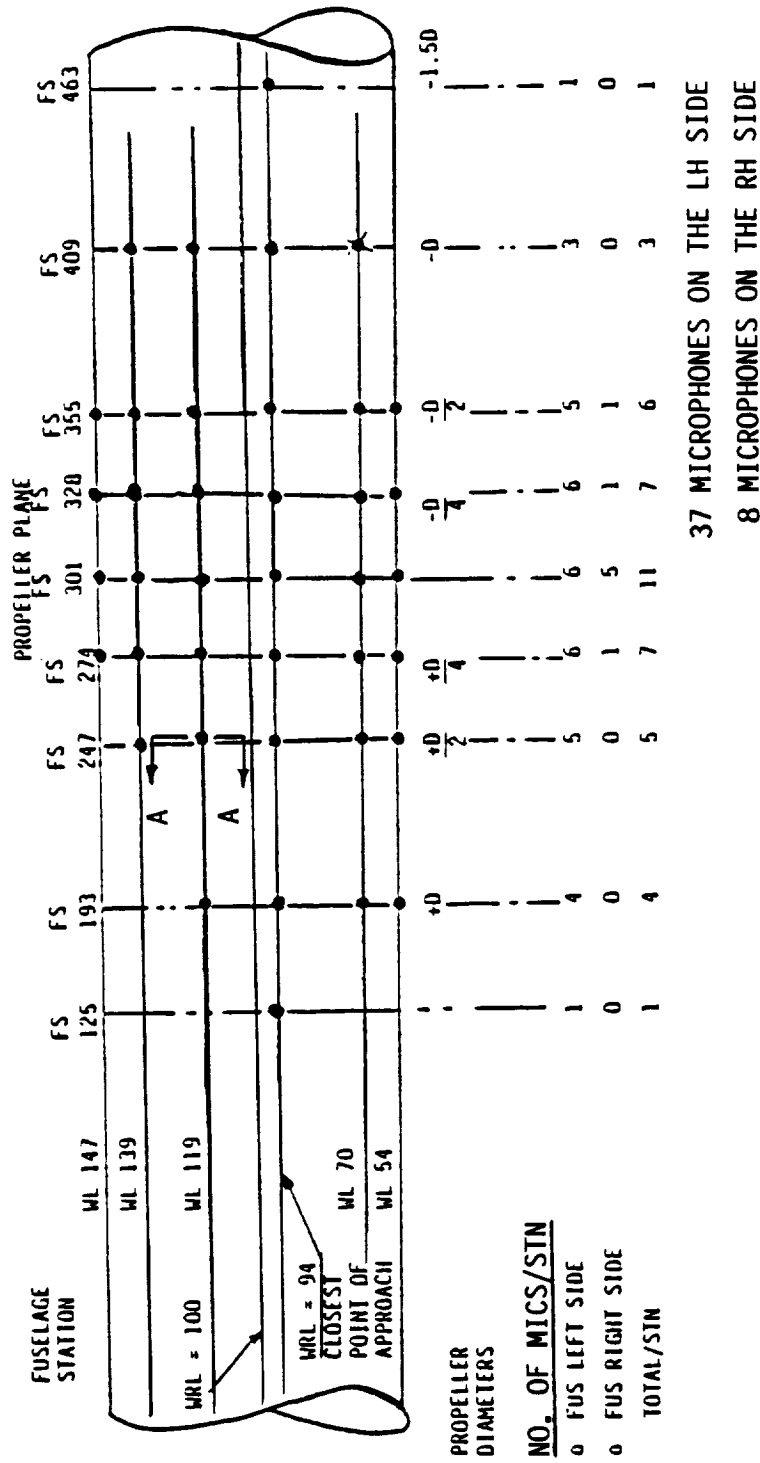


Figure B-1. Fuselage Surface Microphone Locations

* INDICATES WING BOOM CORRESPONDENCE

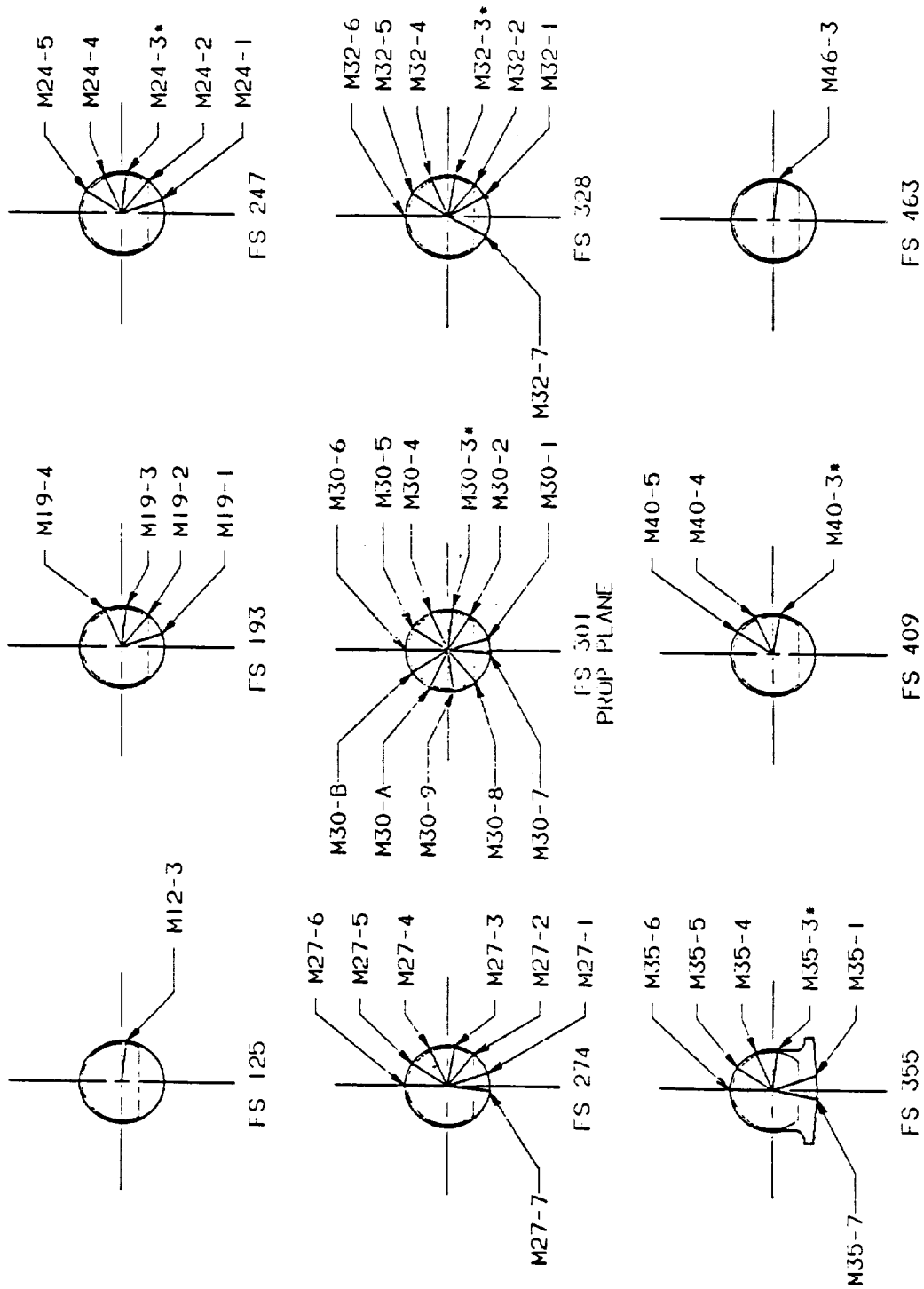


Figure B-2. Fuselage Surface Microphone Locations

TABLE B-1.
FUSELAGE SURFACE MICROPHONE LOCATIONS

FUSELAGE STATION (AXIAL)	125	195	247	274	301	328	355	409	463
PROP DIAMETER (REF TO PP)	+1.63D	+0.98D	+0.5D	+0.25D	PROP PLANE	-0.25D	-0.5D	-1D	-1.5D
<u>WATER LINE</u>									
147.00				0.00	0.00	0.00	0.00		
139.45			25.70	25.70	25.70	25.70	25.70		
118.92		43.03	43.03	43.03	43.03	43.03	43.03	43.03	
93.65	46.57	46.57	46.57		46.57		46.57		46.57
91.71				46.27		46.27		46.27	
70.00		36.17	36.17	36.17	36.17	36.17			
55.85		16.17	16.17	16.17	16.17	16.17*	16.17*		
53.69				8.00R	8.00R	8.00R*	8.00R*		
67.47					33.93R				
93.65					46.57R				
118.92					43.03R				
139.45					25.70R				

* INDICATES EQUIVALENT CYLINDRICAL LOCATIONS (FUSELAGE ACTUALLY HAS A FAIRING)

BUTT LINE LOCATIONS FOR FUSELAGE LEFT SIDE (PROPELLER SIDE)

BUTT LINE LOCATIONS FOR FUSELAGE RIGHT SIDE

NOTE: (1) PROPELLER DIAMETER = 274.3 CM (108")

(2) MICROPHONE DIAPHRAGMS ARE VERTICAL AND ON PROPELLER SIDE OF BOOM

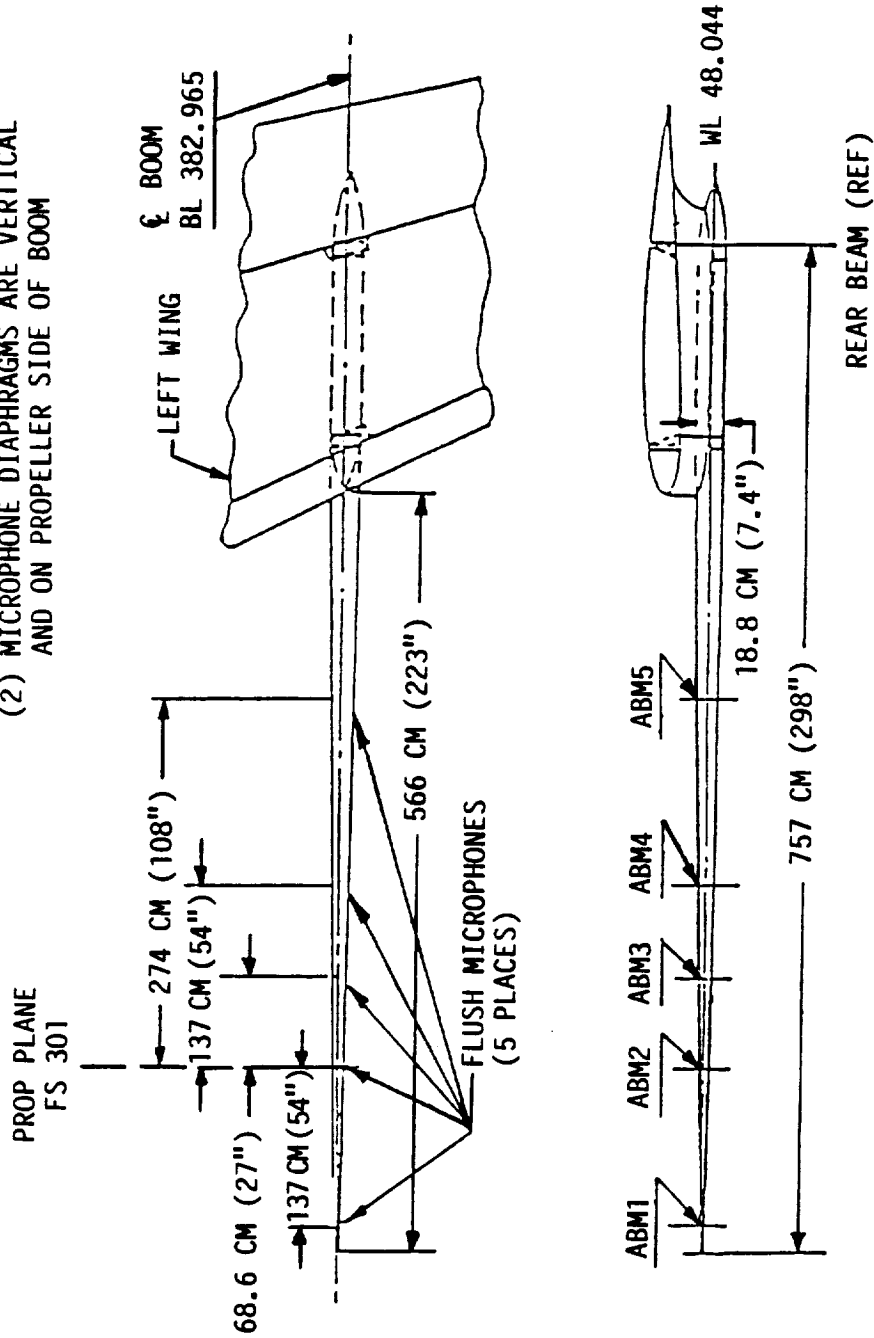


Figure B-3. Acoustic Boom Installation and Microphone Locations

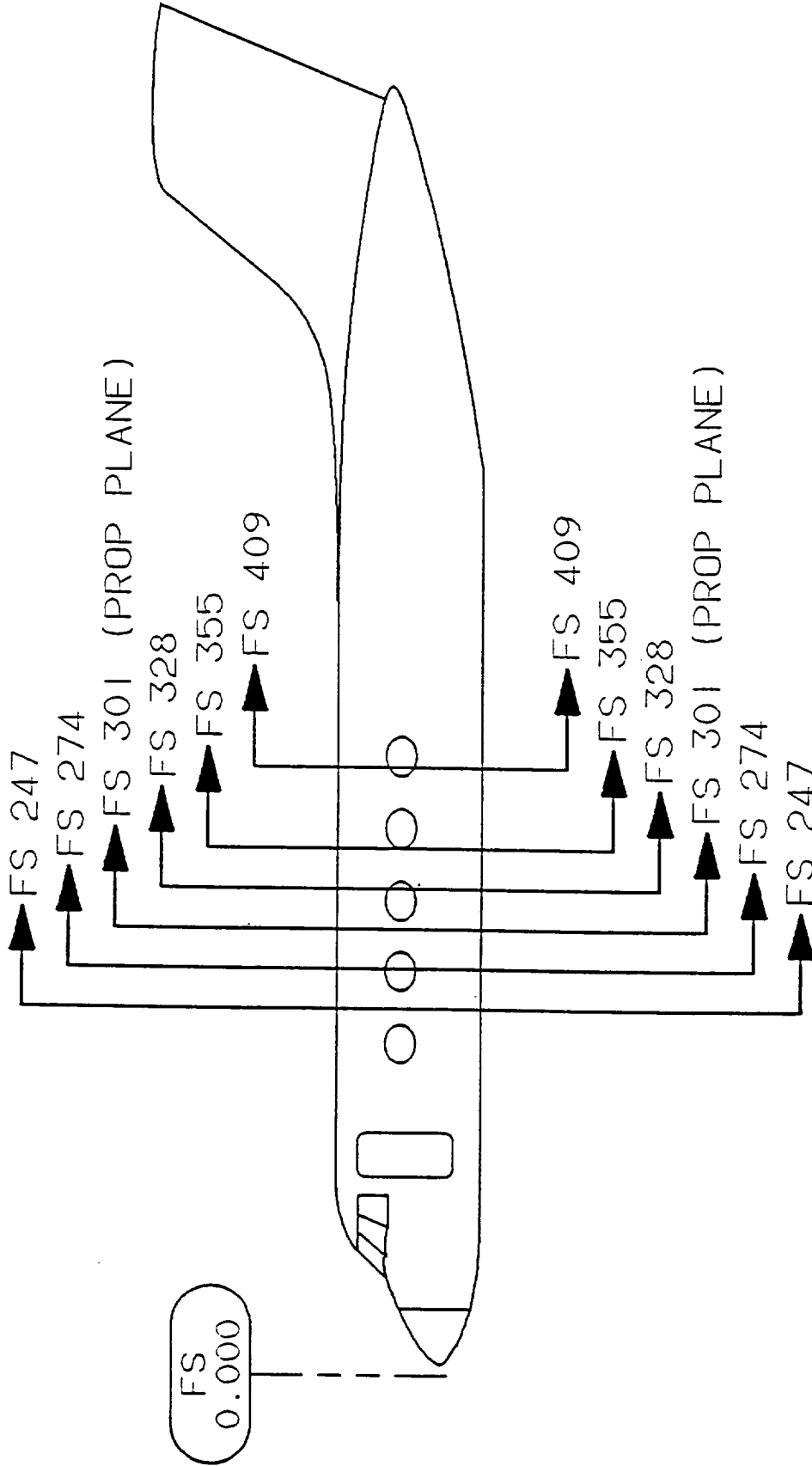


Figure B-4. Fuselage Internal Microphone Stations

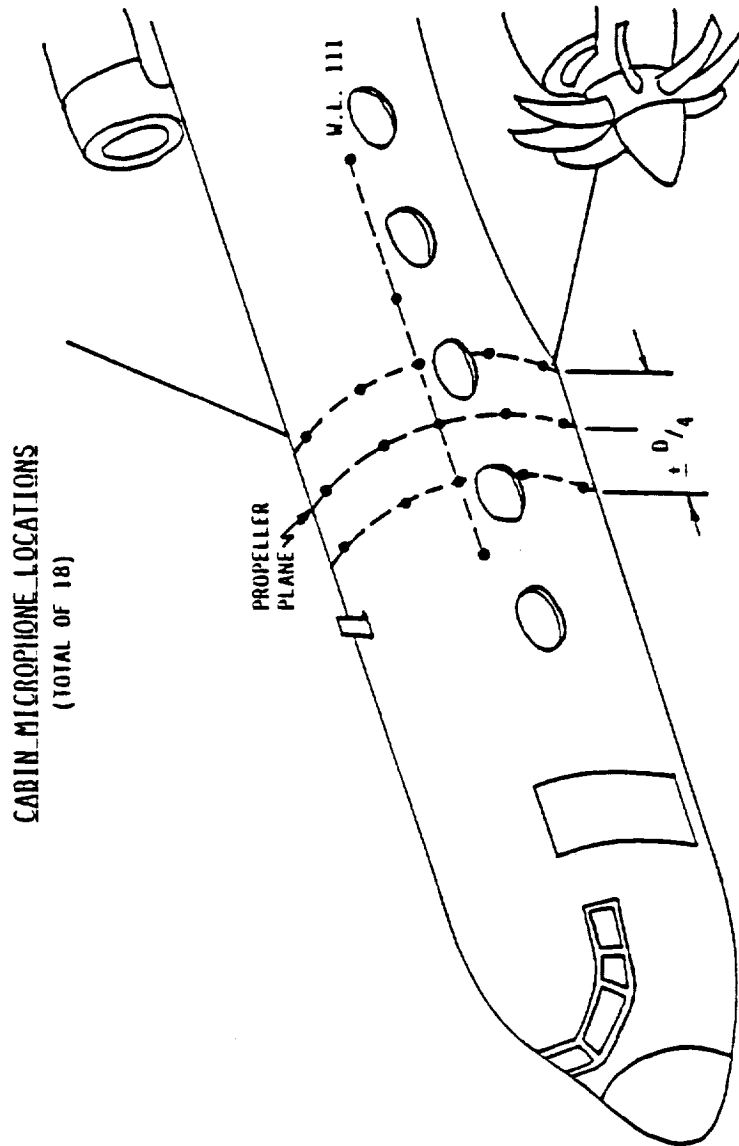


Figure B-5. Cabin Fixed Microphone Locations

TABLE B-2.
CABIN FIXED MICROPHONE LOCATIONS

TRANSDUCER	FUSELAGE STATION	WATER LINE	STRINGER NUMBER	DESCRIPTION
MA01	247	119	9	Axial Array
MA02	274	119	9	Axial Array
MA03	301	119	9	Axial Array
MA04	328	119	9	Axial Array
MA05	355	119	9	Axial Array
MA06	409	119	9	Axial Array
MC01	274	119	1	Circumferential Array
MC02	301	139.9	1	Circumferential Array
MC03	328	139.9	1	Circumferential Array
MC04	274	131.7	5	Circumferential Array
MC05	301	131.7	5	Circumferential Array
MC06	328	131.7	5	Circumferential Array
MC07	274	94.1	13	Circumferential Array
MC08	301	94.1	13	Circumferential Array
MC09	328	94.1	13	Circumferential Array
MC10	274	75.4	17	Circumferential Array
MC11	301	75.4	17	Circumferential Array
MC12	328	75.4	17	Circumferential Array

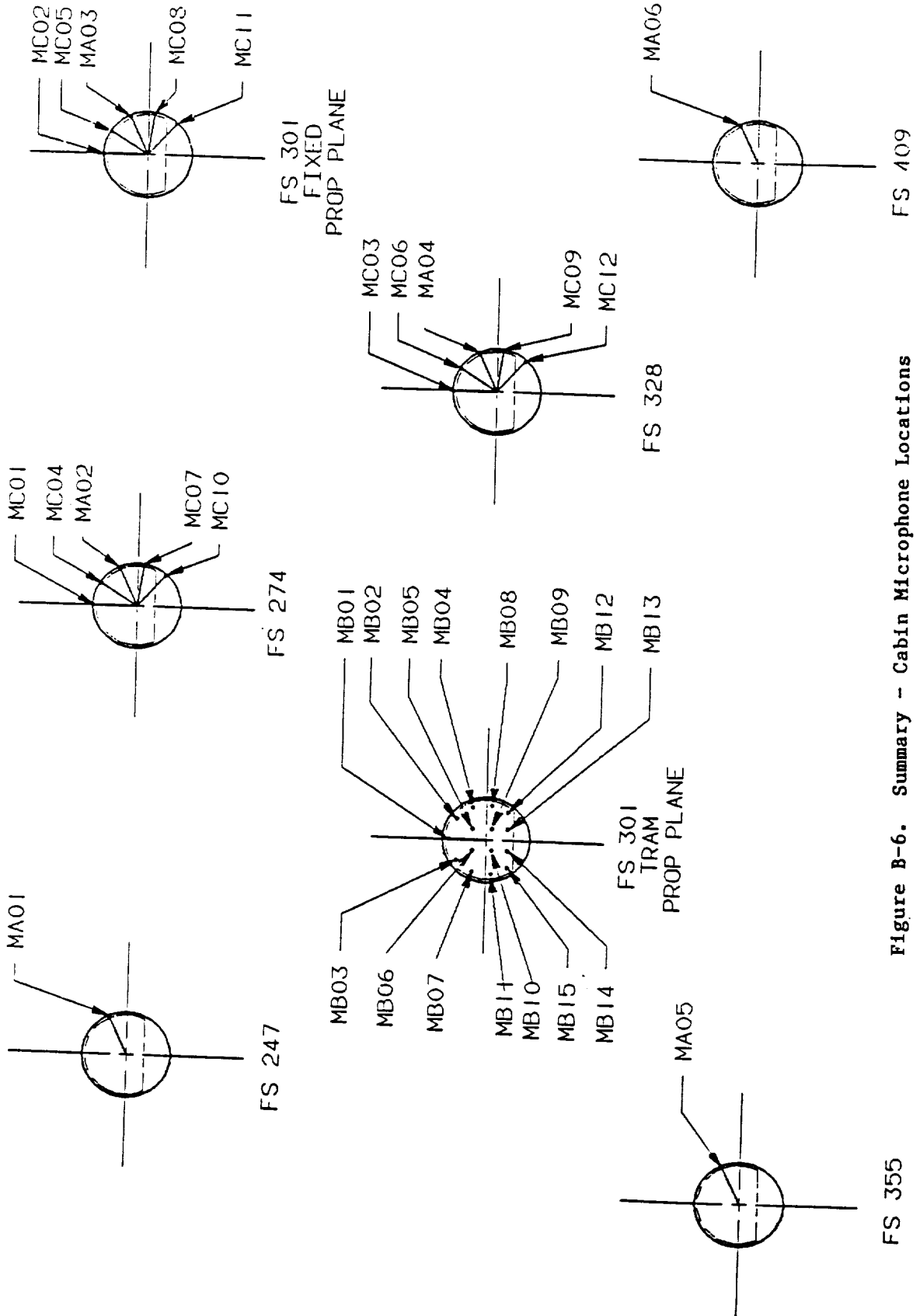


Figure B-6. Summary - Cabin Microphone Locations

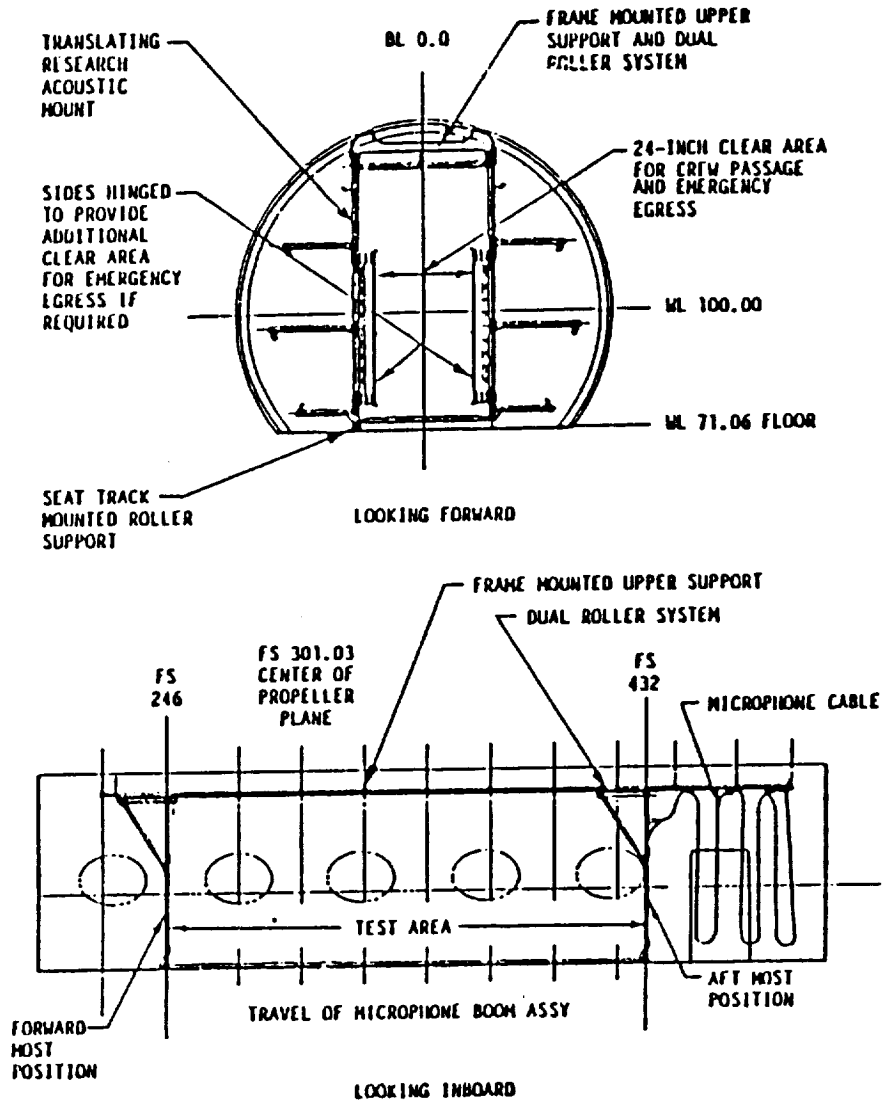


Figure B-7. Cabin Microphone TRAM Assembly

TABLE B-3.
CABIN MOVING MICROPHONE LOCATIONS

TRANSDUCER	FUSELAGE STATION	WATER LINE	BUTT LINE	DESCRIPTION
CBM1	Variable	77	30.8L	Circumferential Array
CBM2	241 to 433	94.1	37.9L	Circumferential Array
CBM3	241 to 433	114.7	35.6L	Circumferential Array
CBM4	241 to 433	131.7	22.7L	Circumferential Array
CBM5	241 to 433	139.9	0	Circumferential Array
CBM6	241 to 433	131.7	22.7R	Circumferential Array
CBM7	241 to 433	114.7	35.6R	Circumferential Array
CBM8	241 to 433	94.1	37.9R	Circumferential Array
CBM9	241 to 433	77	30.8R	Circumferential Array
GBM1	241 to 433	77	12L	Rectangular Grid
GBM2	241 to 433	94.1	12L	Rectangular Grid
GBM3	241 to 433	114.7	12L	Rectangular Grid
GBM4	241 to 433	114.7	12R	Rectangular Grid
GBM5	241 to 433	94.1	12R	Rectangular Grid
GBM6	241 to 433	77	12R	Rectangular Grid

MICROPHONE LOCATIONS
LH WING UPPER AND LOWER SURFACE

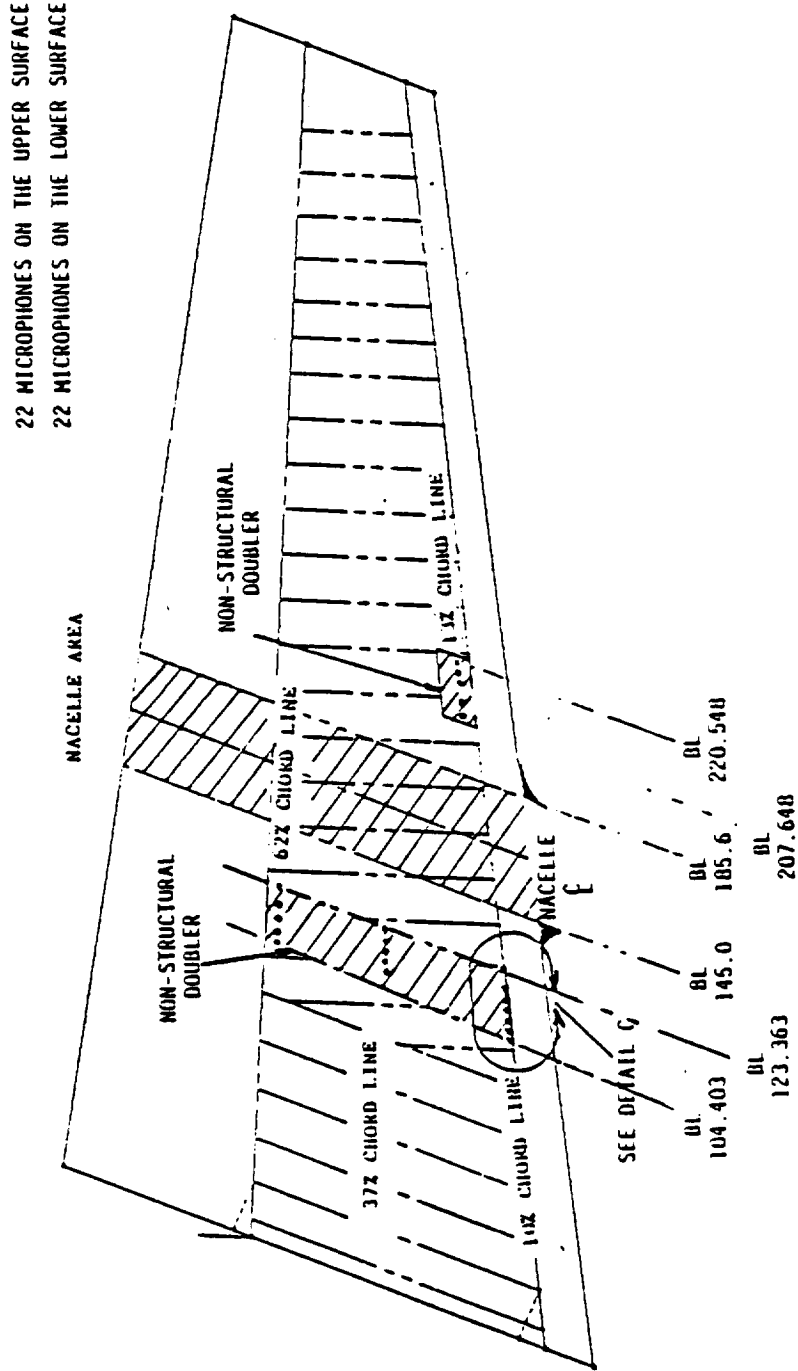


Figure B-8. Microphone Locations Left Wing

0-2

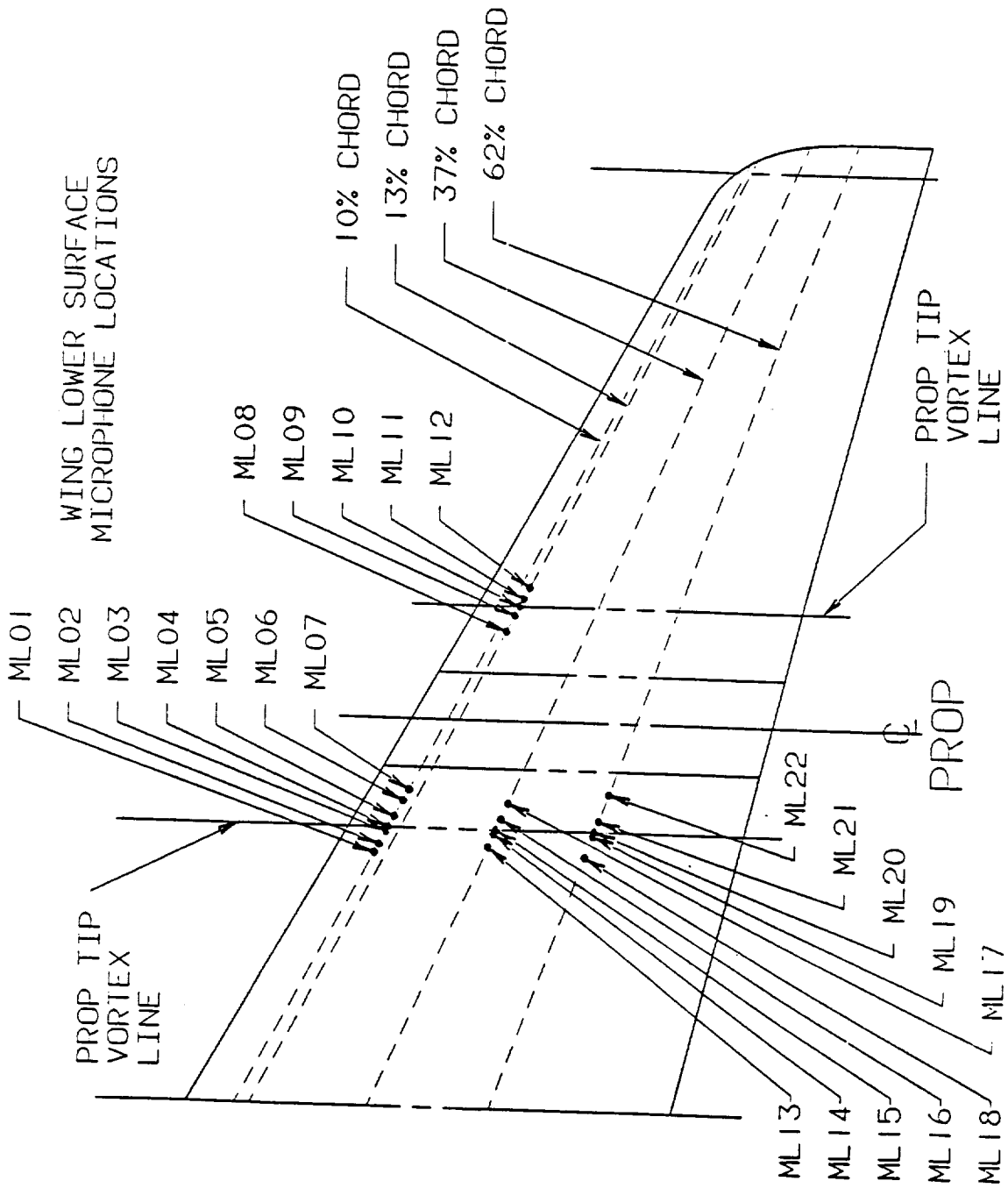


Figure B-9. Wing Lower Surface Microphone Locations

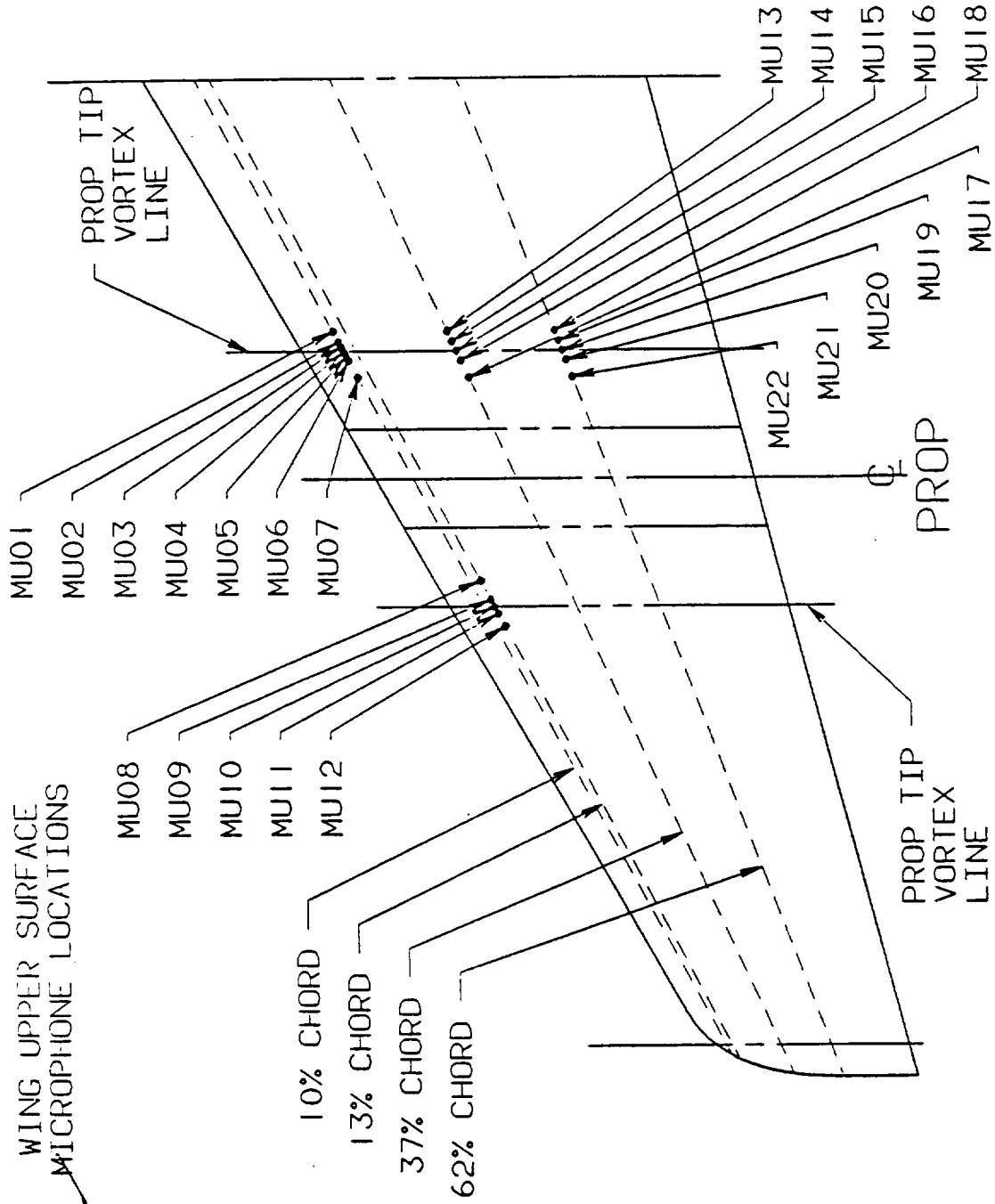


Figure B-10. Wing Upper Surface Microphone Locations

TABLE B-4.
WING LOWER SURFACE MICROPHONE LOCATIONS

WING % CHORD (FROM LE)	WING BUTT LINES										PROP CL	OUTBOARD PROP TIP						
	INBOARD PROP TIP					OUTBOARD PROP TIP						PROP CL	OUTBOARD PROP TIP					
10%	107.943	111.503	116.999	119.060	123.471	130.367	135.000	203.561	210.500	214.353	217.596	222.441	165.300	ML08	ML09	ML10	ML11	ML12
	.21R* ML01**	.14R ML02	.03BR ML03	TIP ML04	.082R ML05	.209R ML06	.295R ML07	0.2R	.071R	TIP	.060R	.15R						
13%	--	111.497	116.349	119.000	123.180	130.567	--	203.561	210.500	214.353	217.596	222.441	165.300	ML08	ML09	ML10	ML11	ML12
	--	.14R ML13	.04R ML14	TIP ML15	.08R ML16	.2R ML17	--	0.2R	.071R	TIP	.060R	.15R						
37%	--	111.497	116.349	119.000	123.180	130.567	--	203.561	210.500	214.353	217.596	222.441	165.300	ML08	ML09	ML10	ML11	ML12
	--	.14R ML13	.04R ML14	TIP ML15	.08R ML16	.2R ML17	--	0.2R	.071R	TIP	.060R	.15R						
62%	107.929	--	115.696	119.000	123.461	--	135.756	203.561	210.500	214.353	217.596	222.441	165.300	ML08	ML09	ML10	ML11	ML12
	.21R ML18	--	.06R ML19	TIP ML20	.083R ML21	--	.31R ML22	0.2R	.071R	TIP	.060R	.15R						

NOTE: 100% CHORD
 * INBD TIP = 146.7"
 ** OUTBD TIP = 110.1"

* DISTANCE FROM PROP TIP IN TERMS OF PROP RADIUS
 ** MICROPHONE DESIGNATION

TABLE B-5.
WING UPPER SURFACE MICROPHONE LOCATIONS

WING % CHORD (FROM LE)	WING BUTT LINES												
	INBOARD PROP TIP					PROP CL	OUTBOARD PROP TIP						
10%	104.456 .15R ^a MU01 **	108.670 .072R MU02	110.621 .036R MU03	112.563 TIP MU04	114.513 .036R MU05	116.465 .072R MU06	123.382 .20R MU07	165.300	207.648 0.2R MU08	215.529 .054R MU09	218.448 TIP MU10	221.359 .054R MU11	226.546 .15R MU12
13%													
37%	104.459 .15R MU13	109.650 .054R MU14		112.563 TIP MU15	115.485 .054R MU16		123.382 0.2R MU17						
62%	104.452 .15R MU18	109.644 .054R MU19		112.563 TIP MU20	115.473 .054R MU21		123.364 0.2R MU22						

NOTE: 100% CHORD
^a INBD TIP = 146.7"
^b OUTBD TIP = 118.1"

^a DISTANCE FROM PROP TIP IN TERMS OF PROP RADIUS
^{**} MICROPHONE DESIGNATION

**CABIN ACCELEROMETER LOCATIONS
(TOTAL 45)**

SUMMARY

- 1 CABIN AXIAL ARRAY (10)
- 2 CABIN CIRCUMFERENTIAL ARRAY (23)
- 3 WING/FLOOR (5)
- 4 WINDOW (3)
- 5 WINDOW FRAME (2)
- 6 TRIM PANEL (2)

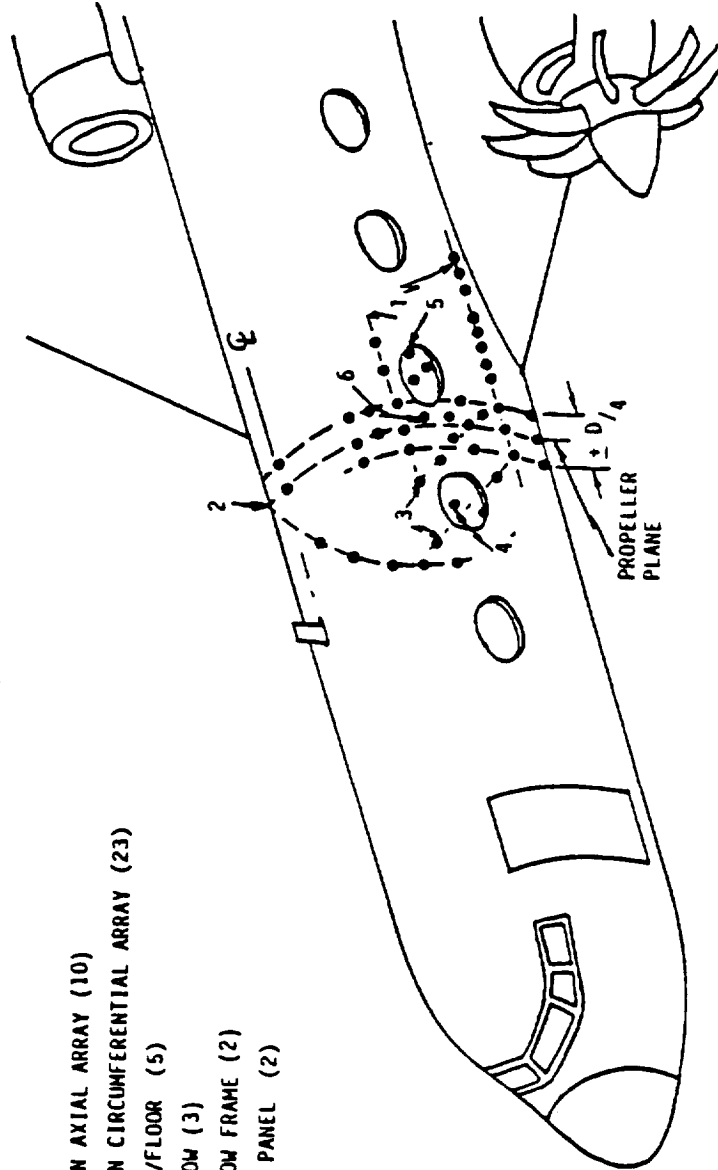


Figure B-11. Cabin Accelerometer Locations

TABLE B-6.
CABIN ACCELEROMETER LOCATIONS

TRANSDUCER	FUSELAGE STATION	WATER LINE	STRINGER BL NUMBER	DESCRIPTION
AF02	297.0	70.1	17	Wing/Floor Array
AF03	297.0	70.1	17	Wing/Floor Array
AF04	297.0	70.1	17	Wing/Floor Array
AF05	379.0	70.1	17	Wing/Floor Array
AF06	379.0	70.1	17	Wing/Floor Array
AP01	301.8	115.2		Panel Array
AP02	301.8	95.8		Panel Array
AWW1	272.5	112.1	10	Window Array
AWW2	284.9	112.1	10	Window Array
AWW3	309.1	112.1	10	Window Array
AWW4	321.5	112.1	10	Window Array
AWW5	321.5	106.0	11	Window Array
*AA01	348.0	71.0	17	Axial Array
*AA01A	348.0	71.0	17	Axial Array
AA02	379.0	71.0	17	Axial Array
*AA03	379.0	71.0	17	Axial Array
*AA03A	379.0	71.0	17	Axial Array
**AA04	412.0	71.0	17	Axial Array
**AA04A	412.0	71.0	17	Axial Array
**AA04B	412.0	71.0	17	Axial Array
*AA05	412.0	71.0	17	Axial Array
*AA05A	445.5	71.0	17	Axial Array
AC01	287.5	139.1	5	Circumferential Array
AC02	287.5	118.2	9	Circumferential Array
AC03	287.5	92.3	13	Circumferential Array
AC04	287.5	70.1	17	Circumferential Array
AC05	297.0	149.1	1	Circumferential Array
AC06	297.0	139.1	5	Circumferential Array
AC07	297.0	118.2	9	Circumferential Array

TABLE B-6.
CABIN ACCELEROMETER LOCATIONS (CONT'D)

TRANSDUCER	FUSELAGE STATION	WATER LINE	STRINGER BL NUMBER	DESCRIPTION
AC08	297.0	92.3	13	Circumferential Array
AC09	297.0	70.1	17	Circumferential Array
AC10	297.0	53.4	21	Circumferential Array
AC11	306.5	149.1	1	Circumferential Array
AC12	306.5	139.1	5	Circumferential Array
AC13	306.5	118.2	9	Circumferential Array
AC14	306.5	92.3	13	Circumferential Array
AC15	306.5	70.1	17	Circumferential Array
AC16	306.5	53.4	21	Circumferential Array
AC17	306.5	139.1	5R	Circumferential Array
AC18	306.5	118.2	9R	Circumferential Array
AC19	306.5	92.3	13R	Circumferential Array
AC20	306.5	70.1	17R	Circumferential Array
AC21	306.5	53.4	21R	Circumferential Array
AC22	321.5	118.2	9	Cabin Sidewall
AC23	370.5	118.2	9	Cabin Sidewall

NOTE: * Intensity pairs (_,A) straddle location ± 0.75 inch in vertical direction.

** Intensity triangle (_,A,B) _,B direction is true airframe fore and aft.

ACCELEROMETER LOCATIONS
LH WING - LOWER SURFACE

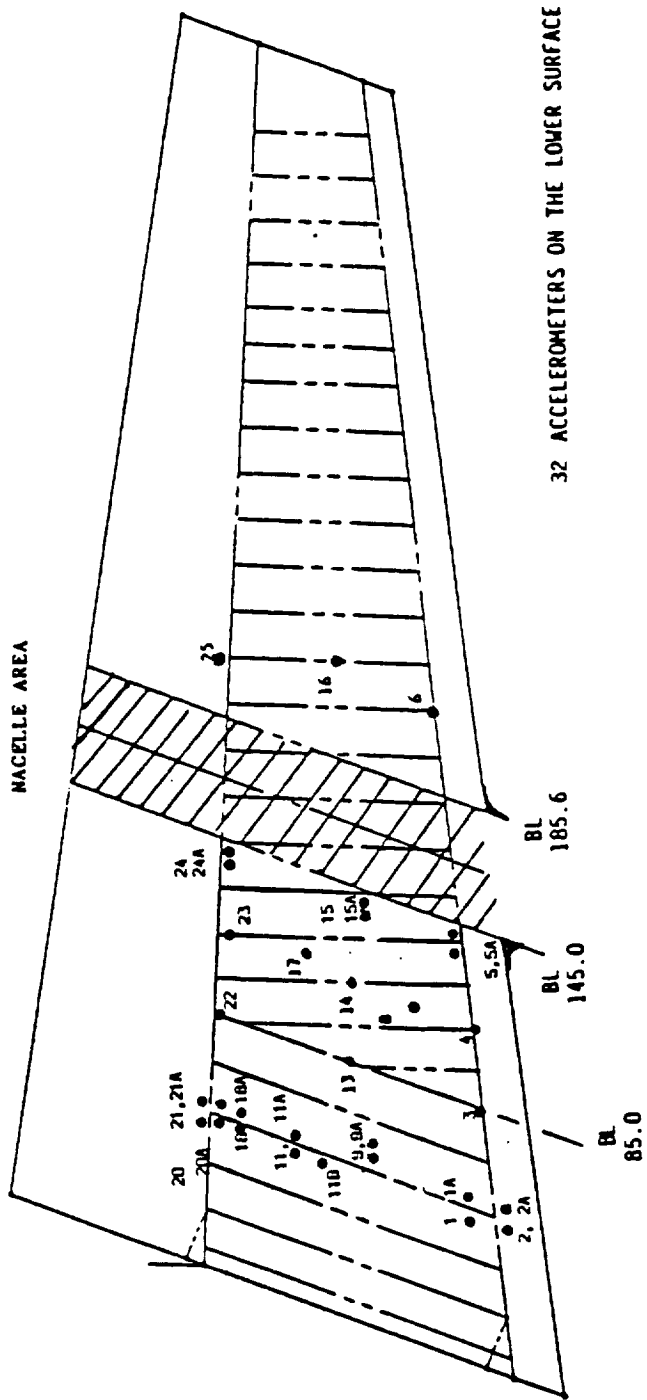


Figure B-12. Wing Accelerometer Locations

TABLE B-7.
WING ACCELEROMETER LOCATIONS

TRANSDUCER	FUSELAGE STATION	BUTT LINE
AW01	352.4	48.00
AW01A	352.4	48.00
*AW02	352.4	48.00
*AW02A	352.4	48.00
AW03	369.9	82.00
AW04	380.1	101.5
AW05	394.5	128.2
AW05A	394.5	128.2
AW06	432.5	201.0
AW08	411.1	112.6
AW09	387.4	48.0
AW11	387.4	48.0
AW11A	411.1	48.0
AW11B	411.1	48.0
AW13	423.3	82.0
AW14	429.9	107.8
AW15	443.5	138.6
AW15A	443.5	138.6
AW16	462.4	191.0
AW17	453.4	112.4
AW18	430.3	48.0
AW18A	430.3	48.0

TABLE B-7.
WING ACCELEROMETER LOCATIONS (CONT'D)

TRANSDUCER	FUSELAGE STATION	BUTT LINE
AW20	455.7	48.0
AW20A	455.7	48.0
**AW21	455.7	48.0
**AW21A	455.7	48.0
AW22	461.7	65.0
AW23	476.4	110.2
AW24	487.0	140.8
AW24A	487.0	140.8
AW25	505.6	193.2

Intensity pairs are installed ± 0.75 inches spanwise except AW11, 11A, and 11B which are ± 0.75 inches spanwise and chordwise.

* On Front Beam

** On Rear Beam

ACOUSTIC STRAIN GAGES
LH WING - UPPER SPAR CAP
AND WEB

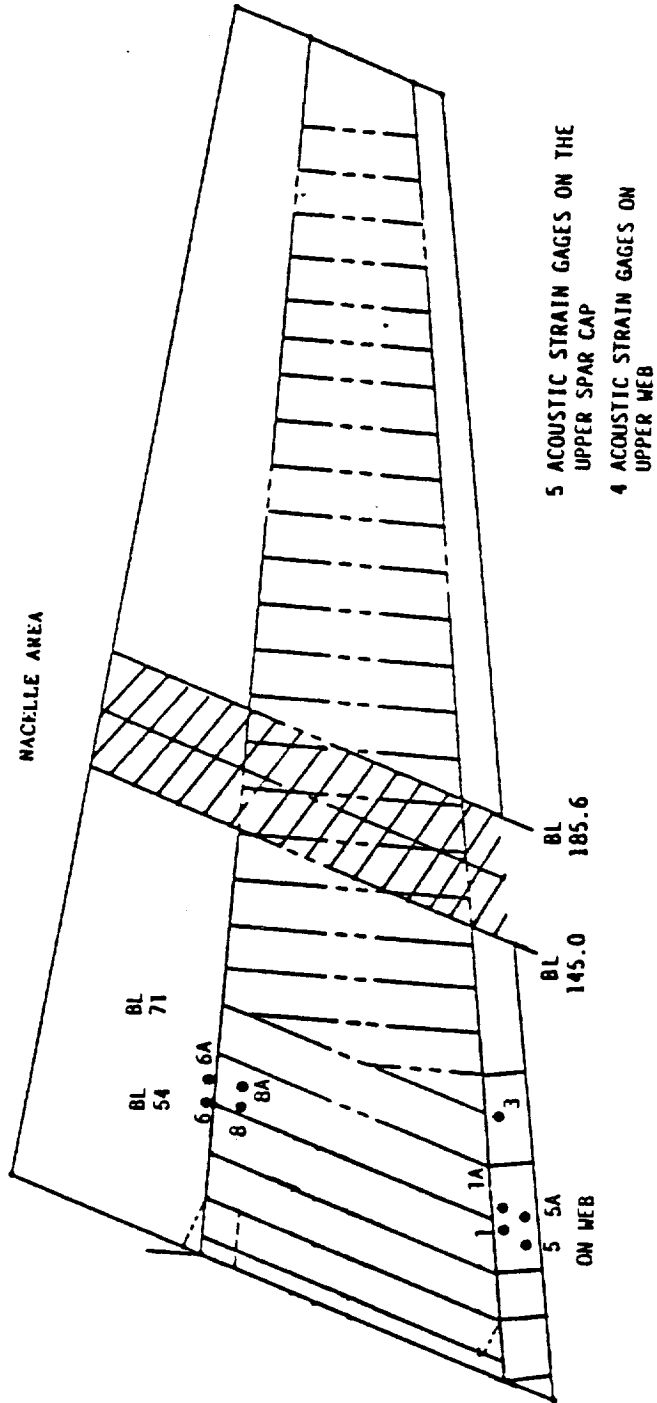


Figure B-13. Acoustic Strain Gages Wing Upper Spar Cap

ACOUSTIC STRAIN GAGES
LH WING - LOWER SPAR CAP

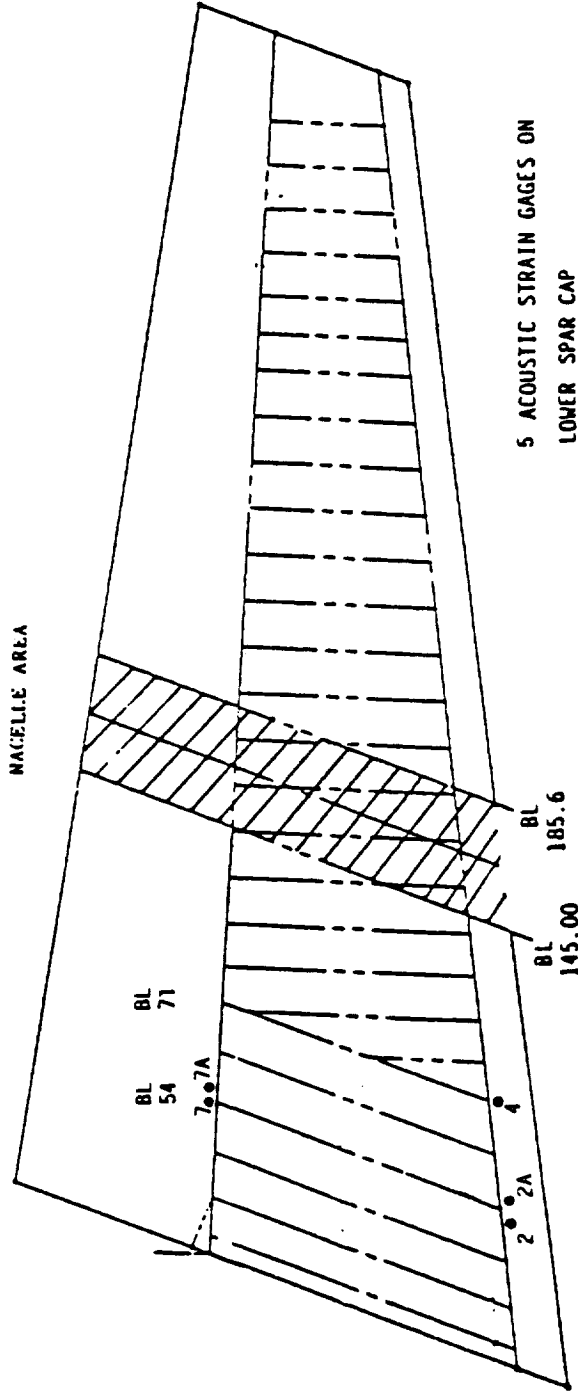


Figure B-14. Acoustic Strain Gages Wing Lower Spar Cap

TABLE B-8.
LEFT WING STRAIN GAGE LOCATIONS

TRANSDUCER	FUSELAGE STATION	BUTT LINE	GAGE DIRECTION	DESCRIPTION
SG01	355.0	54	Parallel to Spars	Upper Spar Cap
SG01A	355.0	54	Parallel to Spars	Upper Spar Cap
SG02	355.0	54	Parallel to Spars	Lower Spar Cap
SG02A	355.0	54	Parallel to Spars	Lower Spar Cap
SG03	363.5	71	Parallel to Spars	Upper Spar Cap
SG04	363.5	71	Parallel to Spars	Lower Spar Cap
SG05	355.6	54	Parallel to Spars	Forward Web
SG05A	355.6	54	Parallel to Spars	Forward Web
SG06	458.5	54	Parallel to Spars	Upper Spar Cap
SG06A	458.5	54	Parallel to Spars	Upper Spar Cap
SG07	458.5	54	Parallel to Spars	Lower Spar Cap
SG07A	458.5	54	Parallel to Spars	Lower Spar Cap
SG08	457.9	54	Parallel to Spars	Rear Web
SG08A	457.9	54	Parallel to Spars	Rear Web

VIBRATION

- NACELLE / WING INTERFACE (2)
- GEARBOX MOUNT - AIRFRAME STRUCT (8)
- ▲ ENGINE MOUNT - AIRFRAME STRUCT (2)

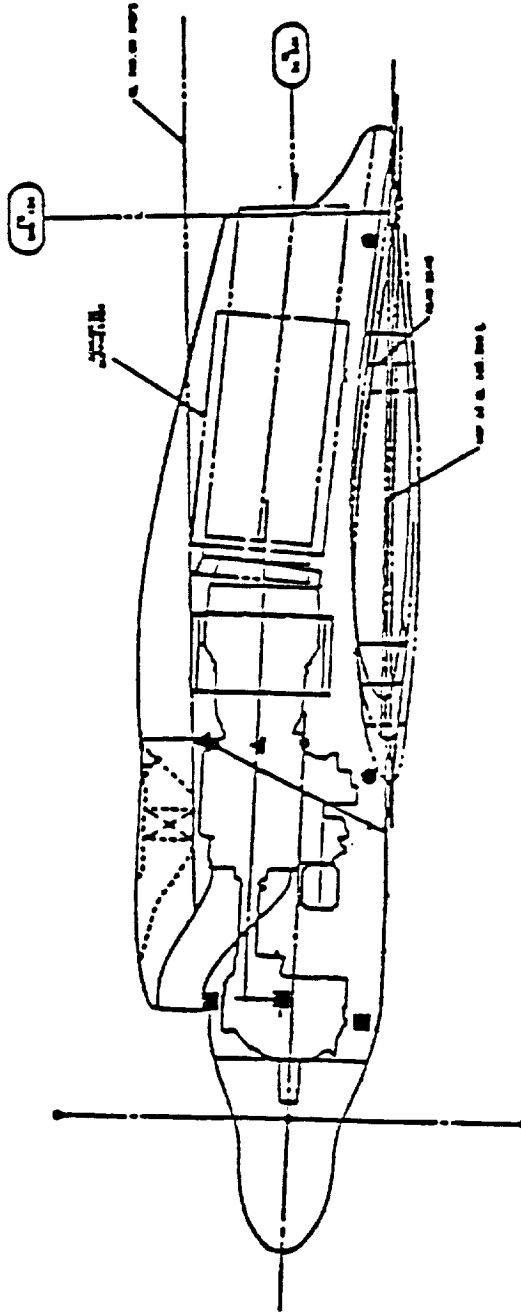


Figure B-15. Accelerometer Locations, Nacelle/Wing

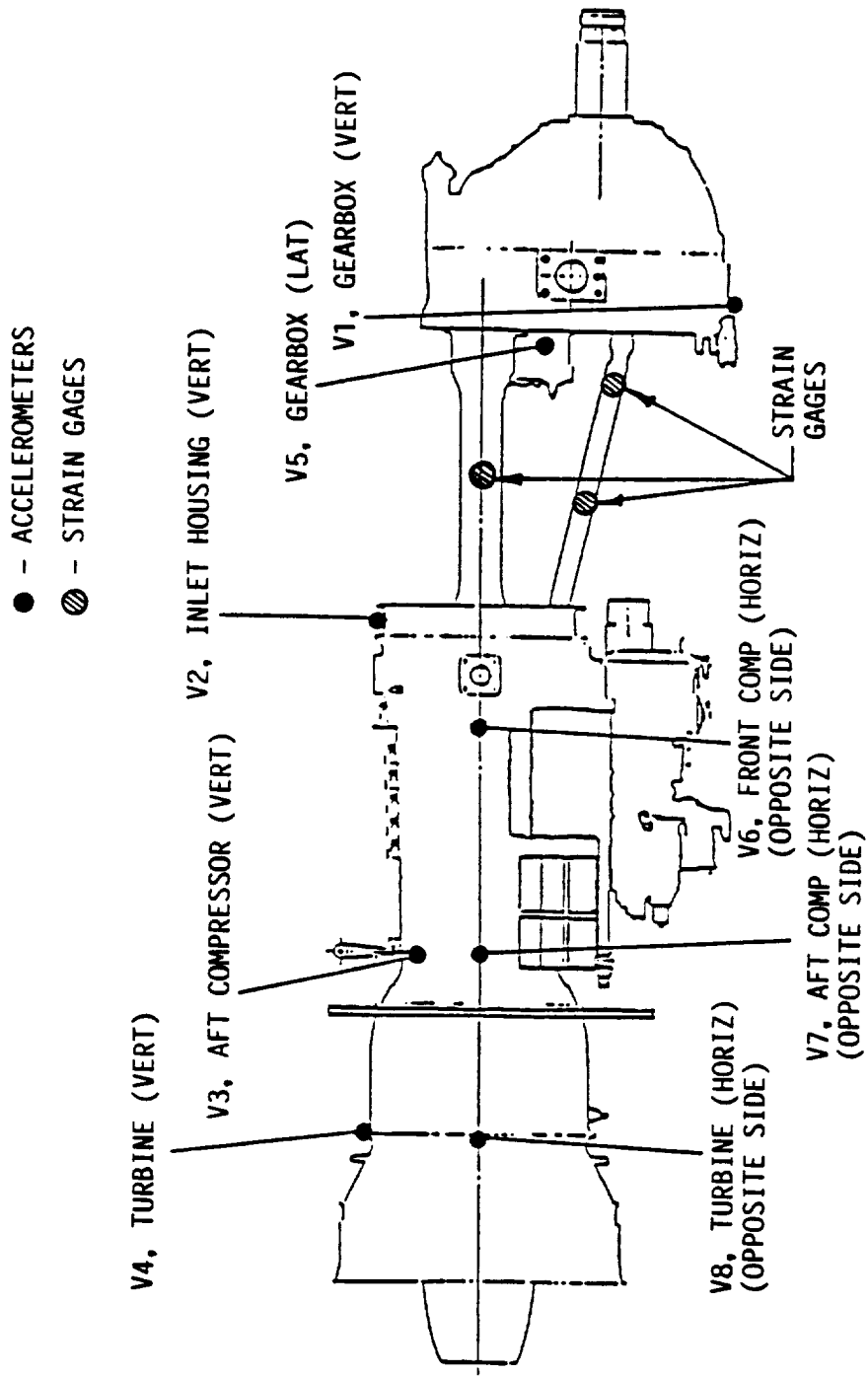


Figure B-16. Propulsion System Accelerometer Locations

REFERENCES

1. DeGeorge, C. L., "Large-Scale Advanced Prop-Fan (LAP) Final Report," NASA CR 182112 (prepared by Hamilton Standard).
2. Hancock, J. P., V. Lyman, and A. P. Pennock, "Analysis of Results from Wind Tunnel Tests of Inlets for an Advanced Turboprop Nacelle Installation," NASA CR 174937 (prepared by Lockheed Aeronautical Systems Company and issued as LG85ER0105), June 1986.
3. Bansal, Prem N., "Experimental and Analytical Evaluation of the Effects of Simulated Engine Inlets on the Blade Vibratory Stresses of the SR-3 Model Propfan," NASA CR 174959, September 1985.
4. Amiet, R. K., "Noise Due to Turbulent Flow Past a Trailing Edge," Journal of Sound and Vibration, Vol. 47, 1946, pp. 367-393.
5. "Acoustic Effects Produced by a Reflecting Plane," SAE AIR 1327, Society of Automotive Engineers, January 1976.
6. "Estimation of One-Third-Octave-Band Lateral Attenuation of Sound from Jet-Propelled Airplanes," SAE AIR 1706, Society of Automotive Engineers, October 1985.
7. Dittmar, James H., and David B. Stang, "Cruise Noise of the 2/9th Scale Model of the Large-Scale Advanced Propfan (LAP) Propeller, SR-7A," NASA Technical Memorandum 100175, September 1987.

FIGURES

PRECEDING PAGE BLANK NOT FILMED

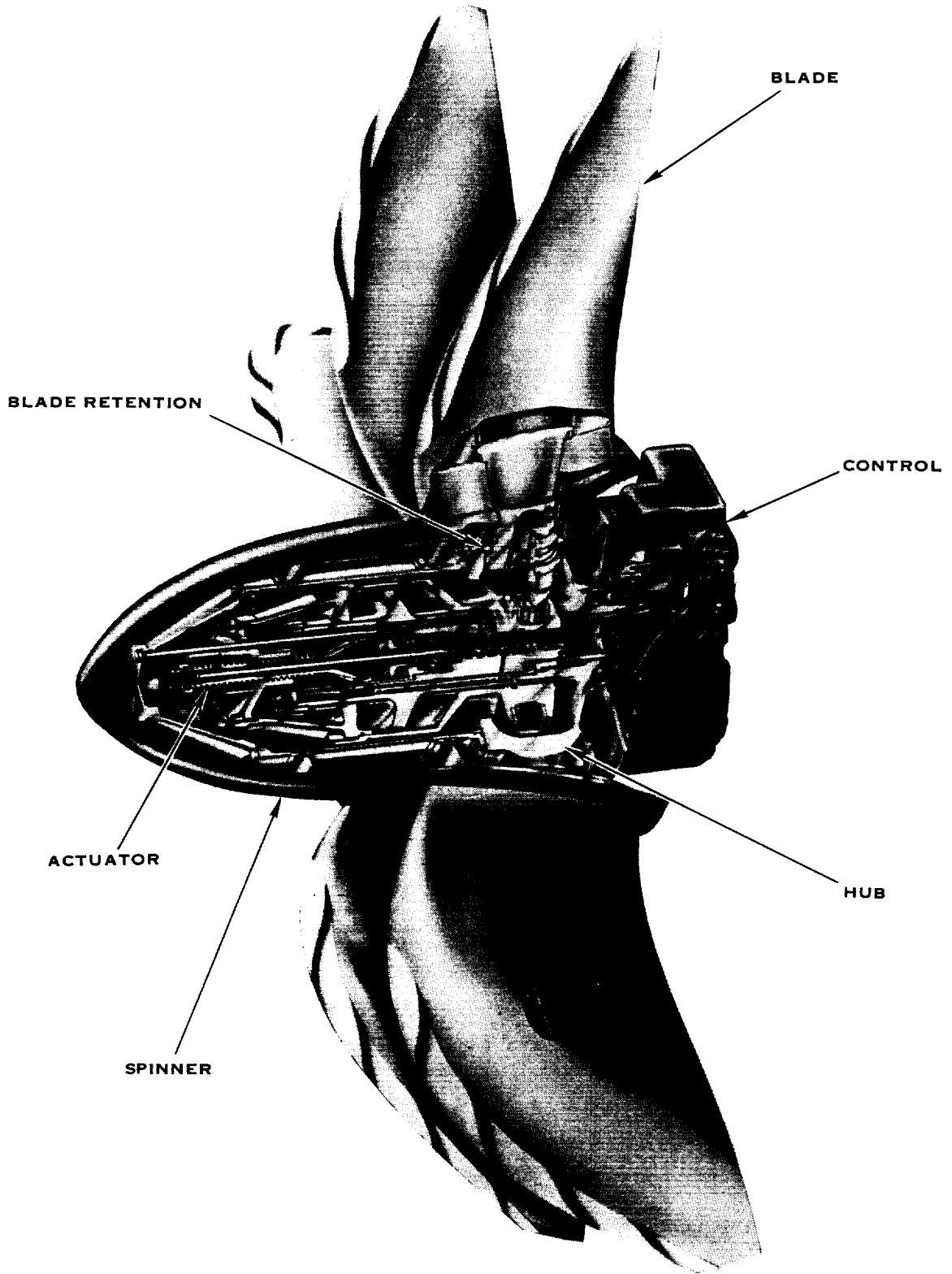
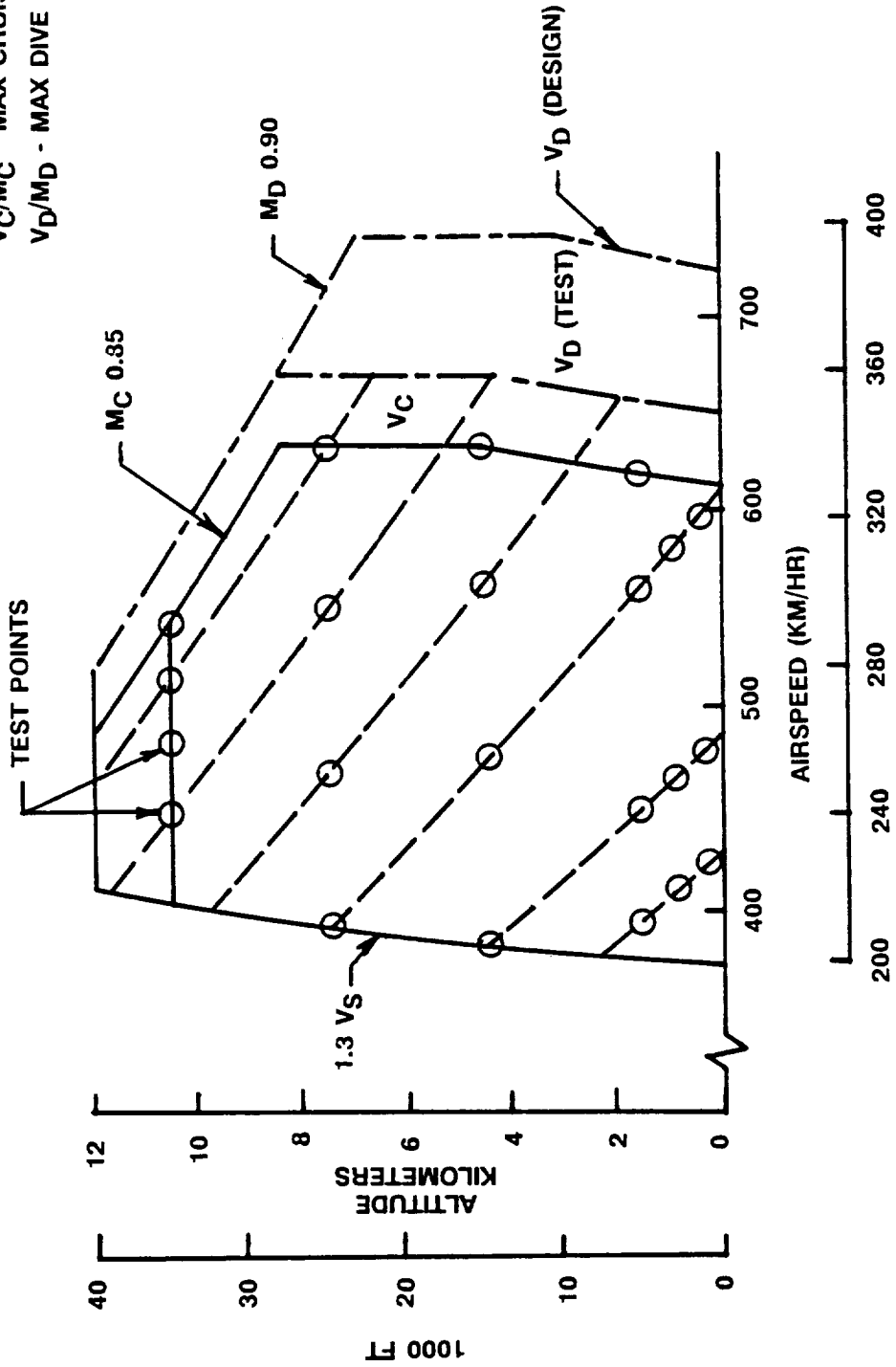


Figure 1. Large-Scale Advanced Propfan (LAP)

V_S - STALL SPEED
 V_C/M_C - MAX CRUISE SPEED
 V_D/M_D - MAX DIVE SPEED



CALIBRATED AIRSPEED (KNOTS)
 AIRSPEED (KM/HR)
 Figure 2. PTA Flight Test Envelope

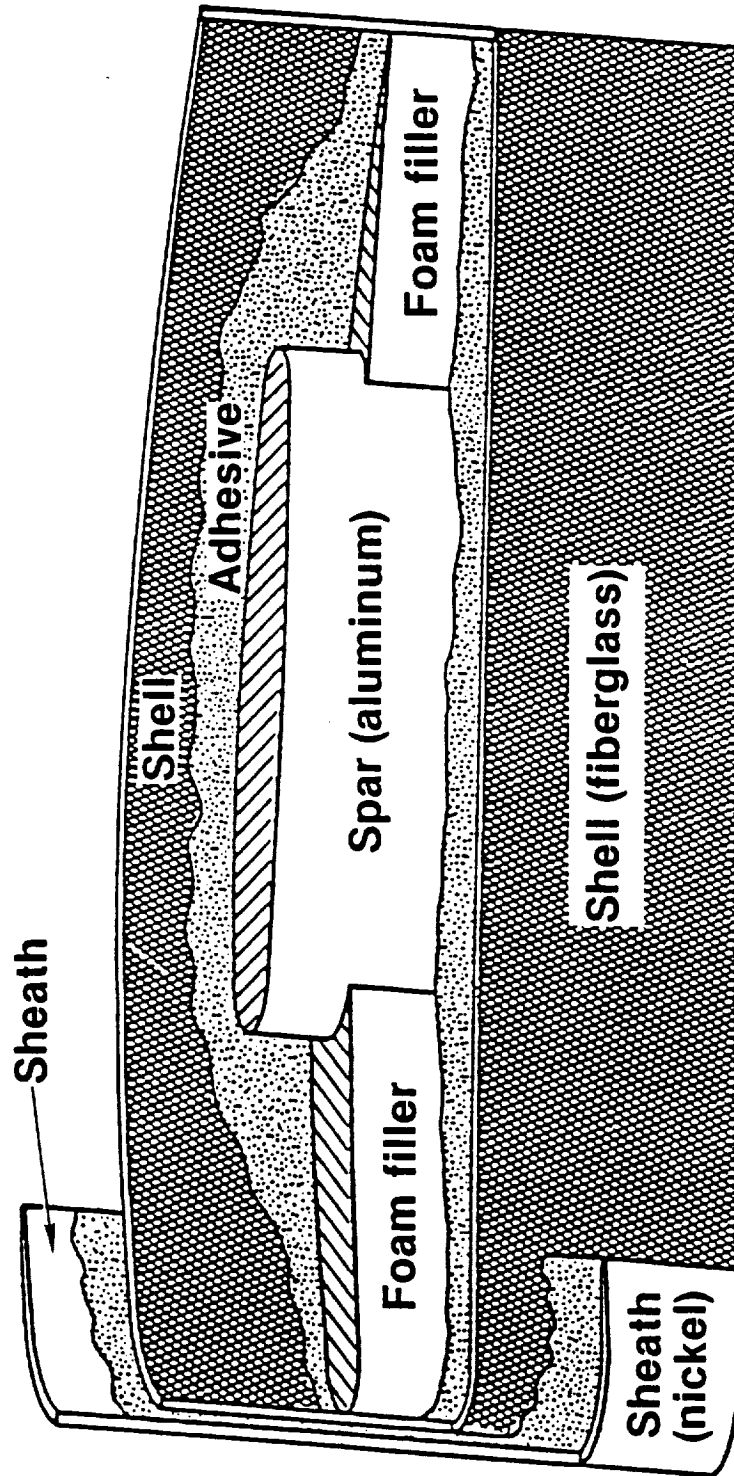


Figure 3. Features of the SR-7L Blade Construction

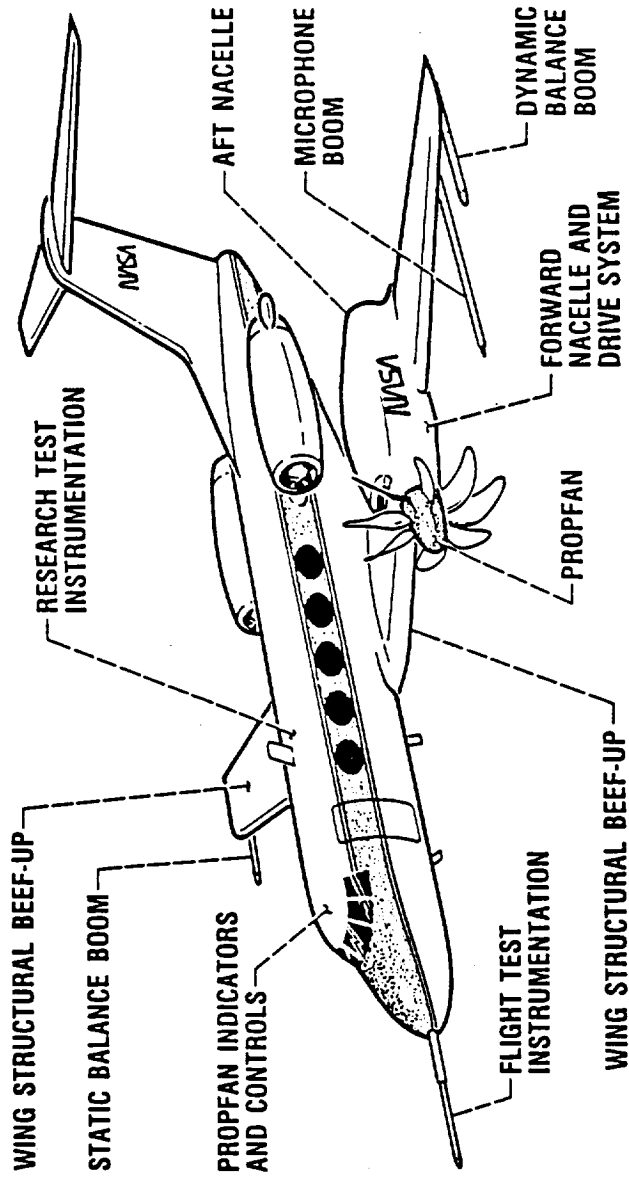


Figure 4. PTA Testbed Aircraft

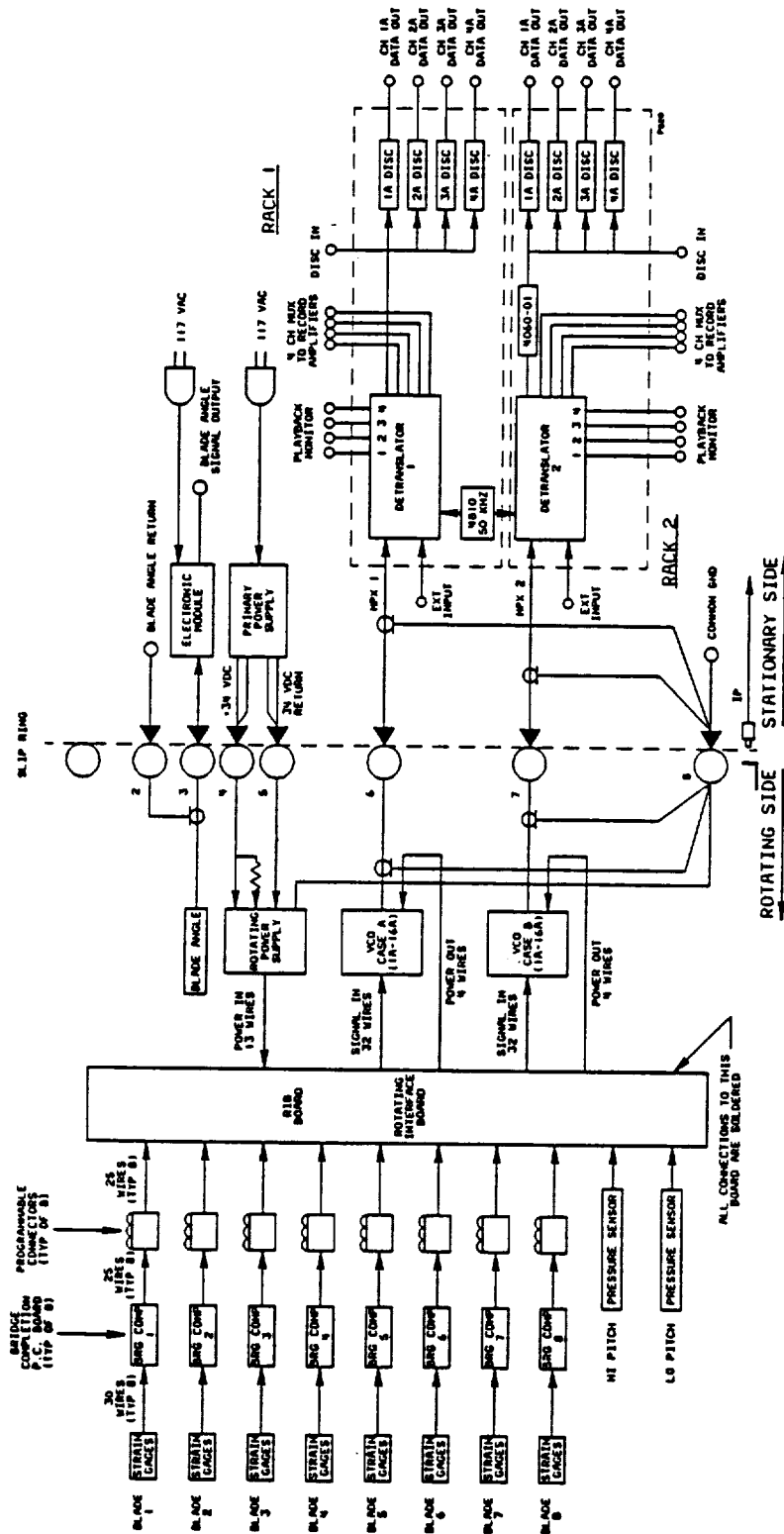


Figure 5. Propfan Electronic Data Acquisition System Schematic

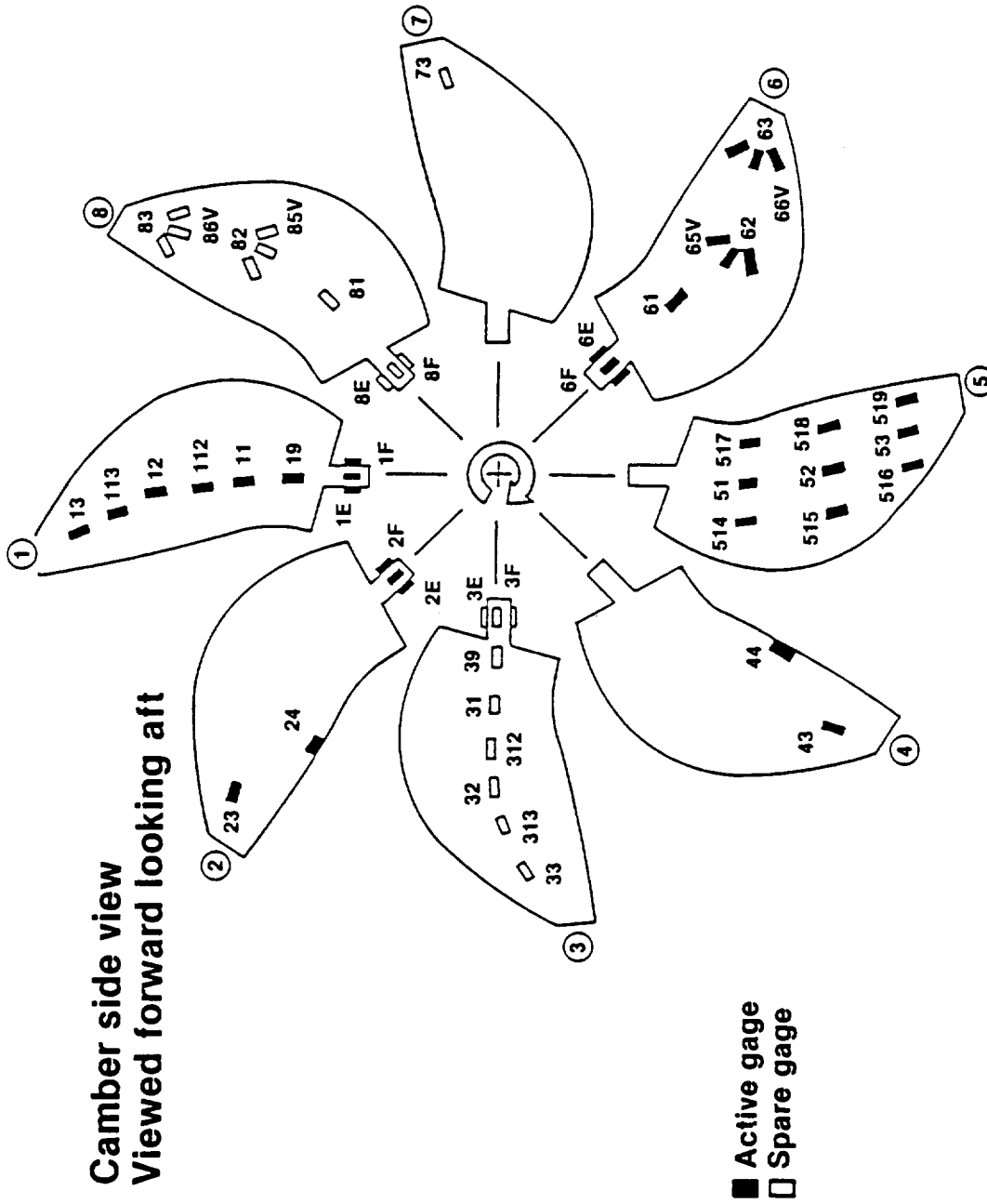


Figure 6. SR-7L Propfan Strain Gage Locations

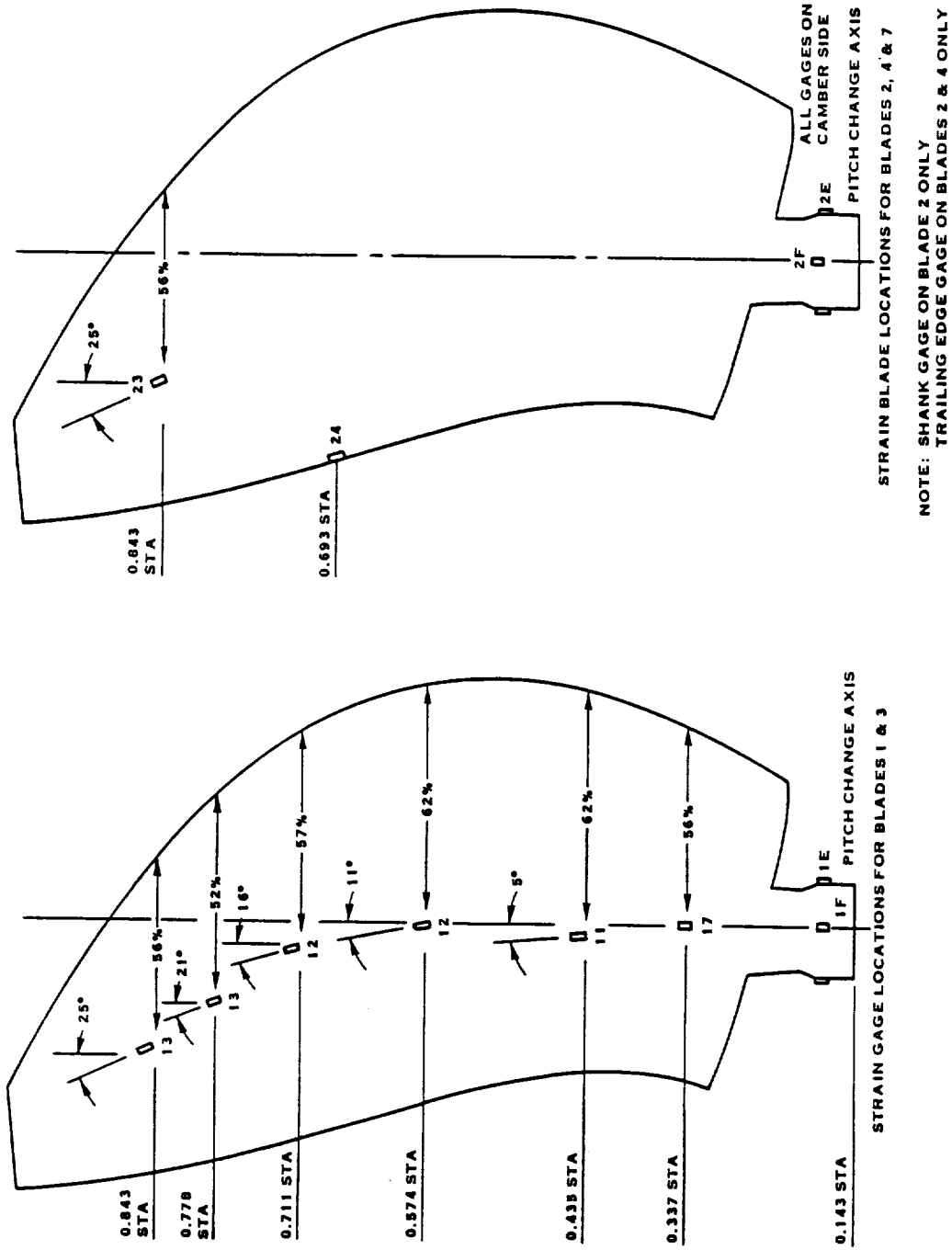


Figure 7. SR-7L Blade Strain Gage Locations

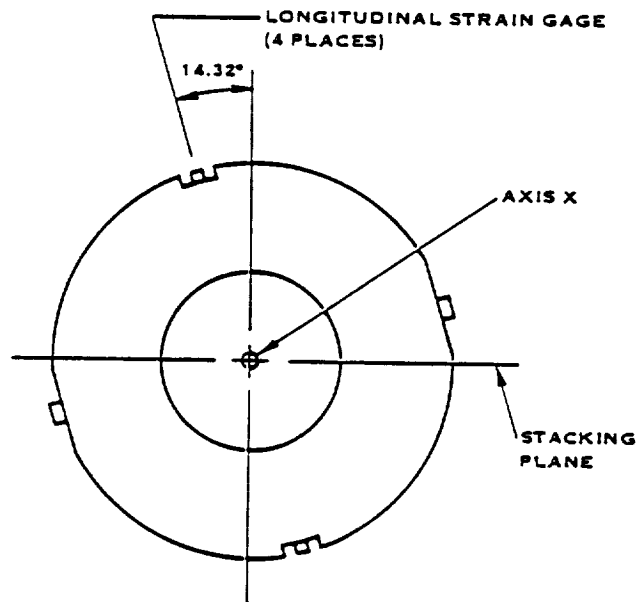
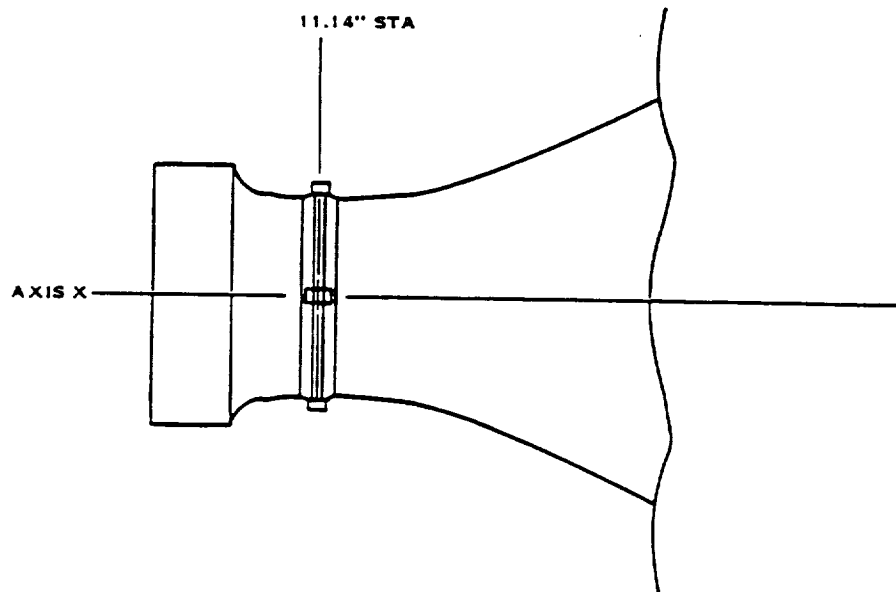


Figure 9. SR-7L Shank Strain Gage Locations

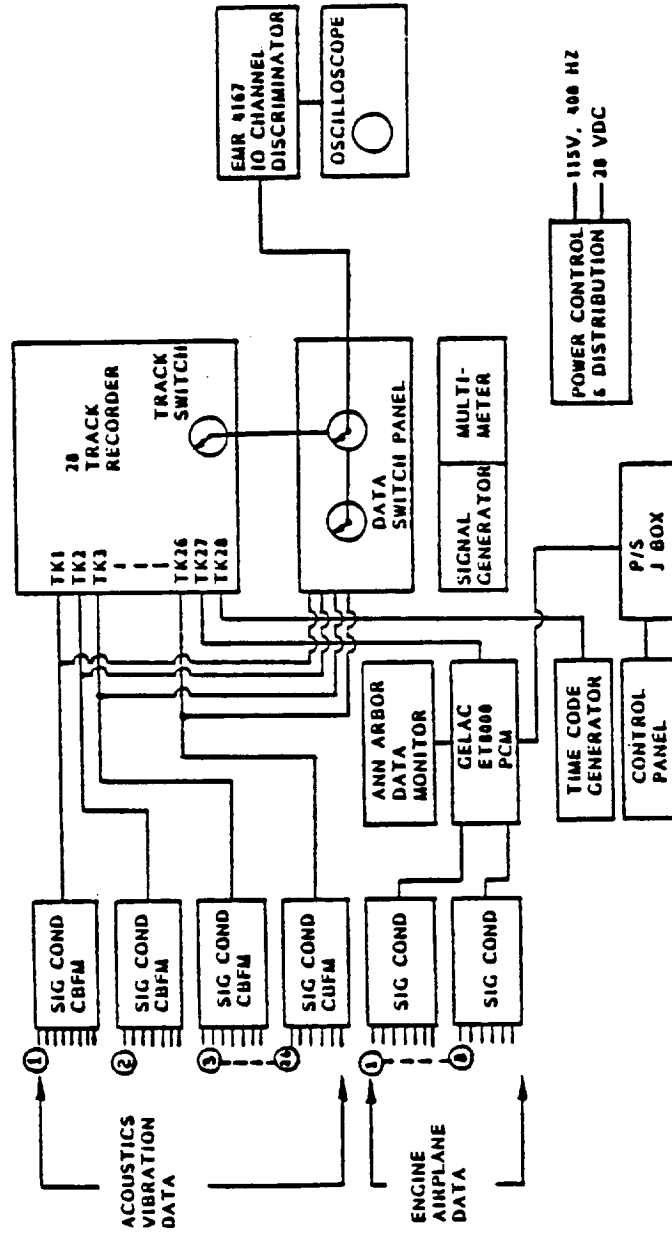


Figure 10. NASA Propfan Data System

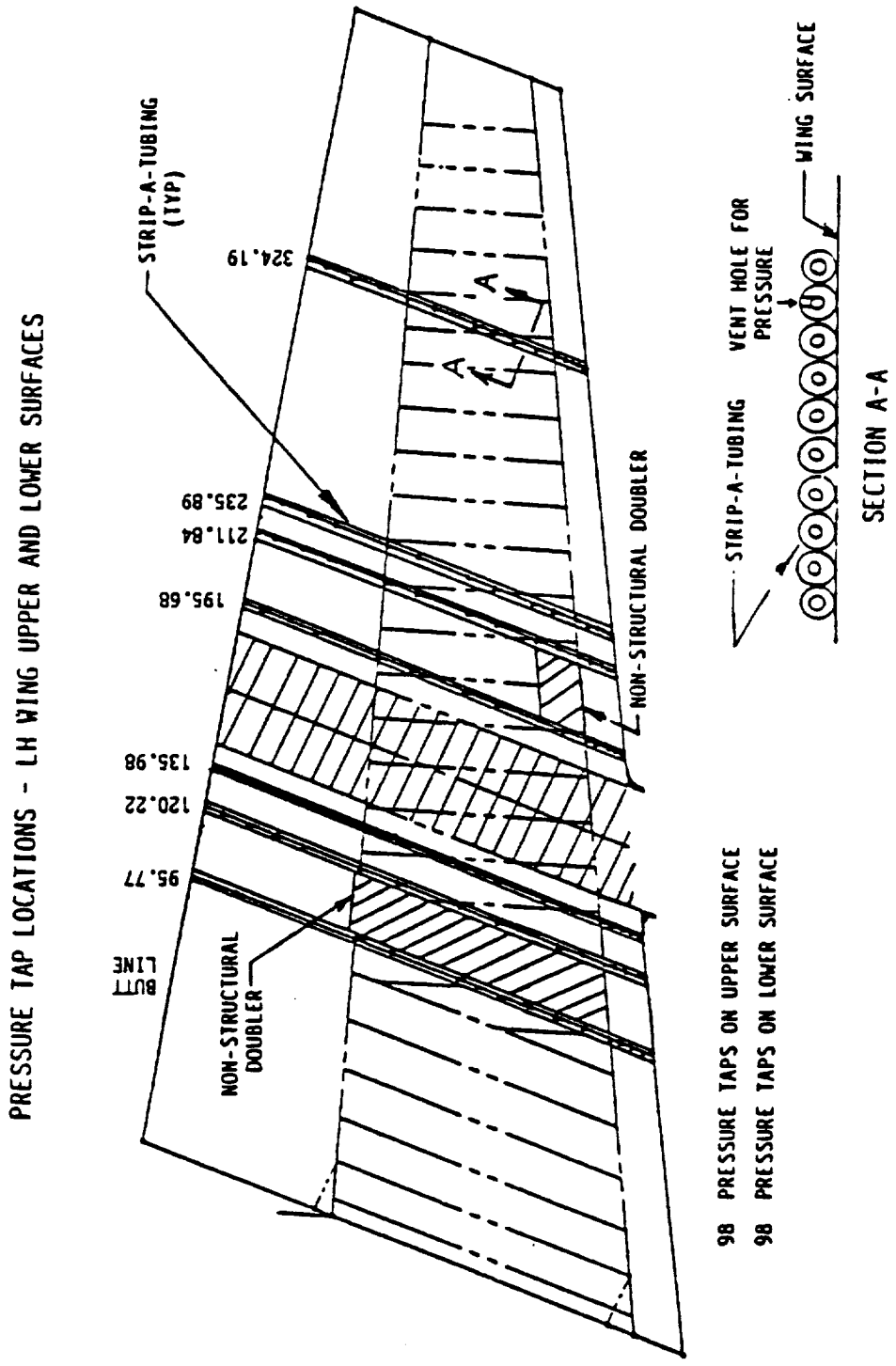


Figure 11. Wing Surface Static Pressures

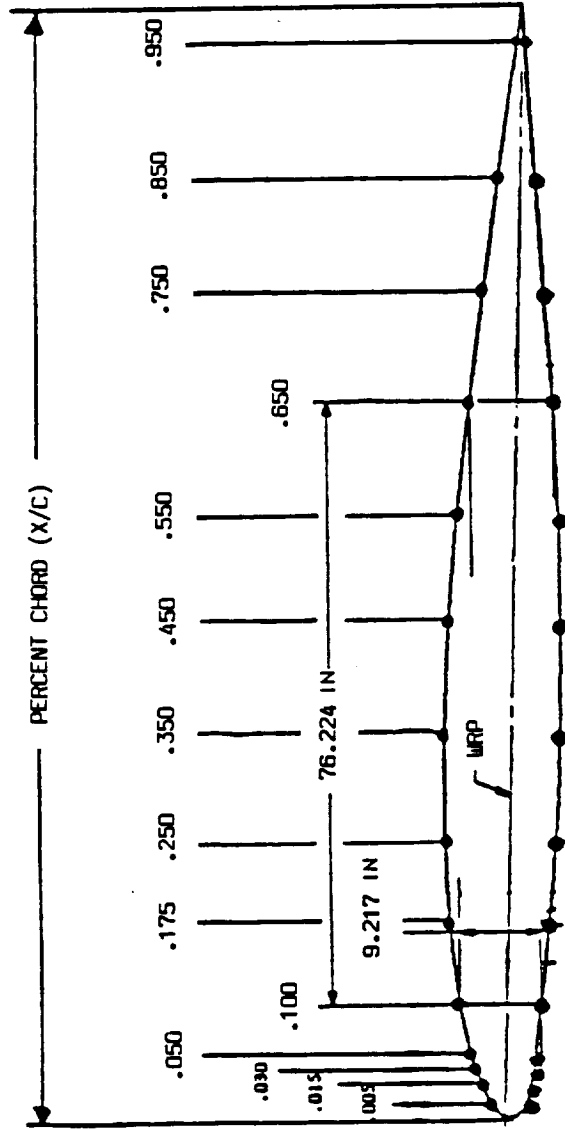


Figure 12. Typical Wing Static Pressure Tap Distribution

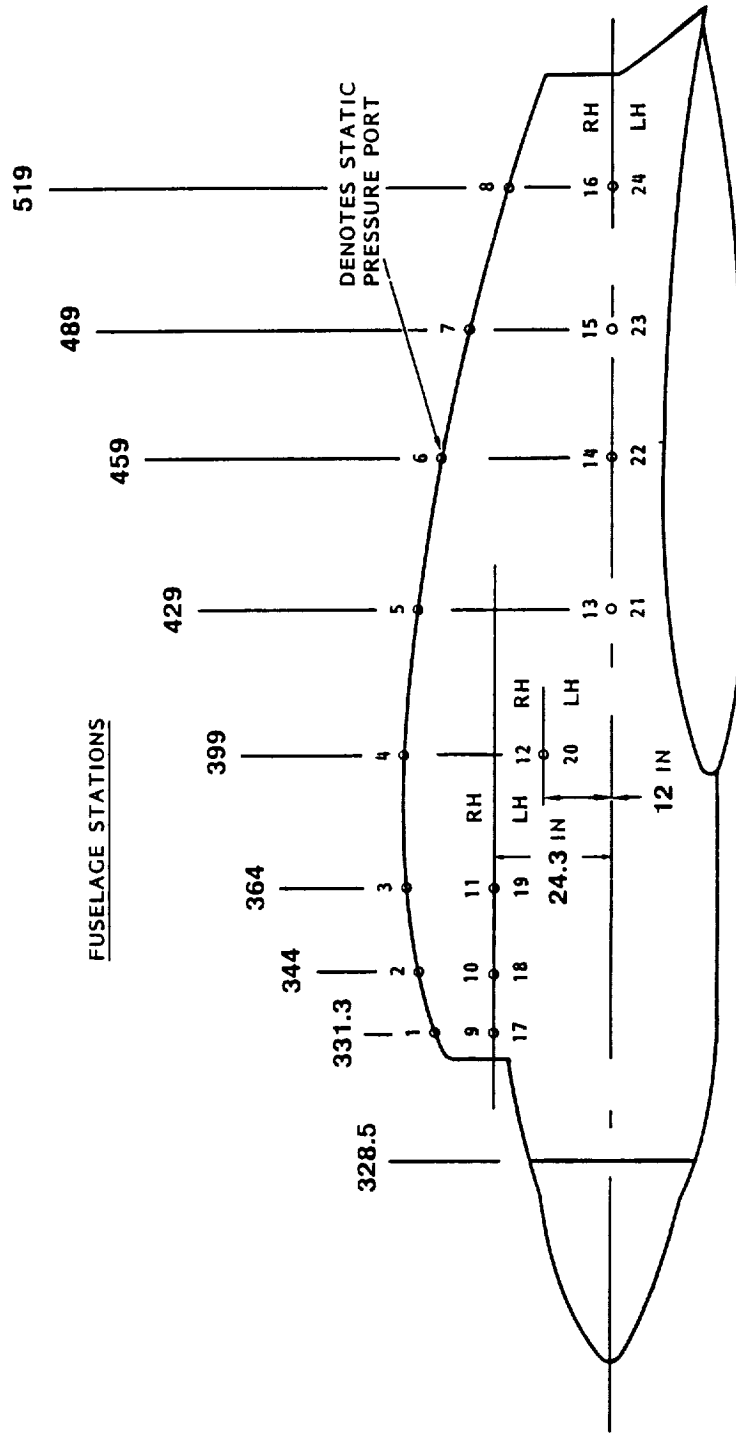
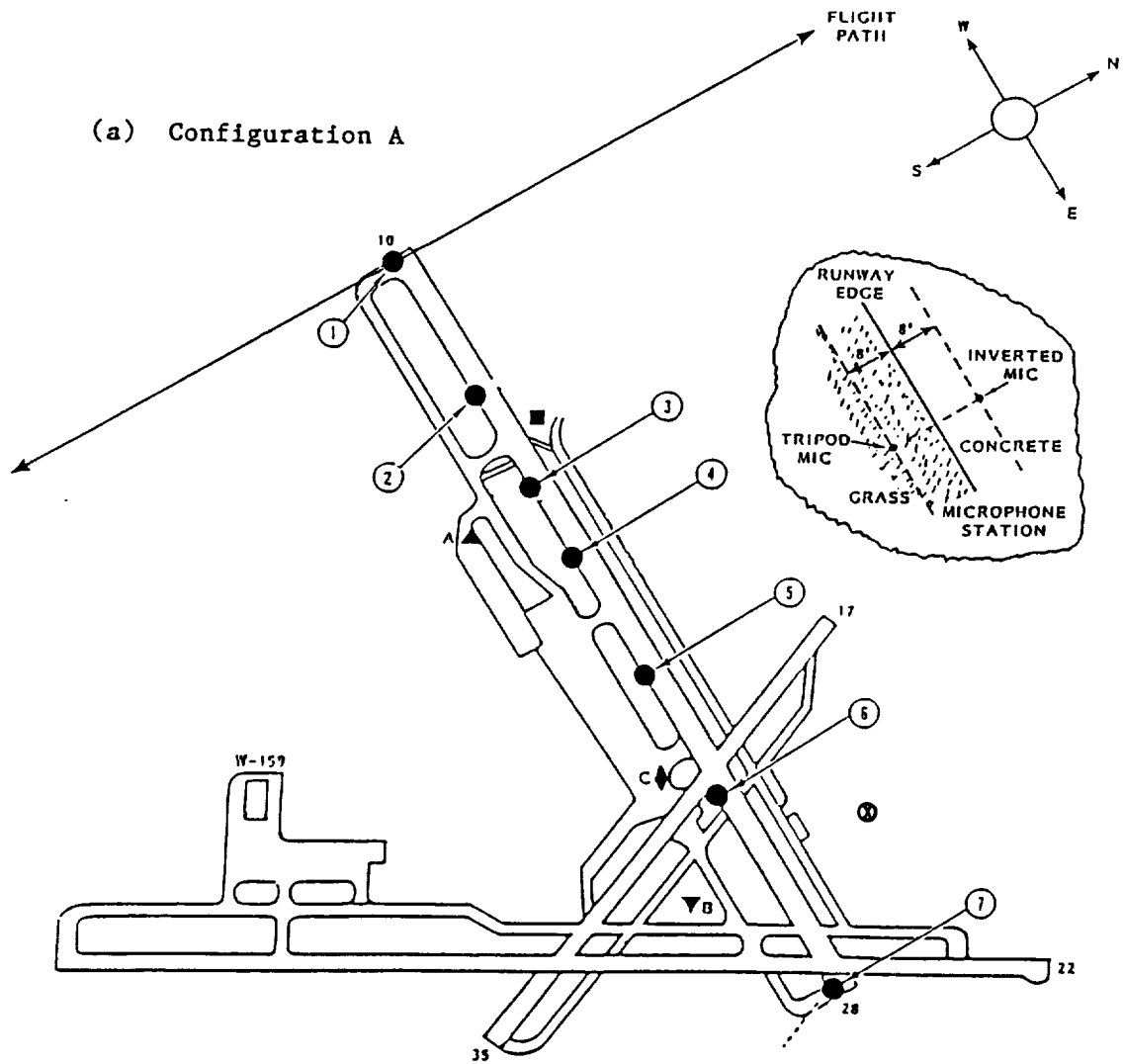


Figure 13. PTA Nacelle Pressure Instrumentation

ZONE	MICROPHONES	ACCELEROMETERS	STRAIN GAGES	TOTAL
FUSELAGE, EXTERNAL	45	NIL	NIL	45
FUSELAGE, INTERNAL	33	45	NIL	78
WING	44	32	14	90
PROPULSION SYSTEM	NIL	20	NIL	20
WING BOOM	5	2	NIL	7
TOTAL	127	99	14	240

Figure 14. Distribution of Acoustic and Vibration Transducers



MICROPHONE STATIONS

NO.	DISTANCE FROM FLIGHT PATH METERS (FT)
1	0 (0)
2	450 (1476)
3	725 (2379)
4	1000 (3281)
5	1377 (4518)
6	1793 (5881)
7	2469 (8100)

- MICROPHONE STATIONS
- ▲ TETHERED WEATHER BALLOON
- LOCKHEED INSTRUMENT VAN
- ◆ OPERATIONS TOWER
- ▼ BASE WEATHER
- ⊗ RADAR CENTER

Figure 15. Ground Instrumentation for Low-Altitude Tests

(b) Configuration B

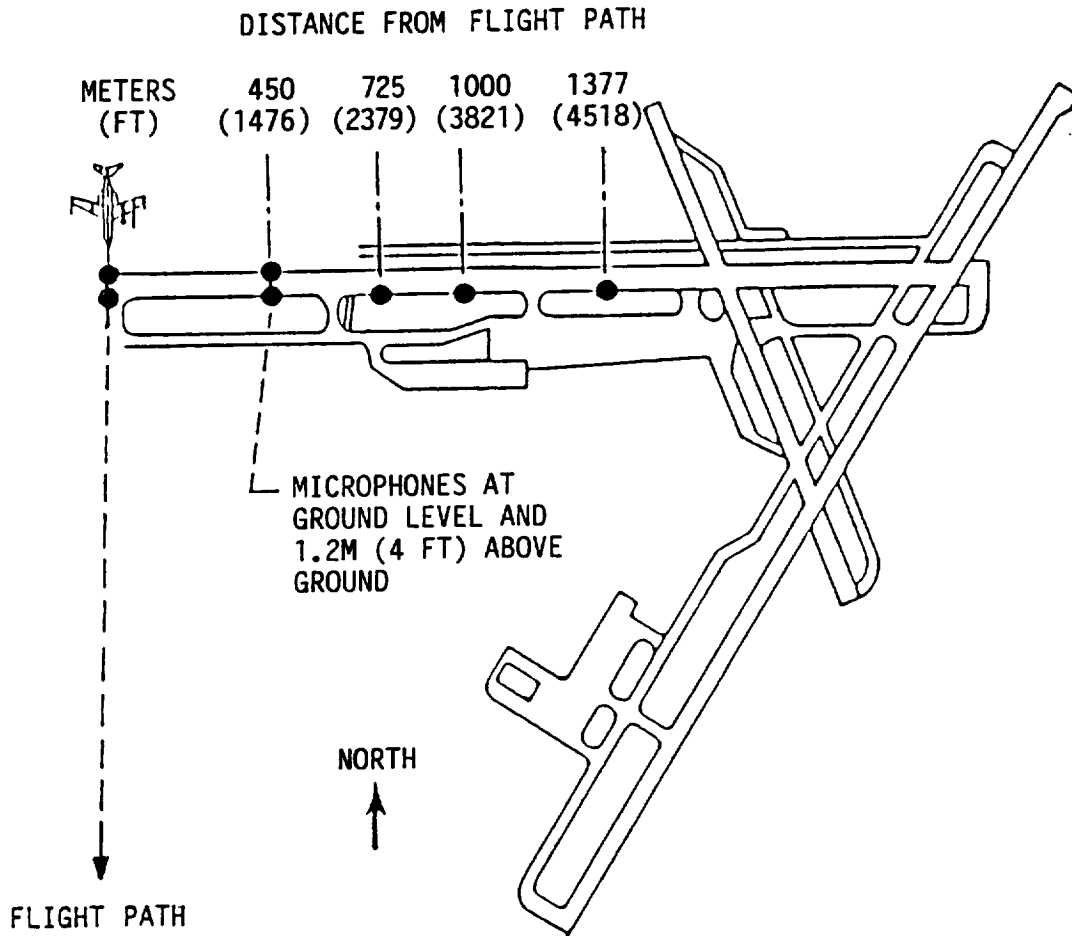


Figure 15. Ground Instrumentation for Low-Altitude Tests (Continued)

(c) Configuration C

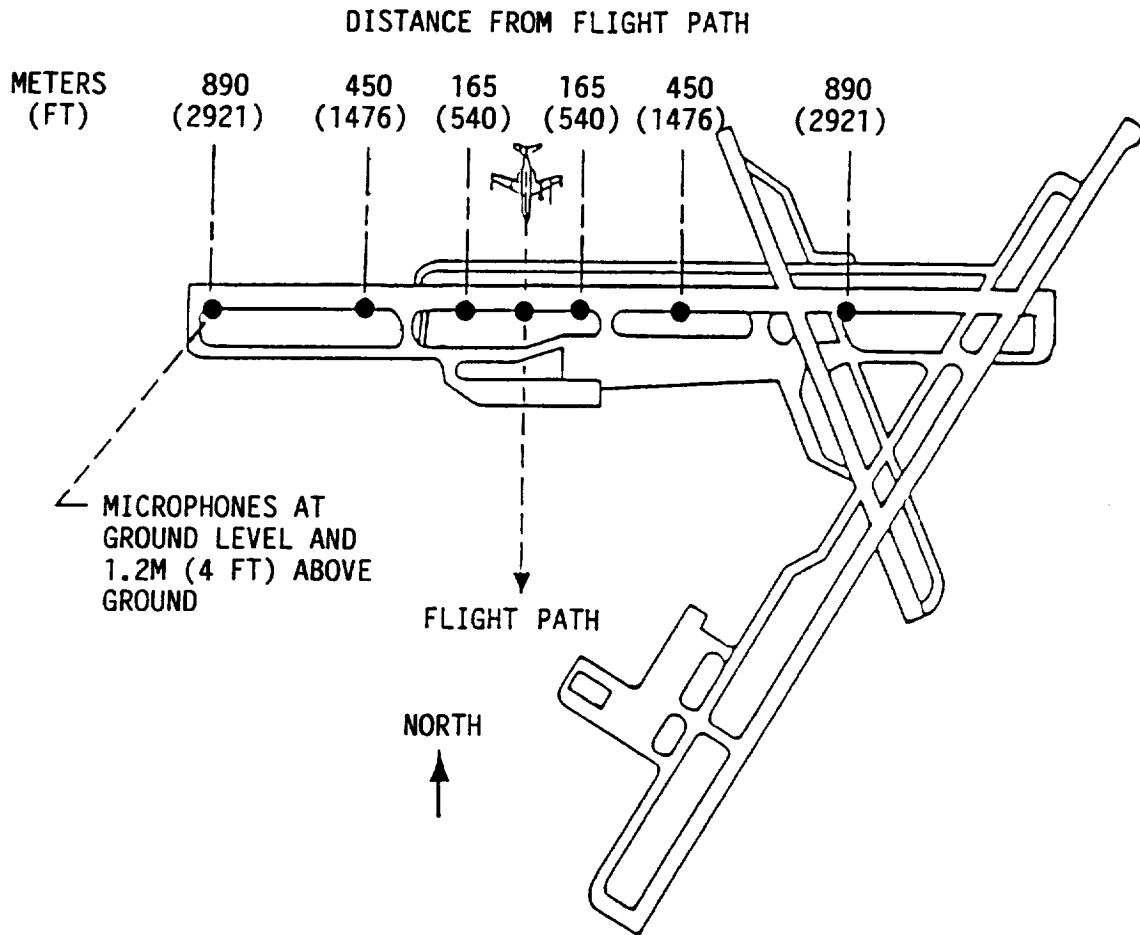
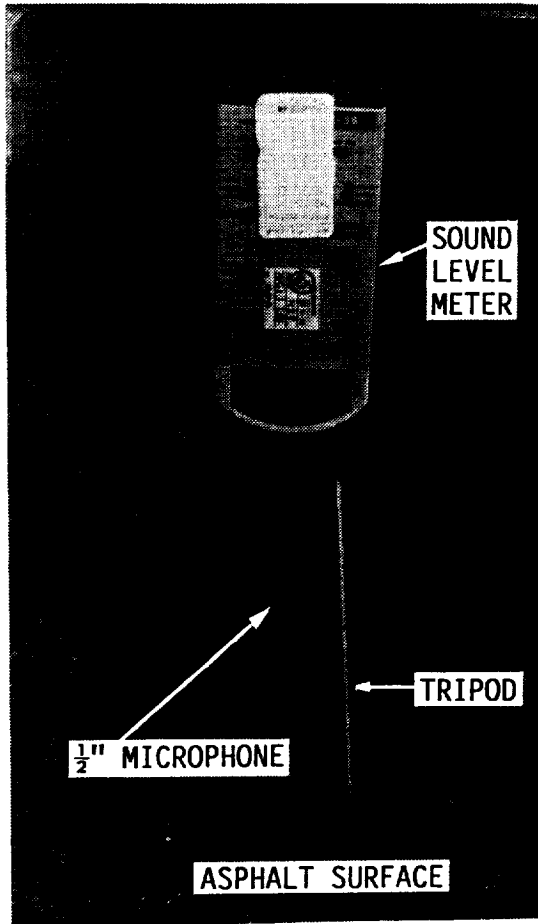
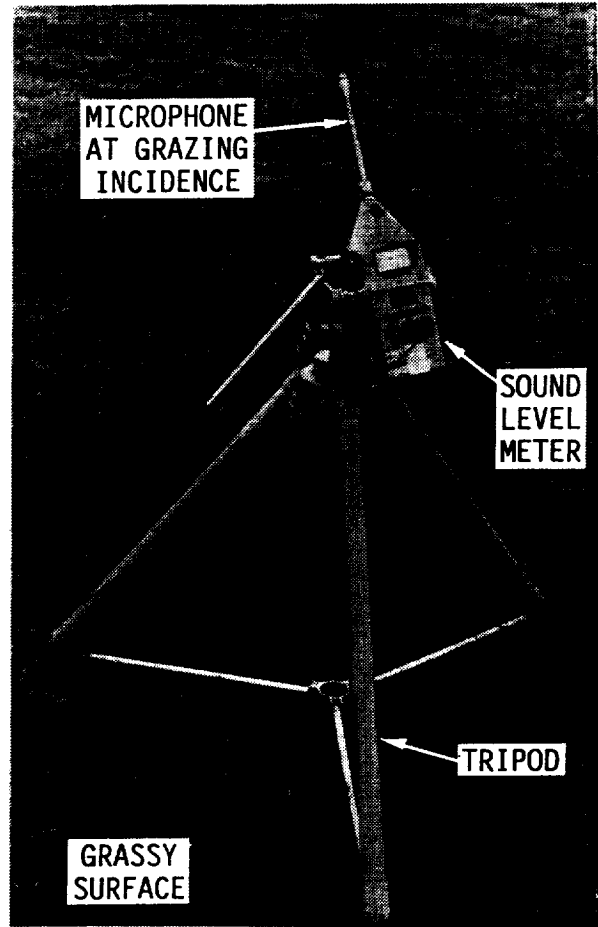


Figure 15. Ground Instrumentation for Low-Altitude Tests (Continued)

ORIGINAL PAGE
BLACK AND WHITE PHOTOGRAPH



(a) Inverted Microphone



(b) 4-Ft Microphone

Figure 16. Ground-Based Microphone Arrangement

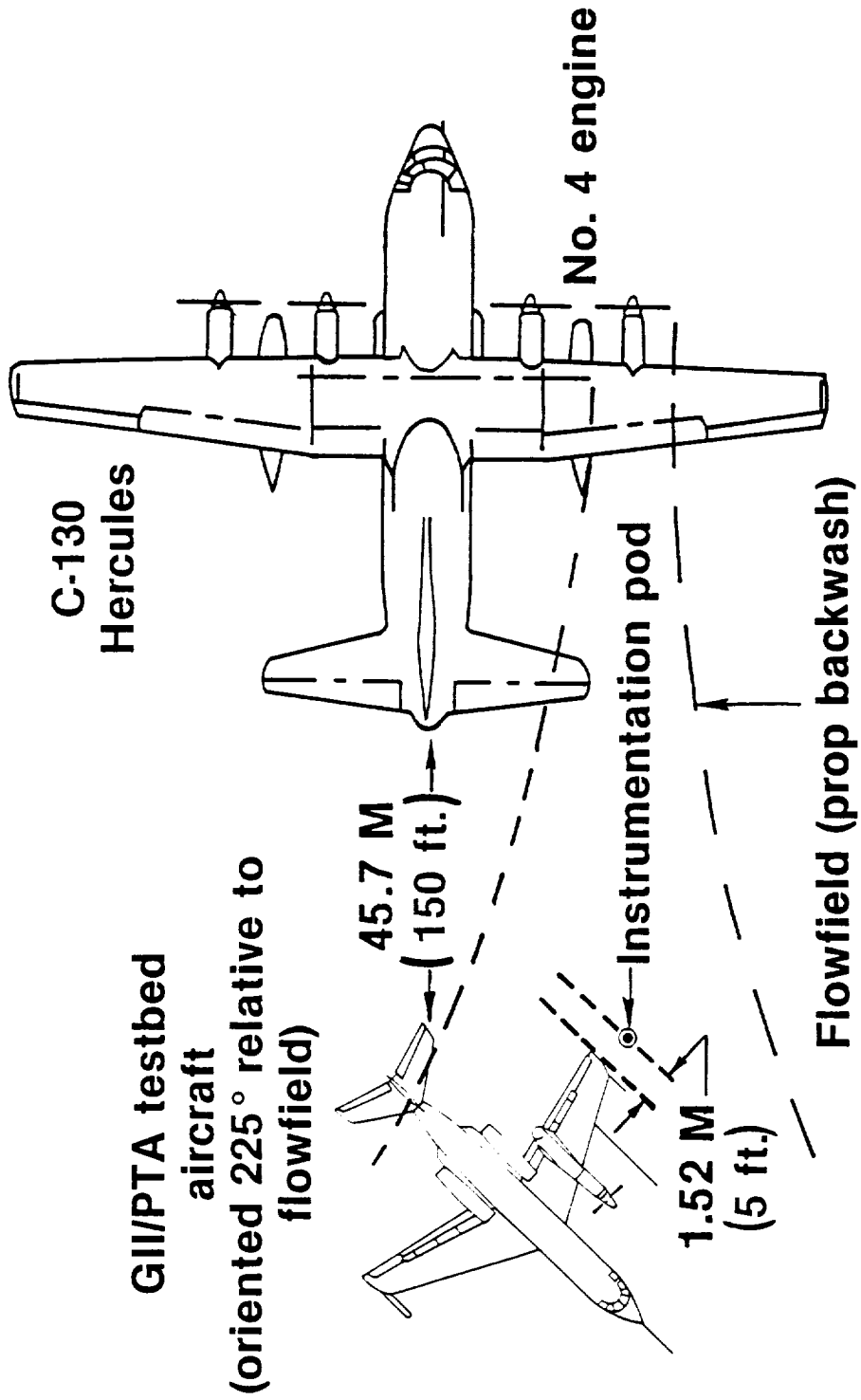


Figure 17. Crosswind Testing Using a C-130 as a "Blower" Aircraft

ORIGINAL PAGE
BLACK AND WHITE PHOTOGRAPH

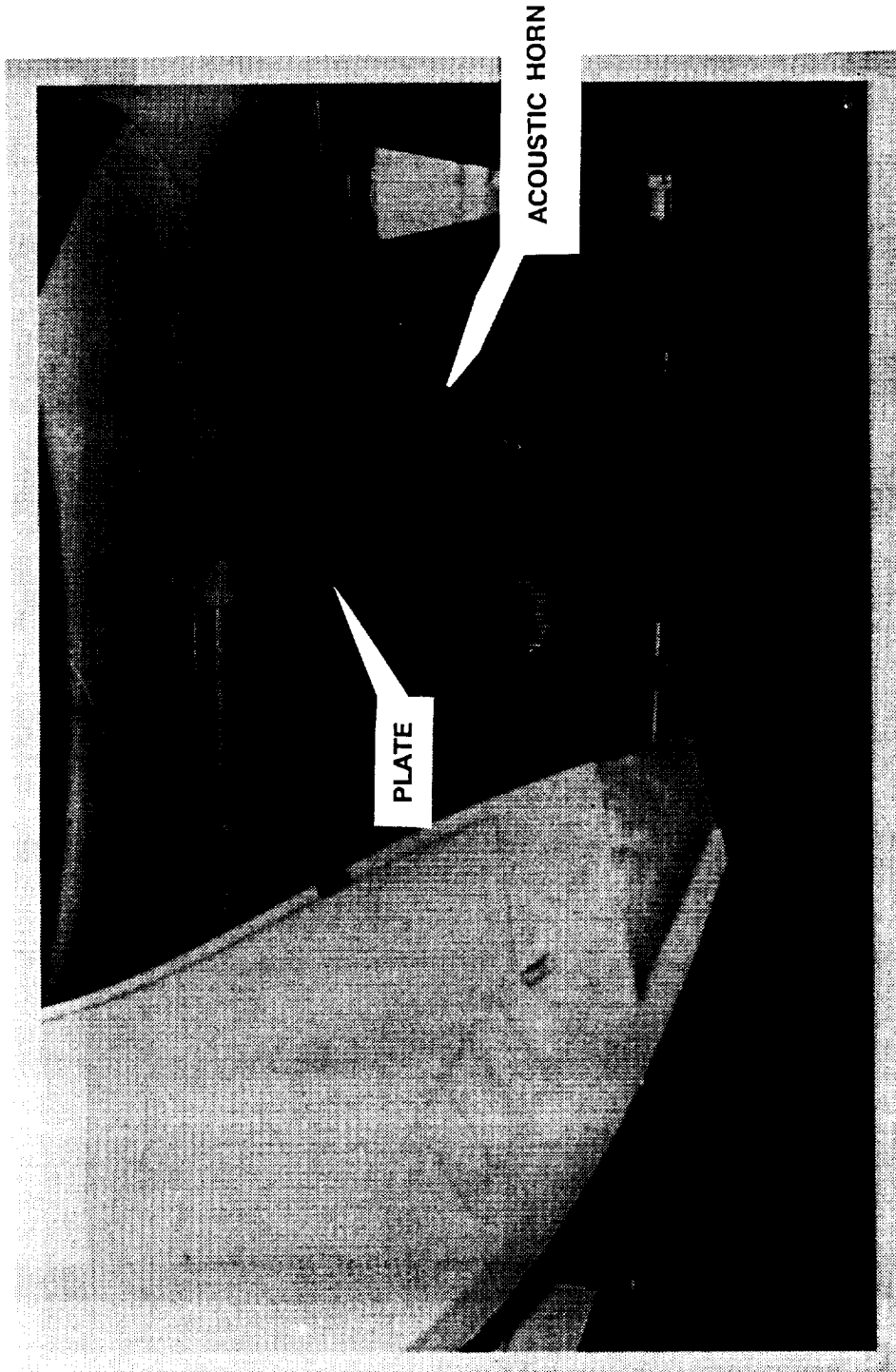


Figure 18. Acoustic Horn and Shaker Input Plate for Baseline Acoustics and Vibration Tests

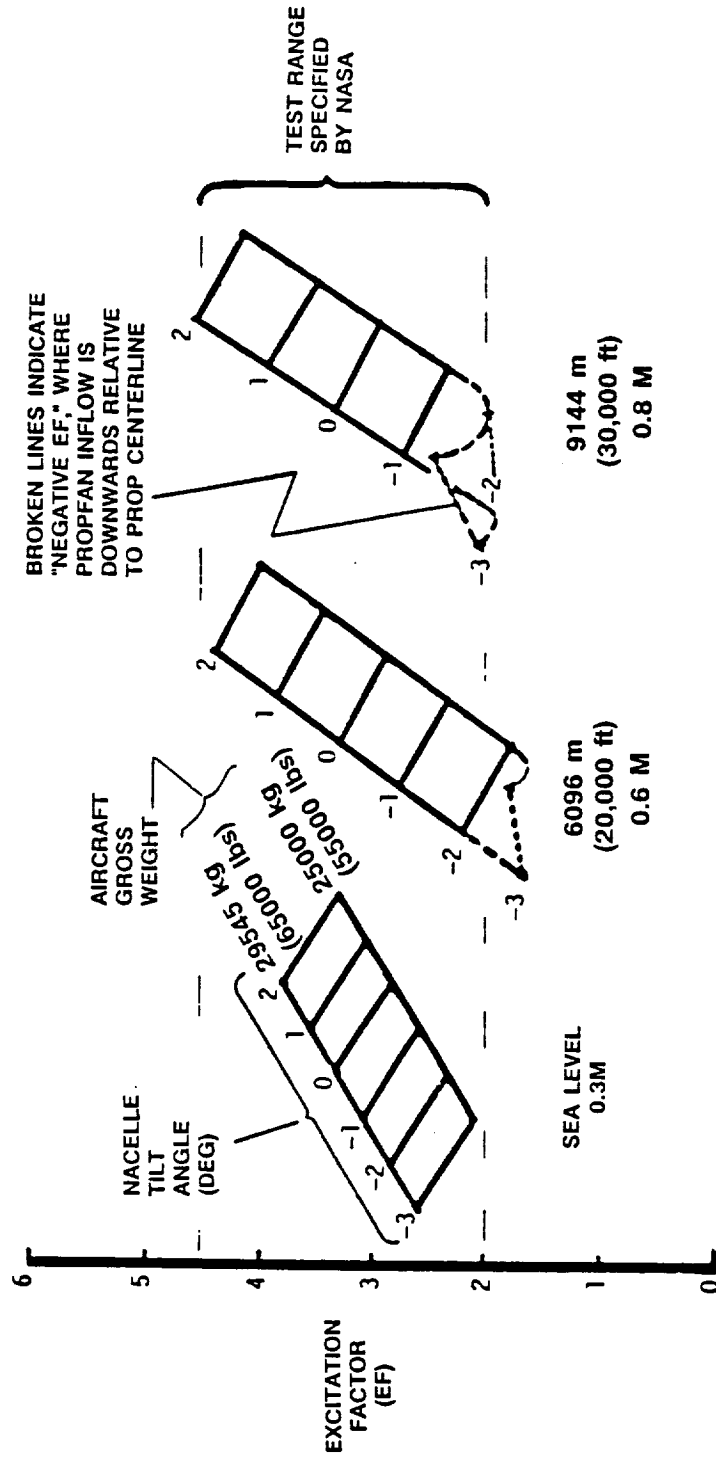


Figure 19. Maps of Excitation Factor

AIRSPEED: 361 KM/HR (195 KCAS)

CONDITIONS TO BE FLOWN ARE INDICATED BY A (✓). UNLESS INDICATED OTHERWISE, ONE FLYOVER WILL BE FLOWN FOR EACH TEST CONDITION.

SHAFT POWER KW (SHIP)	259 m (850 ft) AGL		305 m (1000 ft) AGL		396 m (1300 ft) AGL		488 m (1600 ft) AGL		TBD, ET, AGL	
	M/S (600)	(FT/SEC) (700) (800) (840)	M/S (600)	(FT/SEC) (700) (800) (840)	M/S (600)	(FT/SEC) (700) (800) (840)	M/S (600)	(FT/SEC) (700) (800) (840)	M/S (600)	(FT/SEC) (700) (800) (840)
-1°NT (1790 (2400))	✓	✓	✓	✓	✓	✓	✓	✓	✓	✓
0°ψ (2685 (3600))	✓	✓	✓	✓	✓	✓	✓	✓	✓	✓
0°ψ (3575 (4800))	✓	✓	✓	✓	✓	✓	✓	✓	✓	✓
0°ψ (4978* (6000))	✓(1)	✓(1)	✓	✓(1)(2)	✓	✓(1)	✓	✓	✓	✓(1)
-1°NT (1790 (2400))										
0°ψ (2685 (3600))										
0°ψ (3575 (4800))										
0°ψ (4978* (6000))										
+TBD (1790 (2400))										
-1°NT (1790 (2400))										
0°ψ (2685 (3600))										
0°ψ (3575 (4800))										
0°ψ (4978* (6000))										
+2°NT (1790 (2400))										
0°ψ (2685 (3600))										
0°ψ (3575 (4800))										
0°ψ (4978* (6000))										
-3°NT (1790 (2400))										
0°ψ (2685 (3600))										
0°ψ (3575 (4800))										
0°ψ (4978* (6000))										

* OR MAX OPERABLE

- (1) FLY 2 ADDITIONAL PASSES IN THE SAME DIRECTION FOR A TOTAL OF 3 NORTH-TO-SOUTH PASSES
- (2) FLY 3 ADDITIONAL PASSES IN THE OPPOSITE DIRECTION FOR A TOTAL OF 3 SOUTH-TO-NORTH PASSES
- (3) FLY 1 ADDITIONAL PASS IN THE OPPOSITE DIRECTION

Figure 20. Propfan Installed Low-Altitude Test Conditions

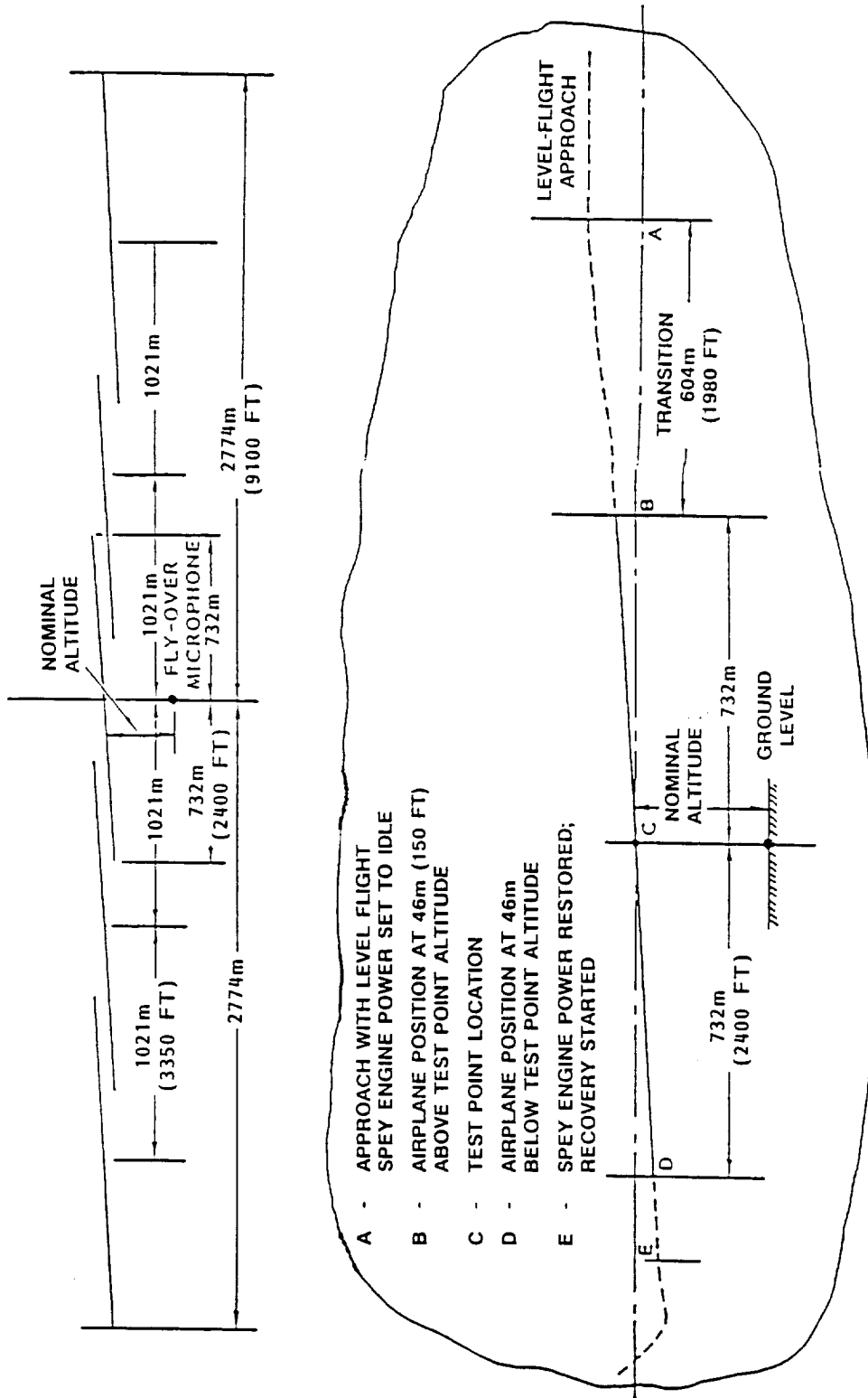


Figure 21. Low-Altitude Test Procedure With Propfan Removed

**FAR-FIELD NOISE
TEST OBJECTIVE**

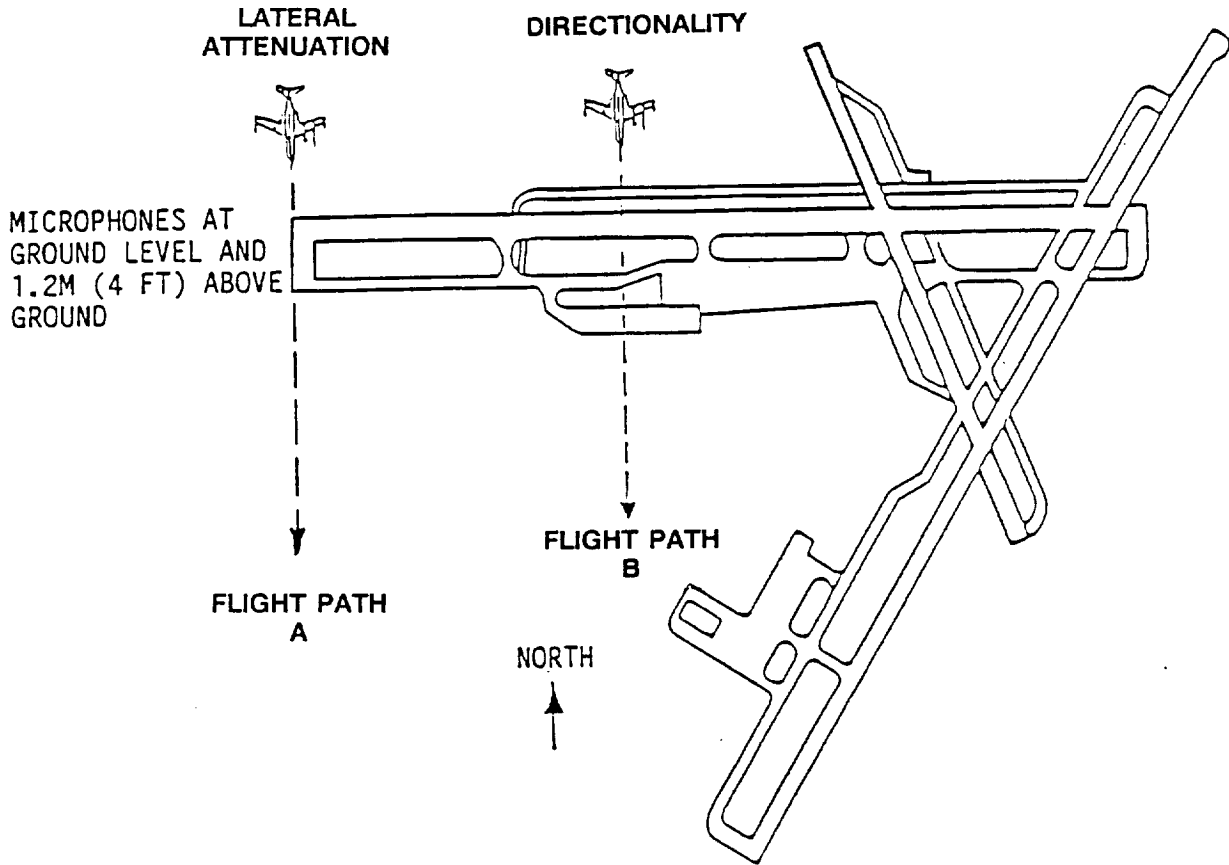


Figure 22. Low-Altitude Flight Paths at NASA Wallops Flight Facility

A	POWER	N _p	77Z	105Z
	MAX CONT		X	X
MINIMUM			X	X

E	POWER	N _p	100Z
	MAX CONT		X

P	POWER	N _p	77Z	100Z
	MAX CONT		X	X
MINIMUM			X	X

B	POWER	N _p	77Z	87.5Z	100Z	105Z
	MAX CONT		X	X	X	X
	80Z				X	
	50Z				X	
MINIMUM				X		

B	POWER	N _p	77Z	87.5Z	100Z	105Z
	MAX CONT		X	X	X	X

C	POWER	N _p	77Z	78.1Z	81.3Z	84.4Z	87.5Z	90.6Z	93.8Z	96.9Z	100Z	102.5Z	105Z
	MAX CONT		X	X	X	X	X	X	X	X	X	X	X
80Z											X		
50Z											X		
MINIMUM											X		

D	POWER	N _p	77Z	81.3Z	87.5Z	93.5Z	100Z	105Z
	MAX CONT		X	X	X	X	X	X
	80Z		X	X	X	X	X	X
	50Z		X	X	X	X	X	X
MINIMUM		X	X	X	X	X	X	

		ZN _p	ZMCP
F		87.0	100.0
G		78.6	81.0
H		105.0	50.5
I		94.8	40.1
J		105.0	100.0
K		94.8	78.4
L		81.0	100.0
M		77.2	93.1
N		105.0	100.0
O		100.1	90.7

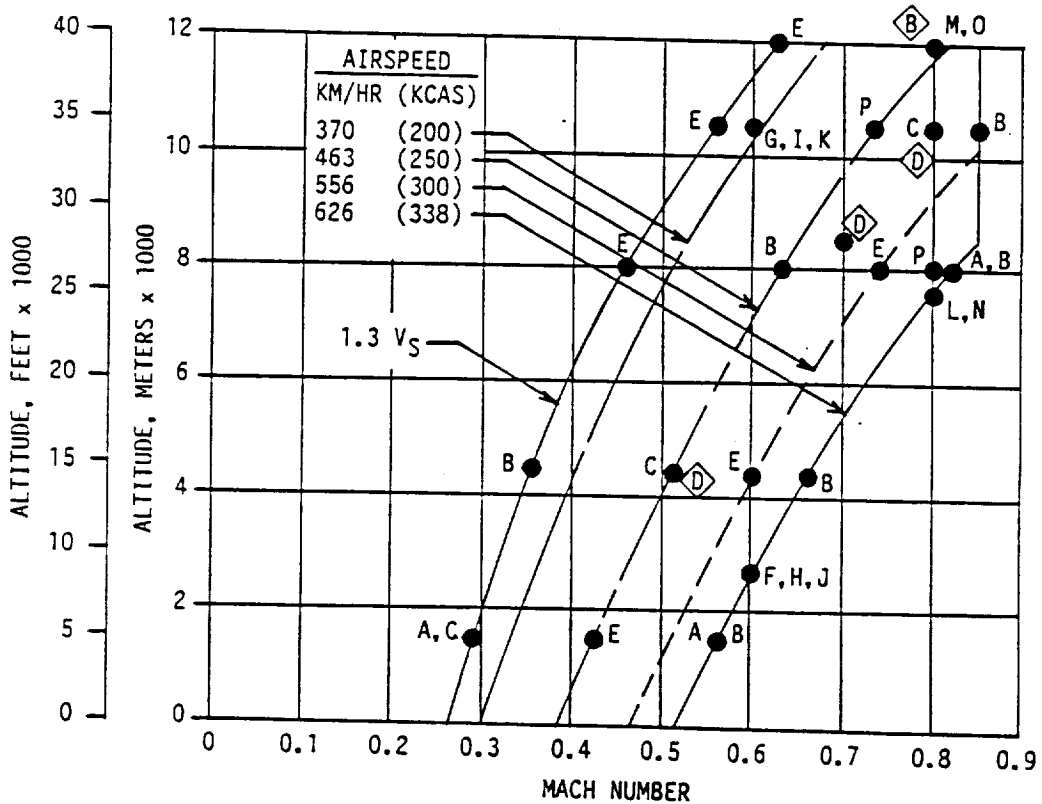


Figure 23. -1° Nacelle Tilt Test Conditions, Propfan On

A

POWER	N_p	77%	105%
MAX CONT		X	X
MINIMUM			X

D

POWER	N_p	100%
MAX CONT		X

B

POWER	N_p	77%	87.5%	100%	105%
MAX CONT		X	X	X	X
50%				X	

E

POWER	N_p	87.5%	100%
MAX CONT		X	X
80%		X	X
50%		X	X
MINIMUM		X	X

C

POWER	N_p	77%	78.1%	81.3%	84.4%	87.5%	90.6%	93.8%	96.9%	100%	102.5%	105%
MAX CONT		X	X	X	X	X	X	X	X	X	X	X
50%										X		X

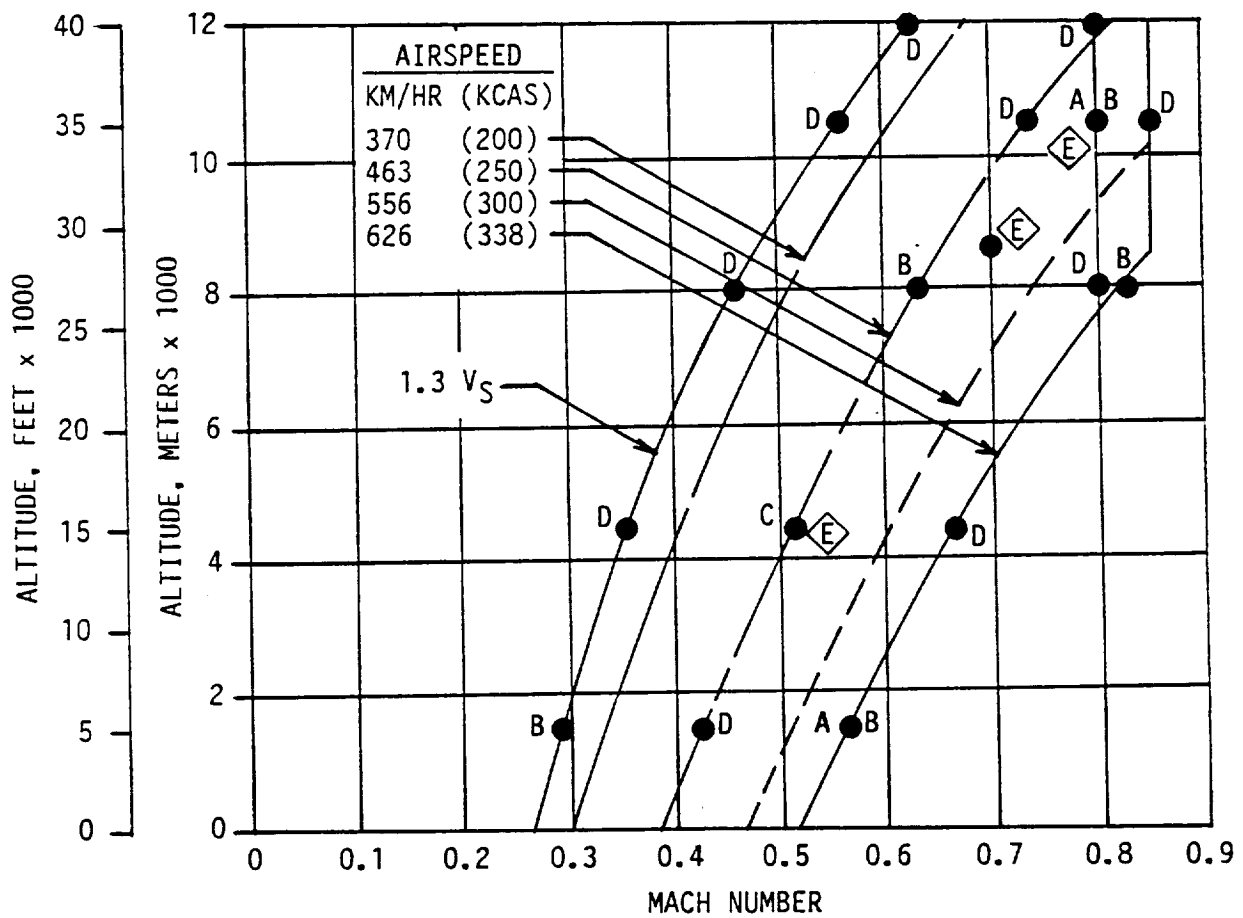


Figure 24. -3° and $+2^\circ$ Nacelle Tilt Test Conditions, Propfan On

A & B	N_p	77%	87.5%	100%	105%
	POWER				
	MAX CONT	X	X	X	X

SET SPEY ENGINES EQUALLY AT THRUST REQUIRED FOR LEVEL FLIGHT

FOR EACH "A" TEST CONDITION SHOWN, POSITION TRAM AT 18 DISCRETE POSITIONS SPACED AT 10.25-INCH INTERVALS BETWEEN FS 250 AND FS 440

FOR EACH "B" CONDITION SHOWN, POSITION TRAM AT FS 301 AND RECORD DATA WITH FUSELAGE UNPRESSURIZED AND WITH MAXIMUM APPROVED CABIN PRESSURE SETTING

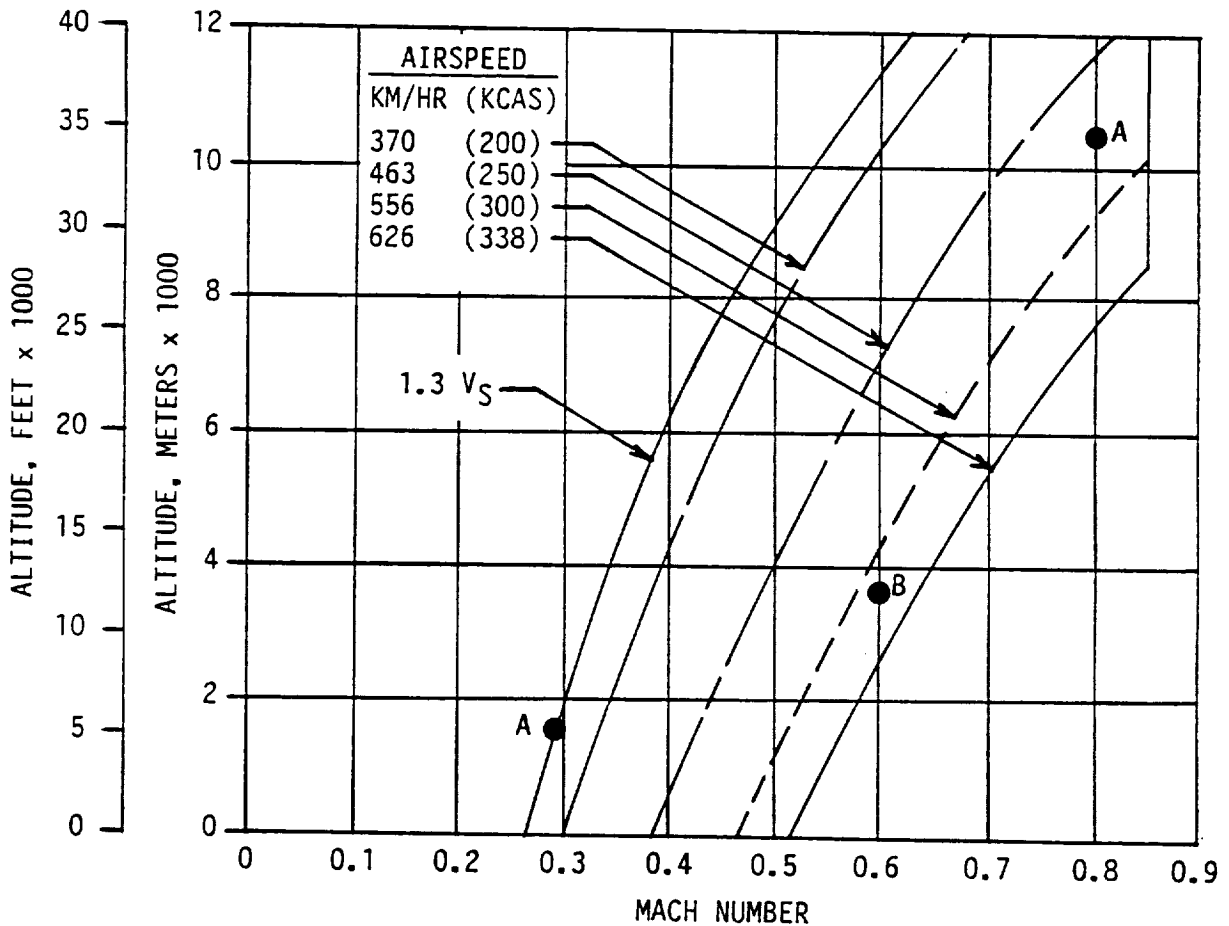


Figure 25. Cabin Noise Survey (TRAM) Test Conditions (-1° Nacelle Tilt)

A

POWER	N_p	77%	105%
MAX CONT		X	X
MINIMUM			X

NACELLE TILT = -1°
 YAW ANGLE = $+2.5^\circ$ & -5°

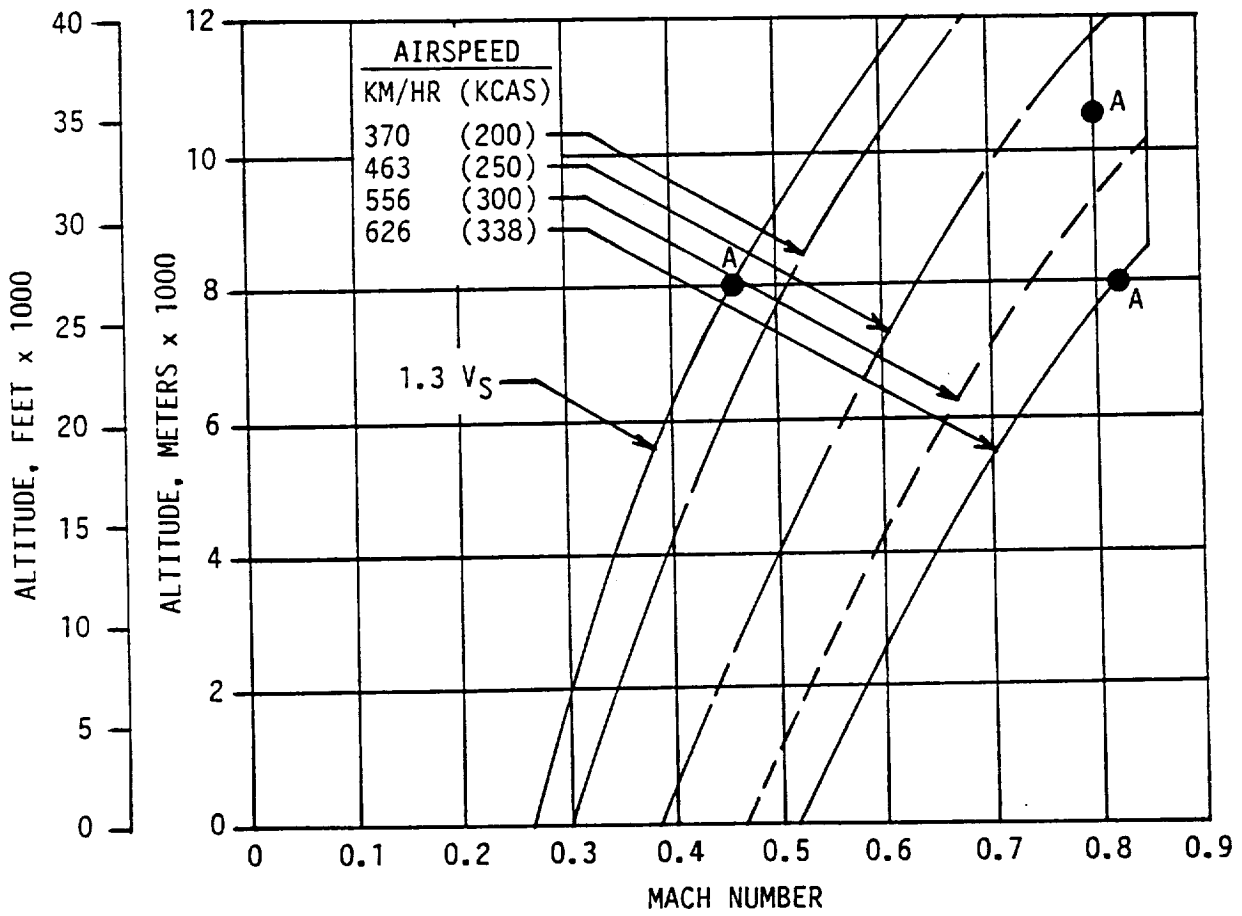


Figure 26. Yaw Angle Test Conditions, Propfan On

A

SPEY ENGINE THRUST	
NO. 1	NO. 2
FLT IDLE	MAX CRUISE
FLT IDLE	70%
FLT IDLE	40%
FLT IDLE	10%

B

SPEY ENGINE THRUST	
NO. 1	NO. 2
MAX CRUISE	MAX CRUISE
70%	MAX CRUISE
40%	MAX CRUISE
FLT IDLE	MAX CRUISE

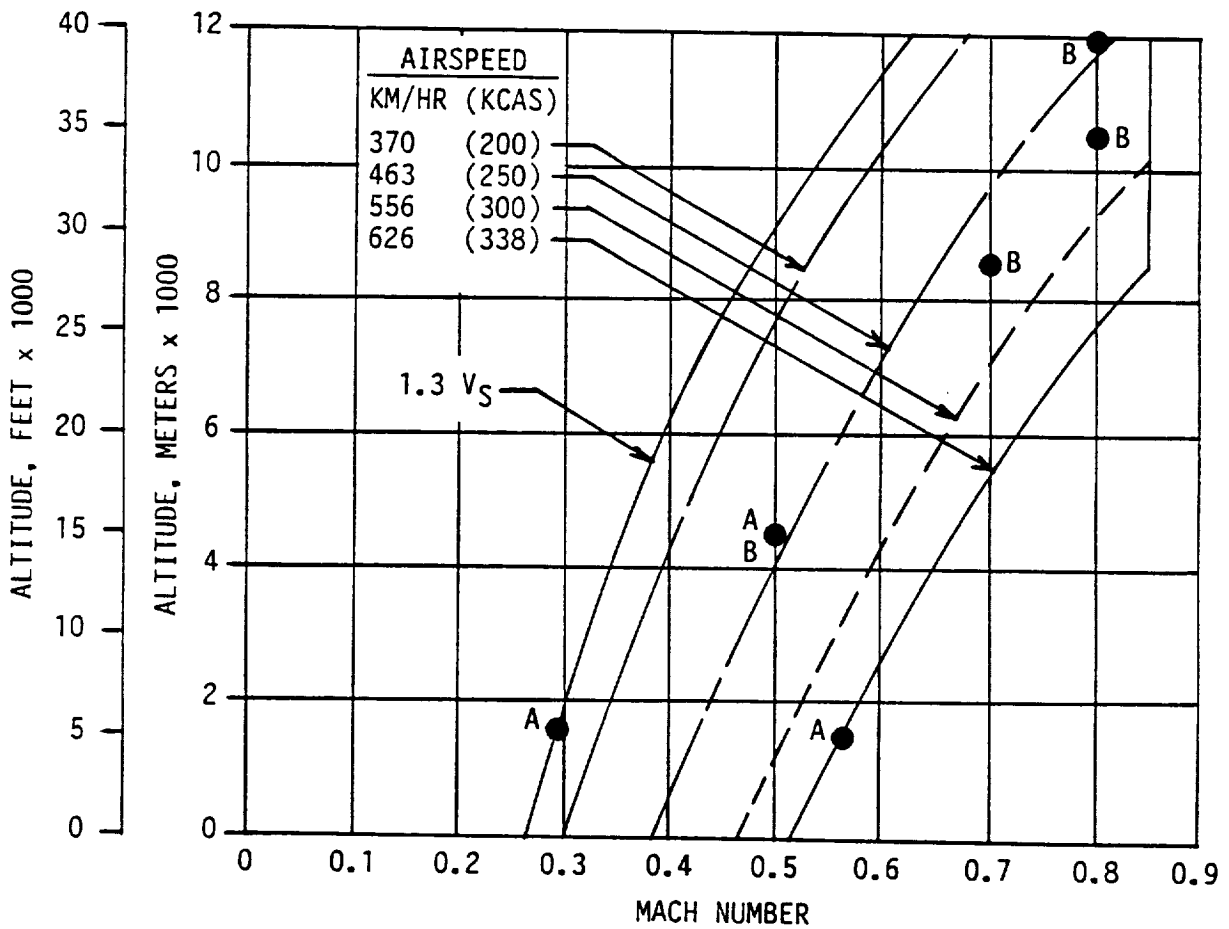


Figure 27. Propfan-Off Test Conditions

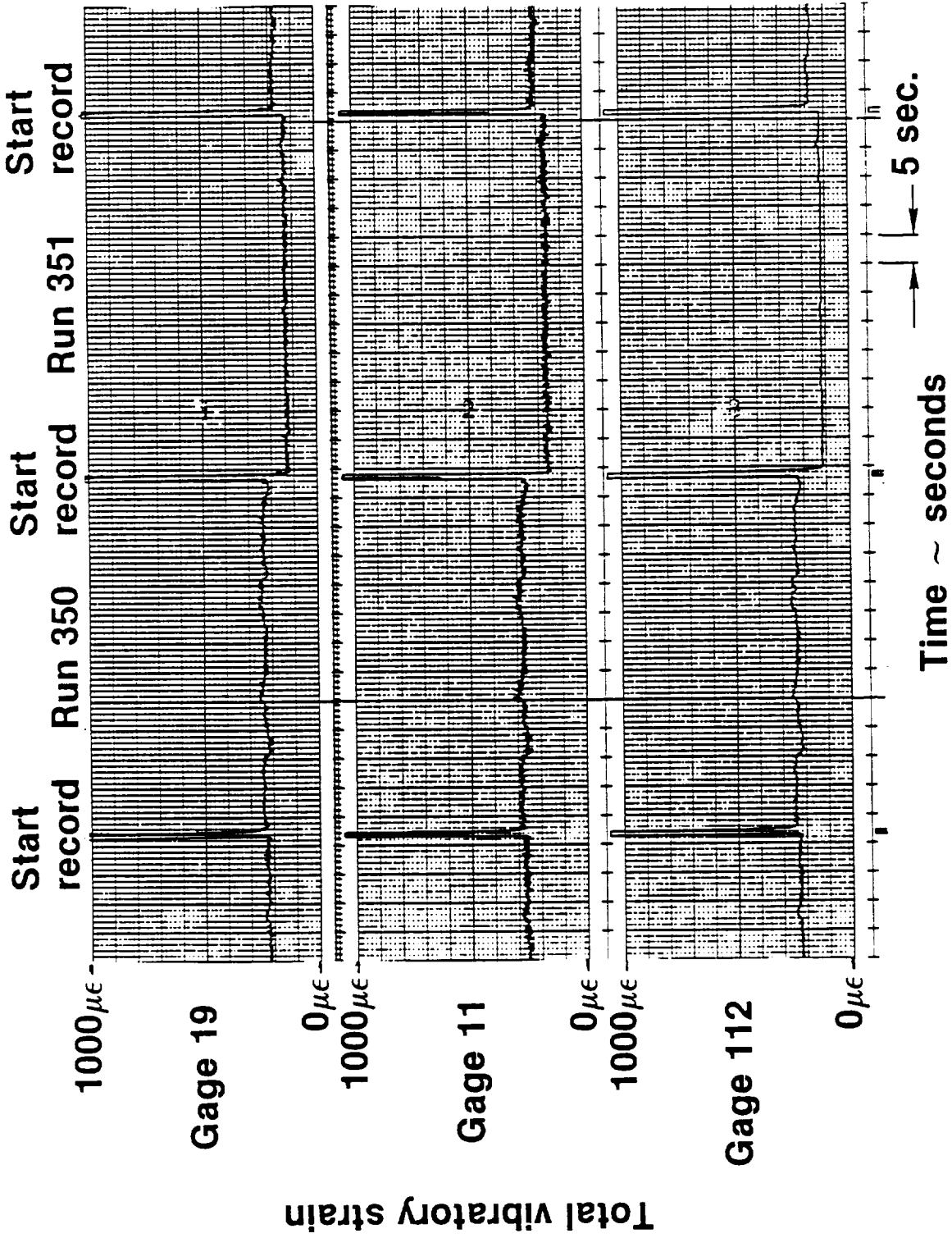


Figure 28. Typical Strip Chart Record



(1) DATE = 710.870	(64) TQSD = 2.14904	FT-LBF
(2) FLT = 16.0000	(65) PSHP = 3129.37	HP
(3) RUN = 0.000000E+00	(66) SHPC = 88888.0	%
(4) STME = 15:03:15.301	(67) RPML = 99.9078	%
(5) ETME = 15:03:59.801	(68) RLMX = 100.070	%
(6) TAMB = 0.000000E+00	(69) RLMN = 99.4531	%
(7) PAMB = 0.000000E+00	(70) RLSD = 0.149800	%
(8) RH = 0.000000E+00	(71) PMCP = 0.000000E+00	%
(9) WSMX = 0.000000E+00	(72) RPT = 11489.4	RPM
(10) WSMN = 0.000000E+00	(73) RPMH = 97.3413	%
(11) WSAG = 0.000000E+00	(74) RHMN = 97.4414	%
(12) WSD = 0.000000E+00	(75) RHMN = 97.1328	%
(13) PAMD = 0.000000E+00	(76) RHSD = 0.581600E-01	%
(14) CG = 1087.11	(77) RPMC = 13919.8	RPM
(15) PMCG = 0.000000E+00	(78) CF1 = 3638.31	HZ
(16) ACGW = 58105.6	(79) TFI = 13787.3	HZ
(17) MTRU = 0.800760	(80) PRPM = 1690.27	RPM
(18) HAGL = 0.000000E+00	(81) VROT = 796.519	FPS
(19) HPT = 34954.9	(82) VFWD = 791.472	FPS
(20) HPMX = 35015.4	(83) VTH = 1122.89	FPS
(21) HPTM = 34911.7	(84) PTMR = 0.806391	
(22) HPSD = 17.8101	(85) MFWD = 0.800760	
(23) KTAS = 468.604	(86) TMTM = 1.13680	
(24) KTMX = 470.279	(87) BAPF = 58.4036	DEGREE
(25) KTMN = 467.279	(88) BAMX = 58.4375	DEGREE
(26) KTS = 0.616170	(89) BAMN = 58.3789	DEGREE
(27) VOO = 791.472	(90) BASD = 0.882000E-02	DEGREE
(28) KCAS = 272.496	(91) IA = 0.809540	DEGREE
(29) TTNB = -18.6970	(92) SHPA = 3072.53	HP
(30) TTMX = -18.4688	(93) PSTQ = 9547.14	FT-LBF
(31) TTMN = -18.9316	(94) FNST = 1583.16	LBF
(32) TTSD = 0.118700	(95) PBHP = 384.066	HP
(33) OATC = -47.6200	(96) PFBT = 1193.39	FT-LBF
(34) PA = 499.025	(97) PFBF = 197.895	LBF
(35) PTOT = 761.262	(98) PDPL = 37.9324	HP/FT*2
(36) COO = 987.758	(99) JP = 3.12151	
(37) SGMA = 0.301300	(100) CP = 1.78716	
(38) PMO = 0.716630E-03	(101) CTP = 0.424520	
(39) PMOC = 0.707857	(102) PFN = 0.741480	%
(40) QE = 223.988	(103) BPF1 = 225.369	HZ
(41) ALPH = 1.80954	(104) RPM3 = 33767.4	%
(42) ALMX = 2.34890	(105) R1MX = 33767.0	%
(43) ALMN = 1.37940	(106) R1MN = 33767.0	%
(44) ALSD = 0.220840	(107) R1SD = 0.000000E+00	%
(45) SSNB = -4.72310	(108) RPM1 = 86.5348	%
(46) SSMX = 0.206100	(109) R1MX = 86.5508	%
(47) SSMN = -0.933600	(110) R1MN = 86.5000	%
(48) SSSD = 0.209750	(111) R1SD = 0.120800E-01	%
(49) NTA = -1.00000	(112) SPN1 = 2072.69	LBF
(50) DHDT = -0.139720	(113) LSF1 = 0.916724E+08	HZ
(51) PCAB = 12.0050	(114) LST1 = 0.362106E+09	HZ
(52) PCMX = 12.0049	(115) RPM4 = 33767.4	%
(53) PCMN = 11.9961	(116) R1MX = 0.000000E+00	%
(54) PCSD = 0.163000E-02	(117) R1MN = 0.000000E+00	%
(55) CDP = 8.53955	(118) R1SD = 0.000000E+00	%
(56) TCAB = 20.6730	(119) RPM2 = 92.8955	%
(57) CC = 1127.52	(120) R2MX = 92.9336	%
(58) SIGC = 0.000000E+00	(121) R2MN = 92.8633	%
(59) PC = 0.190524E-02	(122) R2SD = 0.143300E-01	%
(60) PMCC = 2.14820	(123) SPN2 = 3063.23	LBF
(61) TQE3 = 1430.52	(124) RSP1 = 0.916723E+08	HZ
(62) TQMX = 1435.50	(125) RST1 = 0.362106E+09	HZ
(63) TQMN = 1425.25	(126) = 0.000000E+00	0

Figure 29. Sample of Tabular Listing of Operational Parameters

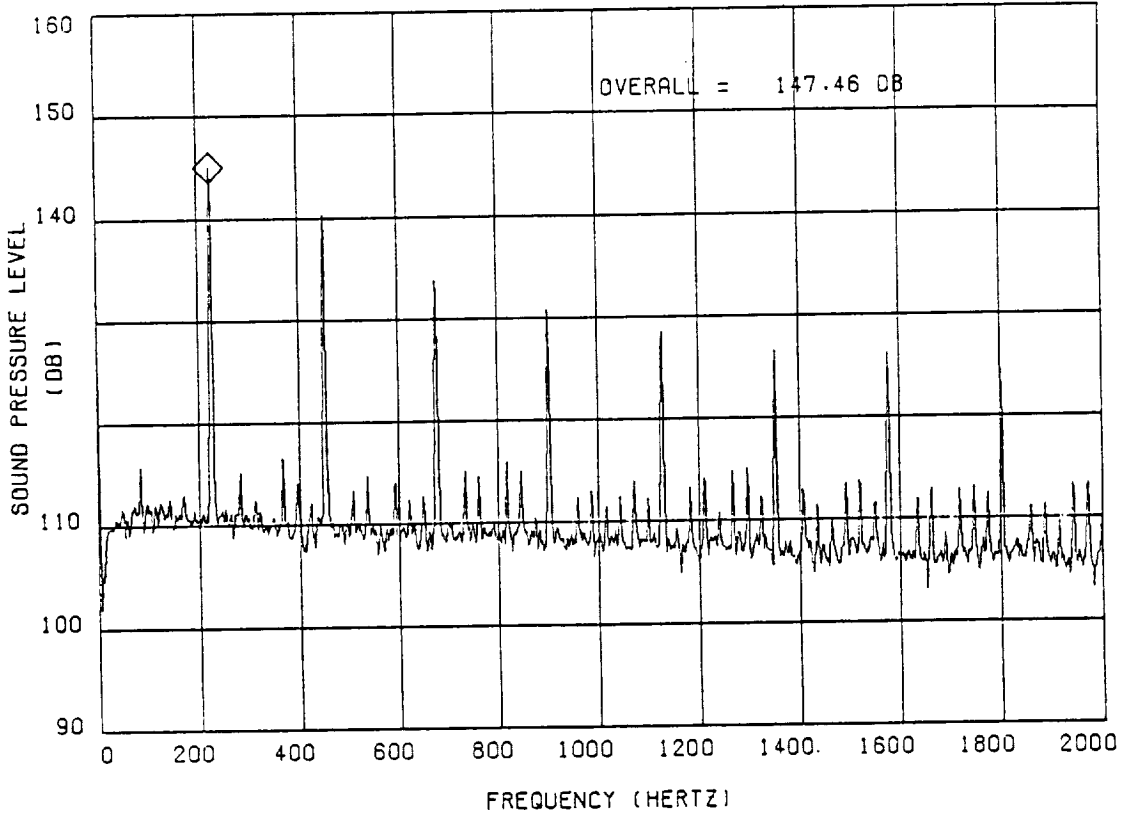


FIGURE PTA FUSELAGE EXTERIOR NOISE SPECTRUM

TRANSDUCER : (M302) SURFACE MICROPHONE AT FS301 WL70.0
 FLIGHT : 16 . RUN : 44 CONDITION NUMBER : 350

FLT SPEED	0.801	MACH	NACELLE TILT	-1.00 DEG
FLT ALTITUDE	10654 (34954)	M (FT)	ATTACK ANG	1.81 DEG
PROPFAN PWR	2291 (3072)	KW (PSHP)	SIDESLIP ANG	-0.47 DEG
PROP TORQ	12944 (9547)	MN (FT-LBS)	BLADE ANG	58.40 DEG
PROPFAN BPF	225.4	HERTZ	PWR COEFF	1.79
TIP ROT SPD	0.806	MACH	THRUST COEFF	0.42
TIP HEL SPD	1.137	MACH	ADV RATIO	3.12
PROP THRUST	7042 (1583)	N (LB)		
DISC PWR LD	304.5 (37.93)	KW/M*2 (PSHP/FT*2)		

MARKER 145.079 DB • 225.000 HERTZ
 40 AVERAGES 56% OVERLAP HANN WINDOW EFF. BW. = 3.8 HERTZ

Figure 30. Sample of Computerized Presentation of Narrow-Band Spectral Data



ORIGINAL PAGE IS
OF POOR QUALITY

LOCKHEED/NASA-LEWIS PROPPAN TEST ASSESSMENT PROGRAM ACOUSTIC FLIGHT RESEARCH DATA											
COND = 350. FLT = 16.00 RUN = 44.0000											
DATA LEVEL AND CORRESPONDING FREQUENCY AT OR WITHIN +/- 5% OF N-TH ORDER OF BPF.											
MEAS	UNIT	N=1	N=2	N=3	N=4	N=5	N=6	N=7	N=8	N=9	N=10
		225.4	450.7	676.1	901.5	1126.8	1352.2	1577.6	1803.0	2028.3	2253.7
=====											
M123	SPL (DB)	-1.0	-1.0	-1.0	-1.0	-1.0	-1.0	-1.0	-1.0	-2.0	-2.0
	HERTZ	-1.0	-1.0	-1.0	-1.0	-1.0	-1.0	-1.0	-1.0	-2.0	-2.0
M191	SPL (DB)	123.4	110.3	103.6	-1.0	-1.0	-1.0	-1.0	-1.0	-2.0	-2.0
	HERTZ	225.0	450.0	675.0	-1.0	-1.0	-1.0	-1.0	-1.0	-2.0	-2.0
M192	SPL (DB)	124.1	111.4	104.4	-1.0	-1.0	-1.0	-1.0	-1.0	-2.0	-2.0
	HERTZ	225.0	450.0	675.0	-1.0	-1.0	-1.0	-1.0	-1.0	-2.0	-2.0
M193	SPL (DB)	123.9	108.7	-1.0	-1.0	-1.0	-1.0	-1.0	-1.0	-2.0	-2.0
	HERTZ	225.0	450.0	-1.0	-1.0	-1.0	-1.0	-1.0	-1.0	-2.0	-2.0
M194	SPL (DB)	114.8	-1.0	-1.0	-1.0	-1.0	-1.0	-1.0	-1.0	-2.0	-2.0
	HERTZ	225.0	-1.0	-1.0	-1.0	-1.0	-1.0	-1.0	-1.0	-2.0	-2.0
M241	SPL (DB)	131.4	115.6	-1.0	-1.0	-1.0	-1.0	-1.0	-1.0	-2.0	-2.0
	HERTZ	225.0	450.0	-1.0	-1.0	-1.0	-1.0	-1.0	-1.0	-2.0	-2.0
M242	SPL (DB)	138.1	133.6	126.2	114.9	111.8	-1.0	-1.0	-1.0	-2.0	-2.0
	HERTZ	225.0	450.0	675.0	900.0	1127.5	-1.0	-1.0	-1.0	-2.0	-2.0
M243	SPL (DB)	134.3	124.1	117.0	110.4	-1.0	-1.0	-1.0	-1.0	-2.0	-2.0
	HERTZ	225.0	450.0	675.0	900.0	-1.0	-1.0	-1.0	-1.0	-2.0	-2.0
M244	SPL (DB)	126.2	108.7	-1.0	-1.0	-1.0	-1.0	-1.0	-1.0	-2.0	-2.0
	HERTZ	225.0	450.0	-1.0	-1.0	-1.0	-1.0	-1.0	-1.0	-2.0	-2.0
M245	SPL (DB)	118.0	-1.0	-1.0	-1.0	-1.0	-1.0	-1.0	-1.0	-2.0	-2.0
	HERTZ	225.0	-1.0	-1.0	-1.0	-1.0	-1.0	-1.0	-1.0	-2.0	-2.0
M271	SPL (DB)	135.7	131.2	119.4	109.0	106.8	103.4	-1.0	-1.0	-2.0	-2.0
	HERTZ	225.0	450.0	675.0	900.0	1127.5	1352.5	-1.0	-1.0	-2.0	-2.0
M272	SPL (DB)	136.4	135.3	129.1	122.0	116.6	114.7	-1.0	-1.0	-2.0	-2.0
	HERTZ	225.0	450.0	675.0	900.0	1127.5	1352.5	-1.0	-1.0	-2.0	-2.0
M273	SPL (DB)	136.2	133.8	129.4	123.7	116.5	115.5	111.6	106.8	-2.0	-2.0
	HERTZ	225.0	450.0	675.0	900.0	1127.5	1352.5	1577.5	1802.5	-2.0	-2.0
M274	SPL (DB)	130.2	124.1	112.5	105.7	-1.0	-1.0	-1.0	-1.0	-2.0	-2.0
	HERTZ	225.0	450.0	675.0	900.0	-1.0	-1.0	-1.0	-1.0	-2.0	-2.0
M275	SPL (DB)	122.0	115.8	-1.0	-1.0	-1.0	-1.0	-1.0	-1.0	-2.0	-2.0
	HERTZ	225.0	450.0	-1.0	-1.0	-1.0	-1.0	-1.0	-1.0	-2.0	-2.0
M276	SPL (DB)	-1.0	-1.0	-1.0	-1.0	-1.0	-1.0	-1.0	-1.0	-2.0	-2.0
	HERTZ	-1.0	-1.0	-1.0	-1.0	-1.0	-1.0	-1.0	-1.0	-2.0	-2.0

Figure 31. Sample of Computerized Tabulation of Spectrum Amplitude and Frequency at Orders of Blade Passage Frequency

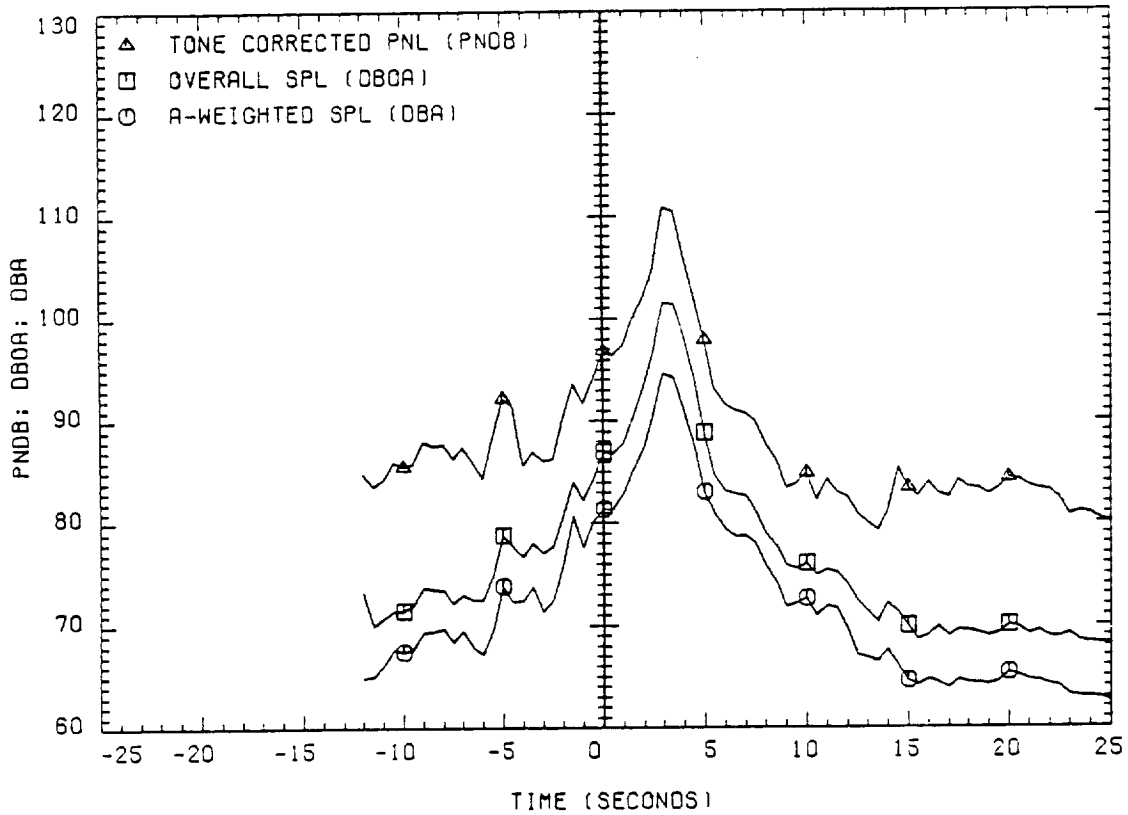


FIGURE PTA ACOUSTIC TIME HISTORY

TRANSDUCER : (1G) GROUND-LEVEL MIC. ON-TRACK
 FLIGHT : 44 RUN : 10 CONDITION NUMBER : 1186

FLT SPEED	0.309	MACH	PROPFAN BPF	236.4 HERTZ
FLT ALTITUDE	304 (998) M (FT)		NACELLE TILT	-1.00 DEG
PROPFAN PWR	4374 (5866) KW (PSHP)		ATTACK ANG	4.82 DEG
PROP TORQ	23565 (17381) MN (FT-LBS)		SIDESLIP ANG	-1.68 DEG
TIP ROT VEL	255 (835) M/SEC (FT/SEC)		BLADE ANG	34.74 DEG
TIP ROT SPD	0.758	MACH	PWR COEFF	0.90
TIP HEL SPD	0.819	MACH	THRUST COEFF	0.49
PROP THRUST	29178 (6559) N (LB)		ADV RATIO	1.28
DISC PWR LO	581.4 (72.43) KW/M ² (PSHP/FT ²)		HEADING	SOUTH

Figure 32. Sample of Computerized Presentation of Flyover Noise Time History Data

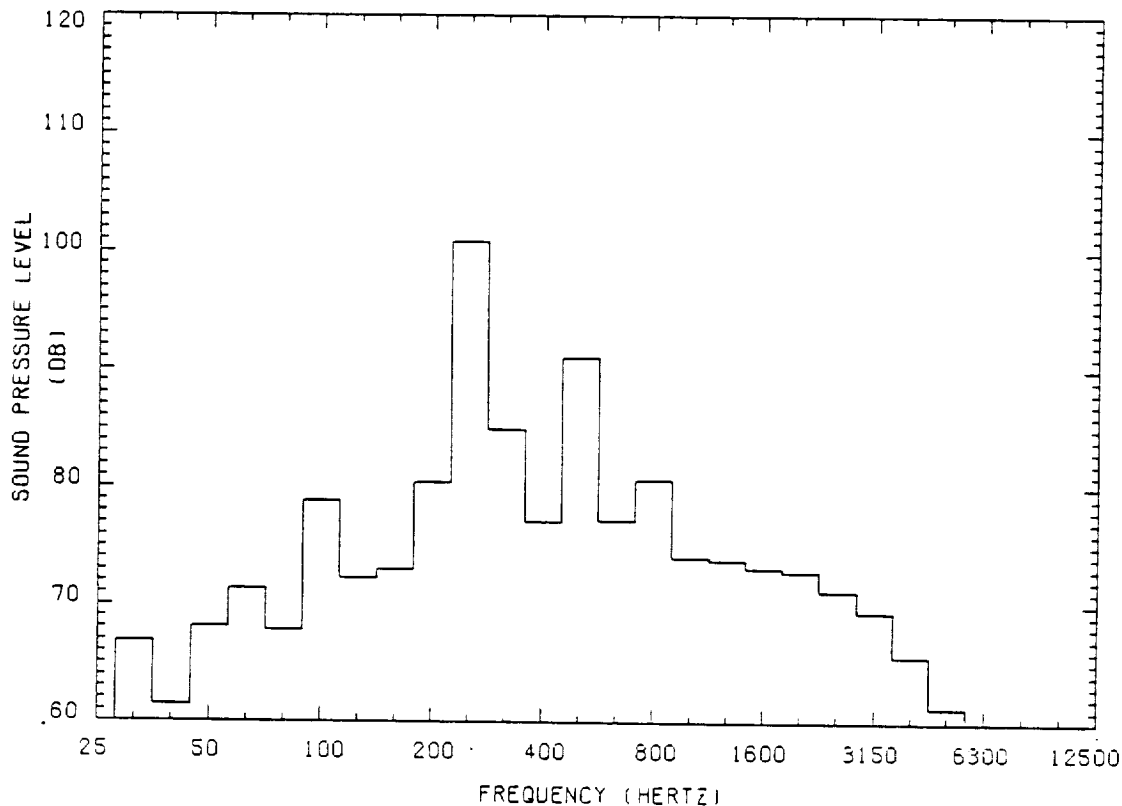


FIGURE PTA 1/3 OCTAVE SPL SPECTRUM AT 3.0 SECONDS

TRANSDUCER : (1G) GROUND-LEVEL MIC. ON-TRACK
 FLIGHT : 44 RUN : 10 CONDITION NUMBER : 1186

FLT SPEED	0.309	MACH	PROPFAN BPF	236.4 HERTZ
FLT ALTITUDE	304 (998) M (FT)		NACELLE TILT	-1.00 DEG
PROPFAN PWR	4374 (5866) KW (PSHP)		ATTACK ANG	4.82 DEG
PROP TORQ	23565 (17381) MN (FT-LBS)		SIDESLIP ANG	-1.68 DEG
TIP ROT VEL	255 (835) M/SEC (FT/SEC)		BLADE ANG	34.74 DEG
TIP ROT SPD	0.758	MACH	PWR COEFF	0.90
TIP HEL SPD	0.819	MACH	THRUST COEFF	0.49
PROP THRUST	29178 (6559) N (LB)		ADV RATIO	1.28
DISC PWR LD	581.4 (72.43) KW/M*2(PSHP/FT*2)		HEADING	SOUTH

Figure 33. Sample of Computerized Presentation of 1/3 Octave Band Spectral Data

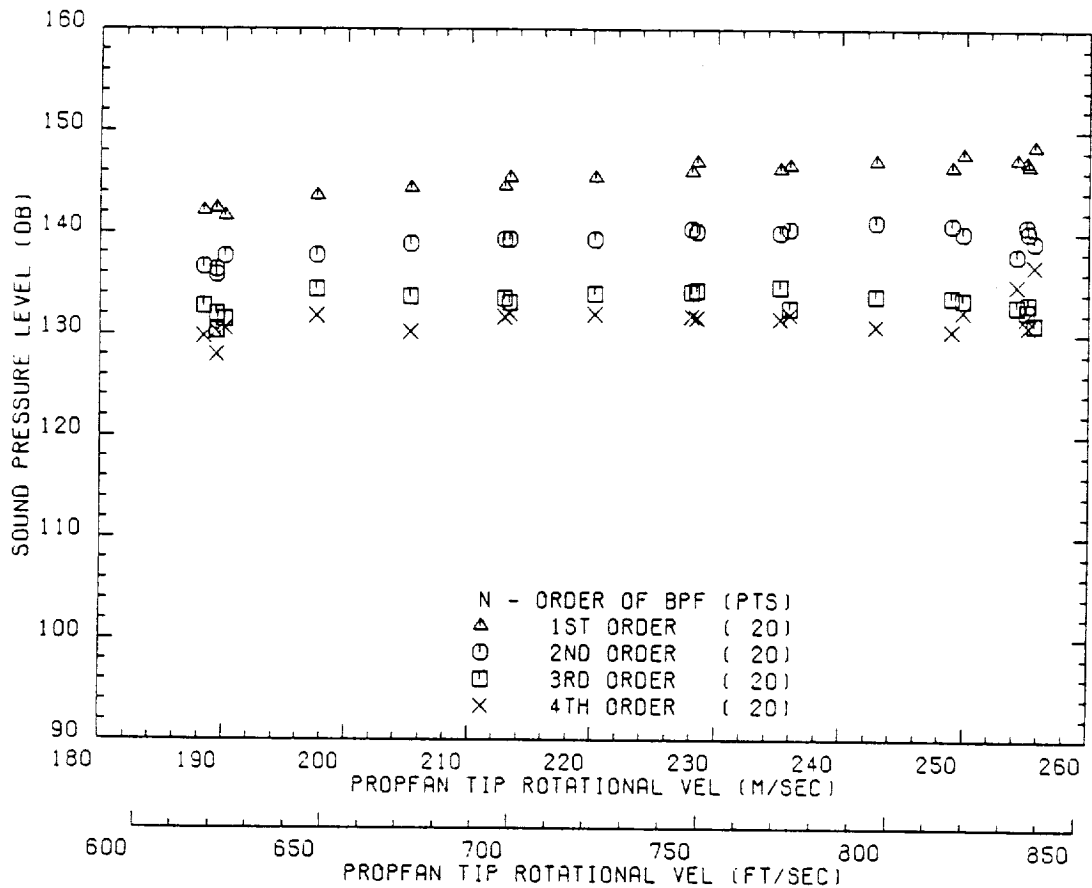


FIGURE PTA/SR-7L NEAR FIELD NOISE; HARMONIC DEPENDENCE ON PROPFAN TIP ROTATIONAL VELOCITY AT H=35000 FT; M=0.8; NT=-1 DEG; MAX POWER.

TRANSDUCER : (L1FM) FUSELAGE SURFACE MAXIMUM NOISE

	MEAN	MEAN ;	RANGE
ALTITUDE	10705. METERS	(35122.;	34833. TO 35602. FEET)
AIRSPPEED	0.803 MACH	(0.803;	0.771 TO 0.817 MACH)
TIP ROTATION VELOCITY	232.64 M/SEC	(763.24;	617.98 TO 839.13 FT/SEC)
TIP HELICAL SPEED	1.120 MACH	(1.120;	1.018 TO 1.178 MACH)
ADVANCE RATIO	3.295	(3.295;	2.832 TO 4.082)
PROPFAN BPF	215.95 HERTZ	(215.95;	174.85 TO 237.43 HERTZ)
PROPFAN SHAFT TORQUE	12821. M-NEWTON	(9456.4;	8452.5 TO 10552. FT-LBS)
PROPFAN THRUST	6202.1 NEWTONS	(1394.3;	913.55 TO 1621.1 LBS)
THRUST COEFFICIENT	0.406	(0.406;	0.355 TO 0.492)
PROPFAN SHAFT POWER	2158.3 KW	(2894.3;	2583.7 TO 3148.0 HP)
POWER COEFFICIENT	2.033	(2.033;	1.389 TO 3.260)
BLADE ANGLE	57.755 DEGREES	(57.755;	51.593 TO 62.633 DEGREES)
NACELLE TILT ANGLE	-1.000 DEGREES	(-1.000;	-1.000 TO -1.000 DEGREES)
ANGLE OF ATTACK	1.748 DEGREES	(1.748;	1.381 TO 2.602 DEGREES)
SIDESLIP ANGLE	-0.204 DEGREES	(-0.204;	-0.683 TO 0.493 DEGREES)
FREESTREAM RHO C2	33213. N/M*2	(693.67;	677.92 TO 703.24 LB/FT*2)

Figure 35. Sample Parametric Plot of Near-Field Noise Data

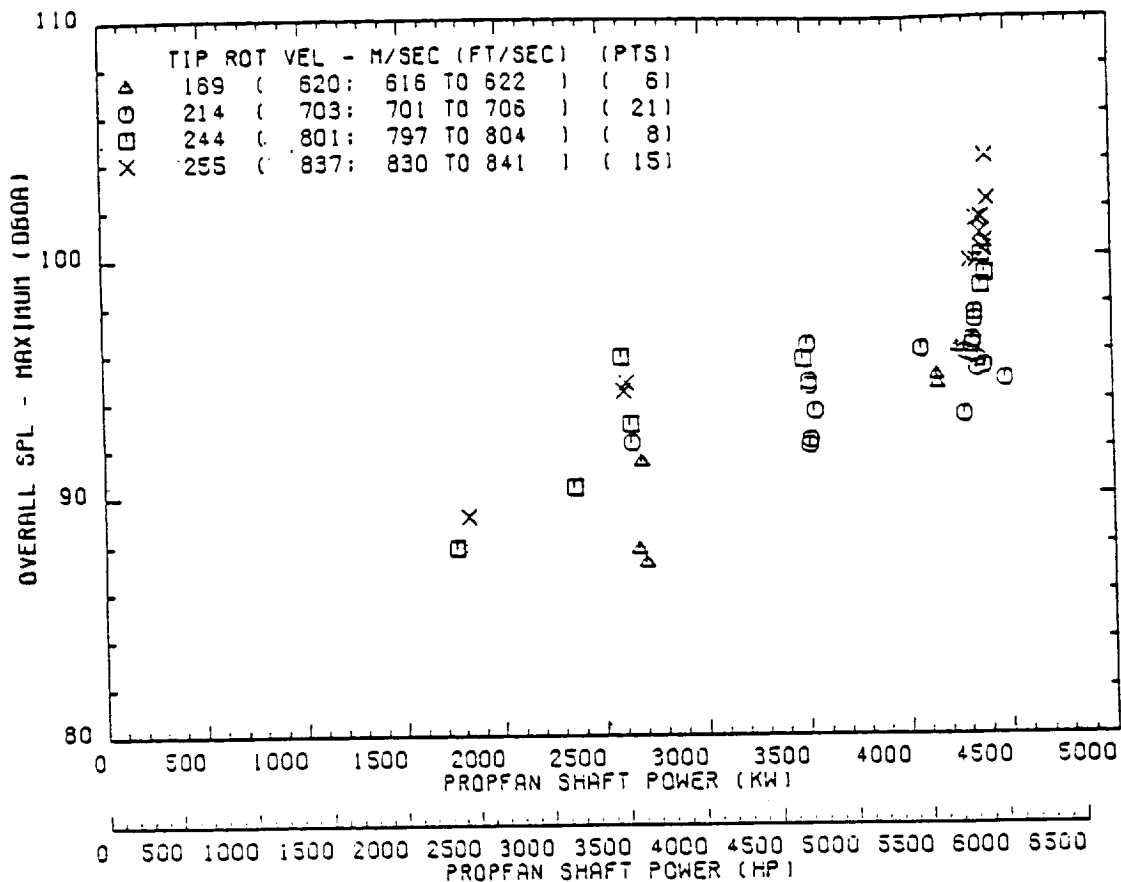


FIGURE PTA/SR7L FAR-FIELD OVERALL SOUND PRESSURE LEVEL DEPENDENCE ON POWER AND TIP SPEED

TRANSDUCER : (1G) (OG) GROUND-LEVEL MICROPHONES ON FLIGHT TRACK

	MEAN	MEAN :	RANGE
ALTITUDE	310.04 METERS	(1017.2 :	912.00 TO 1150.0 FEET)
AIRSPEED	0.310 MACH	(0.310 :	0.291 TO 0.338 MACH)
TIP ROTATION VELOCITY	229.43 M/SEC	(752.73 :	516.25 TO 840.80 FT/SEC)
TIP HELICAL SPEED	0.746 MACH	(0.746 :	0.634 TO 0.821 MACH)
ADVANCE RATIO	1.452	(1.452 :	1.250 TO 1.880)
PROPFAN RPM	212.98 HERTZ	(212.98 :	174.36 TO 237.90 HERTZ)
PROPFAN SHAFT TORQUE	22822. N-NEWTON	(16833. :	7281.3 TO 22757. FT-LBS)
PROPFAN THRUST	24632. NEWTONS	(5537.6 :	2758.9 TO 6697.5 LBS)
THRUST COEFFICIENT	0.523	(0.523 :	0.215 TO 0.729)
PROPFAN SHAFT POWER	3789.9 KW	(5082.4 :	2361.4 TO 6010.9 HP)
POWER COEFFICIENT	0.969	(0.969 :	0.000 TO 2.108)
BLADE ANGLE	39.823 DEGREES	(39.823 :	31.906 TO 51.303 DEGREES)
NACELLE TILT ANGLE	-1.000 DEGREES	(-1.000 :	-1.000 TO -1.000 DEGREES)
ANGLE OF ATTACK	5.221 DEGREES	(5.221 :	3.205 TO 4.531 DEGREES)
SIDESLIP ANGLE	-1.018 DEGREES	(-1.018 :	-4.822 TO 2.150 DEGREES)
FREESTREAM RHO C2	137111. N/M ²	(2863.6 :	2828.7 TO 2908.0 LB/FT ²)

Figure 36. Sample Parametric Plot of Far-Field Noise Data

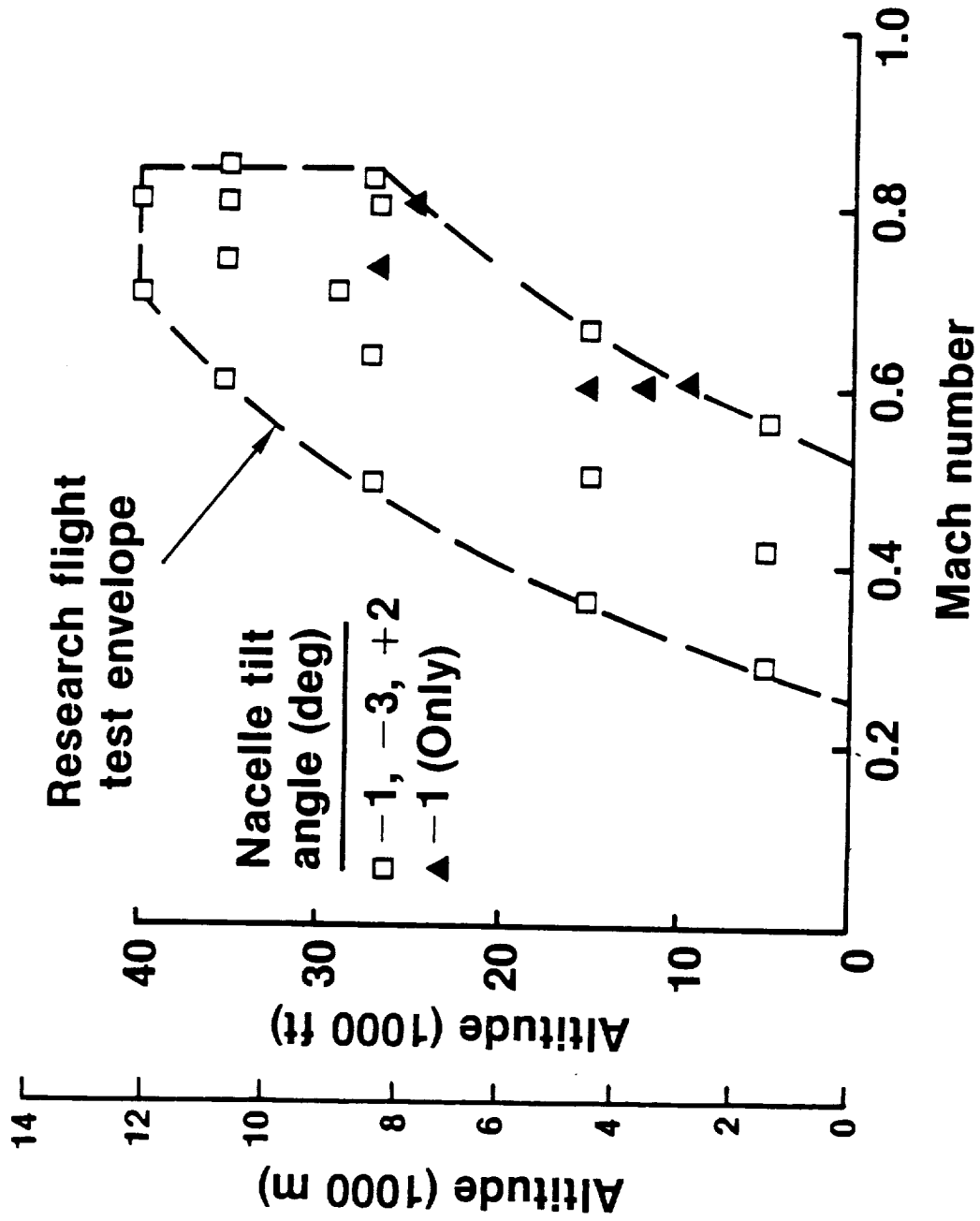


Figure 37. Flight Conditions for Propfan Structural Tests

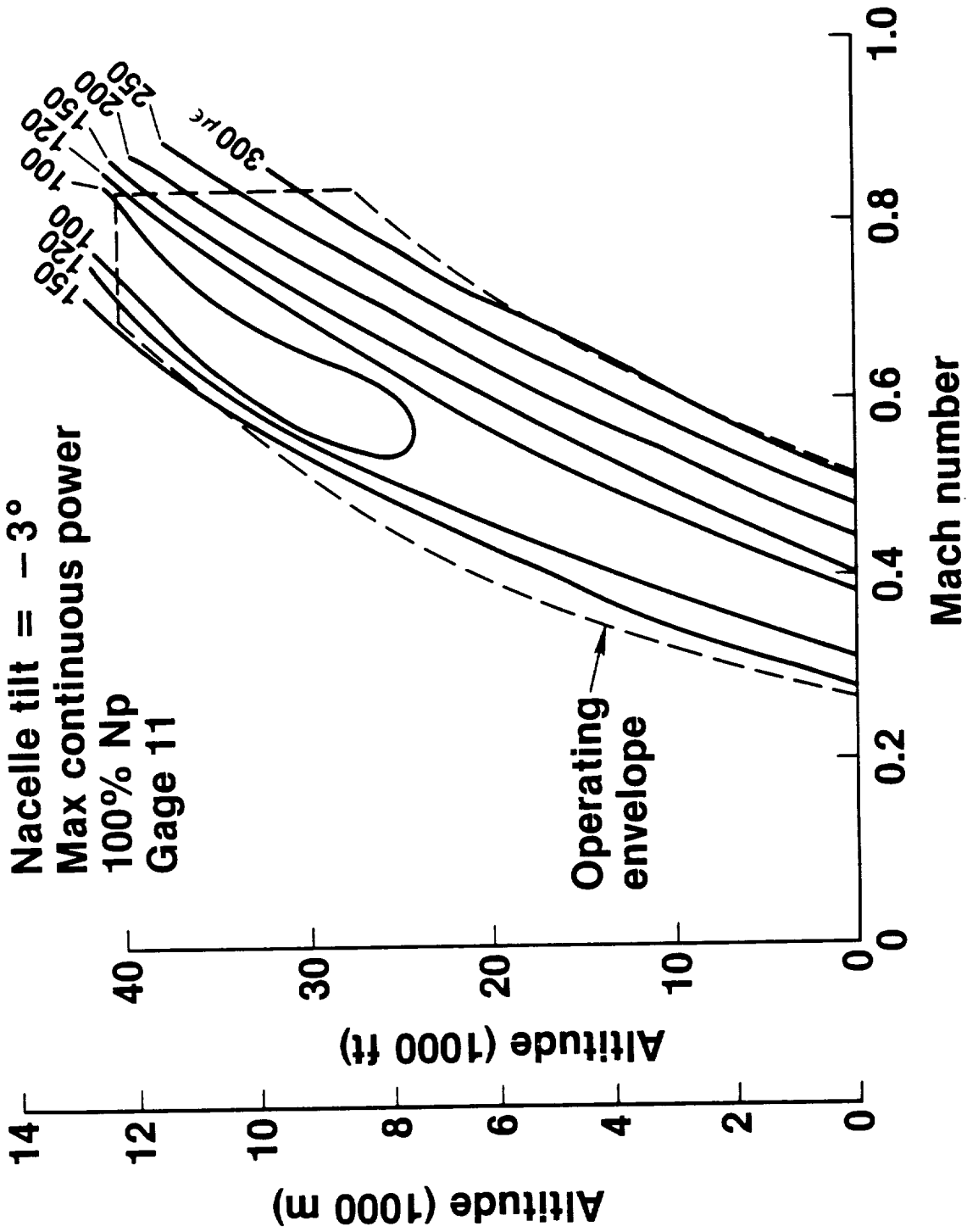


Figure 38. Inboard Bending Vibratory Strain Over the -3° Nacelle Tilt Flight Envelope

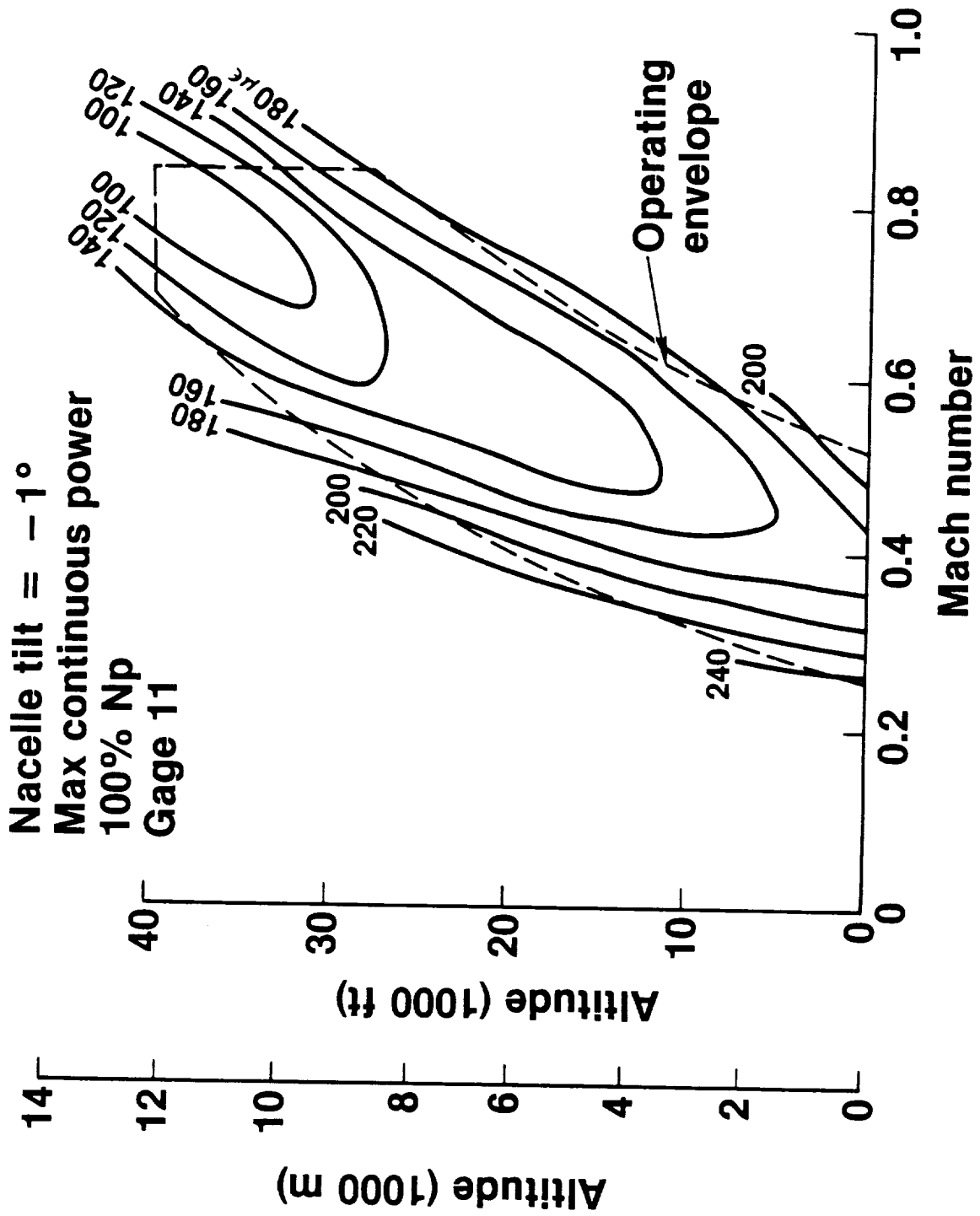


Figure 39. Inboard Bending Vibratory Strain Over the -1° Nacelle Tilt Flight Envelope

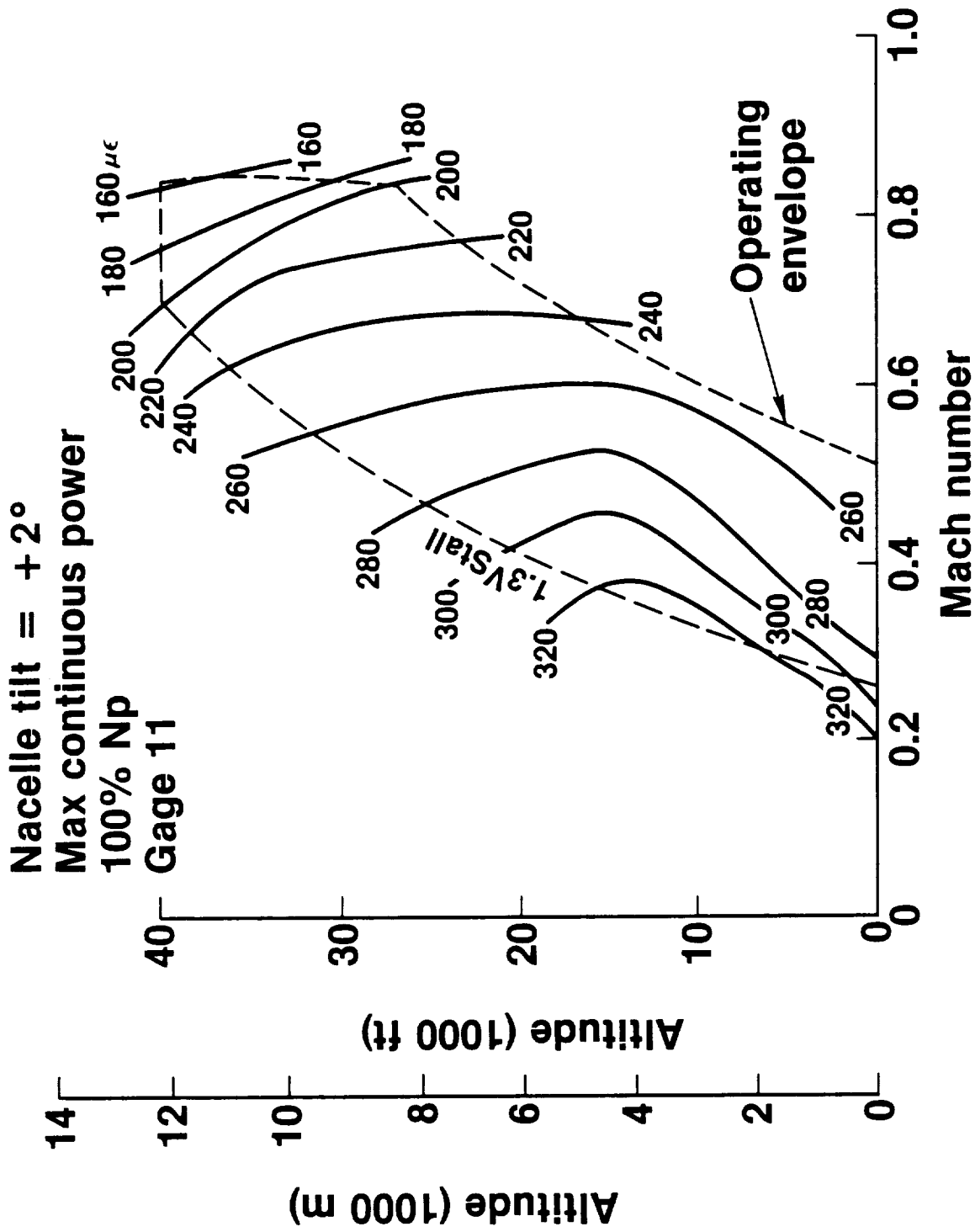


Figure 40. Inboard Bending Vibratory Strain Over the +2° Nacelle Tilt Flight Envelope

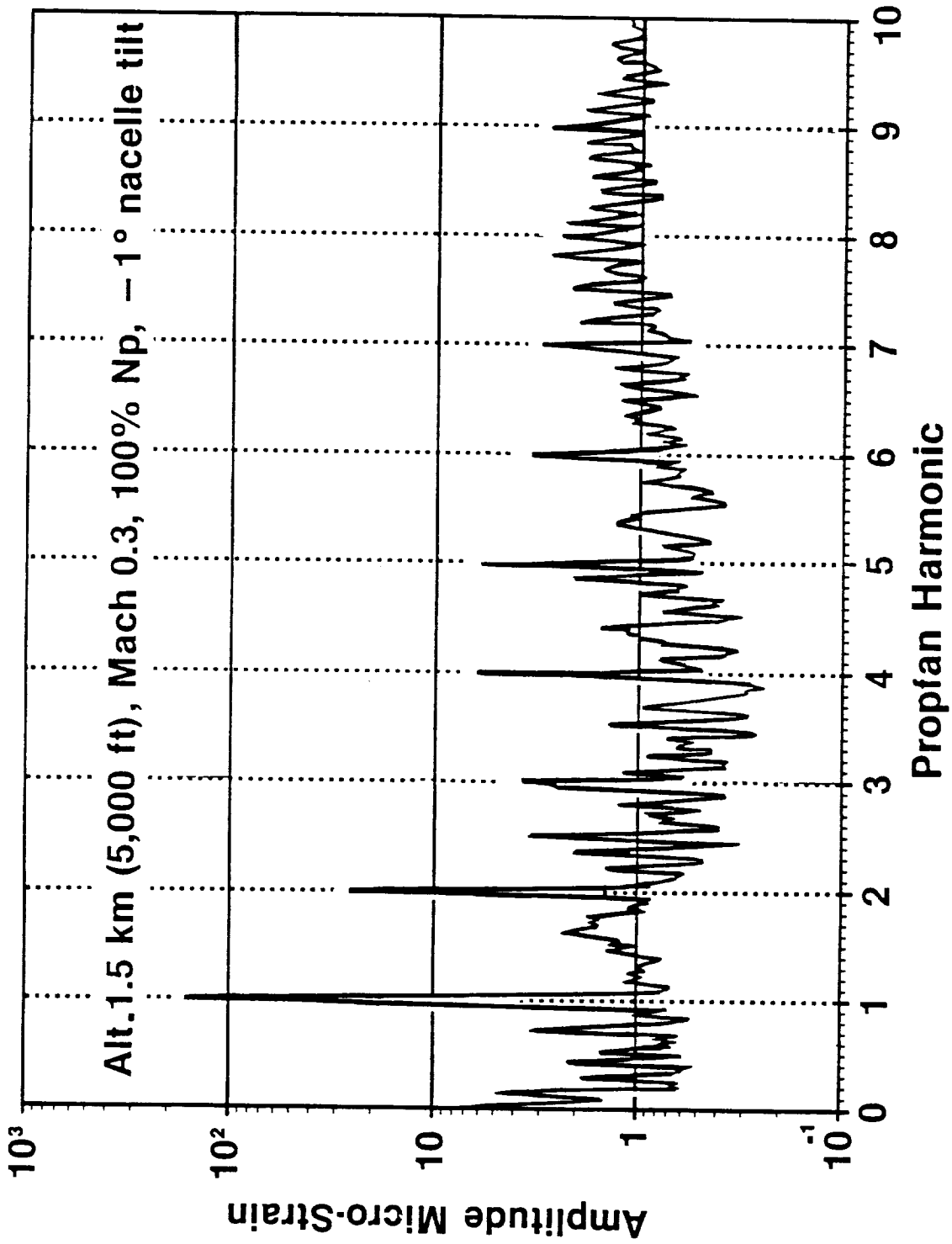


Figure 41. Typical Frequency Spectrum for an Inboard Bending Strain Gage

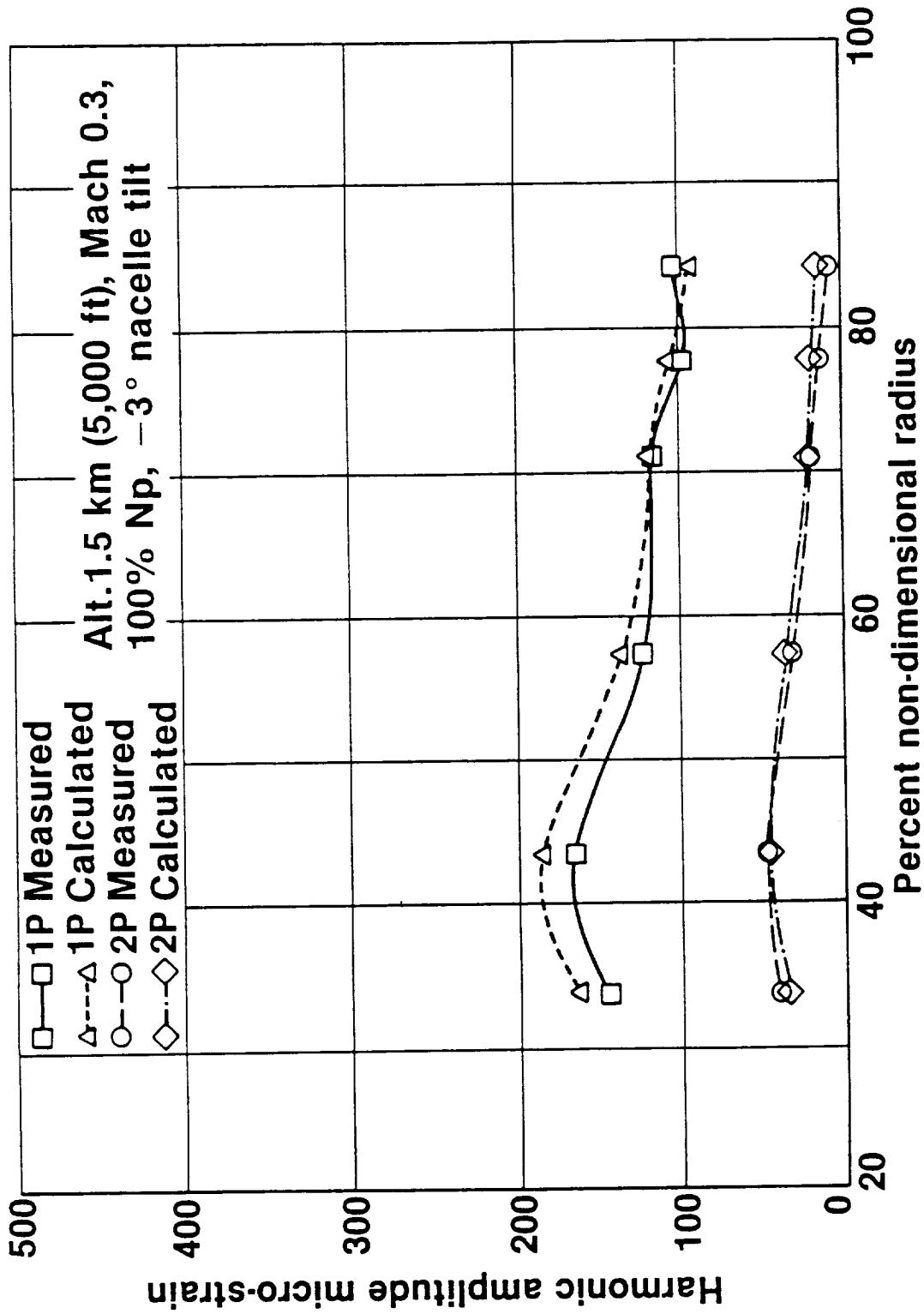


Figure 42. Radial Distribution of Calculated and Measured 1P and 2P Strain at -3° Nacelle Tilt

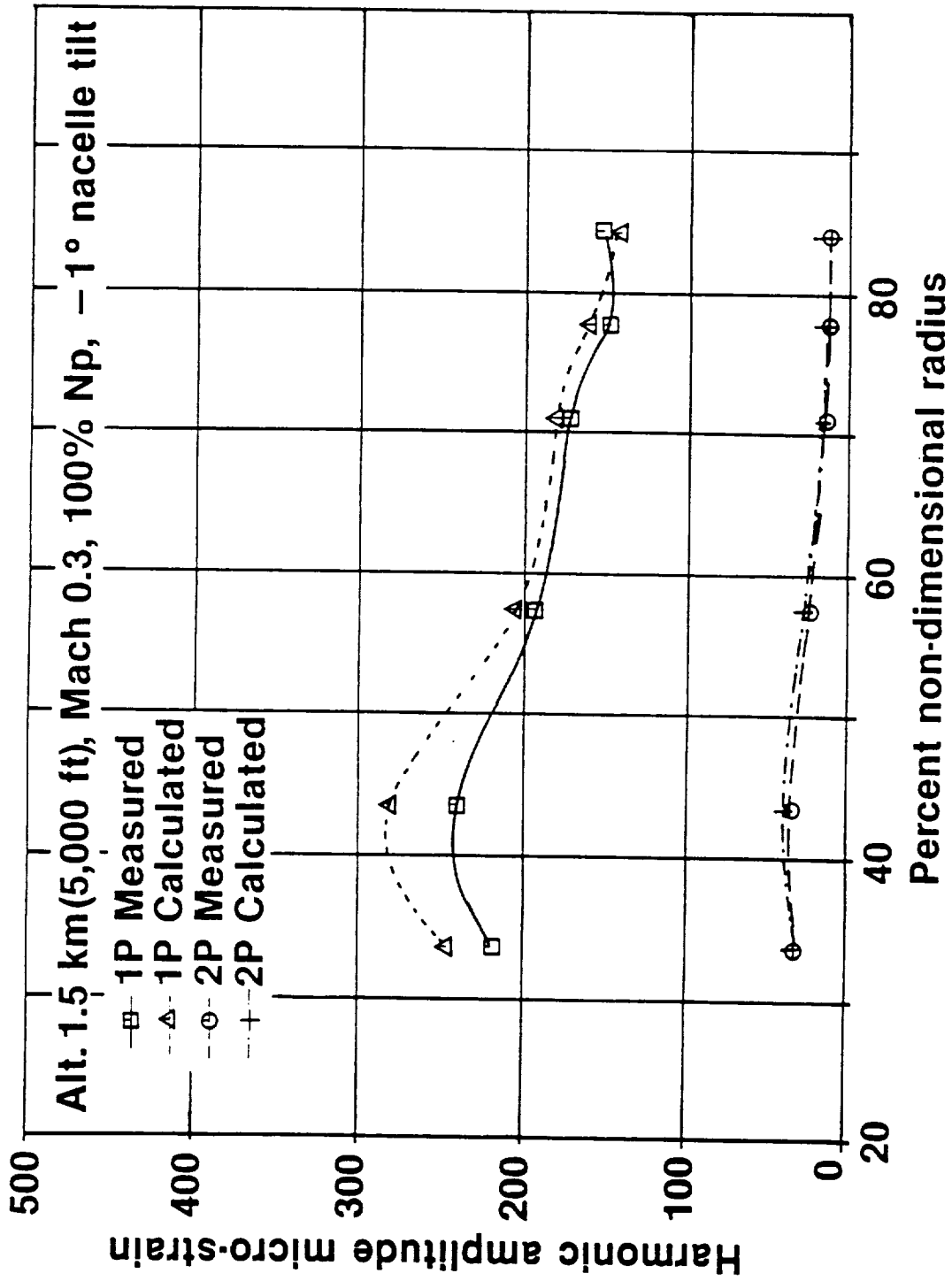


Figure 43. Radial Distribution of Calculated and Measured IP and 2P Strain at -1° Nacelle Tilt

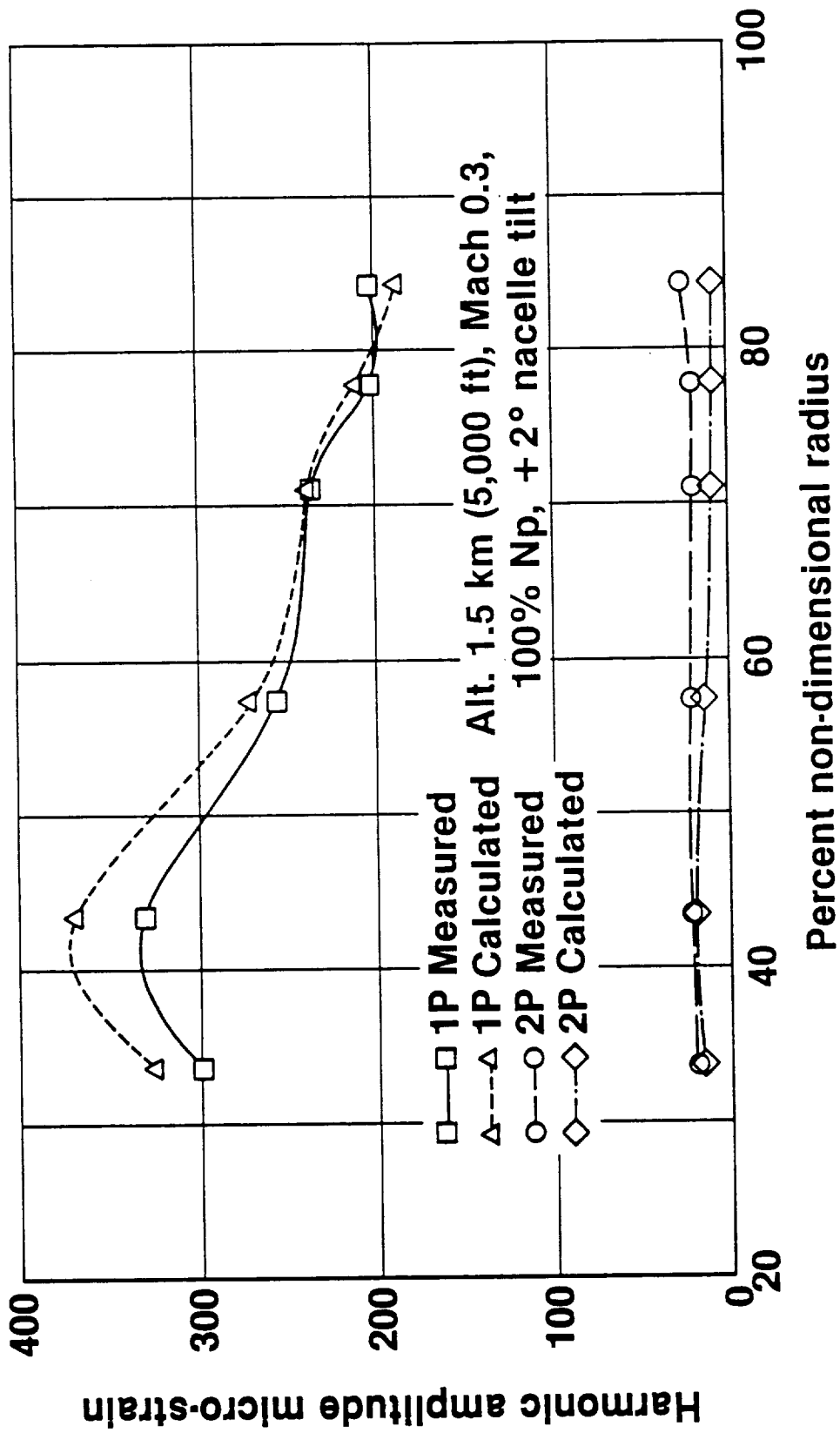


Figure 44. Radial Distribution of Calculated and Measured 1P and 2P Strain at +2° Nacelle Tilt

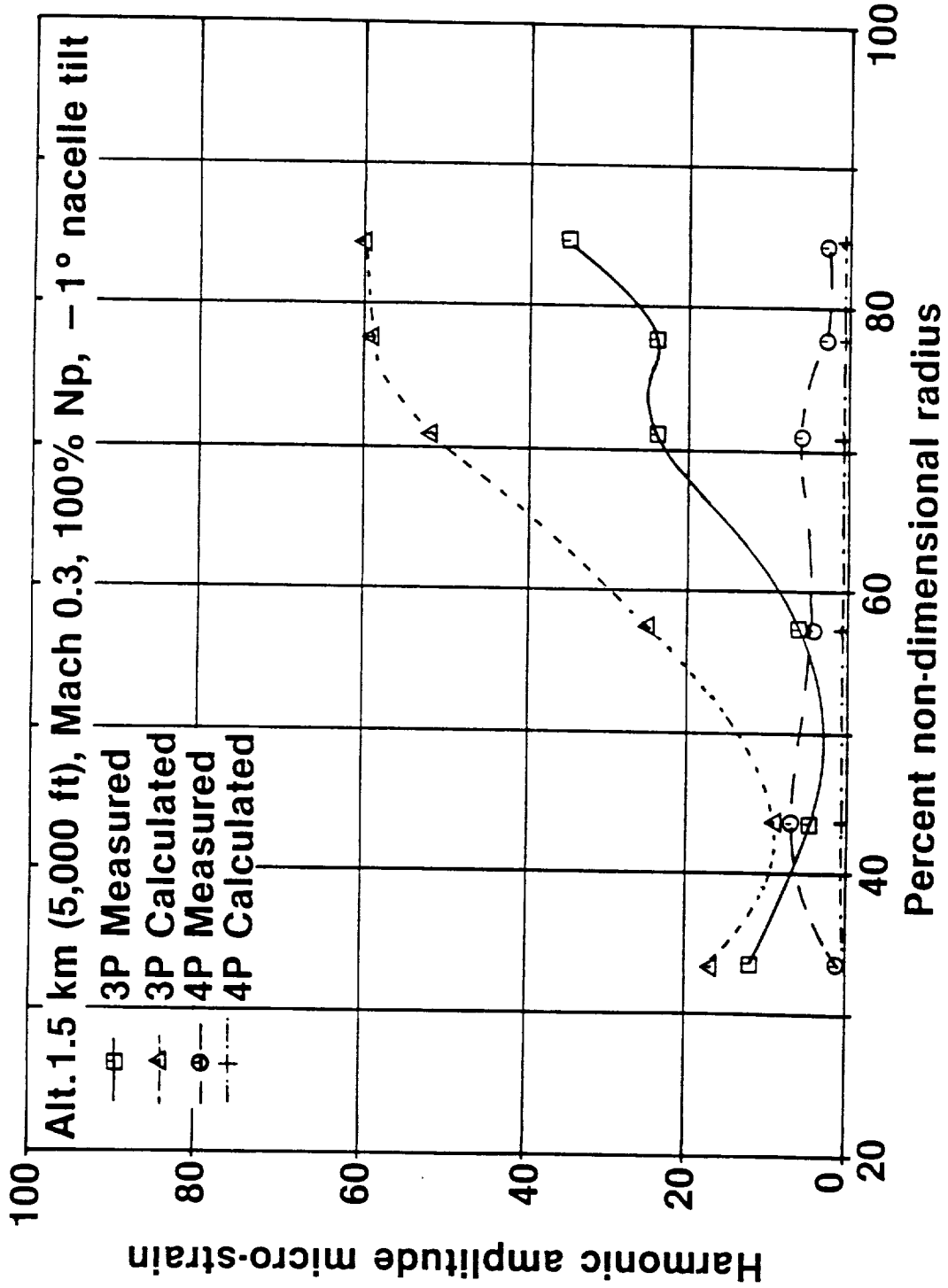


Figure 45. Radial Distribution of Calculated and Measured 3P and 4P Strain at -1° Nacelle Tilt

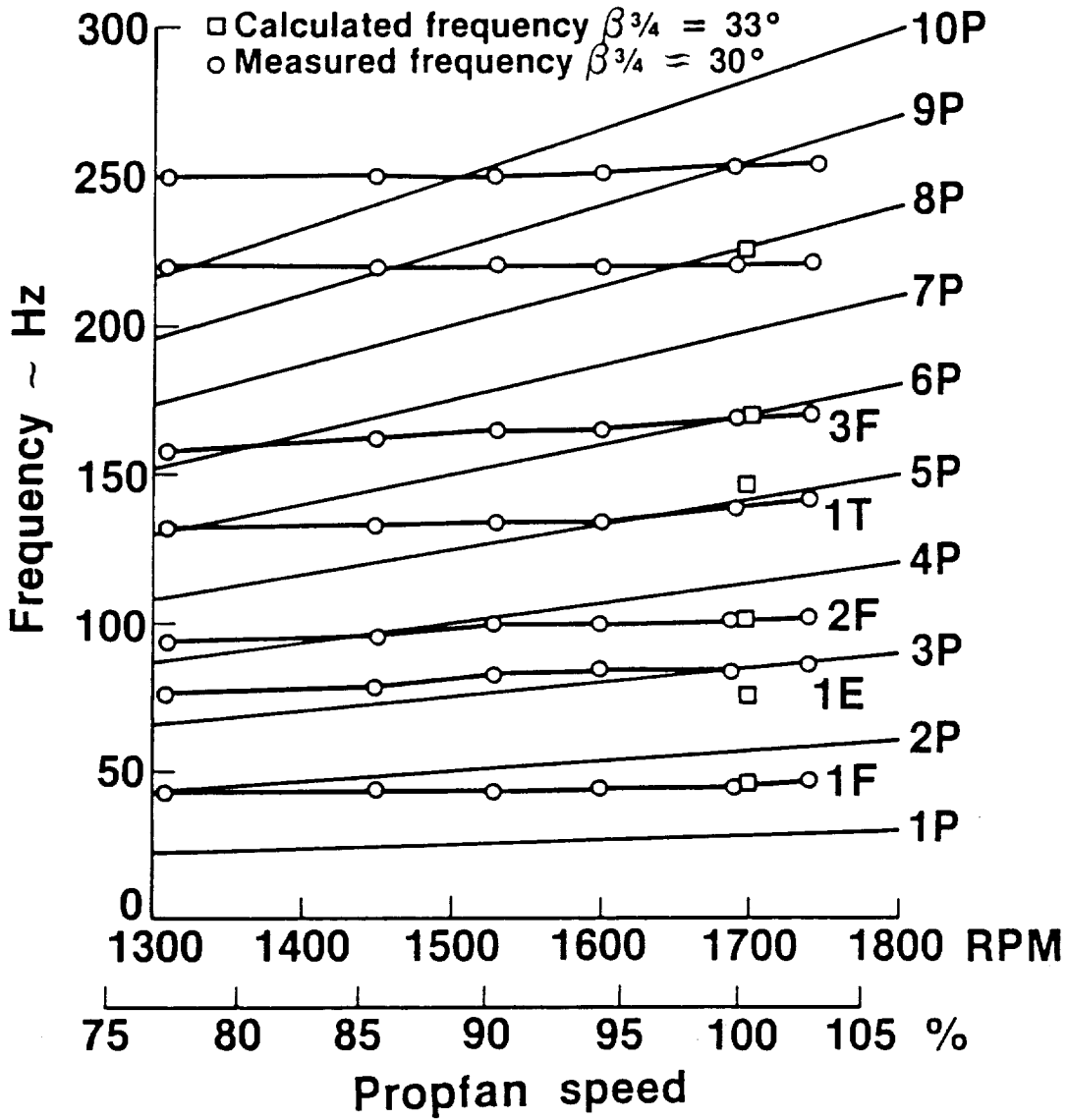


Figure 46. SR-7L Blade Natural Frequencies

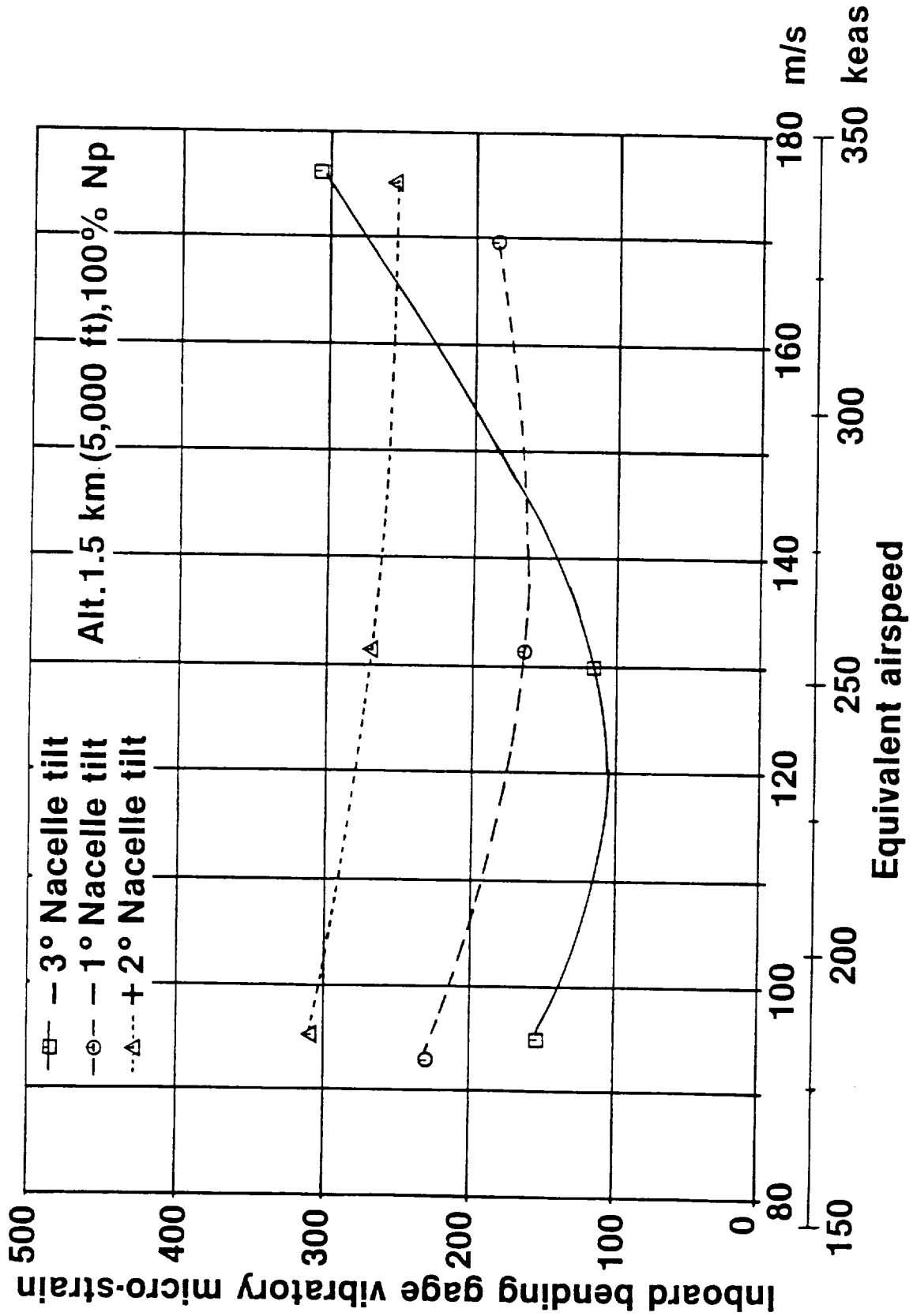


Figure 47. Effect of Equivalent Airspeed on Propfan Response at Low Altitude

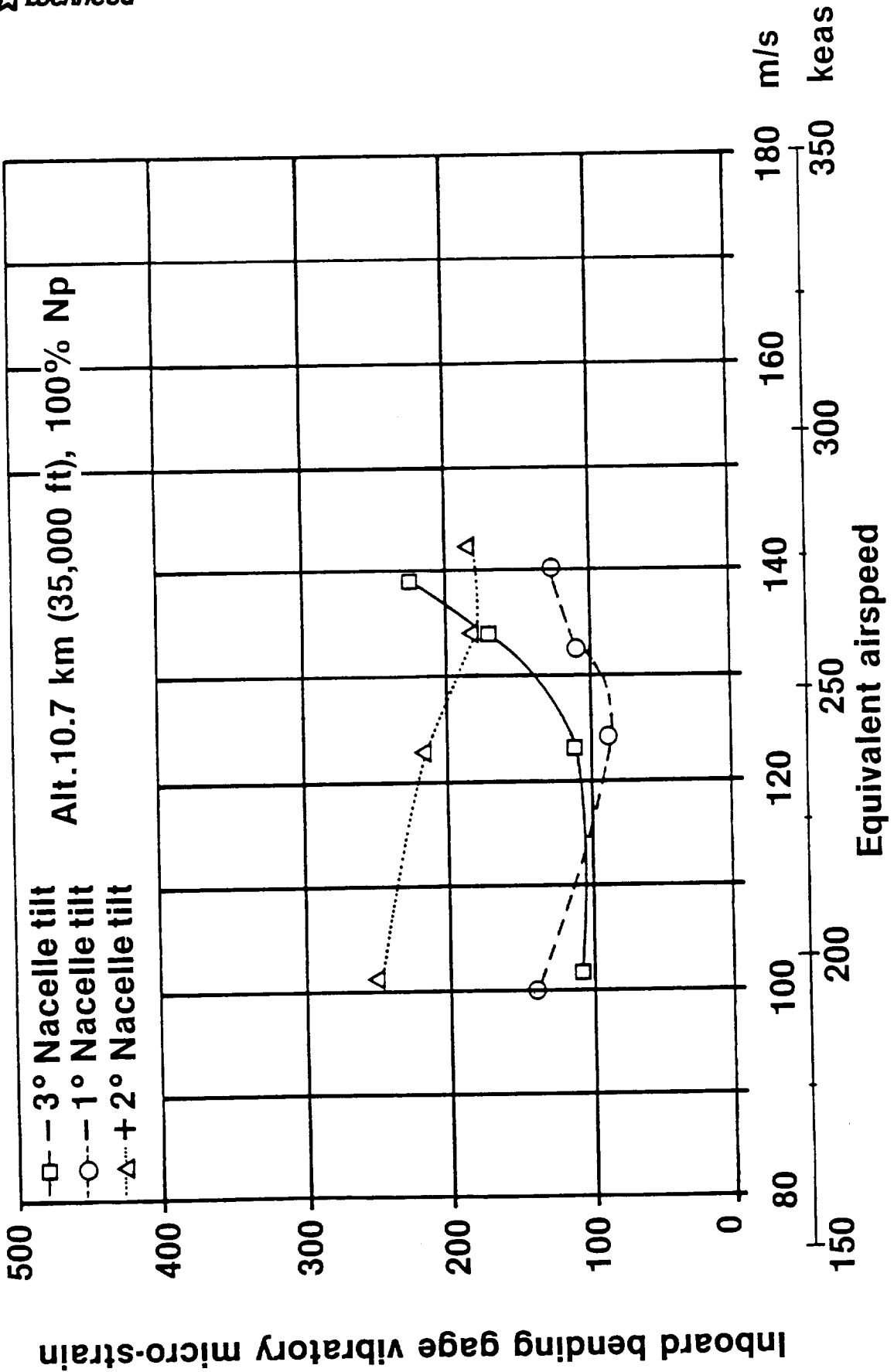


Figure 48. Effect of Equivalent Airspeed on Propfan Response at High Altitude

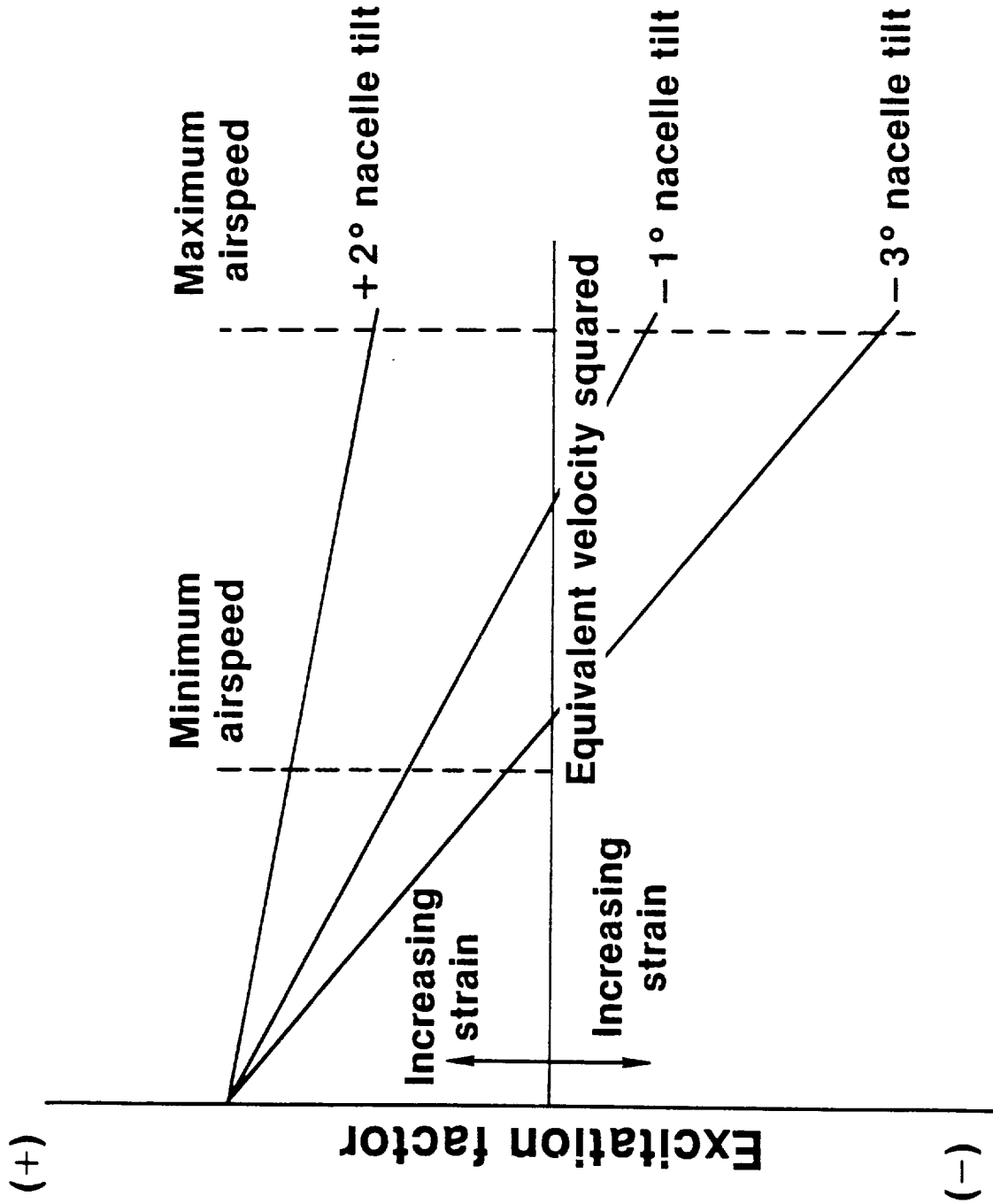


Figure 49. Propfan Relative Excitation Factor

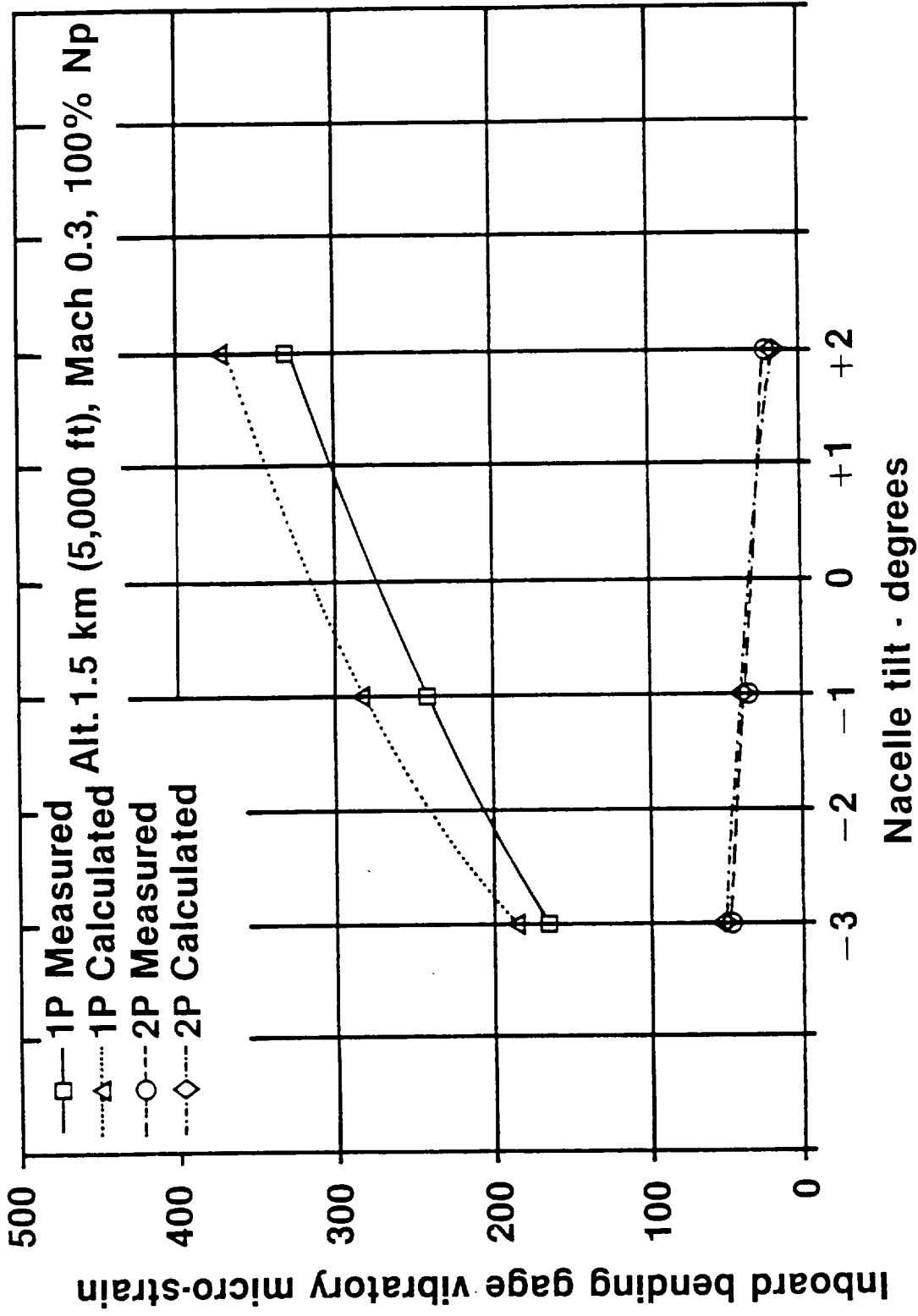


Figure 50. Effect of Nacelle Tilt on Propfan Response at Low Speed

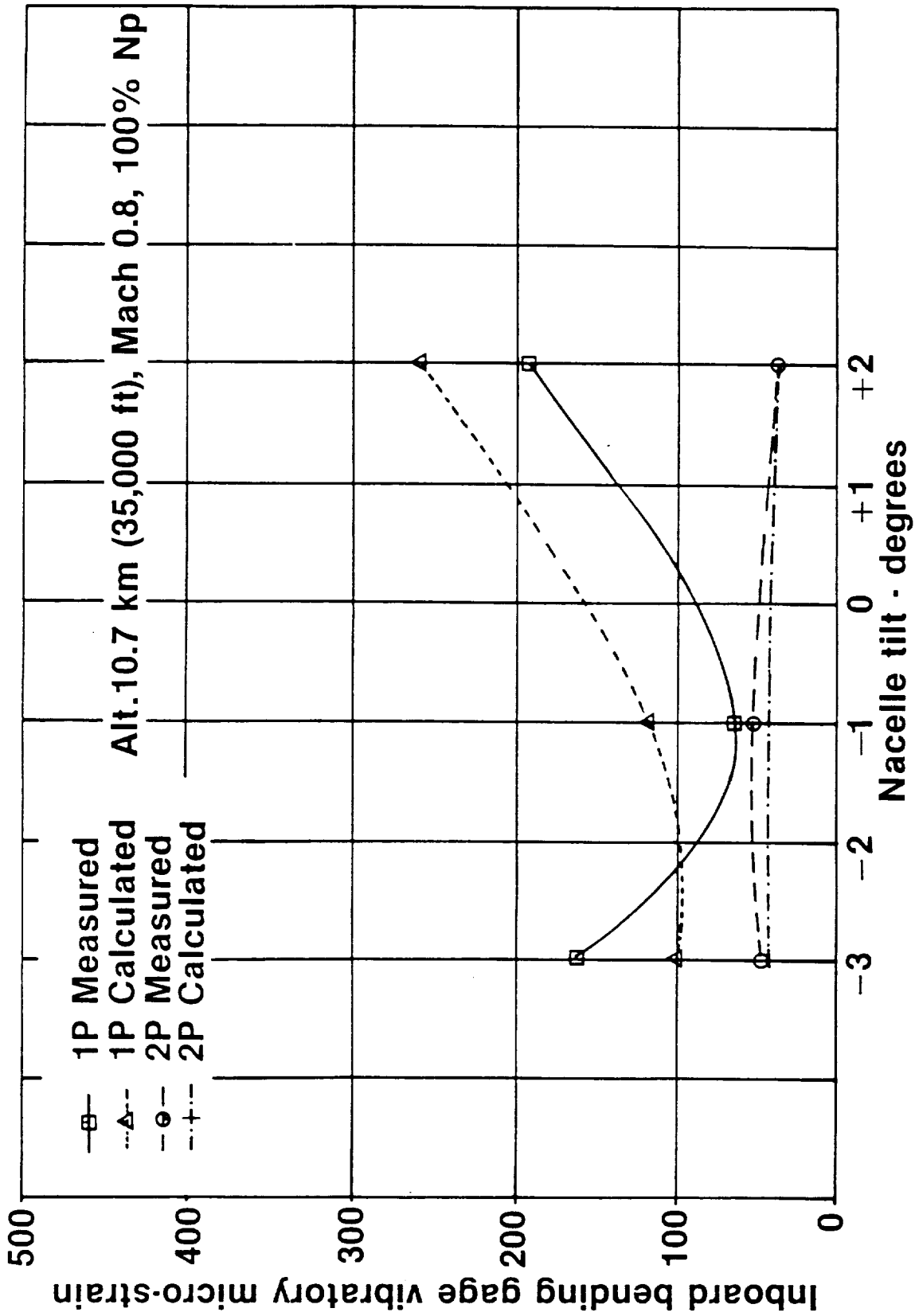


Figure 51. Effect of Nacelle Tilt on Propfan Response at High Speed

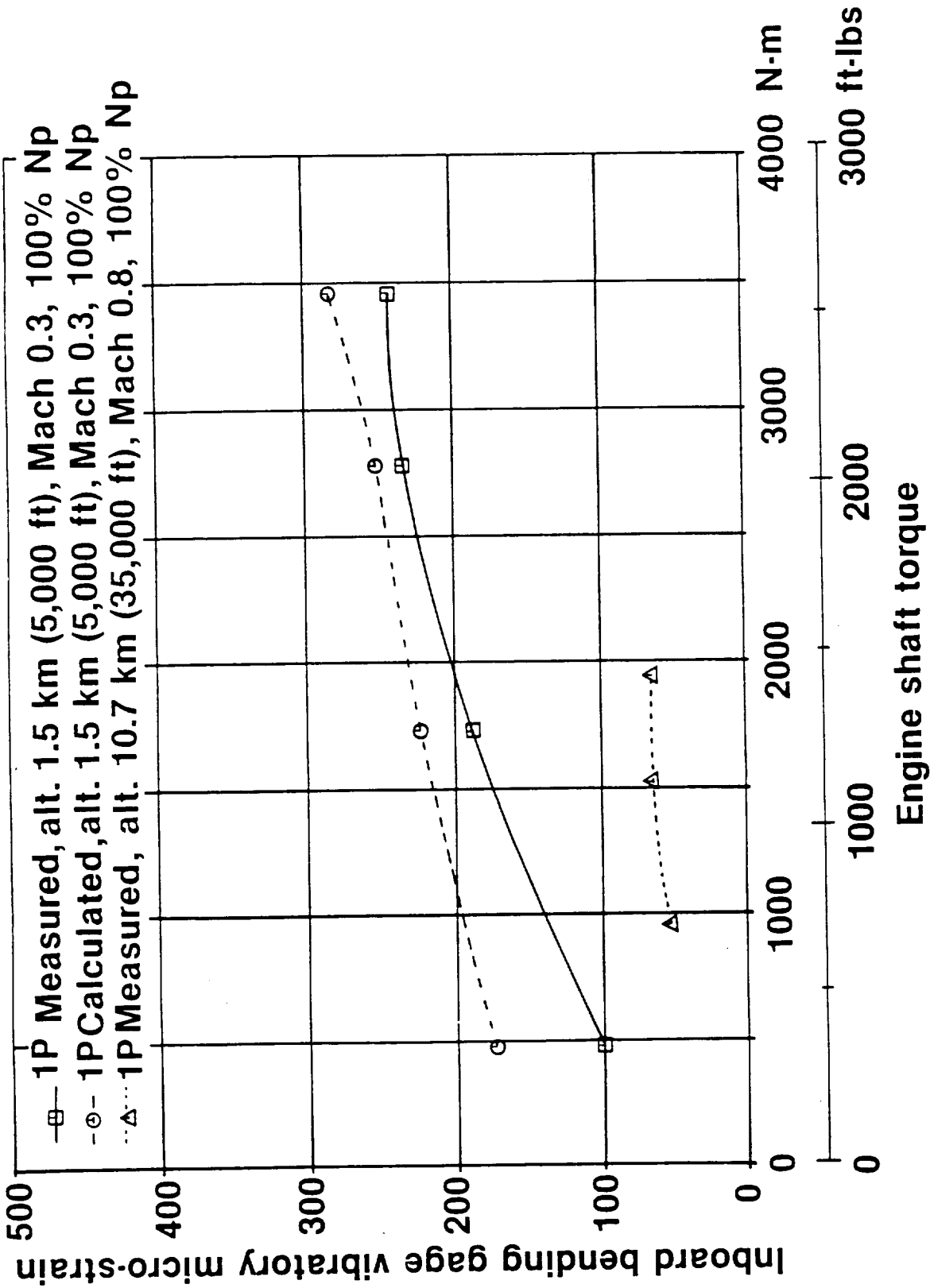


Figure 52. Effect of Torque on Propfan Response

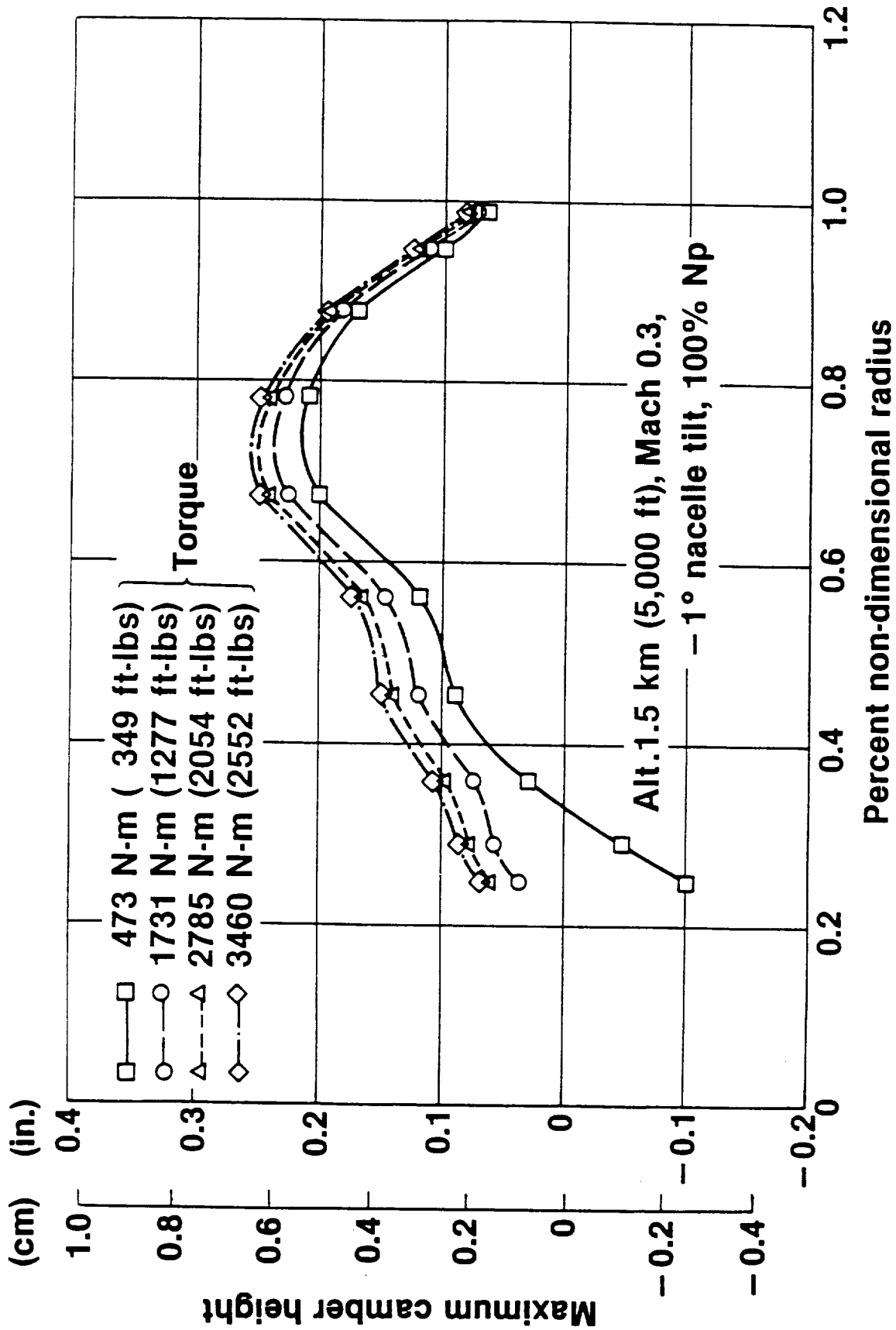


Figure 53. Calculated Camber Change with Torque

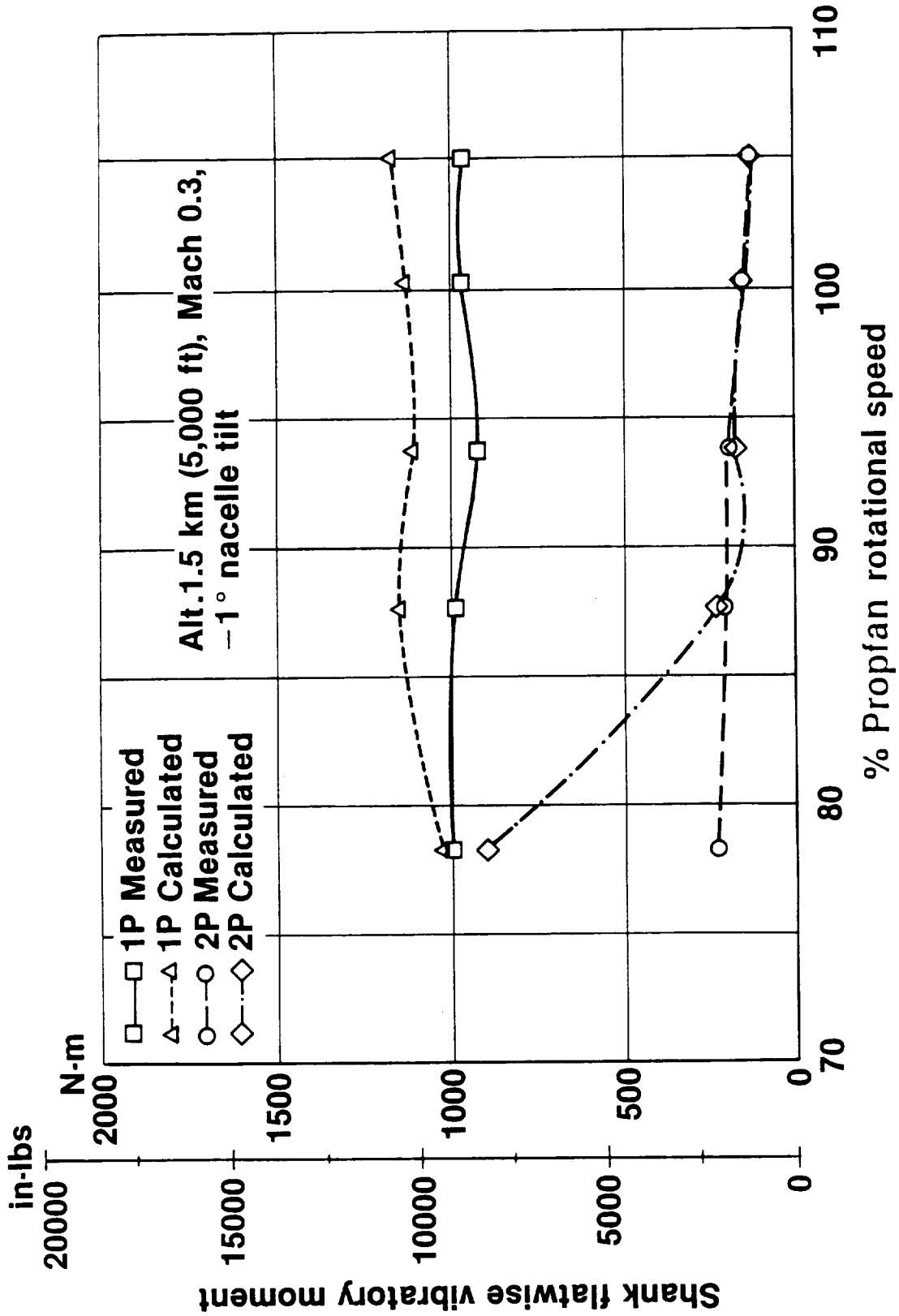


Figure 54. Effect of Rotational Speed on Propfan 1P and 2P Shank Flatwise Response at Low-Speed Conditions

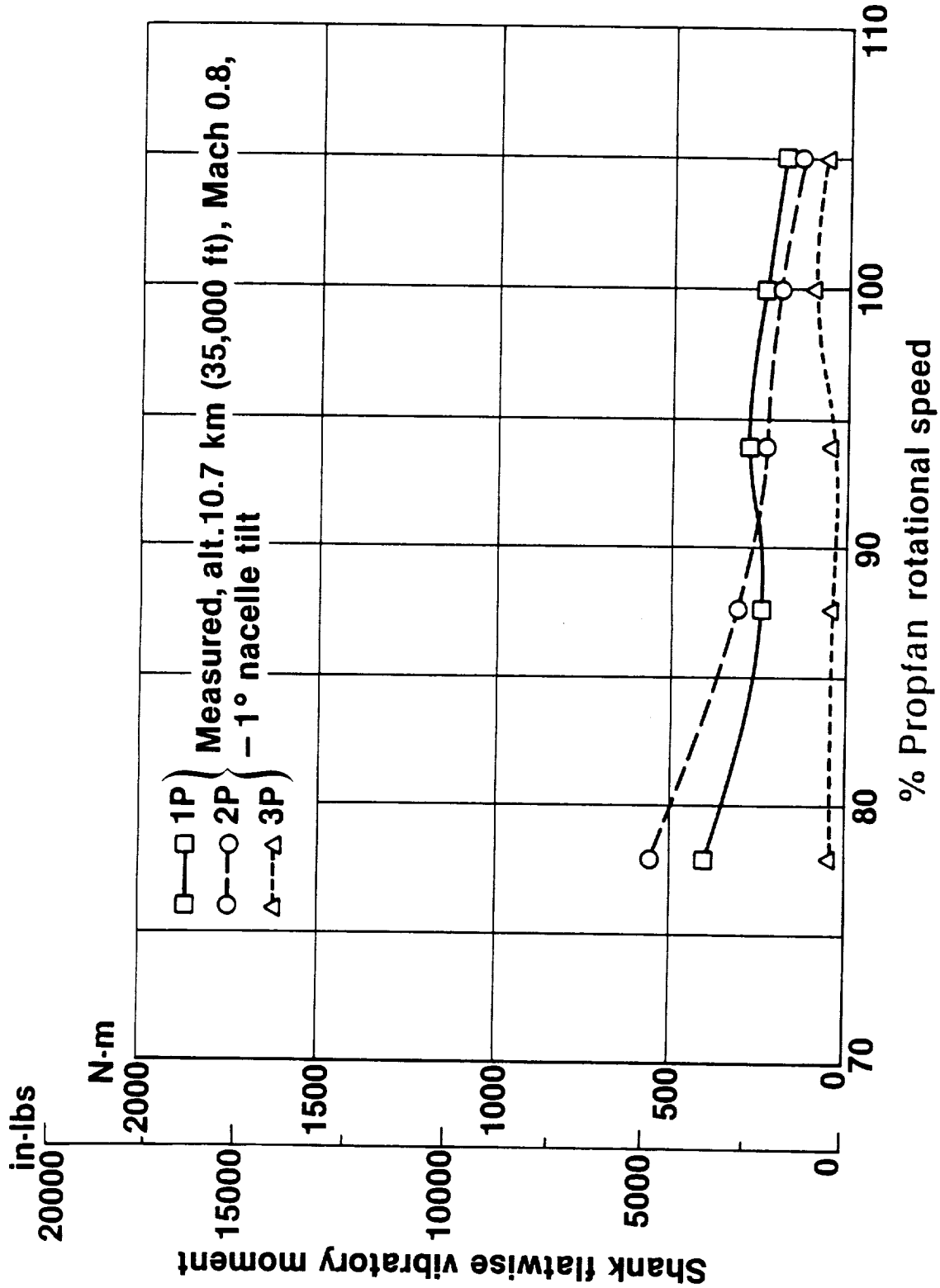


Figure 55. Effect of Rotational Speed on Propfan 1P and 2P Response at High-Speed Conditions

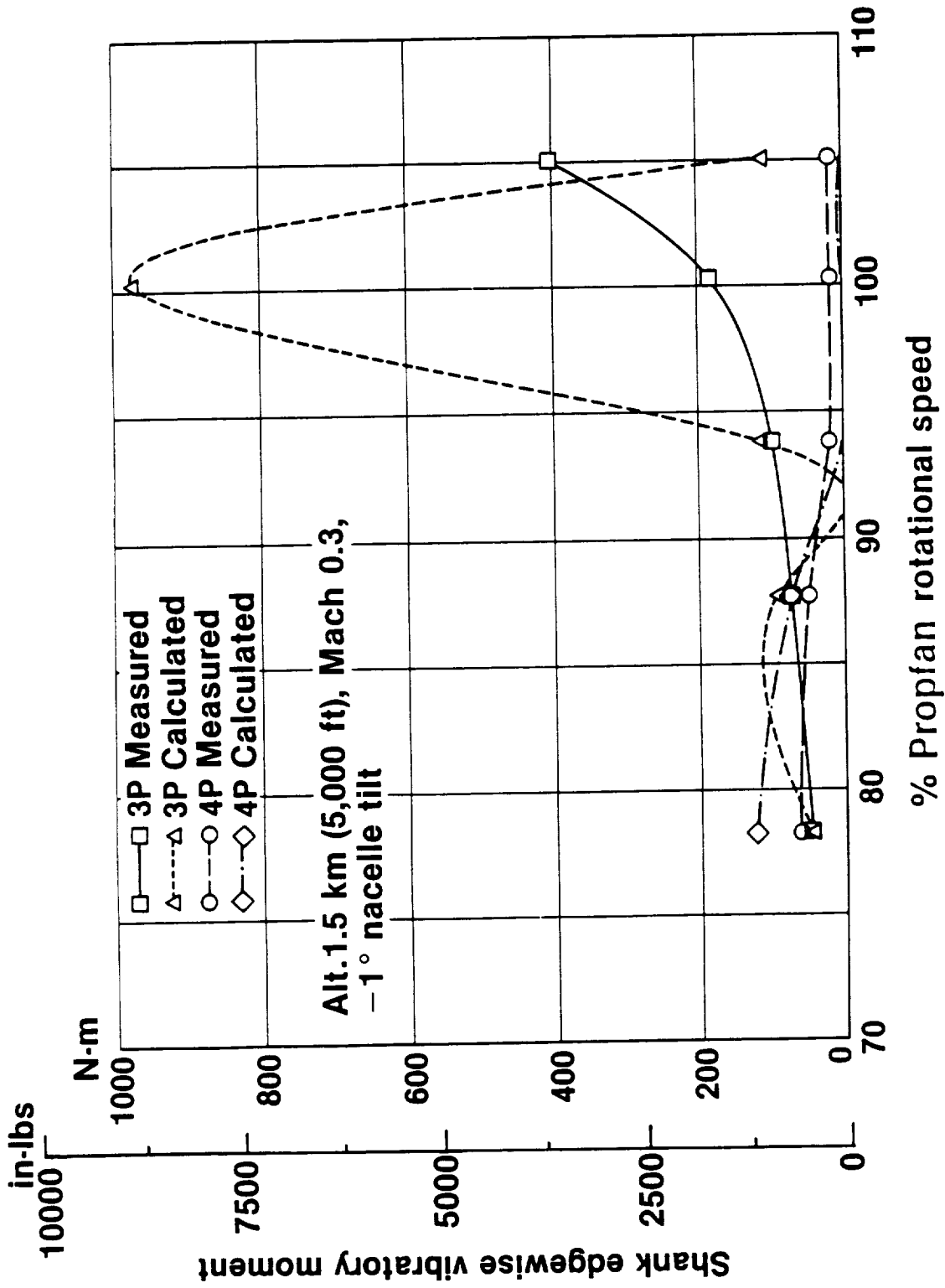


Figure 56. Effect of Rotational Speed on Propfan 3P and 4P Shank Edgewise Response

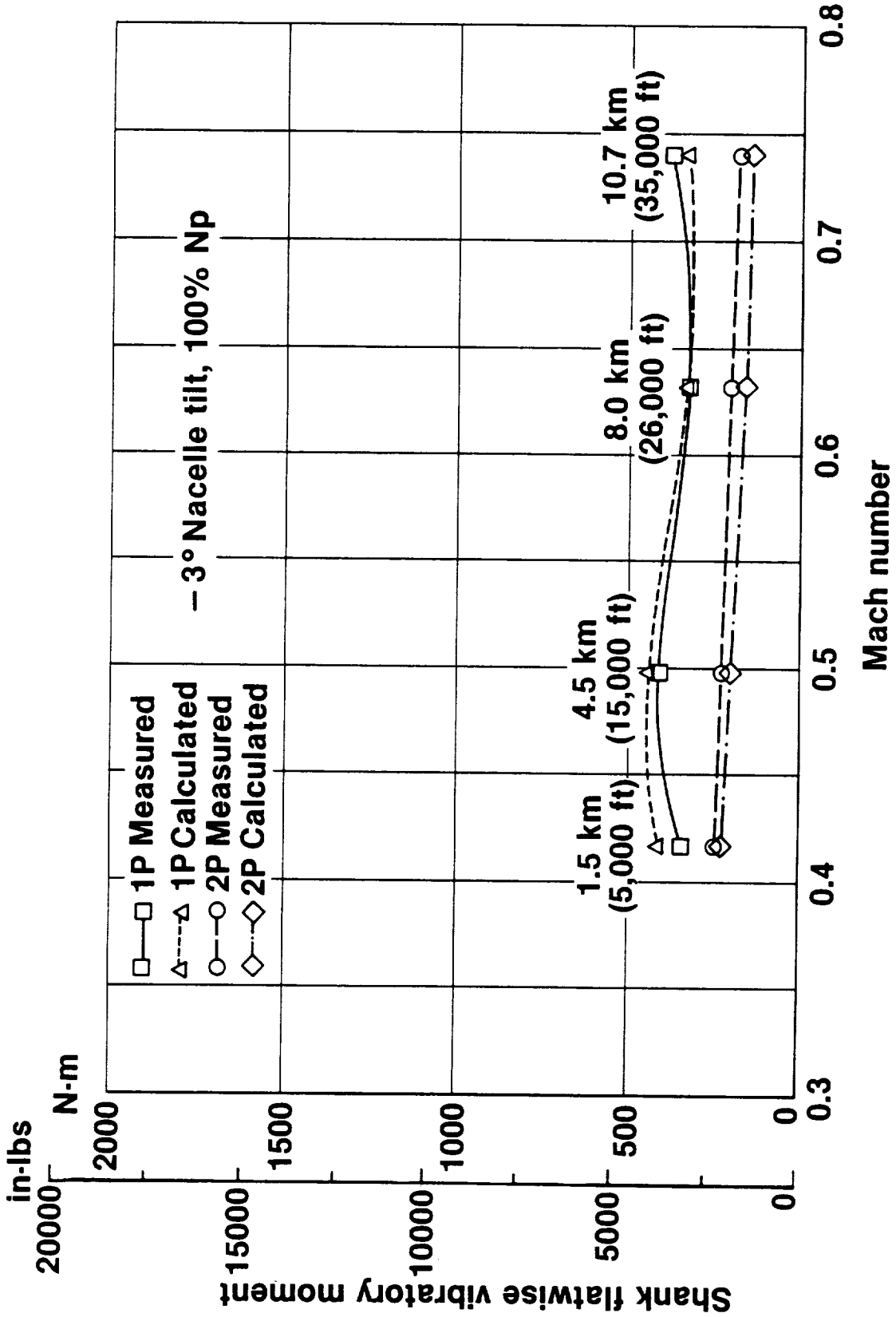


Figure 57. Effect of Mach Number on Propfan Response at a Constant Airspeed of 126 mps (250 KEAS)

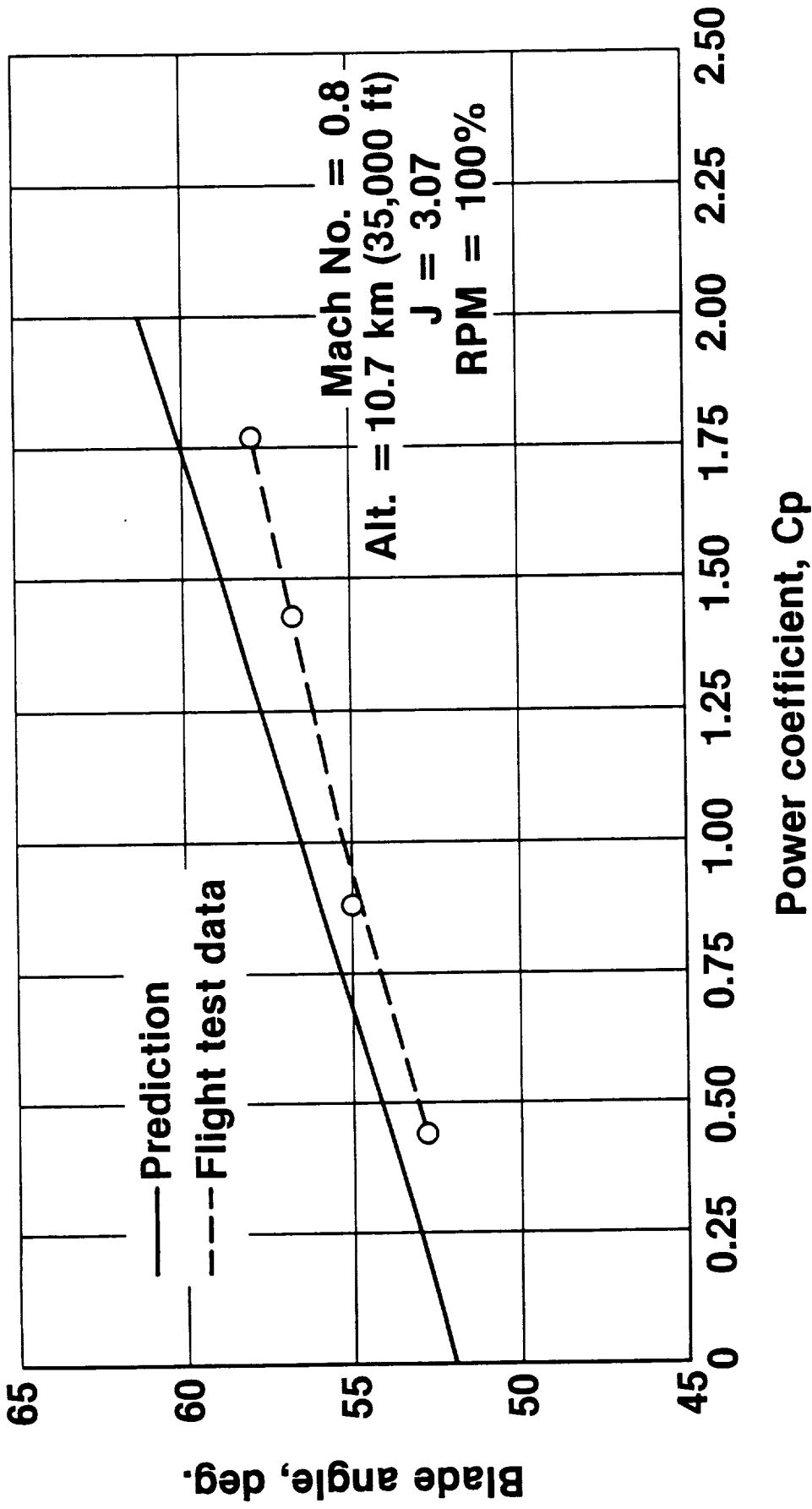


Figure 58. Comparison of Measured and Predicted Performance, Mach 0.8, J = 3.07

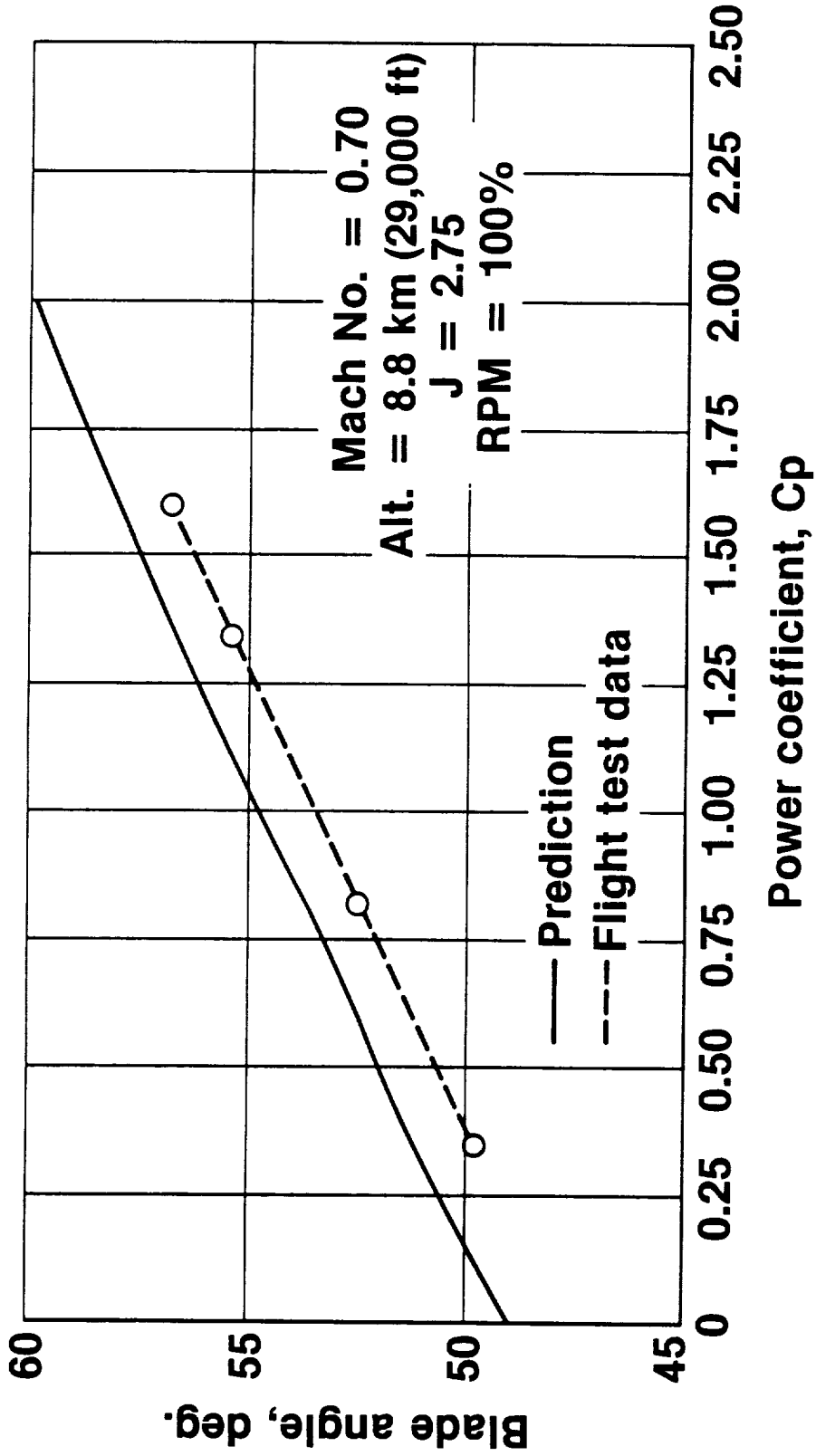


Figure 59. Comparison of Measured and Predicted Performance, Mach 0.7, J = 2.75

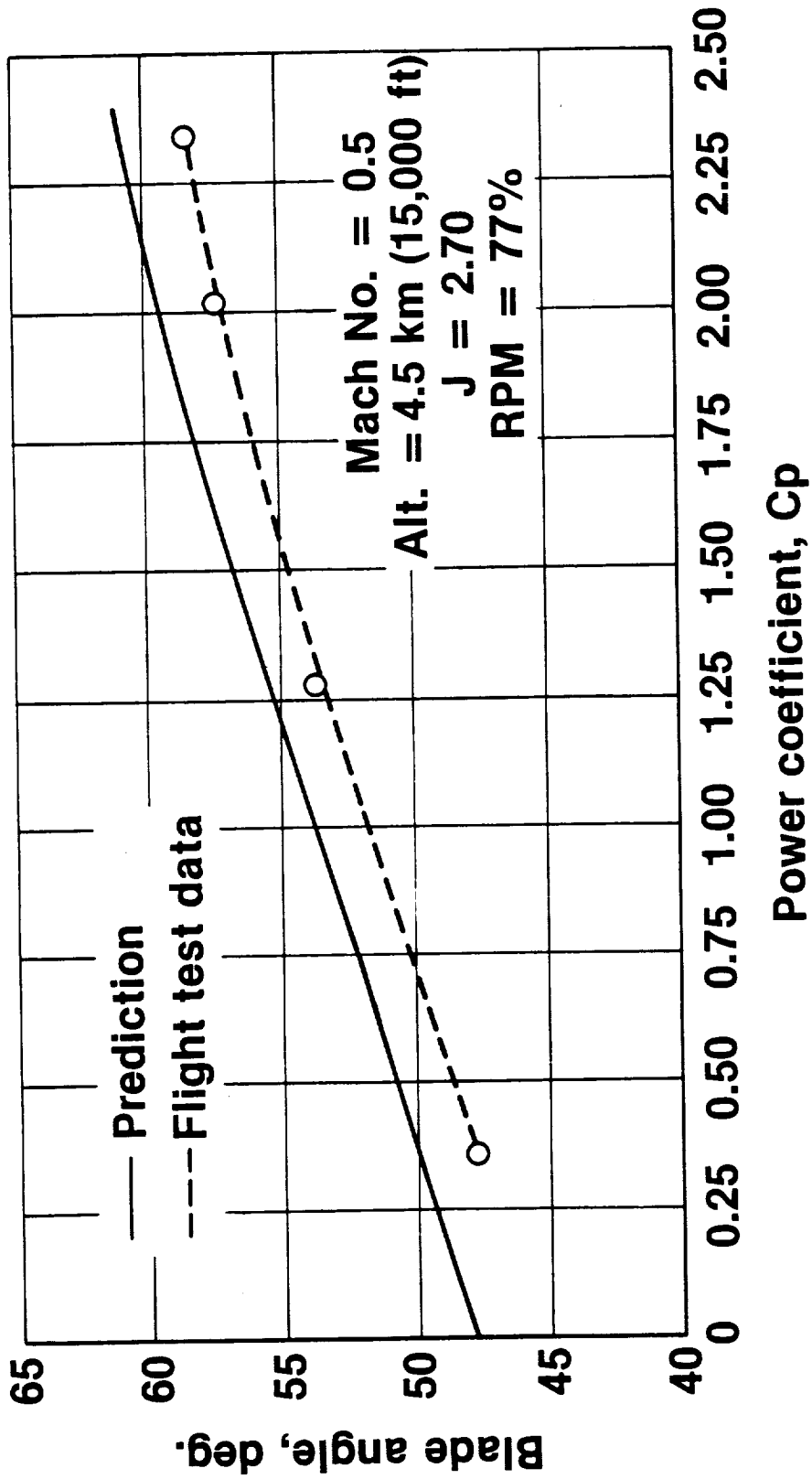


Figure 60. Comparison of Measured and Predicted Performance, Mach 0.5, J = 2.70

ALTITUDE AGL	SPEY ENGINE POWER
305 m (1000 ft)	MINIMUM POWER FOR LEVEL FLIGHT
305 m (1000 ft)	SOFT FLIGHT IDLE
396 m (1300 ft)	SOFT FLIGHT IDLE
488 m (1600 ft)	SOFT FLIGHT IDLE

Figure 61. Planned Nominal Low-Altitude Test Conditions,
Propfan Removed

NT - NACELLE TILT ANGLE
 α - ANGLE OF ATTACK
 β - SIDESLIP ANGLE

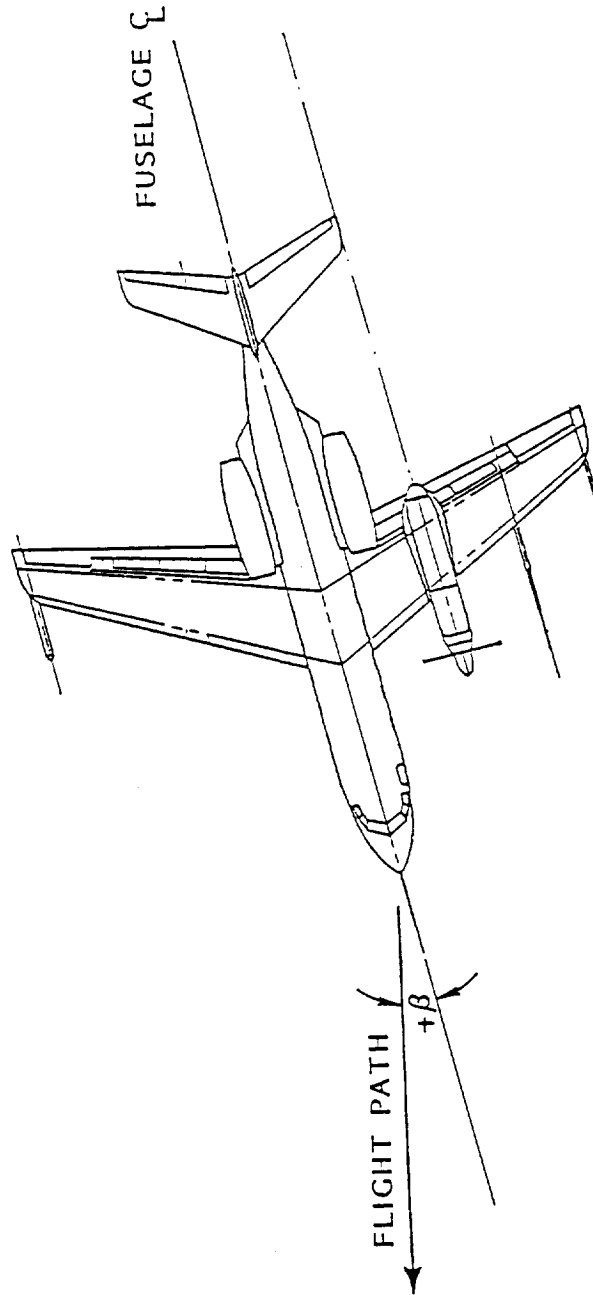
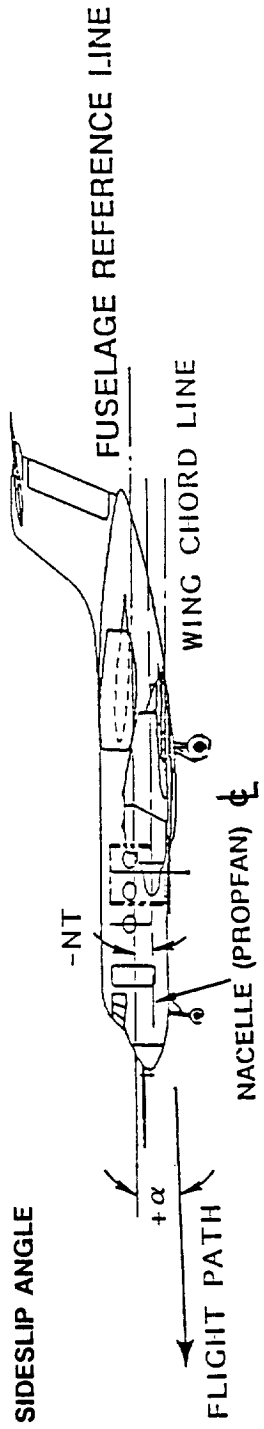


Figure 62. Illustration of Nacelle Tilt, Angle of Attack, and Sideslip Angle

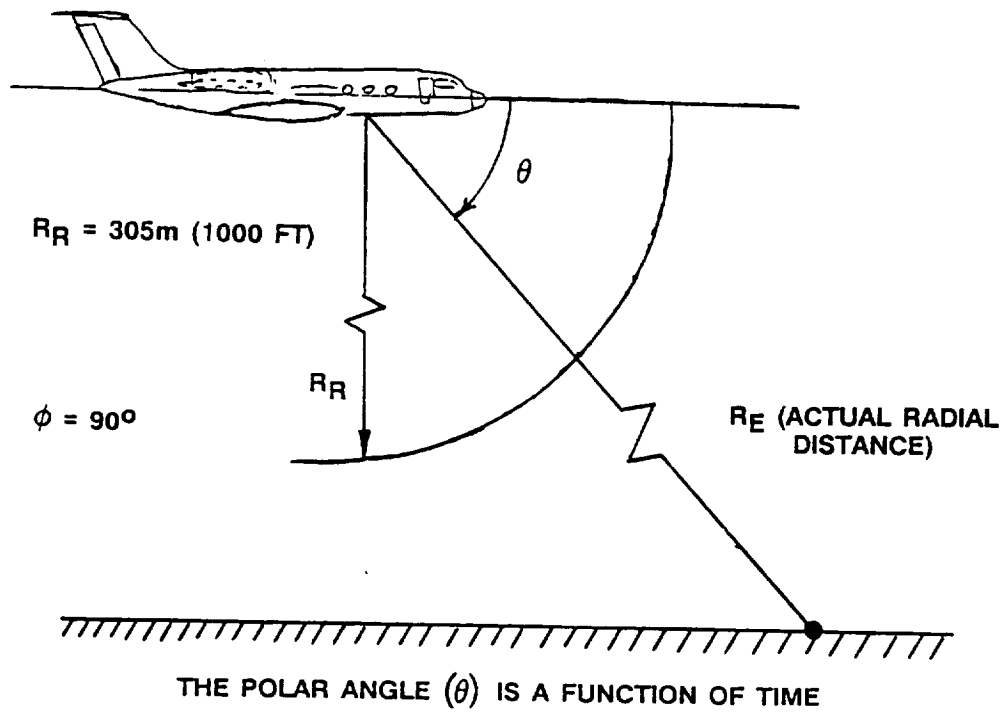
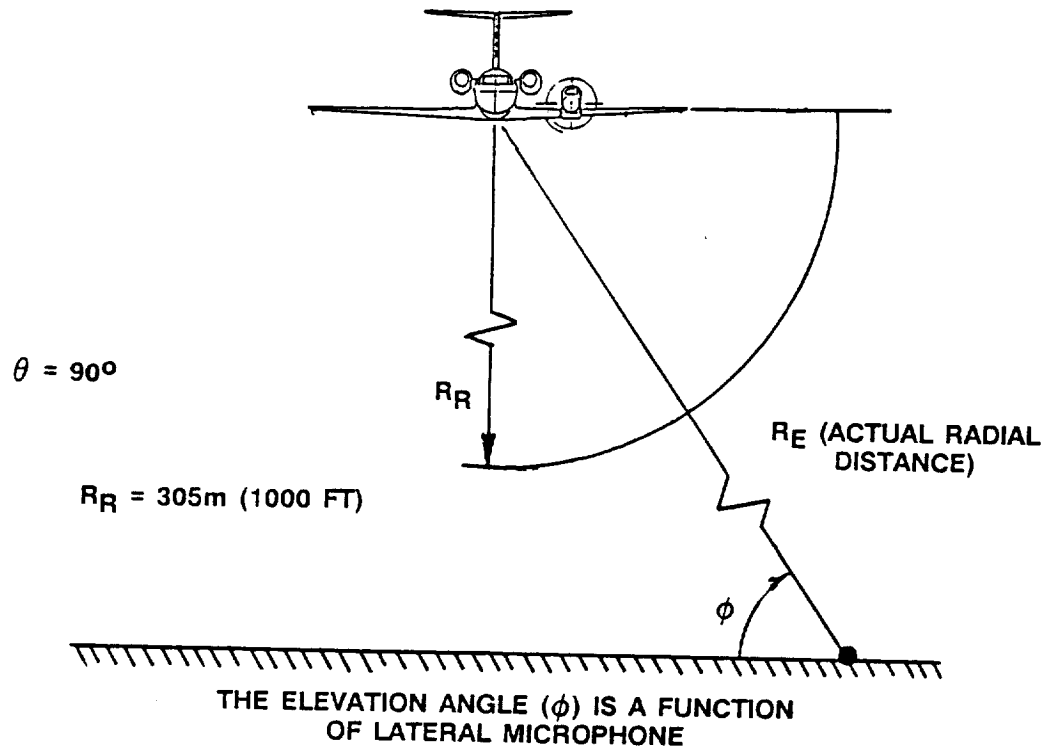


Figure 63. Coordinates for Normalized Lossless Data

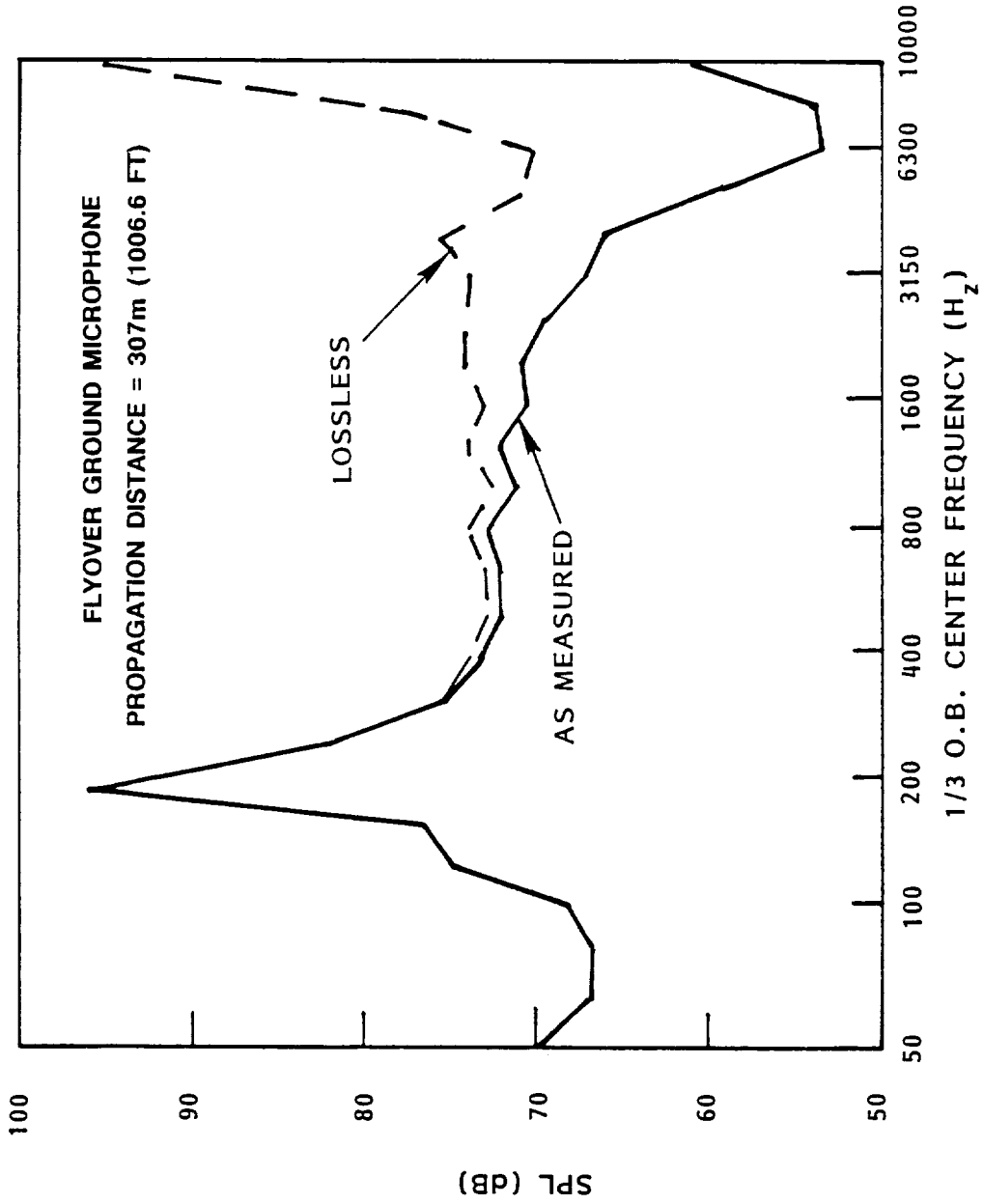


Figure 64. Illustration of Anomalous High Frequency Noise

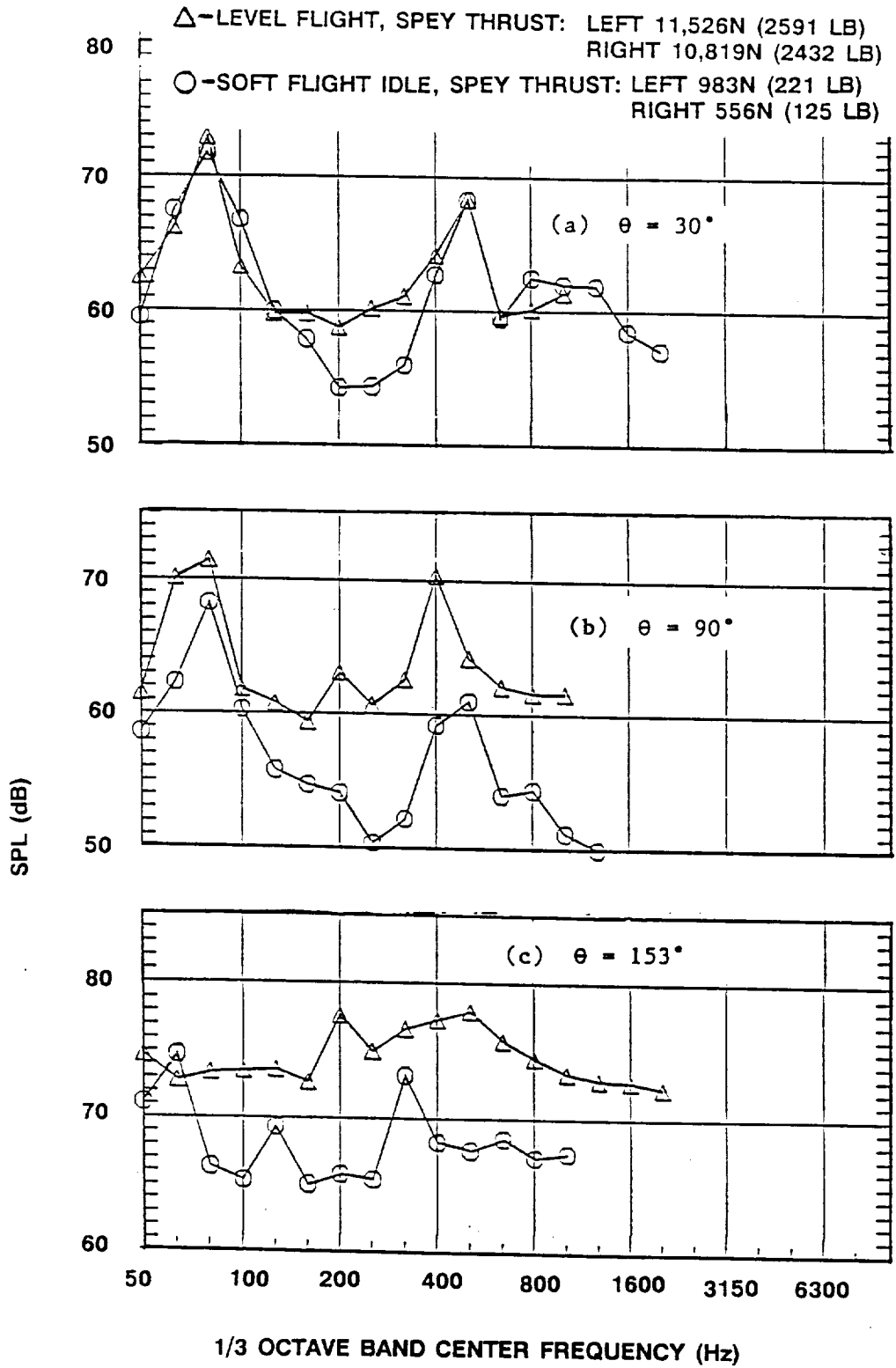


Figure 65. Effect of Spey Engine Thrust on Far-Field Noise - Propfan Blades Removed; Flyover Position at 305m (1000 ft) Radius

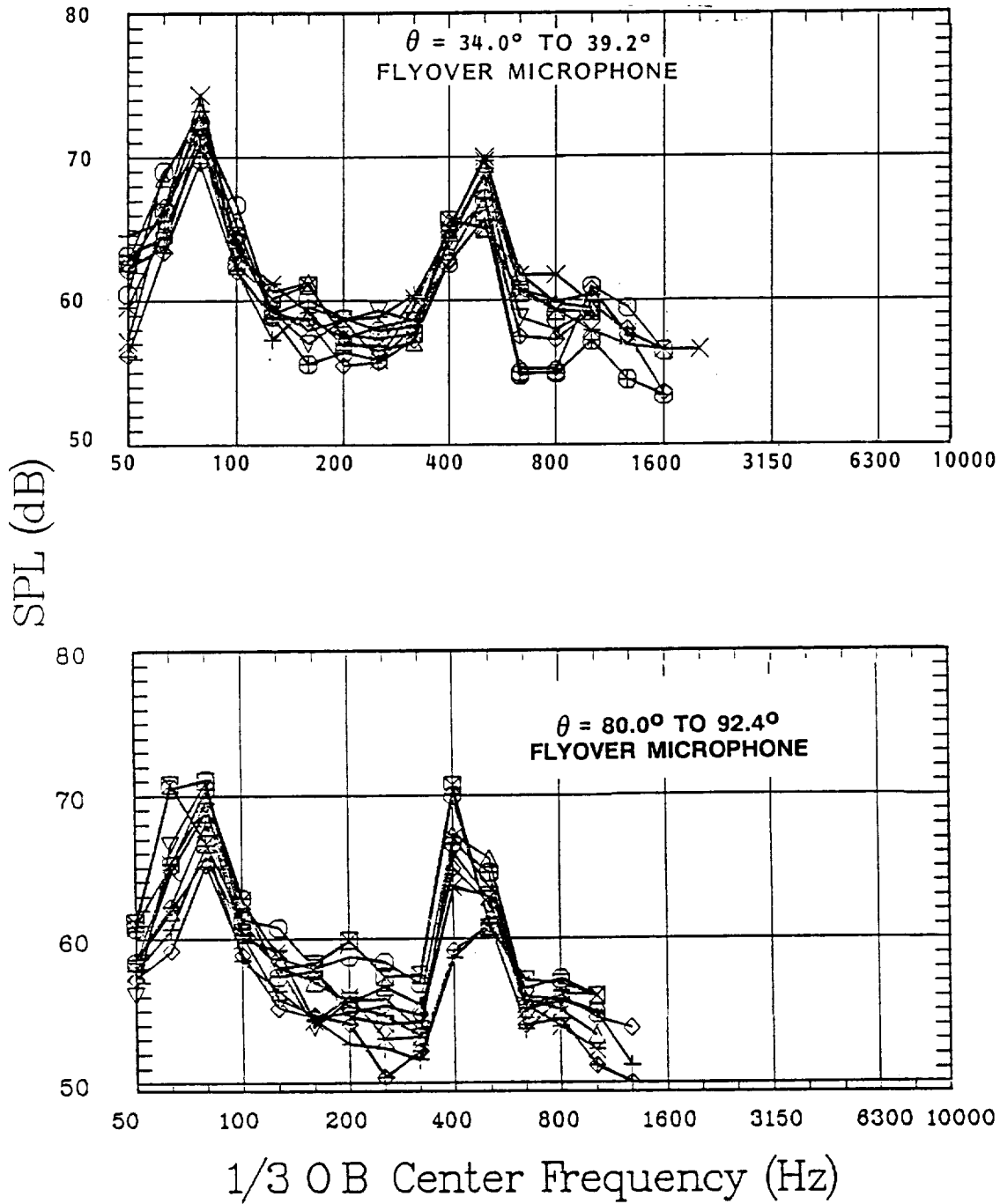


Figure 66. Noise Spectra With Propfan Blades Removed; Free-Field Lossless Data at 305m (1000 ft) Radius

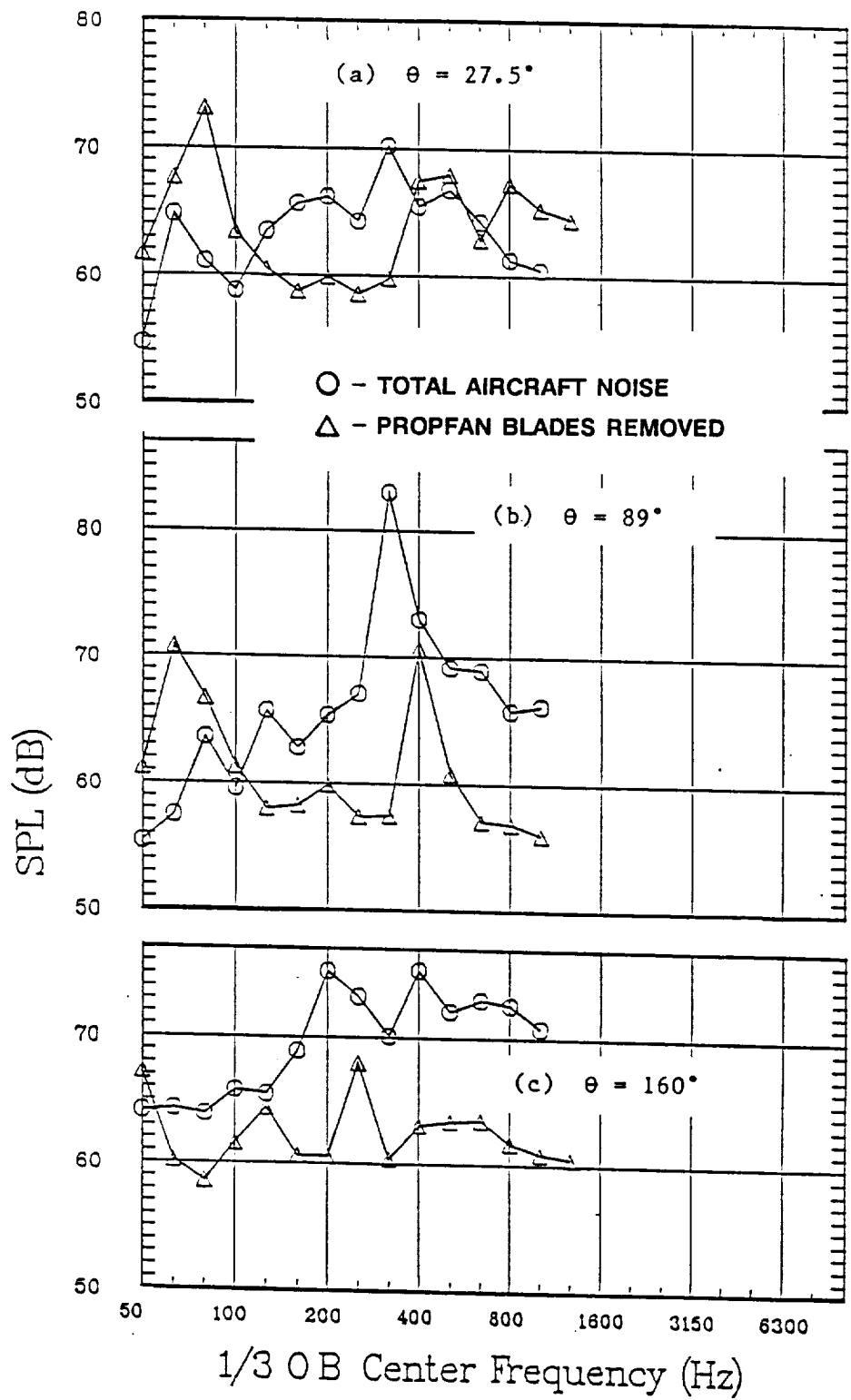


Figure 67. Comparison of 305m (1000 ft) Flyover Noise for Propfan Blades On and Off

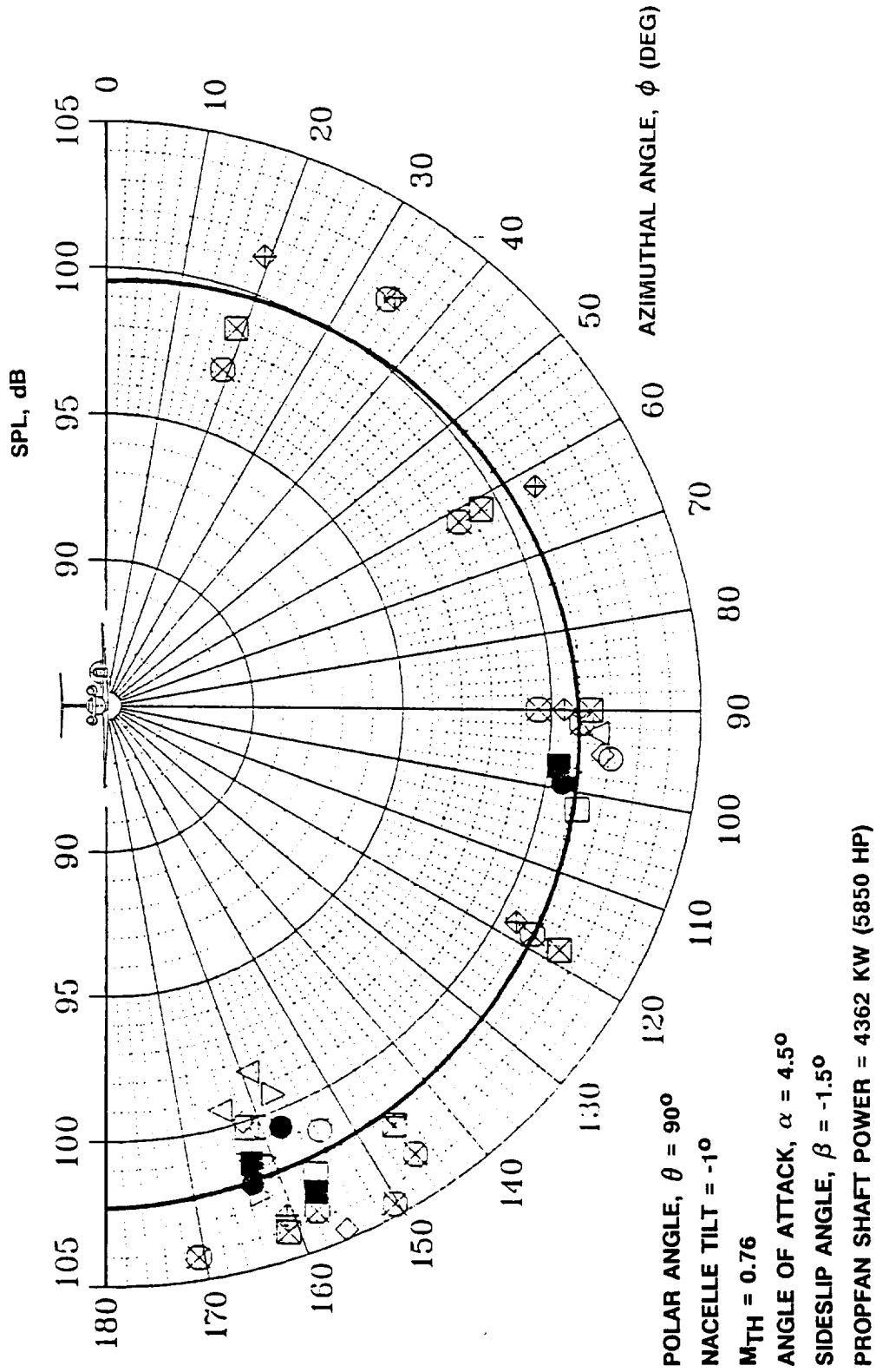


Figure 68. Lossless SPL Azimuthal Directivity at Blade Passing Frequency

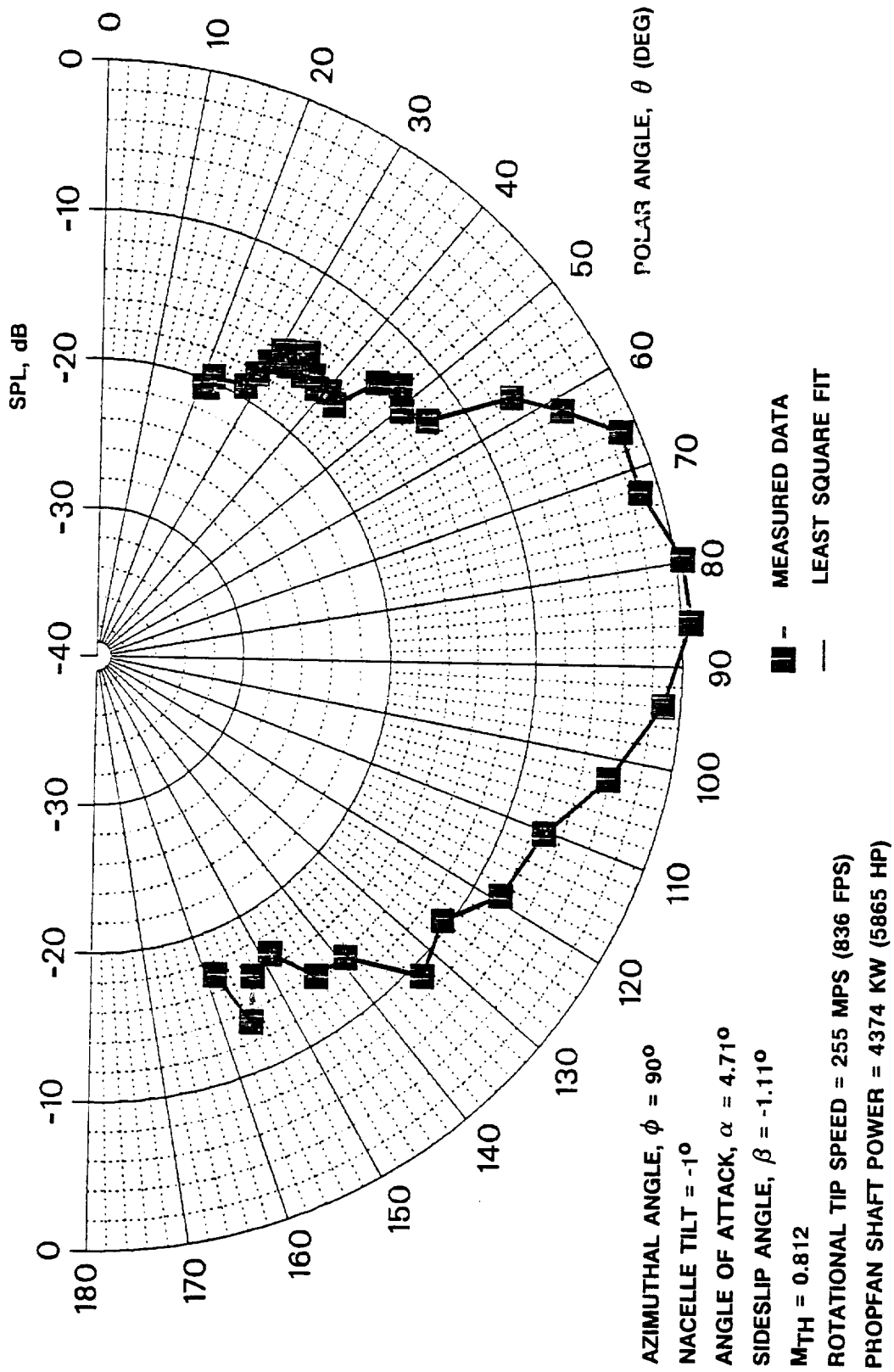


Figure 69. Lossless SPL Polar Directivity at Blade Passing Frequency

NACELLE TILT = -1°
 HELICAL M_{TIP} = 0.781 TO 0.791
 ROTATIONAL TIP SPEED = 244 MPS (800 FPS)
 ALTITUDE \approx 305m (1000 FT)
 ANGLE OF ATTACK, α = 4.3° TO 5.2°
 SIDESLIP ANGLE, β = -2.35° TO 2.15°

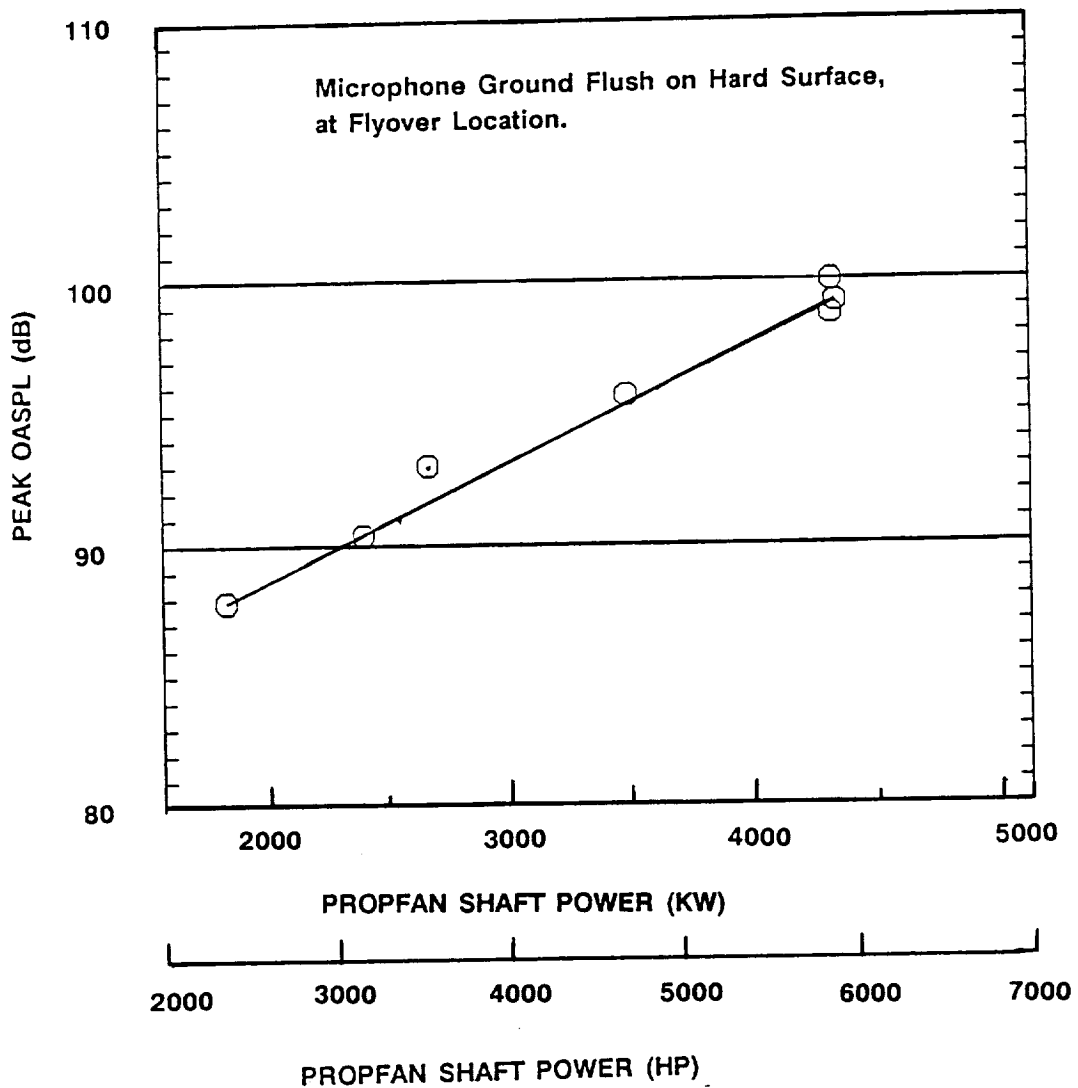


Figure 70. Variation of Noise With Propfan Power

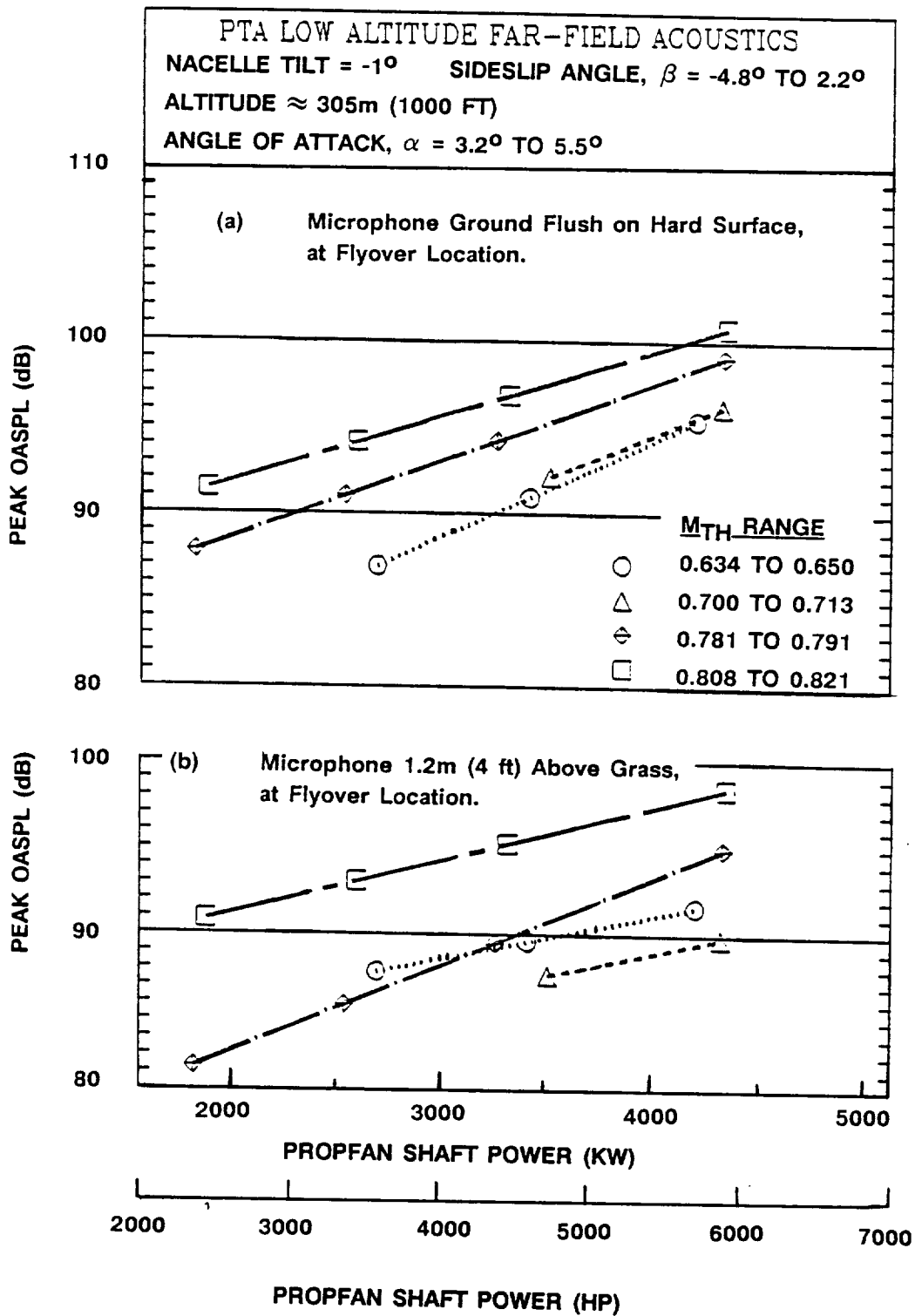


Figure 71. Effect of Power and Helical Tip Mach Number on Peak OASPL

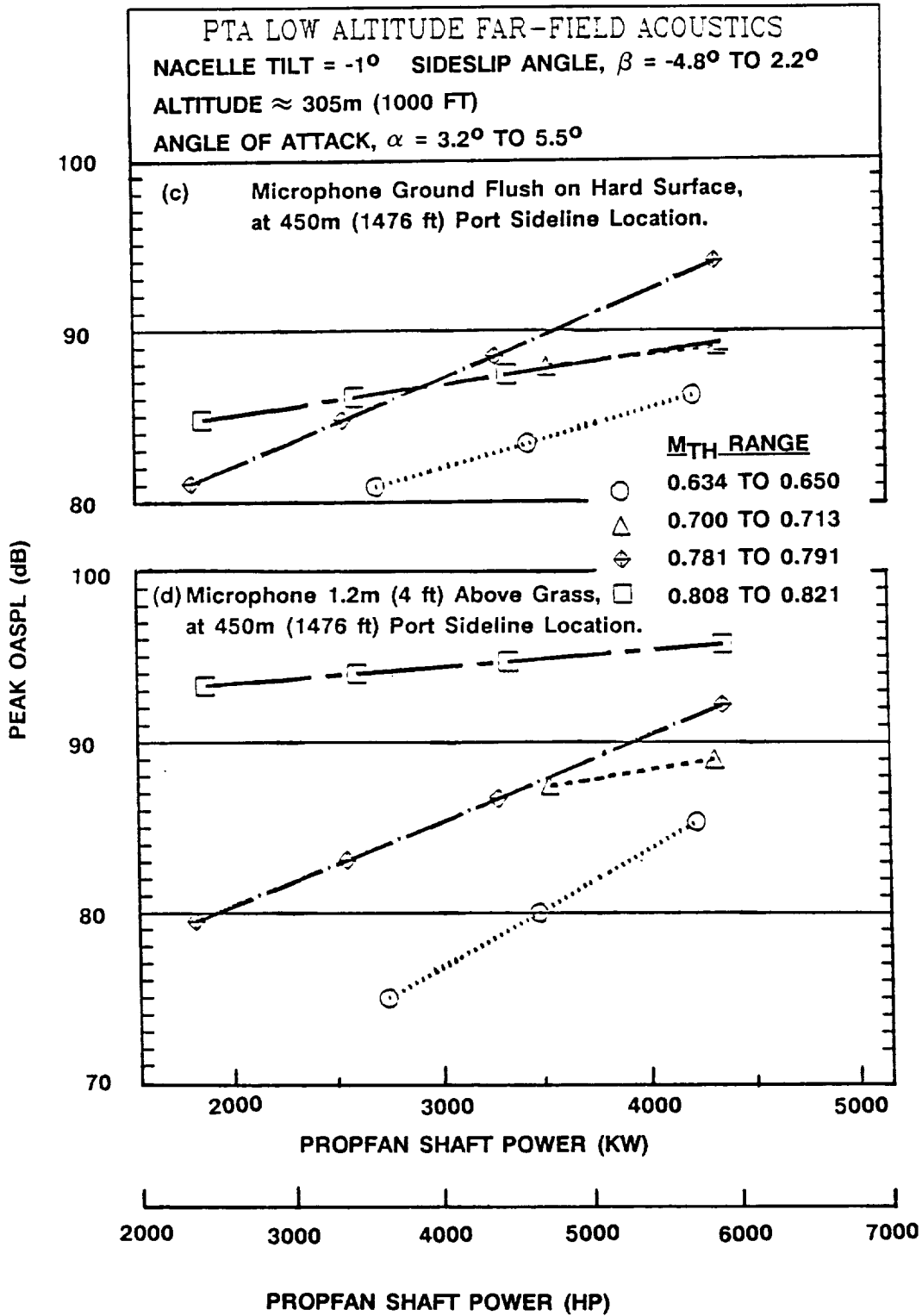


Figure 71. Effect of Power and Helical Tip Mach Number on Peak OASPL (Continued)

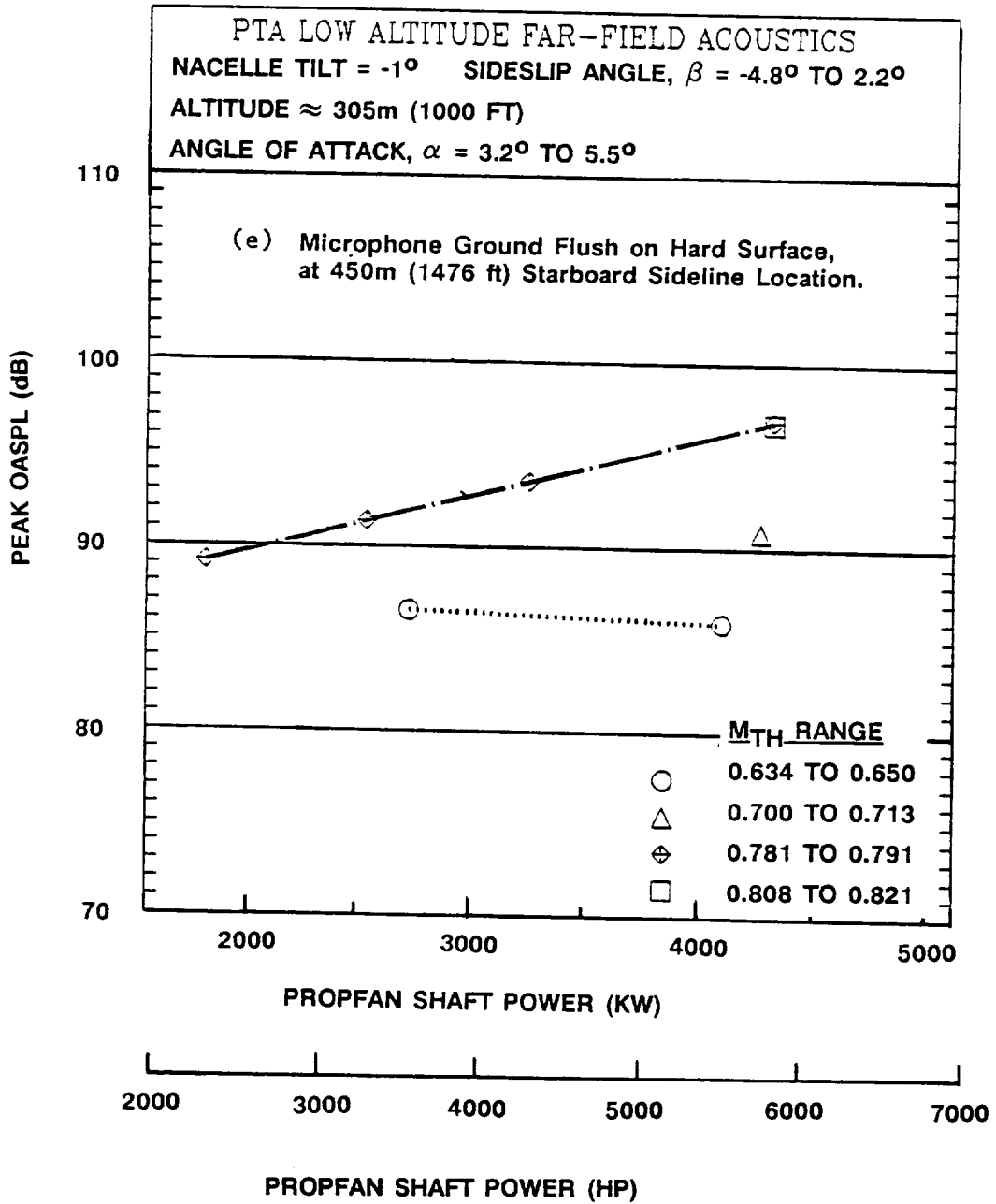


Figure 71. Effect of Power and Helical Tip Mach Number on Peak OASPL (Continued)

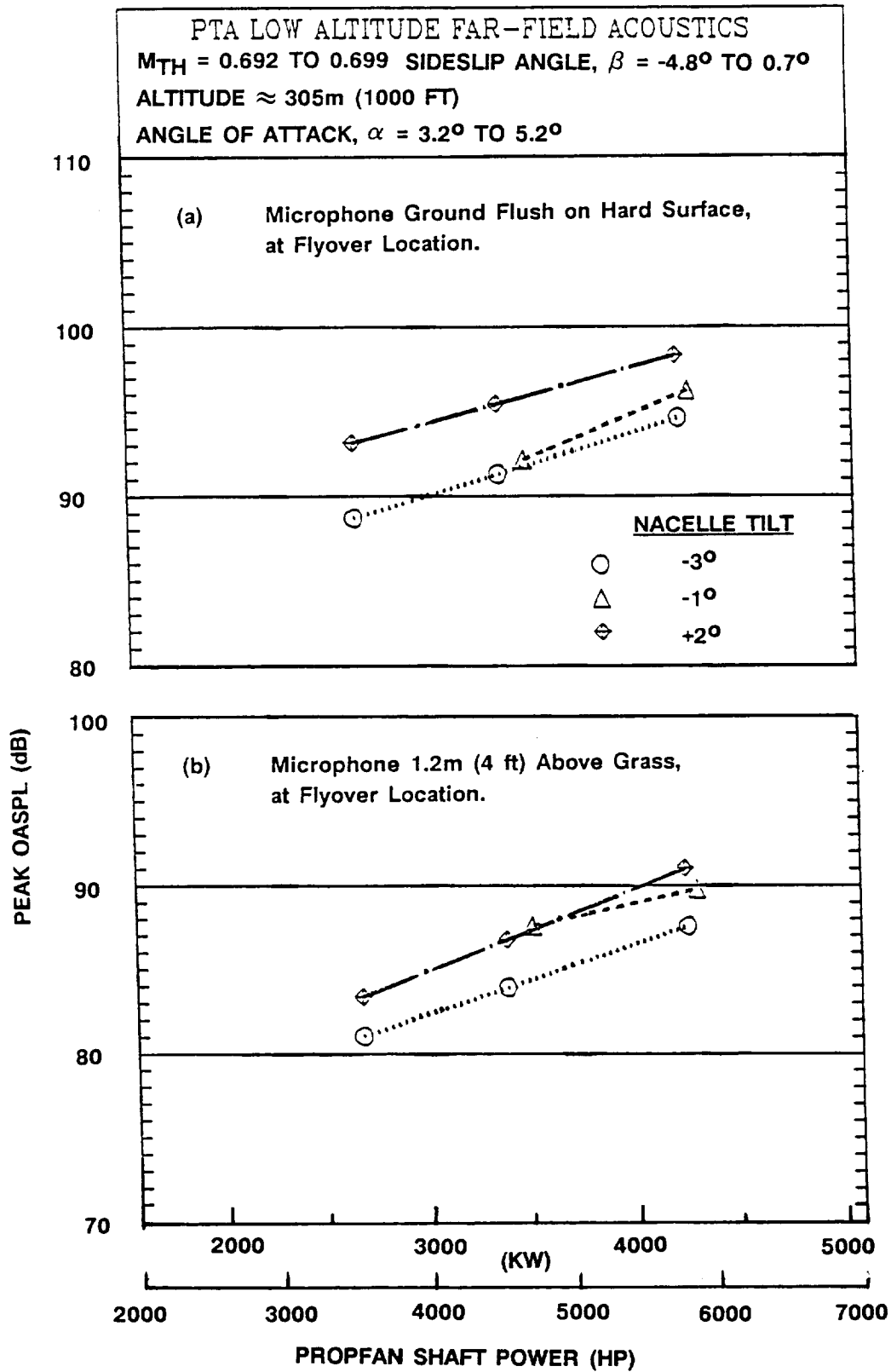


Figure 72. Effects of Power and Nacelle Tilt on Peak OASPL

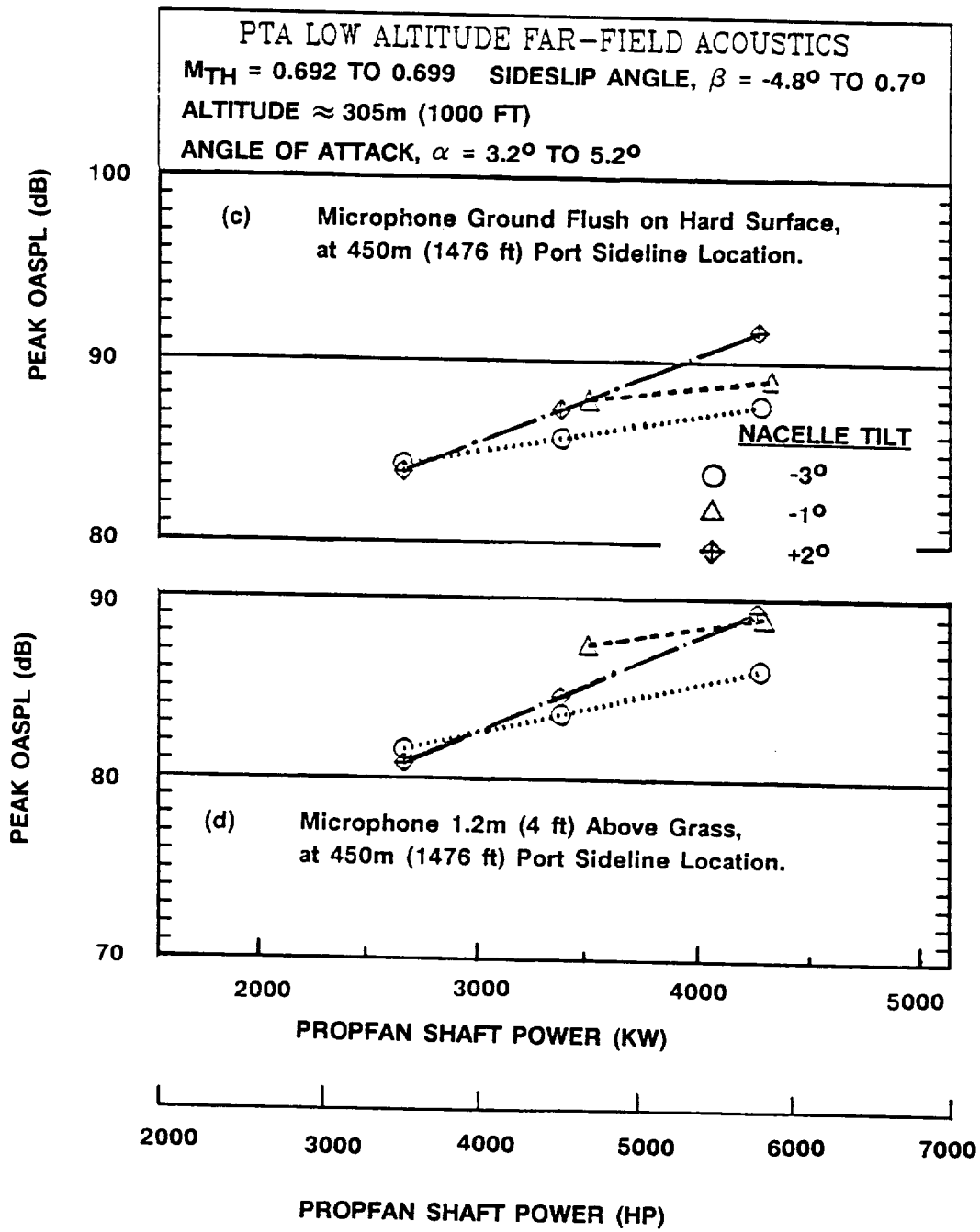


Figure 72. Effects of Power and Nacelle Tilt on Peak OASPL (Continued)

PTA LOW ALTITUDE FAR-FIELD ACOUSTICS

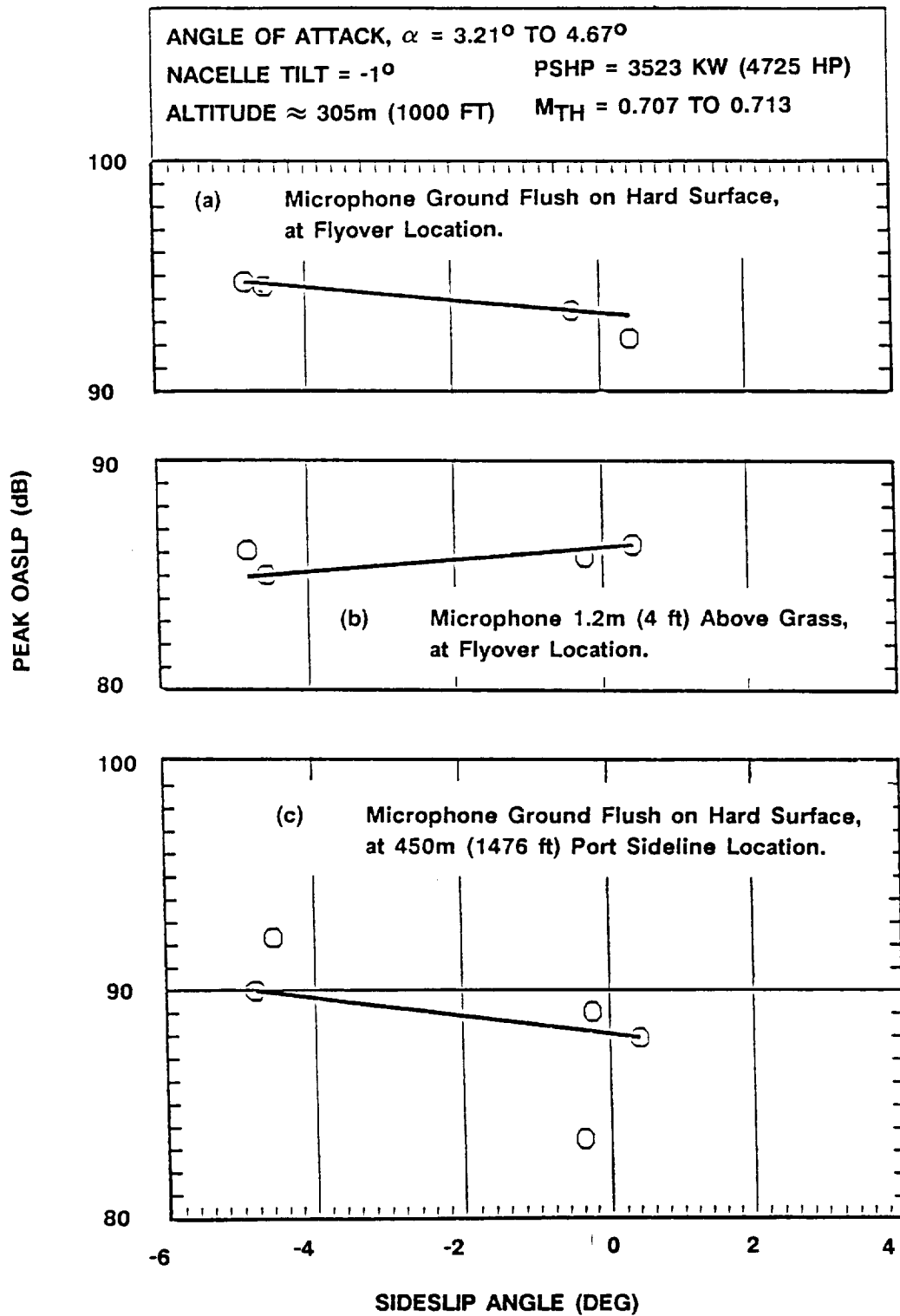


Figure 73. Effect of Sideslip on Peak OASPL

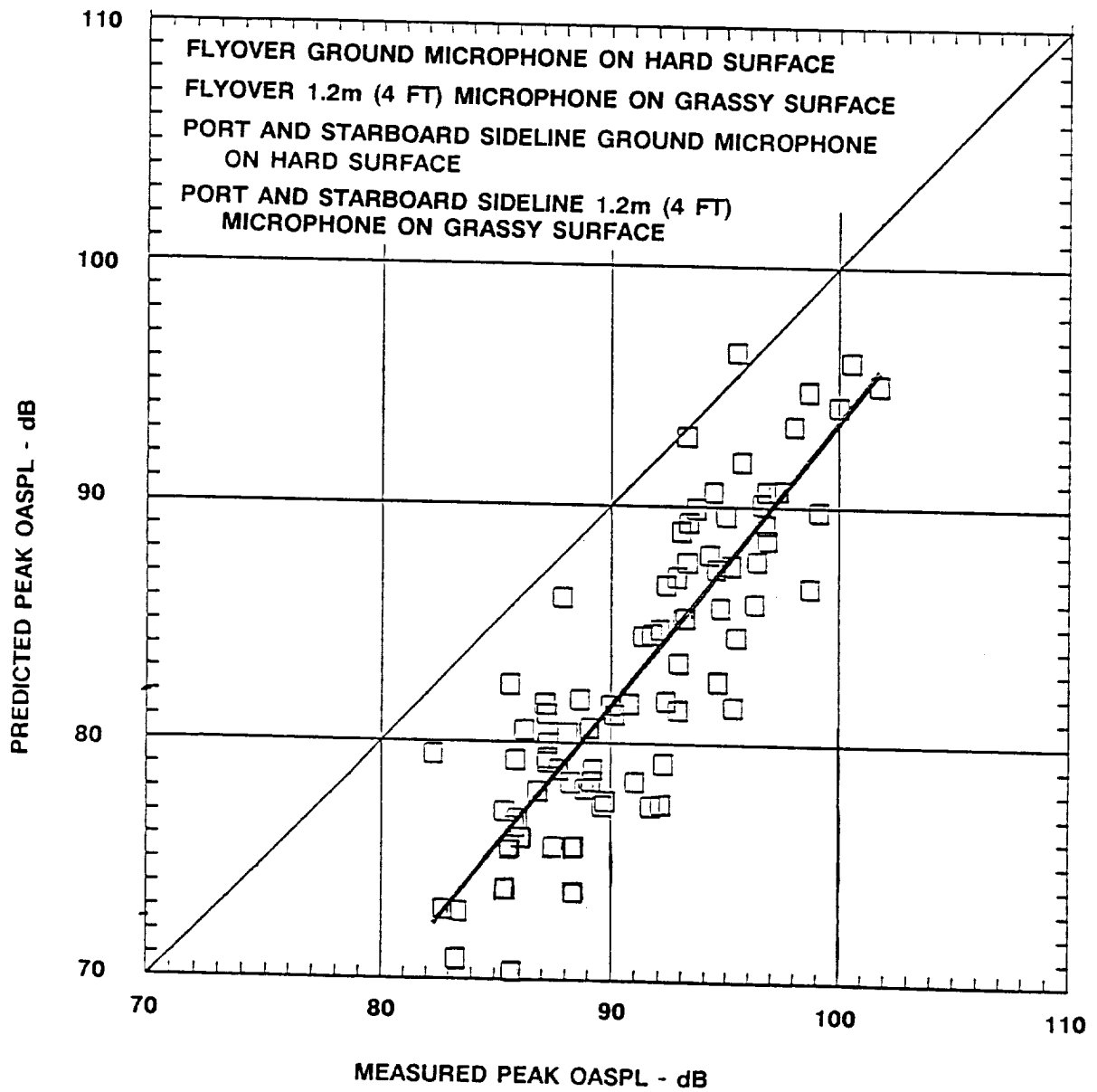


Figure 74. Comparison of Predicted and Measured Peak OASPLs

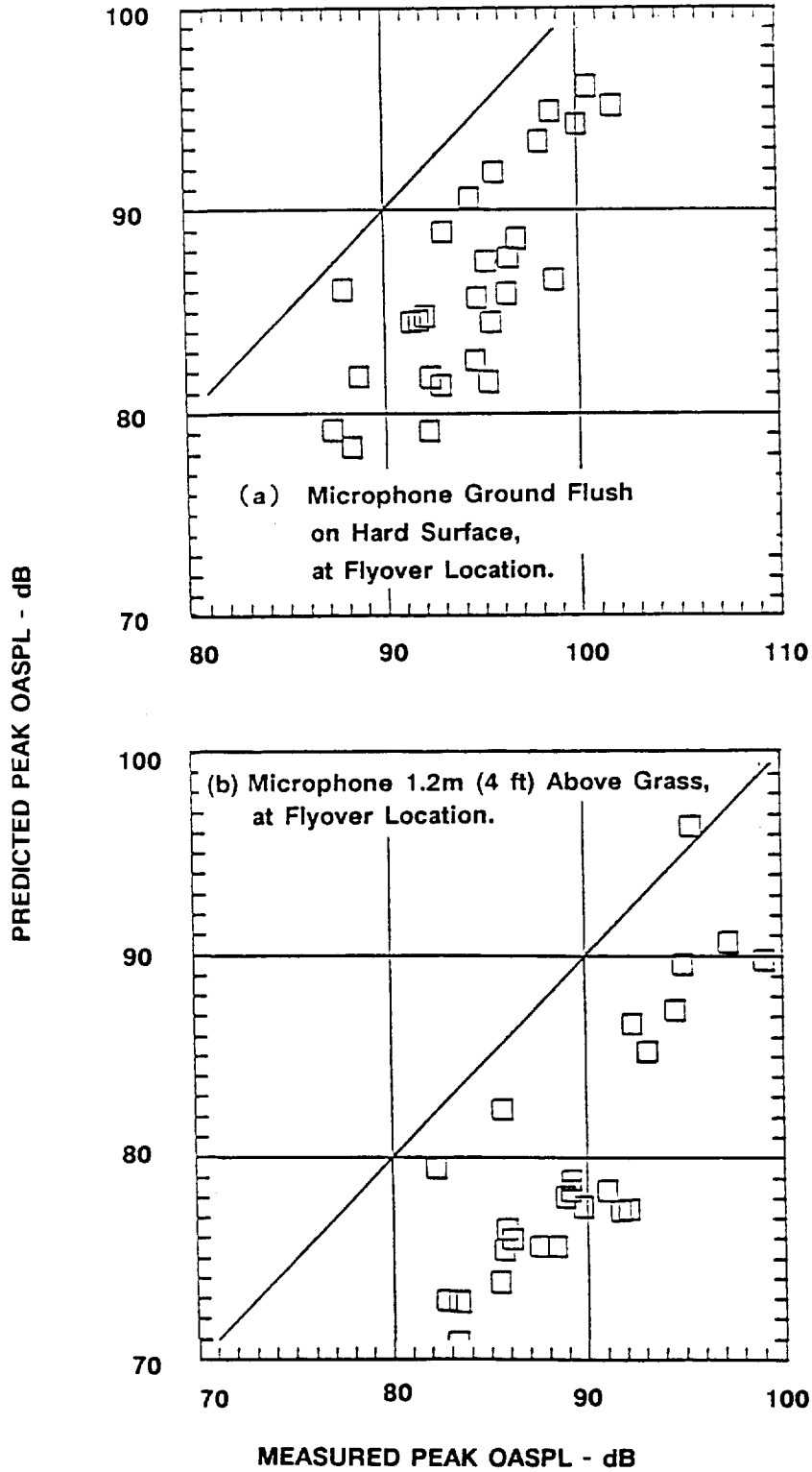


Figure 75. Comparison of Predictions With Measurements

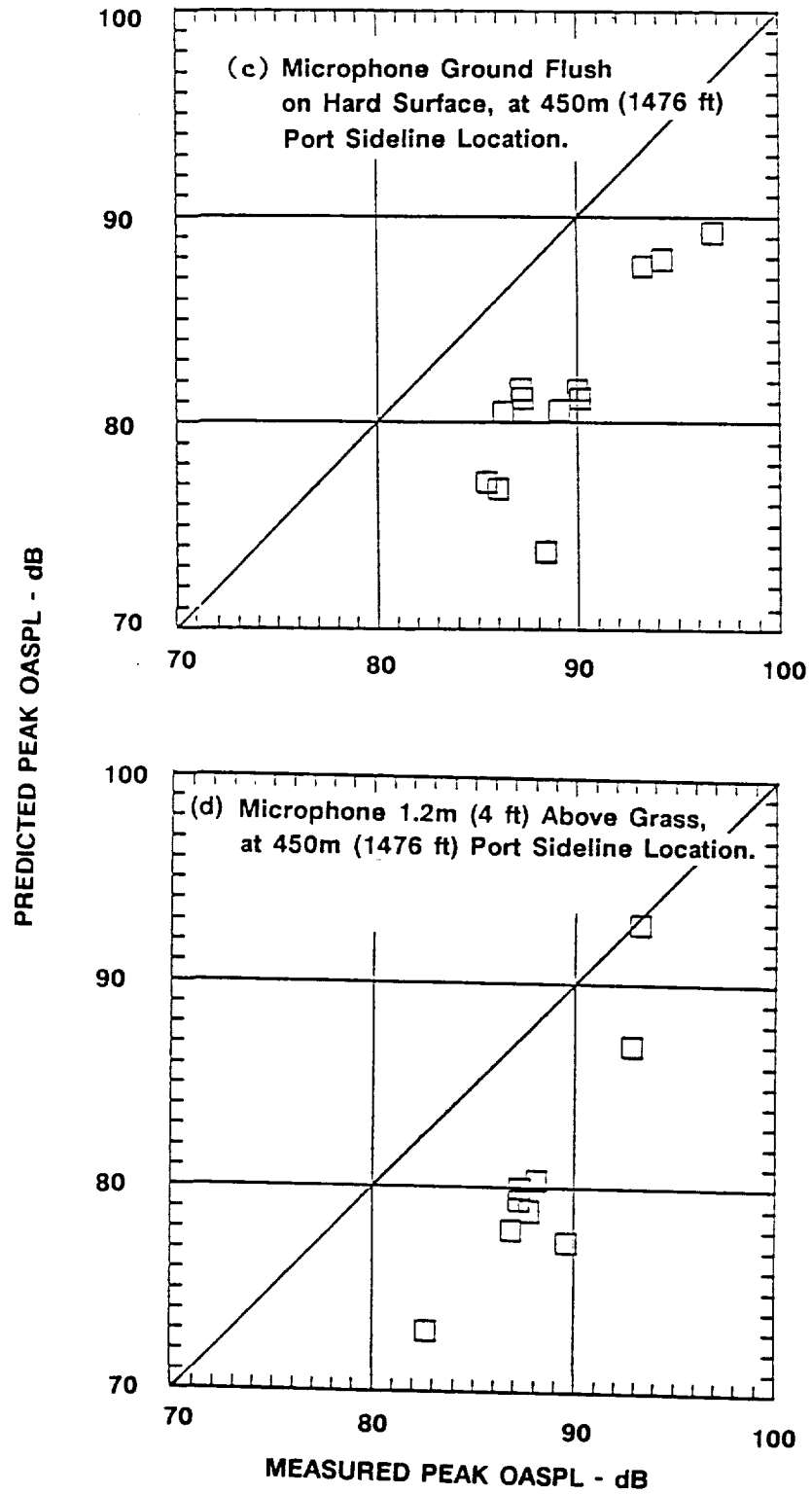


Figure 75. Comparison of Predictions With Measurements (Continued)

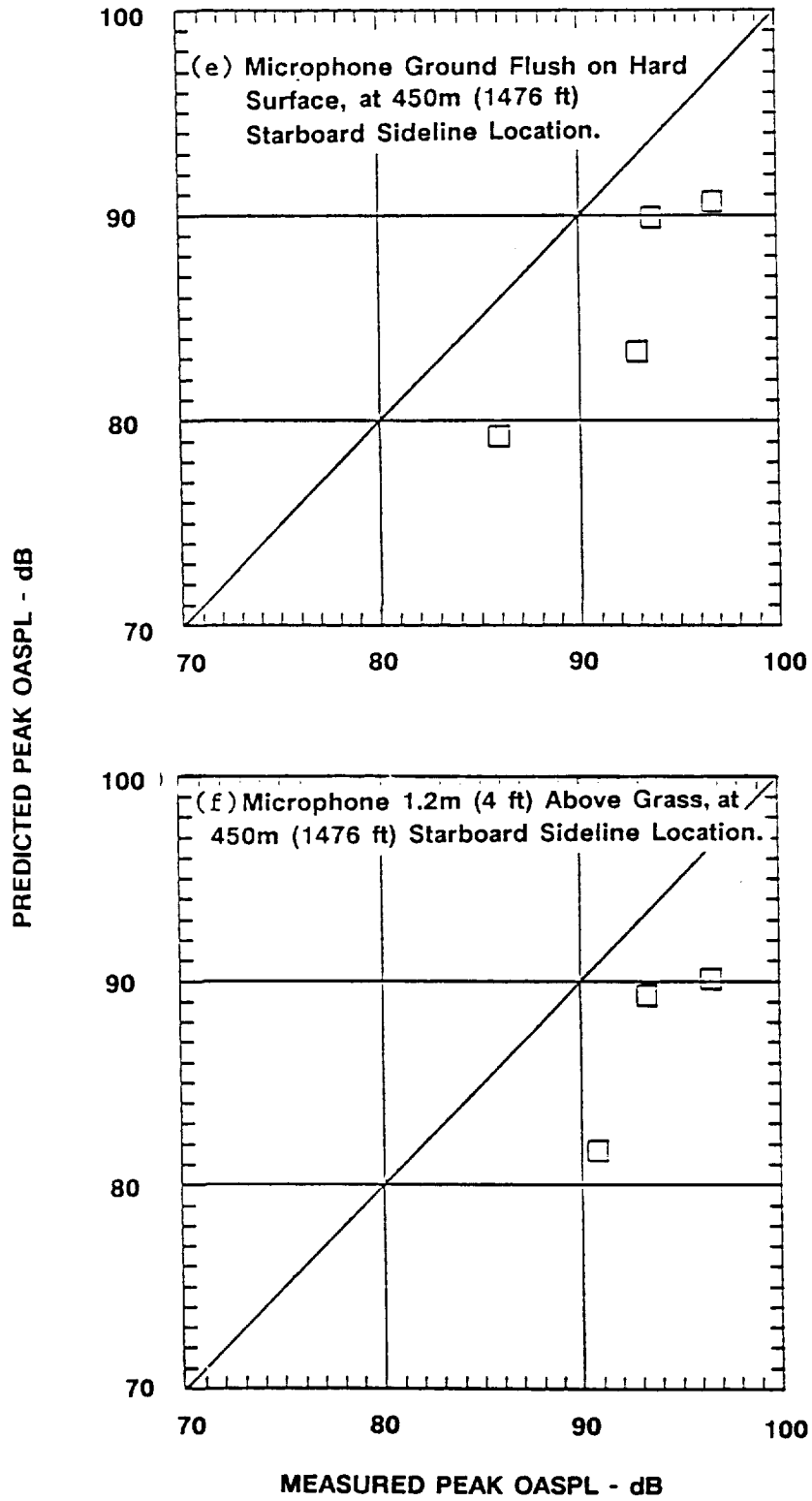


Figure 75. Comparison of Predictions With Measurements (Continued)

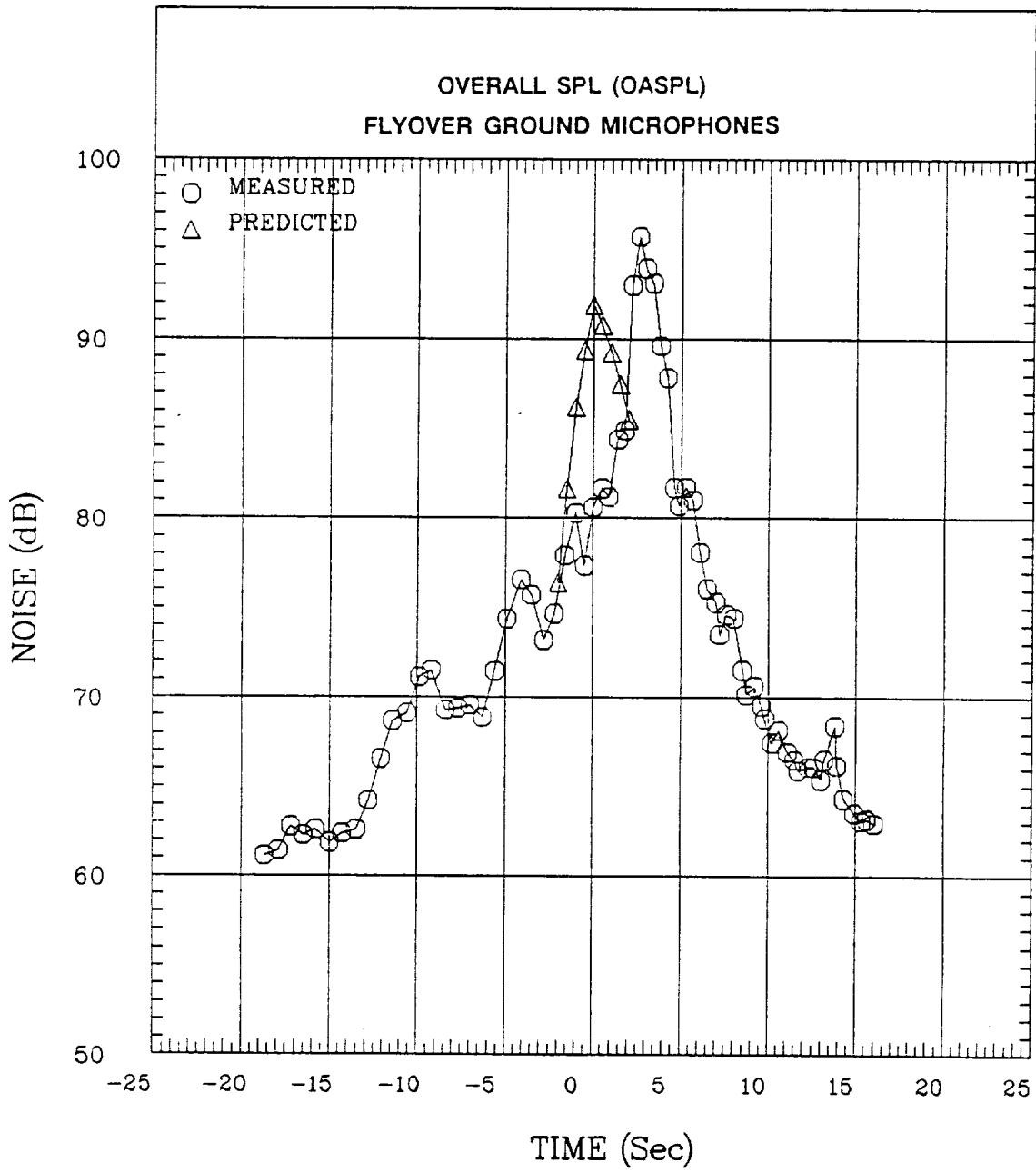


Figure 76. Comparison of Predicted and Measured Time Histories

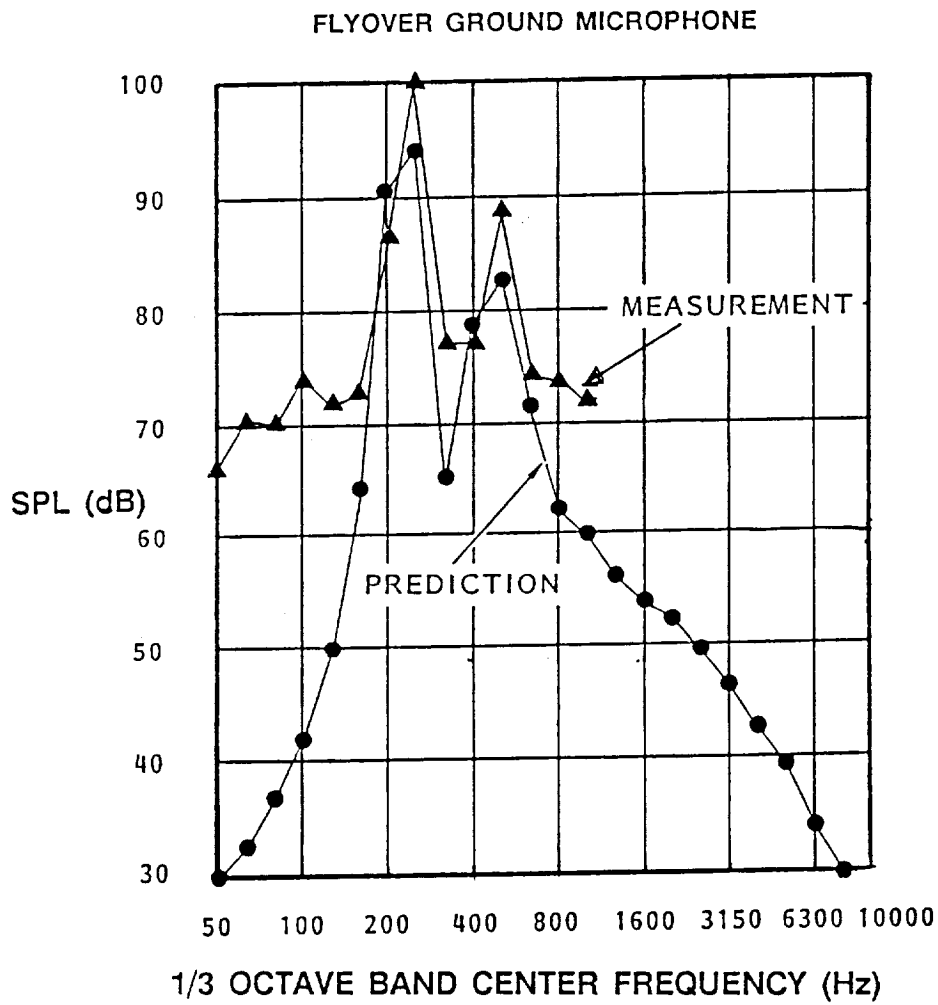


Figure 77. Typical Comparison of Predicted and Measured Noise Spectra

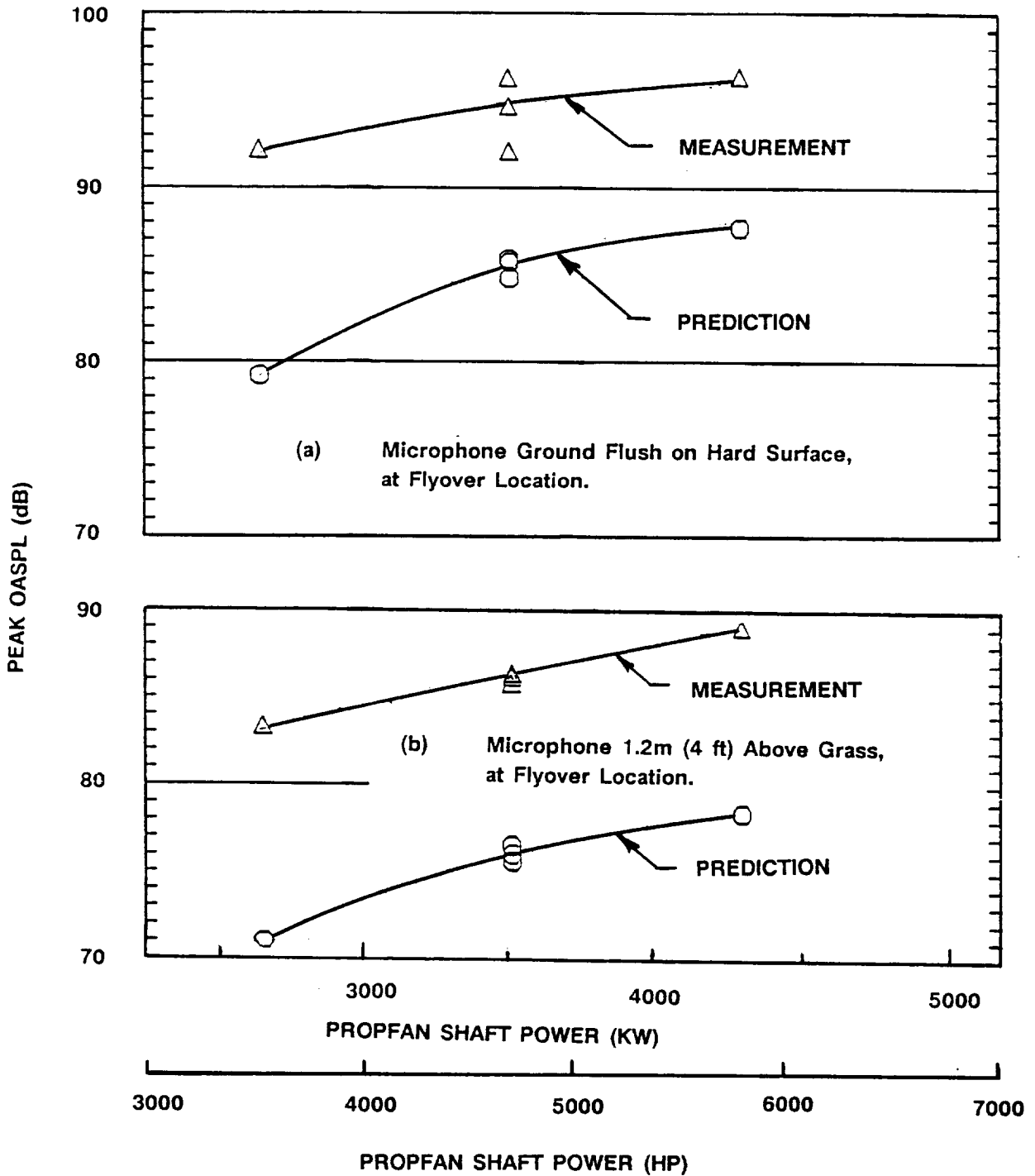


Figure 78. Effects of Shaft Horsepower on Predicted and Measured Noise at the Nominal Conditions of: Altitude = 305 m (1000 ft); $V_{ROT} = 213$ m/s (700 fps); $M_{TH} = 0.7$; $NT = -1^\circ$; Angle of Attack = 4.3° ; Sideslip Angle = -1° .

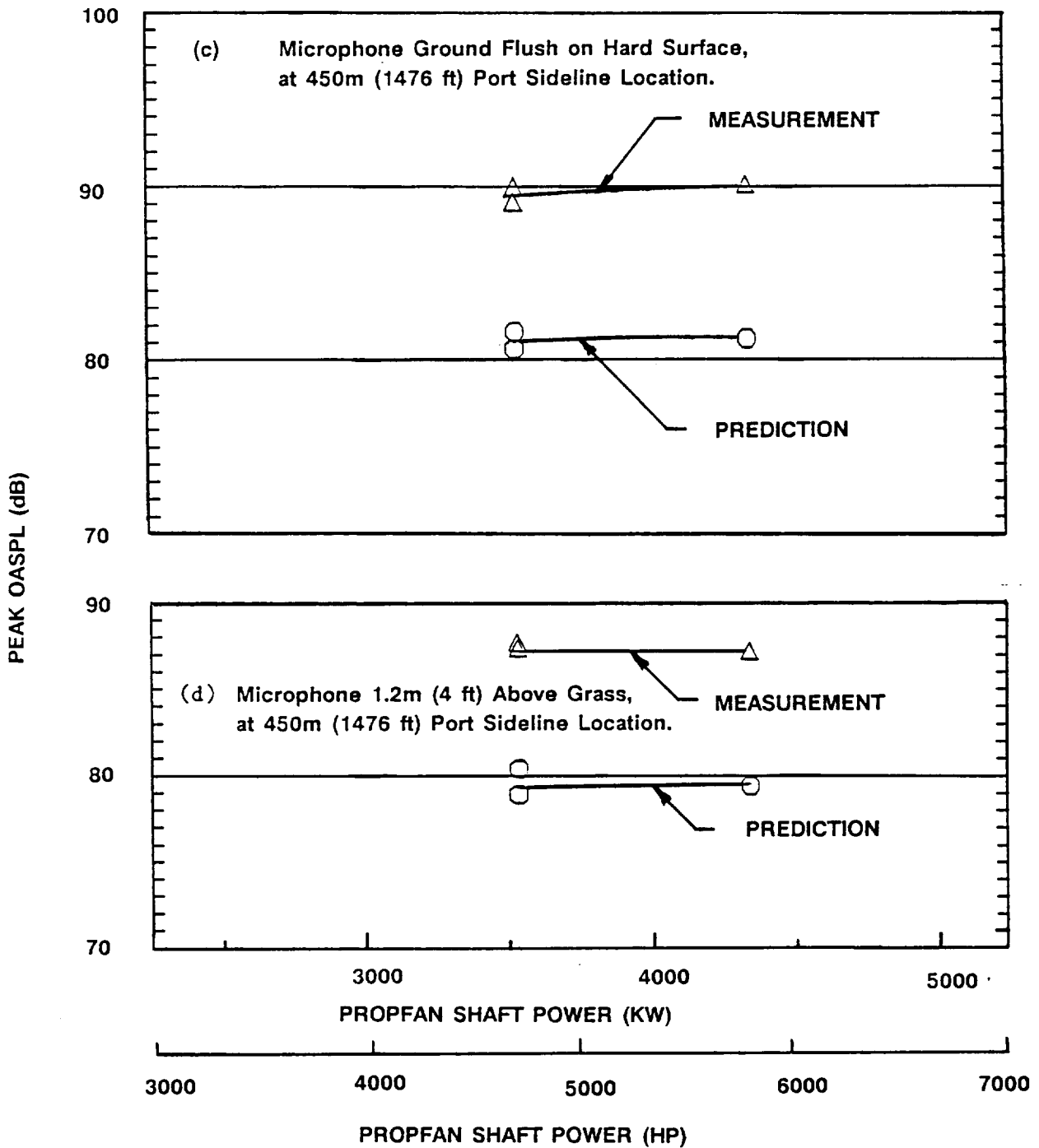


Figure 78. Effect of Shaft Horsepower (Continued)

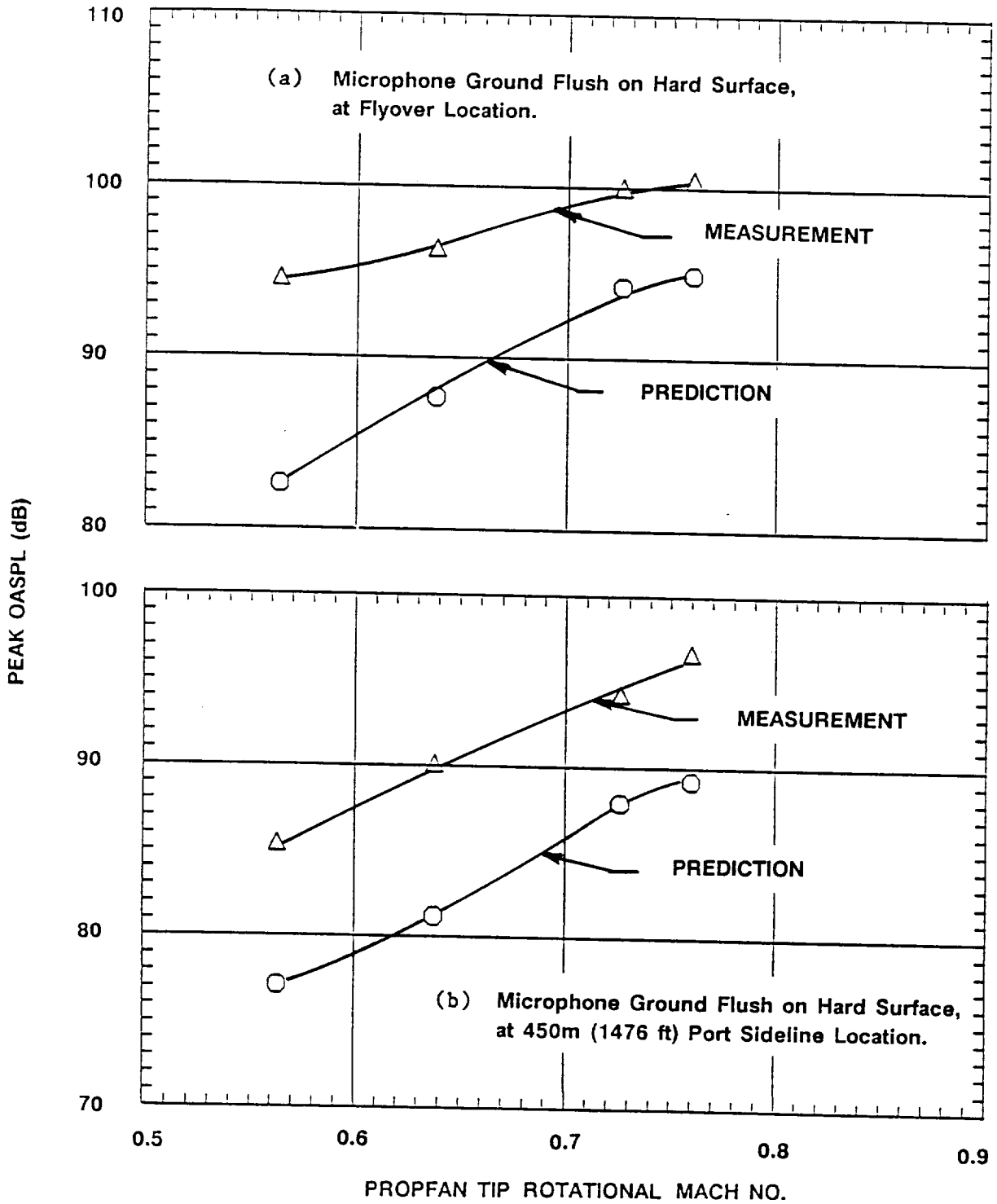


Figure 79. Effects of Tip Speed on Predicted and Measured Noise at the Nominal Conditions of: Altitude = 305 m (1000 ft); Power = 4320 kw (5790 PSHP); NT = -1°; Angle of Attack = 4.3°; Sideslip Angle = -1°.

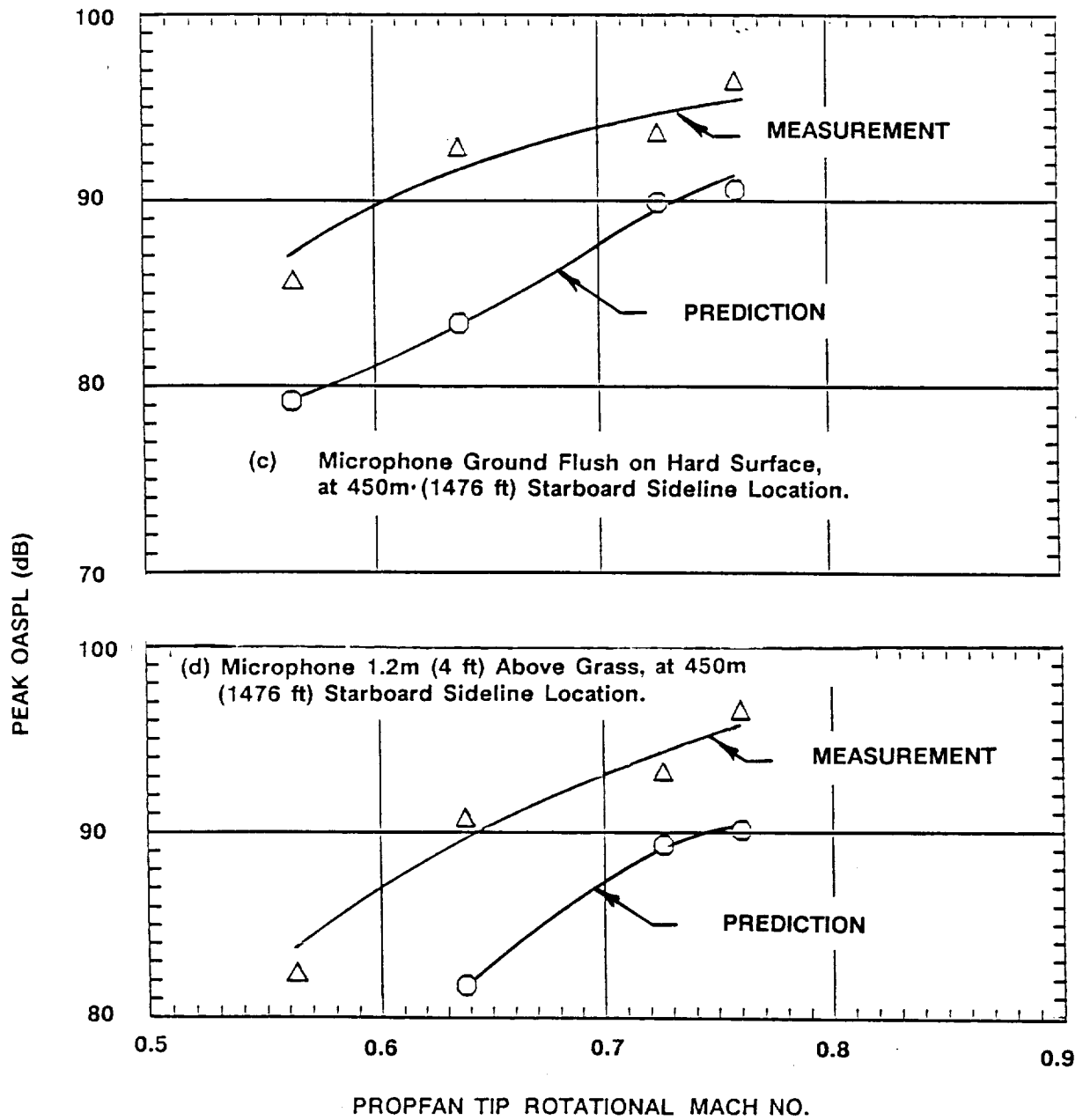


Figure 79. Effect of Propfan Tip Mach Number (Continued)

NOMINAL CONDITIONS

PROPFAN POWER = 4320 KW (5790 HP)

$M_{TH} = 0.70$

ALTITUDE = 305m (1000 FT)

ANGLE OF ATTACK = 4.3°

SIDSLIP ANGLE = -1°

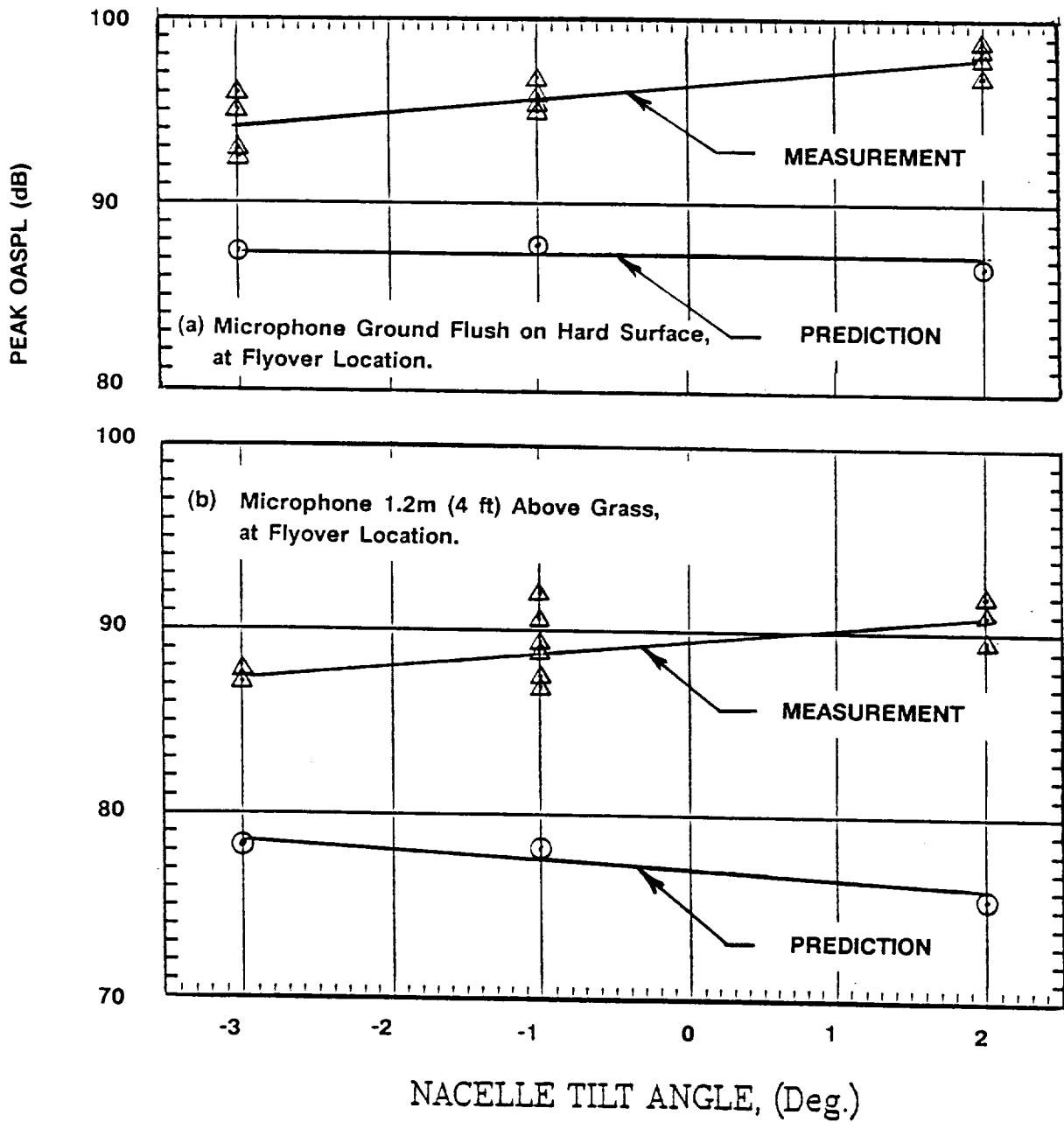


Figure 80. Effects of Nacelle Tilt On Predicted and Measured Noise

LATERAL NOISE ATTENUATION:

$$\text{LNA}_\theta = \text{SPL}'_2 - \text{SPL}_1$$

$$\text{SPL}'_2 = \text{SPL}_2 - \Delta \text{SPL}$$

ΔSPL = CORRECTION FOR DISTANCE, $(R - H)$

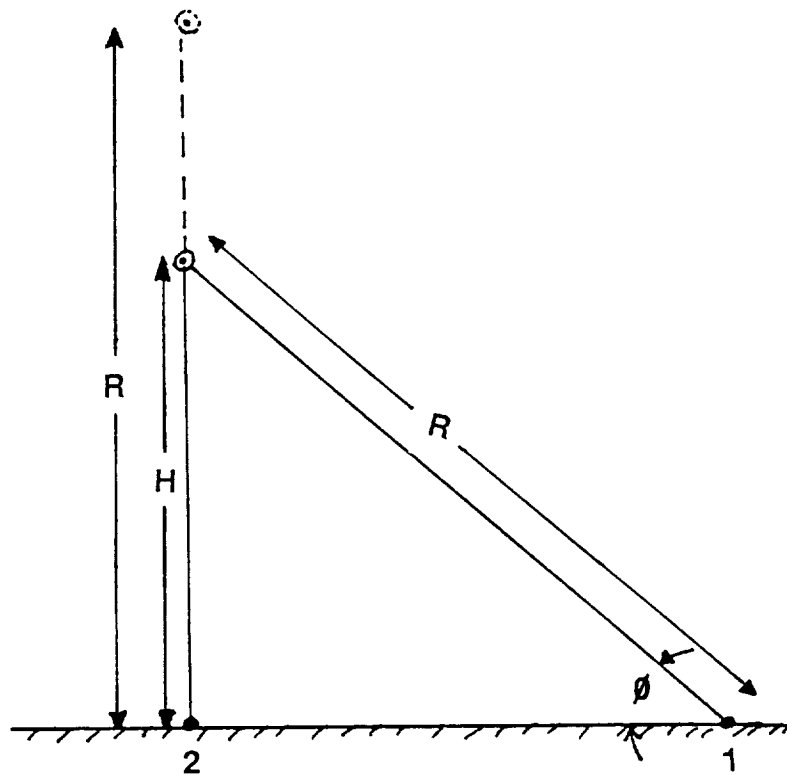


Figure 81. Calculation Procedure for Lateral Noise Attenuation

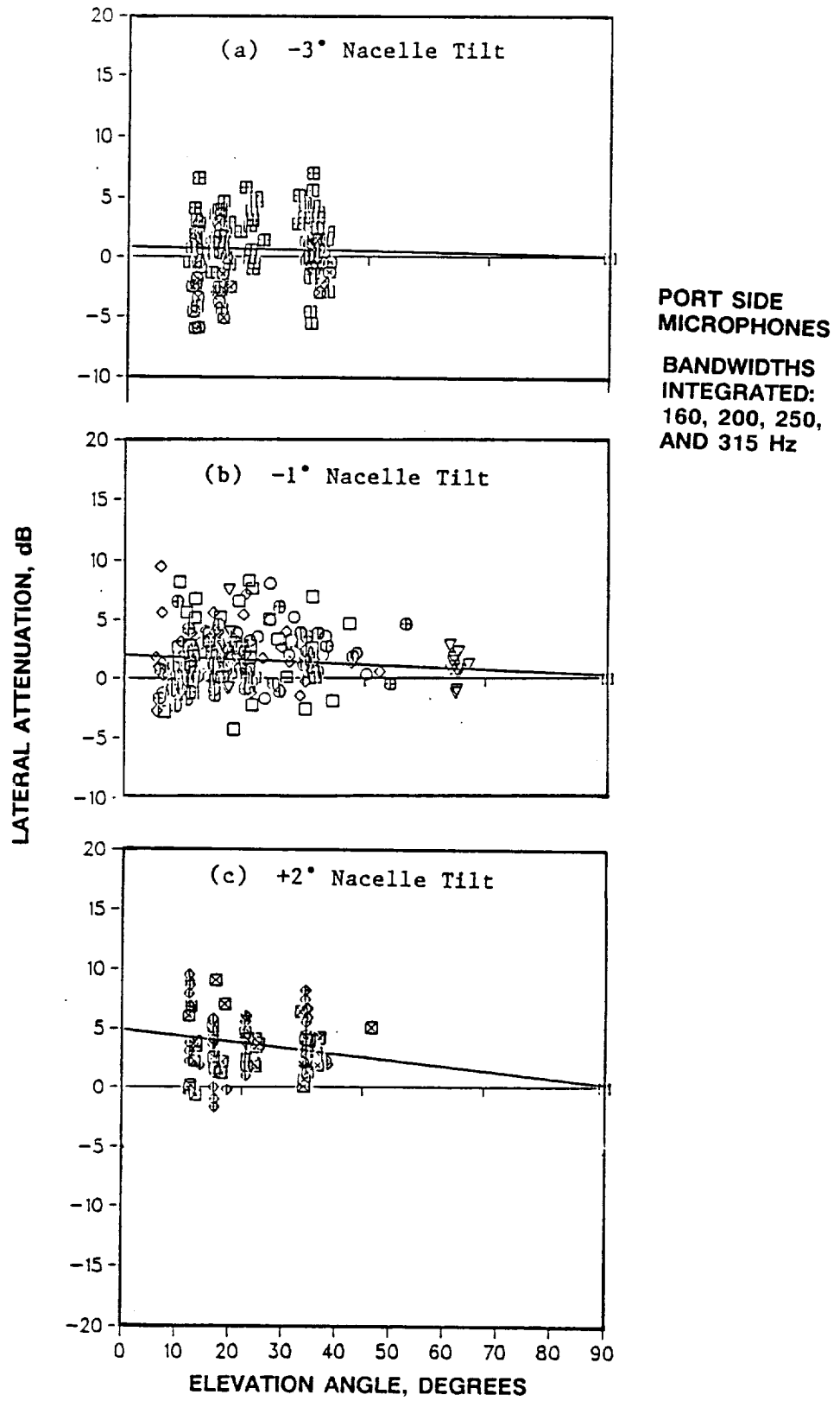


Figure 82. Lateral Attenuation as a Function of Elevation Angle

STARBOARD SIDE MICROPHONES

BANDWIDTHS INTEGRATED: 160, 200, 250, 315 Hz

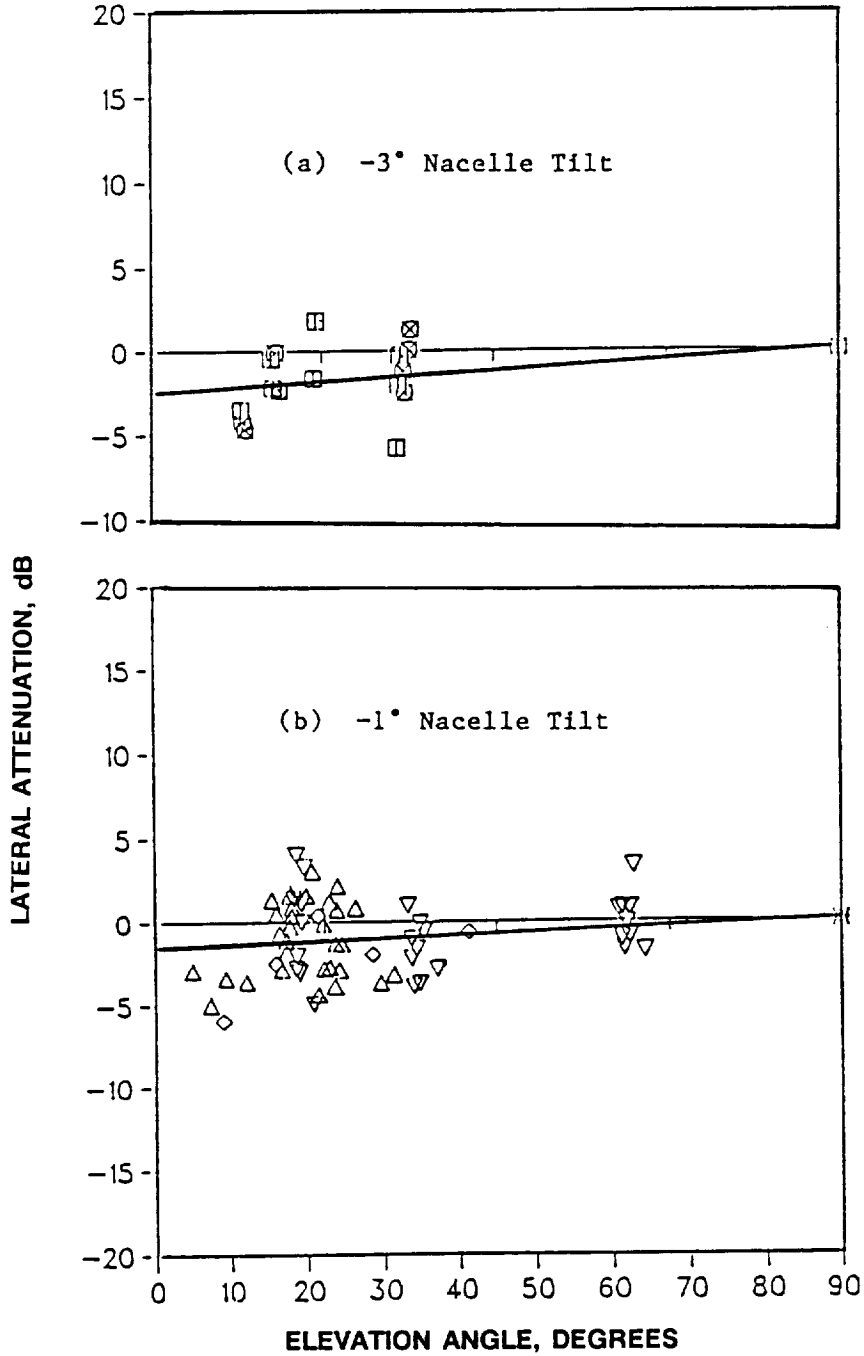


Figure 83. Lateral Attenuation as a Function of Elevation Angle

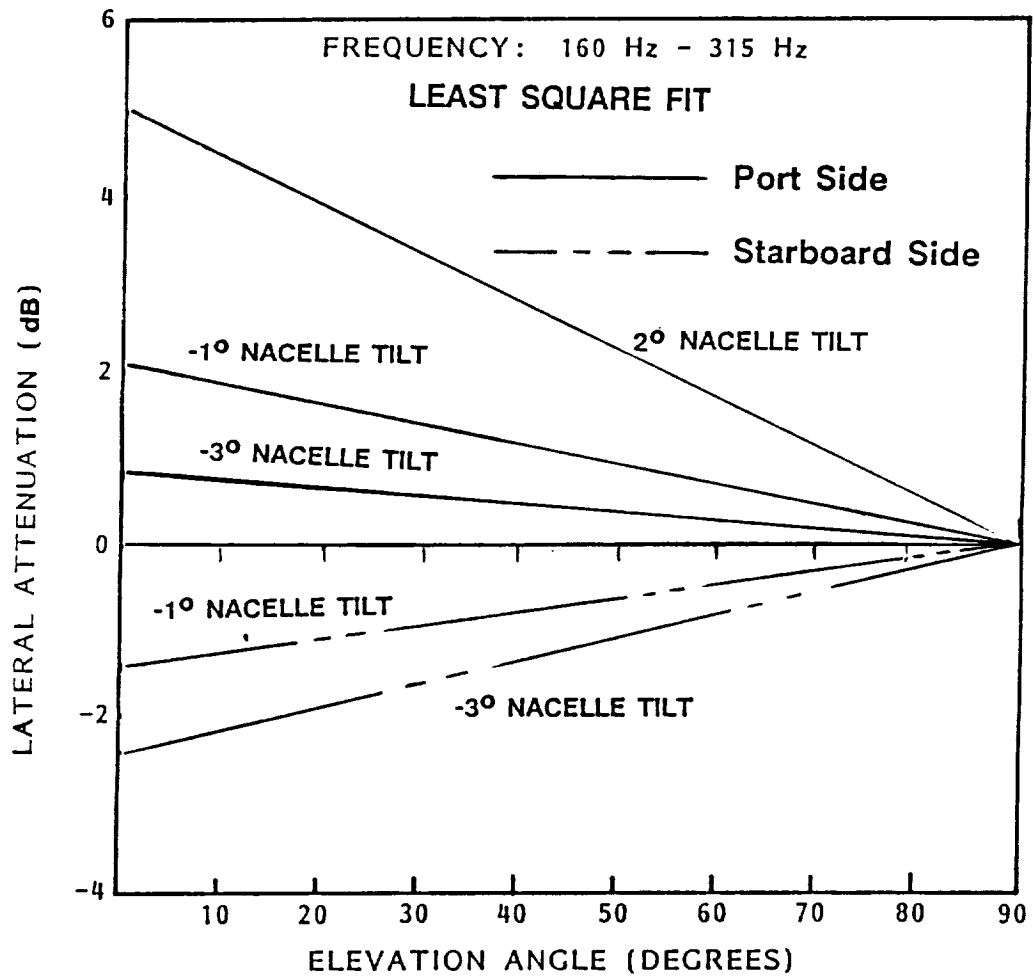


Figure 84. Lateral Attenuation of PTA Aircraft

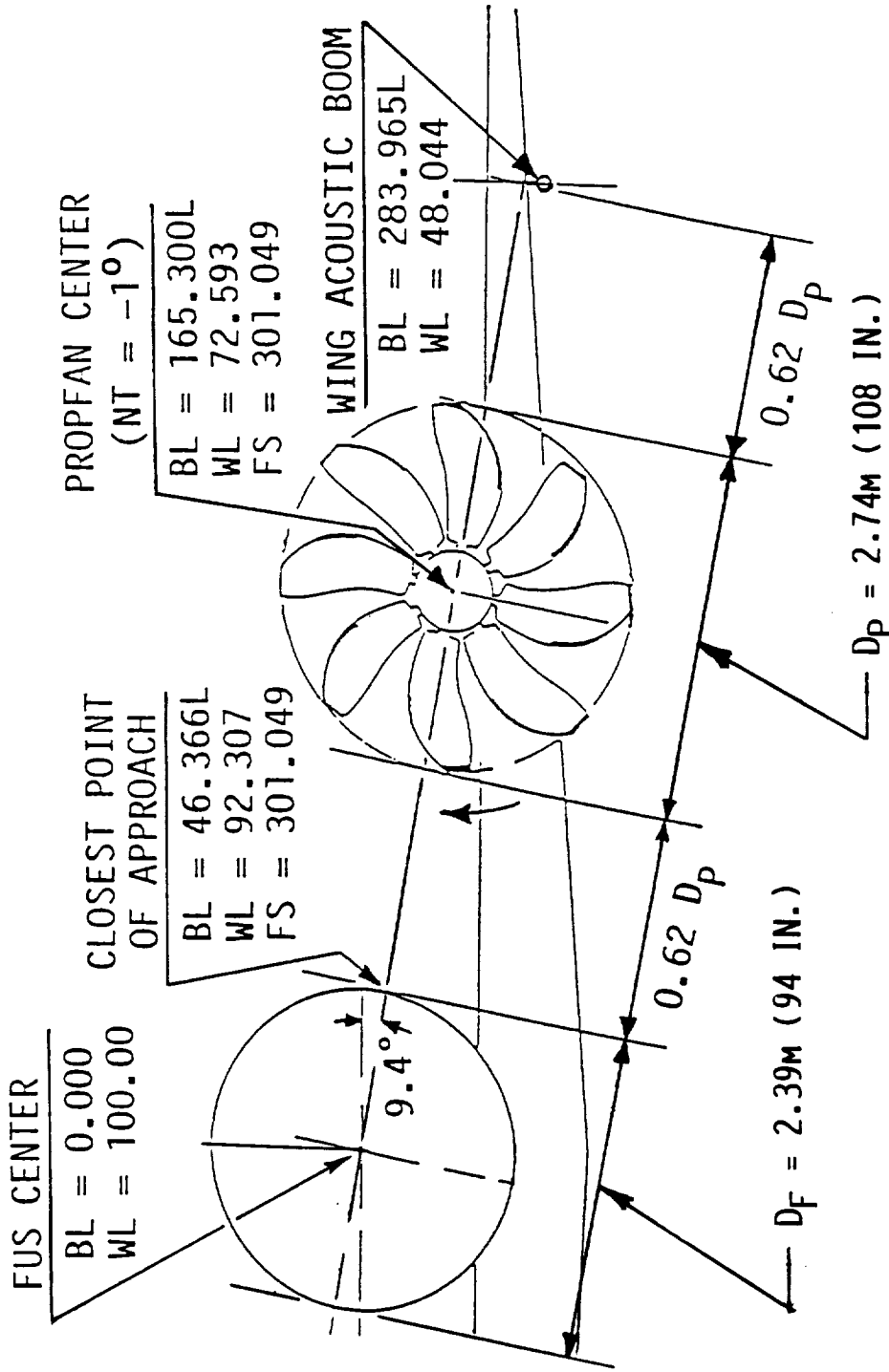


Figure 85. PTA Acoustic Geometry

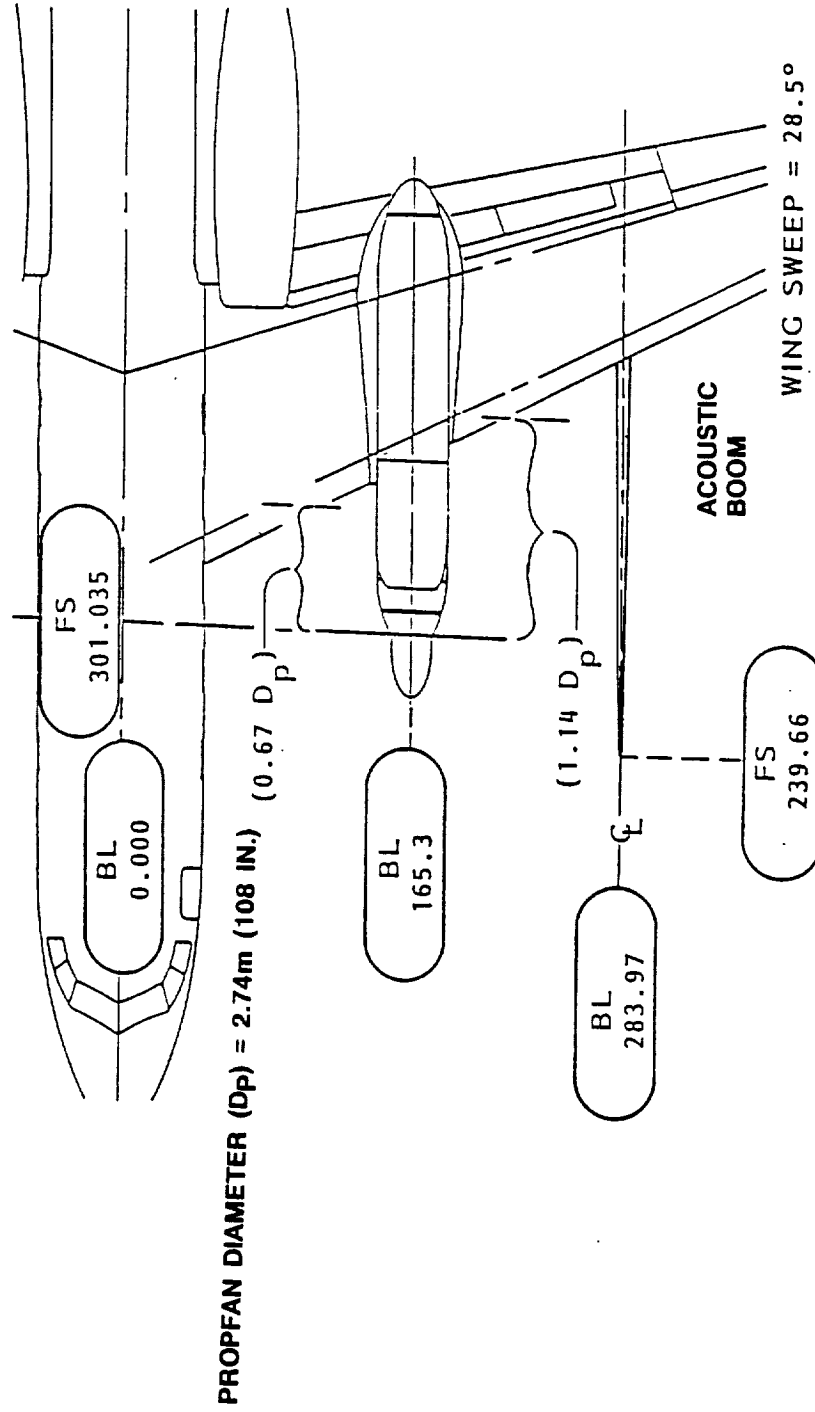


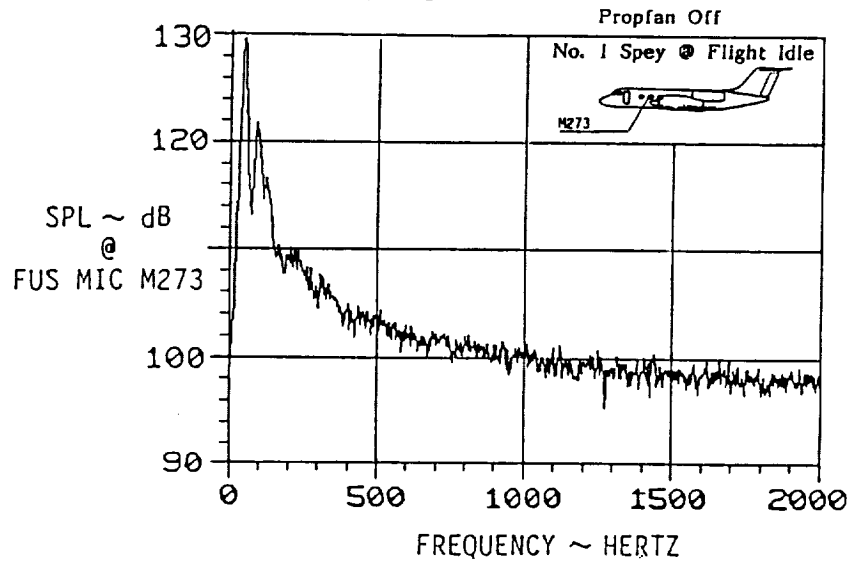
Figure 86. PTA Propfan and Wing Geometry

(a) No. 1 Spey at Flight Idle

ALTITUDE = 10,668m (35,000 FT)

AIRSPPEED = 0.80 MN

NO. 2 SPEY = 100% MCT



(b) No. 1 Spey at 70% MCT

ALTITUDE = 10,668m (35,000 FT)

AIRSPPEED = 0.80 MN

NO. 2 SPEY = 100% MCT

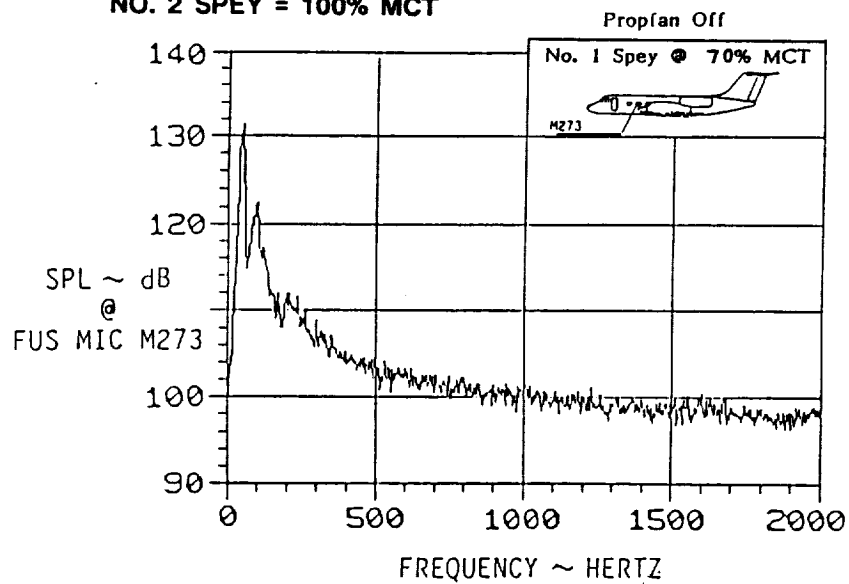


Figure 88. Effect of Near-Side Spey Power on Fuselage Noise

(c) No. 1 Spey at 100% MCT
 ALTITUDE = 10,668m (35,000 FT)
 AIRSPEED = 0.80 MN
 NO. 2 SPEY = 100% MCT

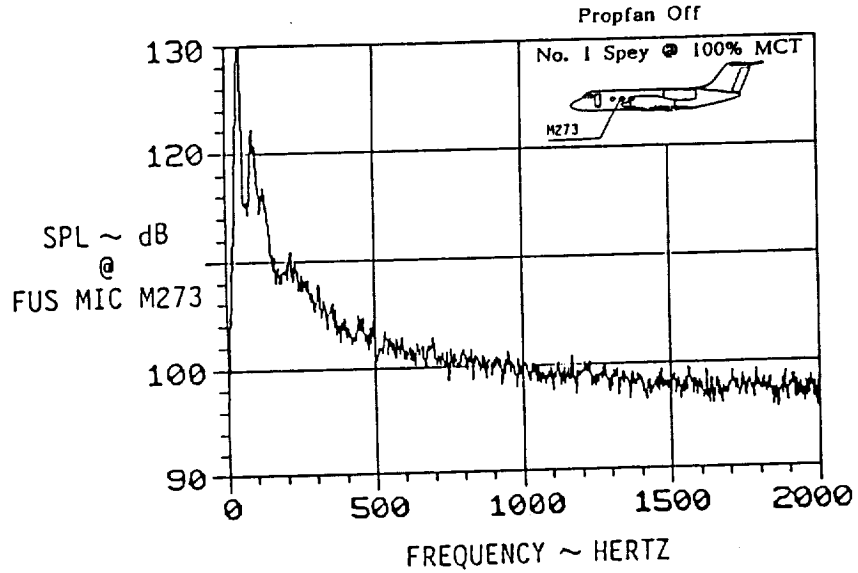


Figure 88. Effect of Near-Side Spey Power on Fuselage Noise (Continued)

ALTITUDE = 10,668m (35,000 FT) NO. 1 SPEY = 70% MCT
 AIRSPEED = 0.80 MN NO. 2 SPEY = 100% MCT

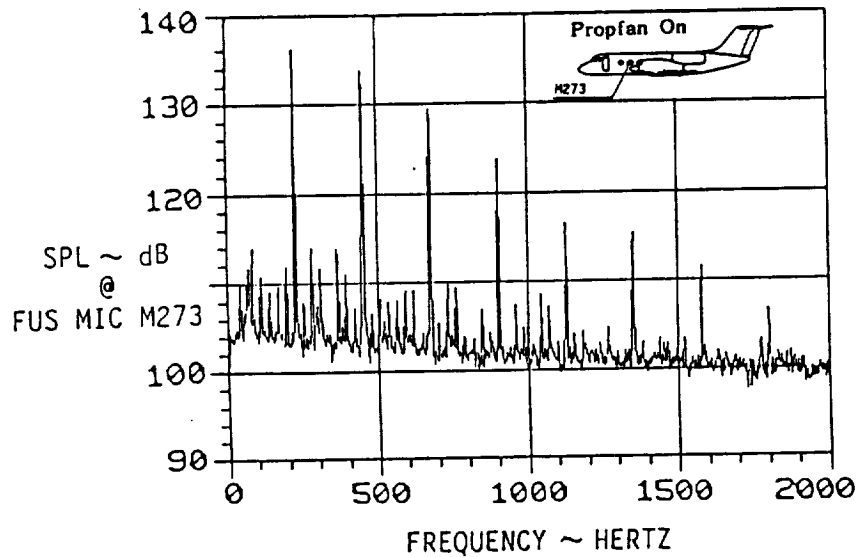


Figure 89. Effect of Near-Side Spey Power on Fuselage Noise - Propfan MCT

ALTITUDE = 10,668m (35,000 FT)

NO. 1 SPEY = 70% MCT

AIRSPEED = 0.80 MN

NO. 2 SPEY = 100% MCT

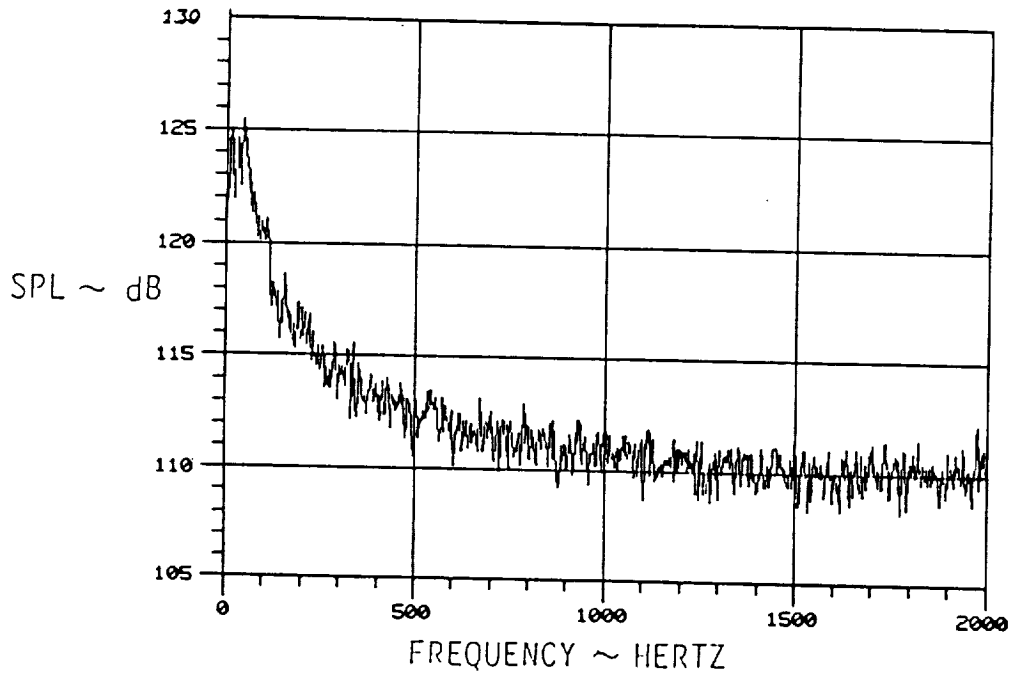


Figure 90. Wing Boom Acoustic Data - Prop Off

ALTITUDE = 10,668m (35,000 FT)

NO. 1 SPEY = 70% MCT

AIRSPEED = 0.80 MN

NO. 2 SPEY = 100% MCT

PROPFAN = 100% MCP

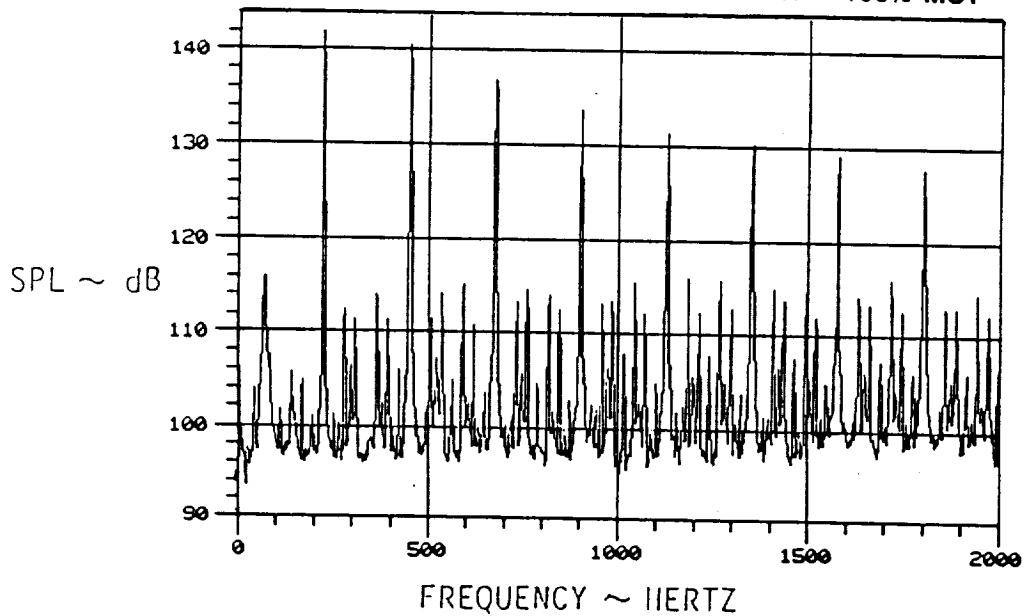
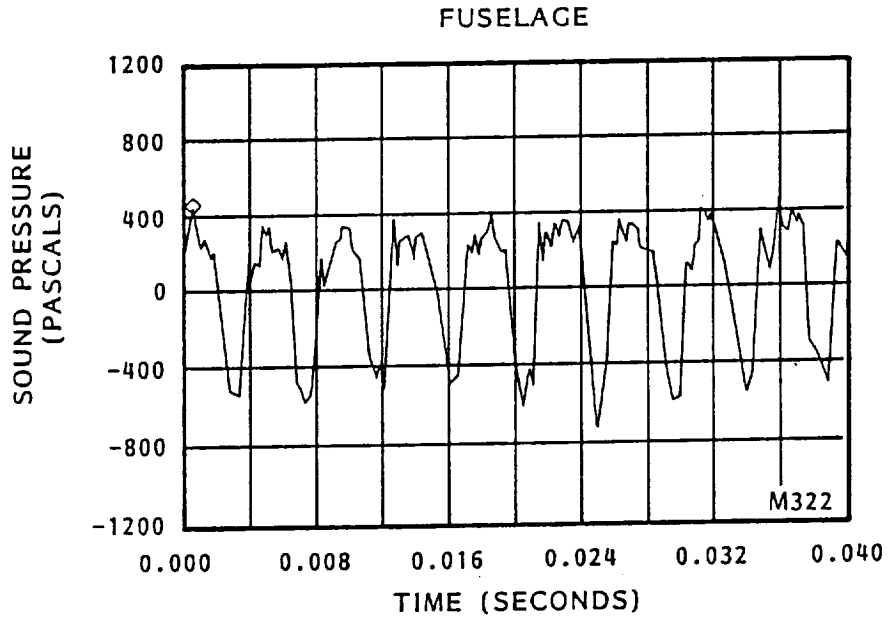


Figure 91. Wing Boom Acoustic Data - Prop On



NACELLE TILT = -1°

ALTITUDE = 10,668m (35,000 FT)

AIRSPEED = 0.80 MN

POWER = 2295 KW (3077 HP)

V_{ROT} = 243 MPS (797 FPS)

M_{TH} = 1.137

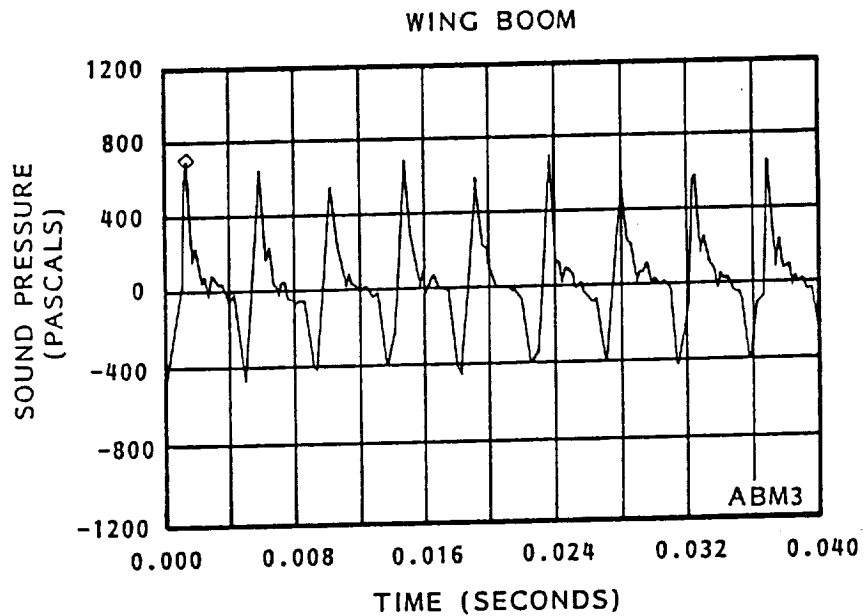
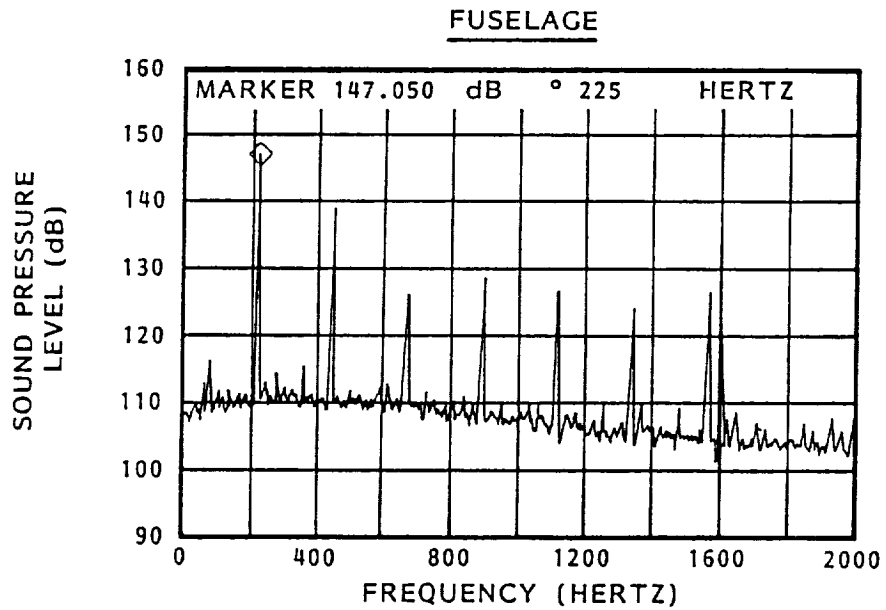


Figure 92. Sound Pressure at 0.25 Propfan Diameter Aft of Propfan Plane



NACELLE TILT = -1°	V_{ROT} = 243 MPS (797 FPS)
ALTITUDE = 10,668m (35,000 FT)	M_{TH} = 1.137
AIRSPEED = 0.80 MN	EFFECTIVE BANDWIDTH = 3.8 Hz
POWER = 2292 KW (3073 HP)	

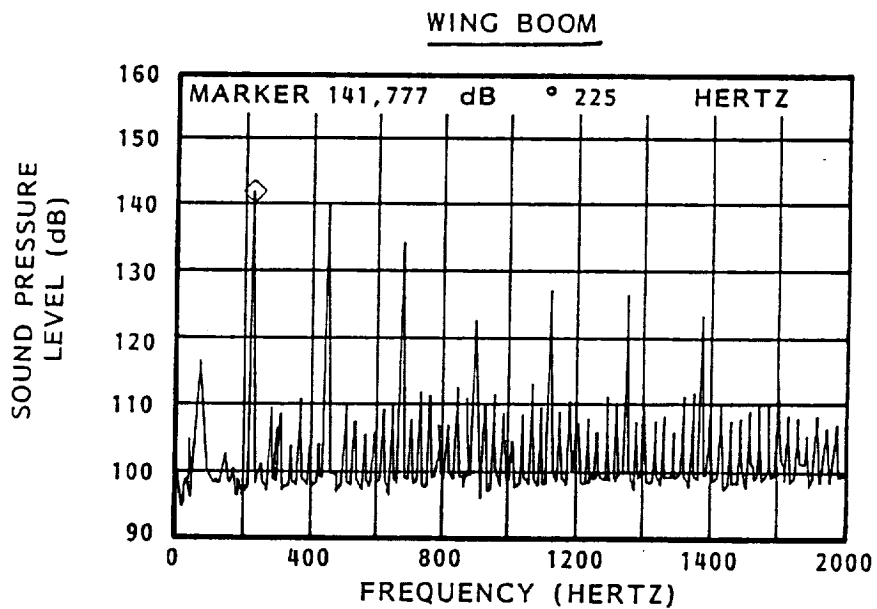


Figure 93. Sound Pressure Spectra at 0.25 Propfan Diameter Aft of Propfan Plane

FIRST 5 ORDERS OF BPF
NACELLE TILT = -1°
ALTITUDE = 10,654m (34,954 FT)
AIRSPEED = 0.80 MN
VROT = 243 MPS (797 FPS)
POWER = 2292 KW (3073 HP)
MTH = 1.137

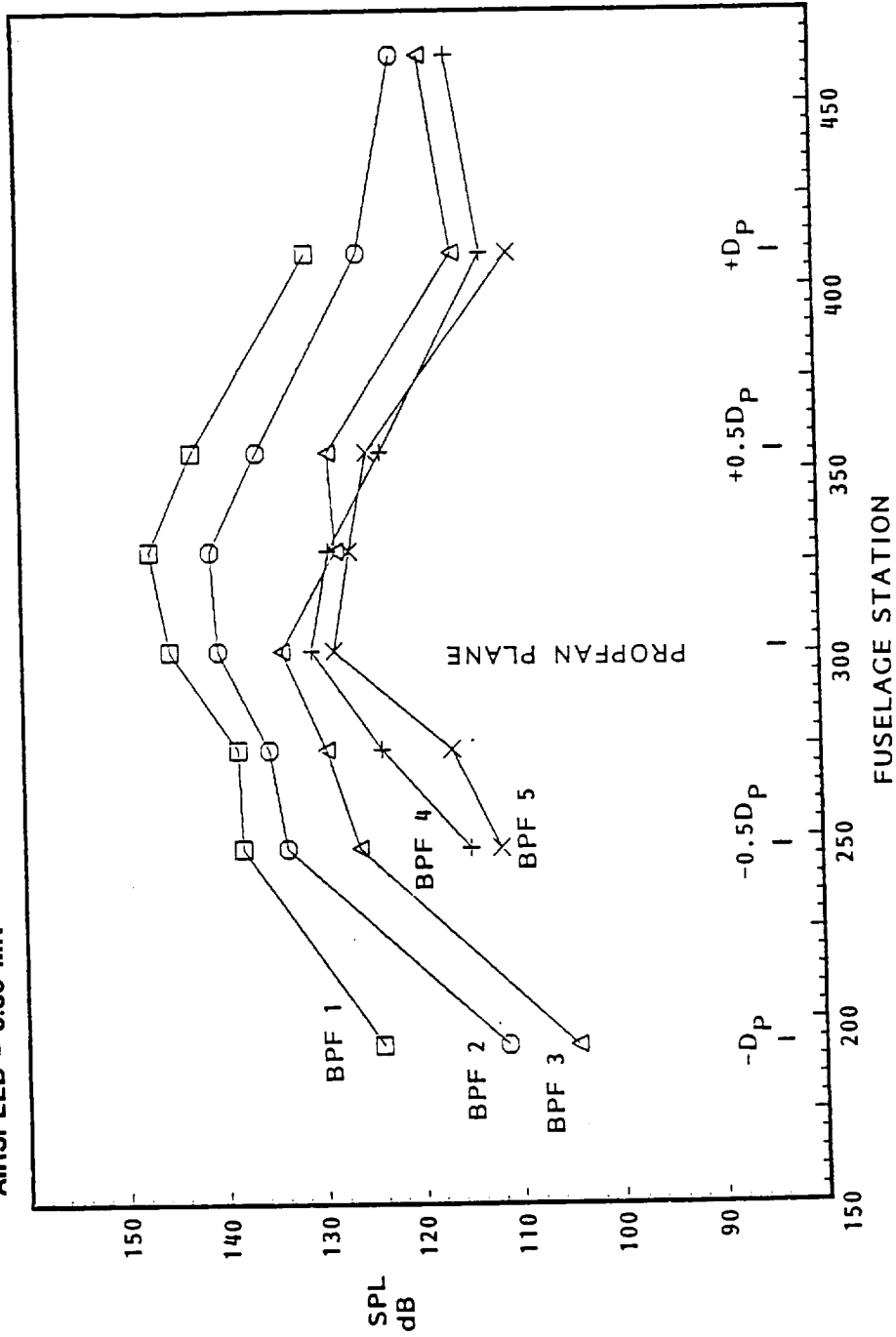


Figure 94. Fuselage Axial Distribution of Measured Sound Pressure Level Along WL 70

FIRST ORDER OF BPF (226 Hz)
NACELLE TILT = -1°
ALTITUDE = 10,654m (34,954 FT)
AIRSPEED = 0.80 MN

VROT = 243 MPS (797 FPS)
POWER = 2292 KW (3073 HP)
MTH = 1.137

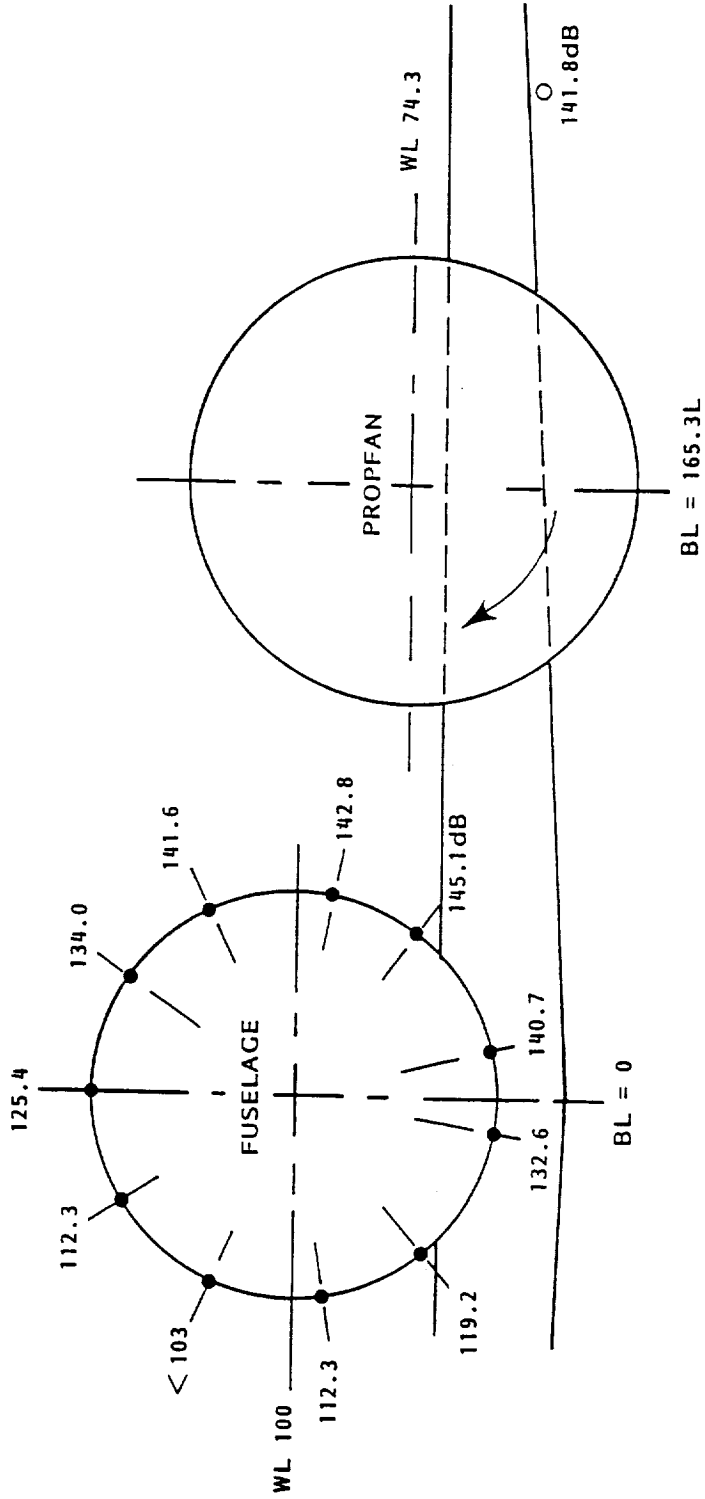


Figure 95. Fuselage Circumferential Distribution of Measured SPL in Propfan Plane

FIRST ORDER OF BPF (226 Hz)
NACELLE TILT = -1°
ALTITUDE = 10,654m (34,954 FT)
AIRSPEED = 0.80 MN

VROT = 243 MPS (797 FPS)
POWER = 2292 KW (3073 HP)
MTH = 1.137

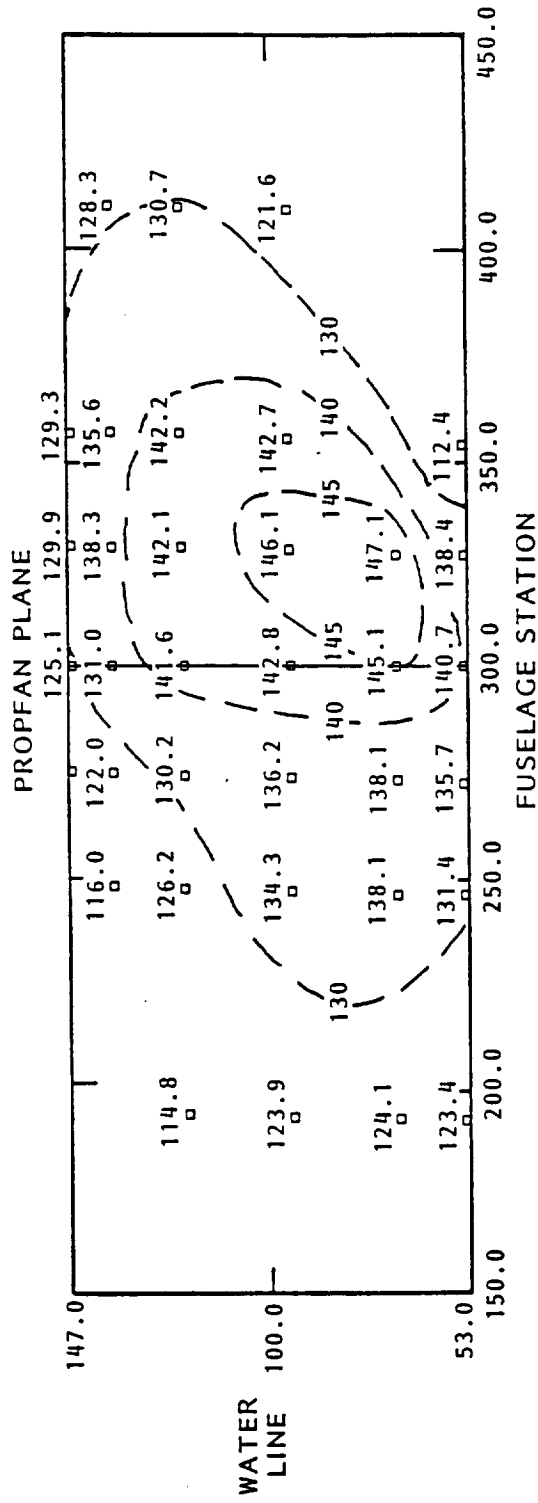


Figure 96. Fuselage Surface Measured SPL

FIRST 5 ORDERS OF BPF

NACELLE TILT = -1°

ALTITUDE = 10,654m (34,954 FT)

AIRSPEED = 0.80 MN

VROT = 243 MPS (797 FPS)

POWER = 2292 KW (3073 HP)

MTH = 1.137

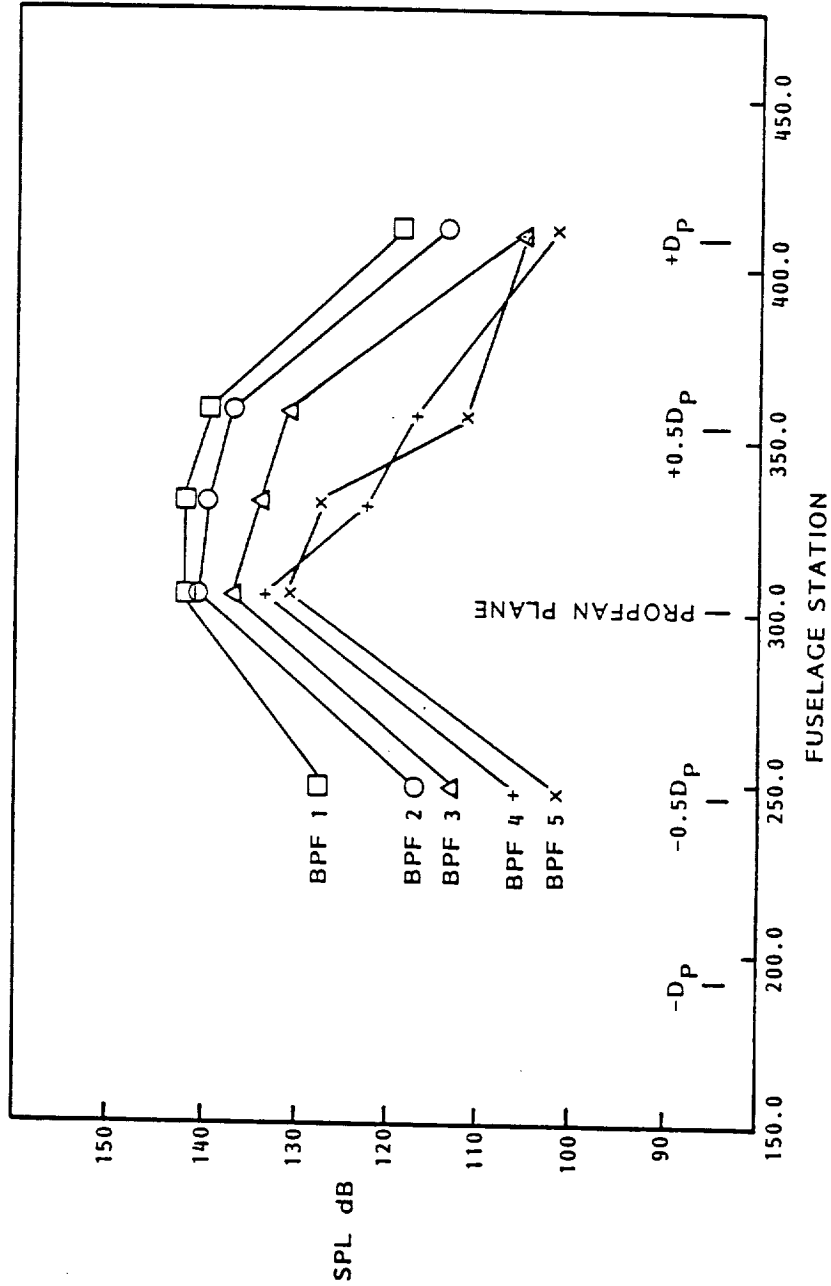


Figure 97. Wing Boom Axial Distribution of Measured SPL

FIRST ORDER OF BPF (226 Hz)
 NACELLE TILT = -1°
 ALTITUDE = 10,654m (34,954 FT)
 AIRSPEED = 0.80 MN

VROT = 243 MPS (797 FPS)
 POWER = 2292 KW (3073 HP)
 MTH = 1.137

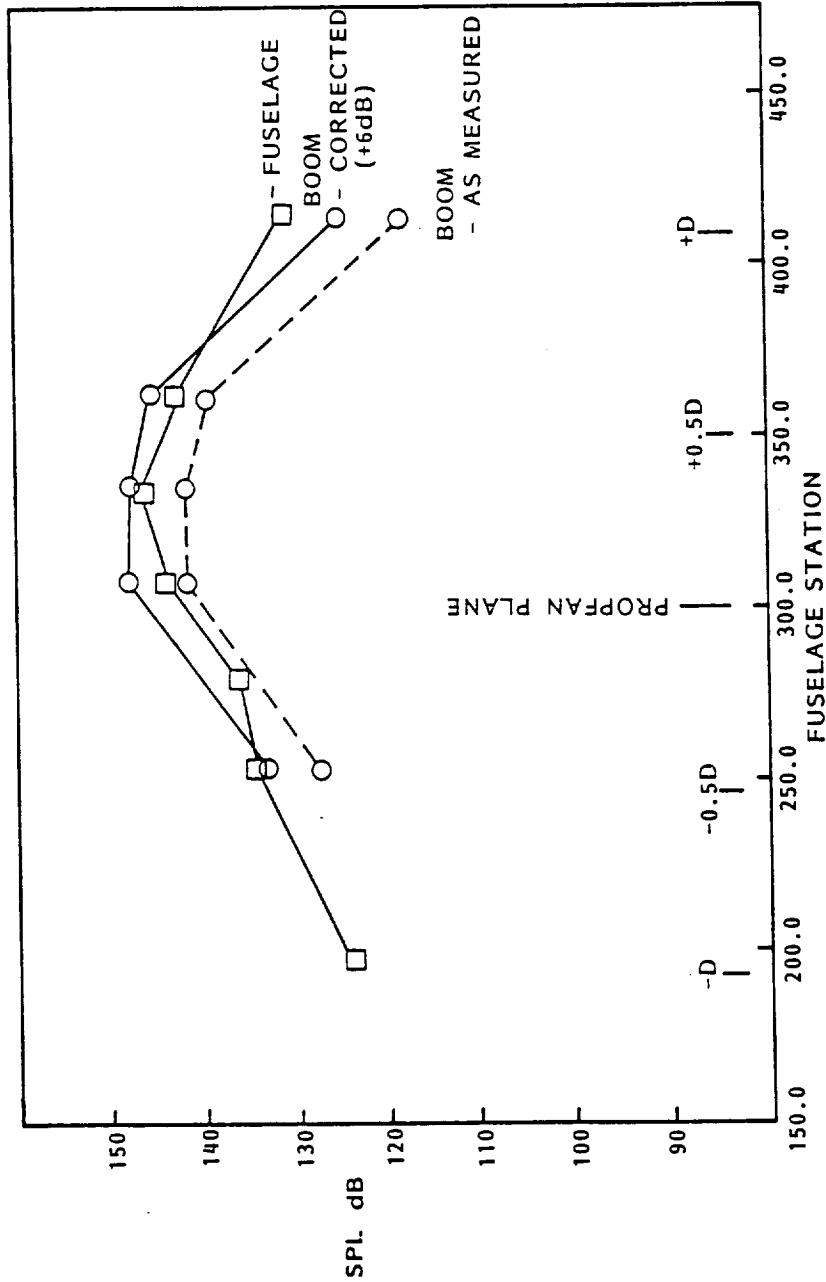


Figure 98. Comparison of Measured SPLs on Fuselage WL 94 and on Wing Boom

(b) Tip Speed Variation at Constant Power

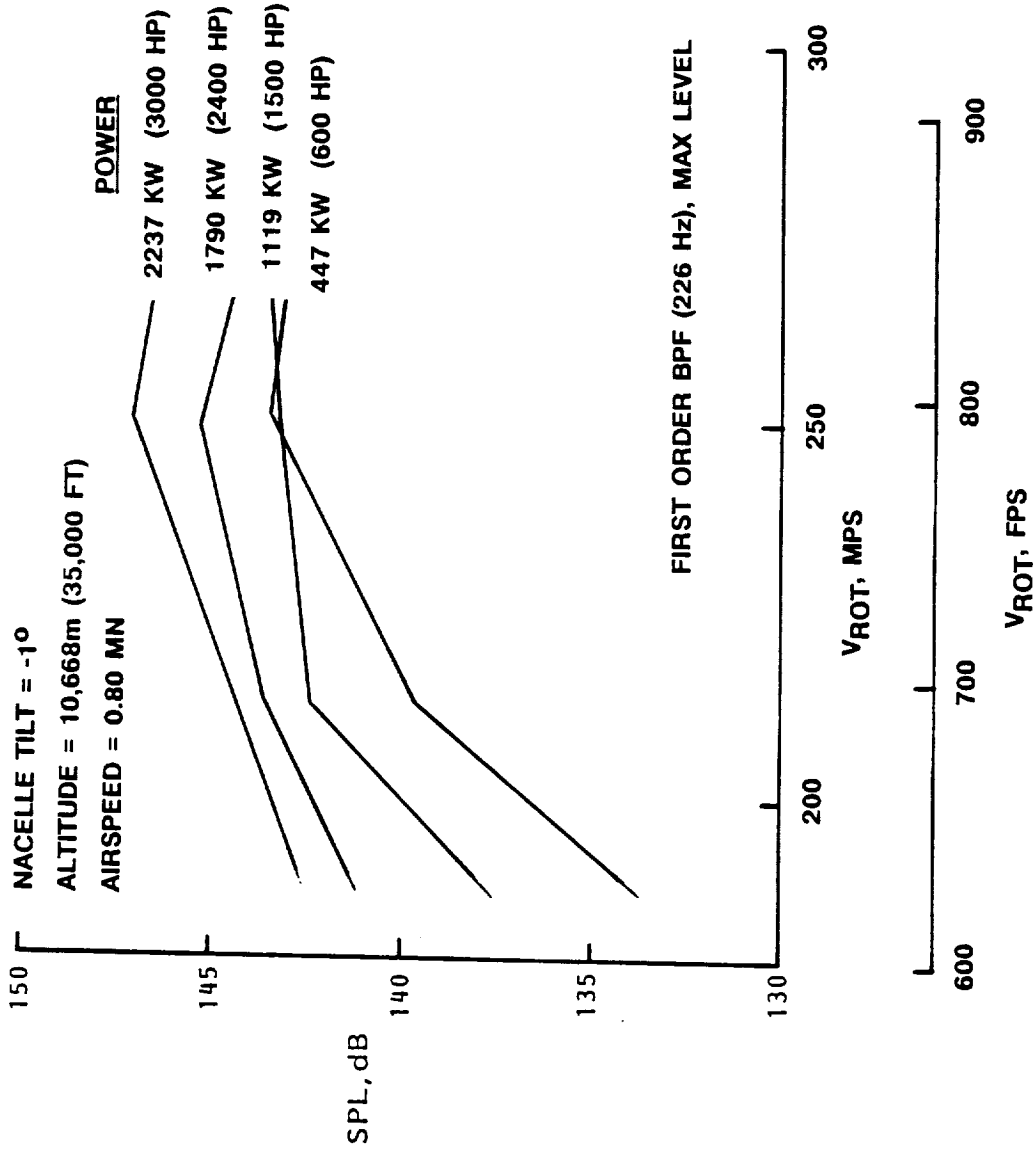


Figure 99. Fuselage Measured SPL Dependence on Propfan Tip Speed and Power (Continued)

(a) Power Variation at Constant Tip Speed

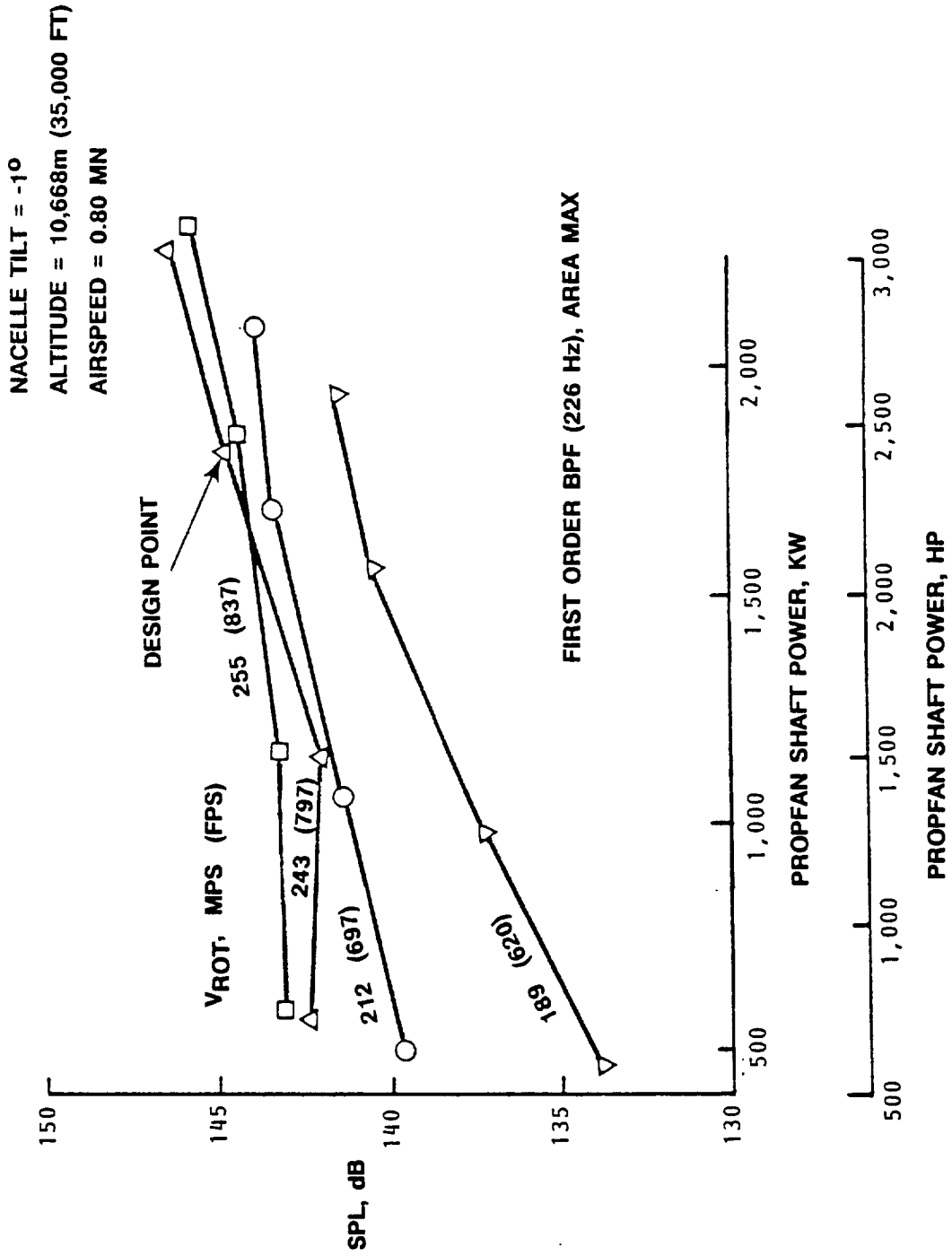


Figure 99. Fuselage Measured SPL Dependence on Propfan Tip Speed and Power

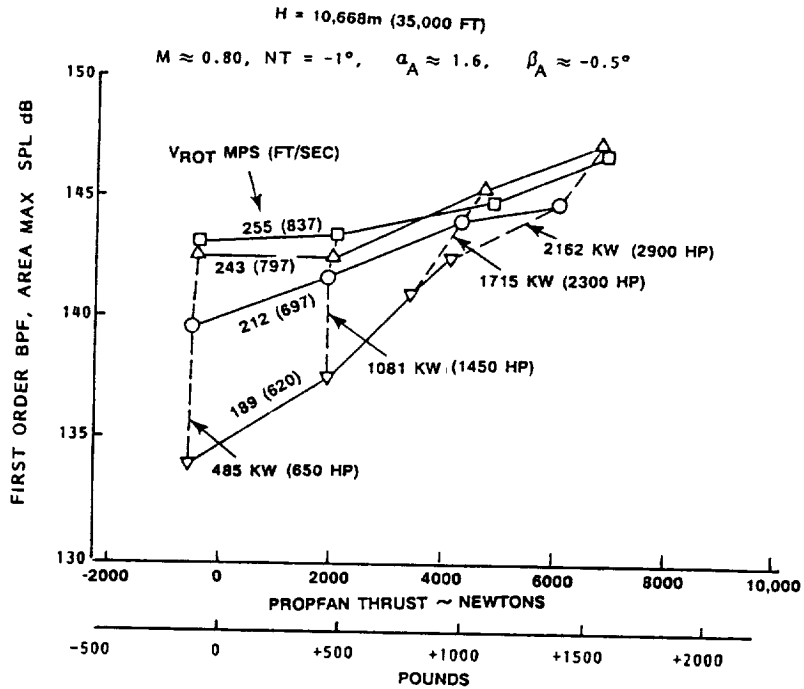


Figure 100. Fuselage Measured SPL Dependence on Propfan Thrust and Tip Speed

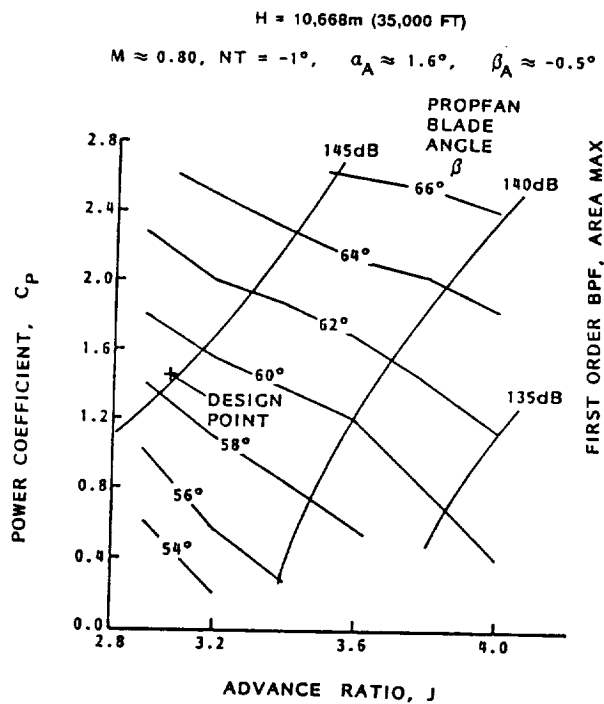


Figure 101. Fuselage Measured SPL Dependence Upon Propfan Advance Ratio and Power Coefficient

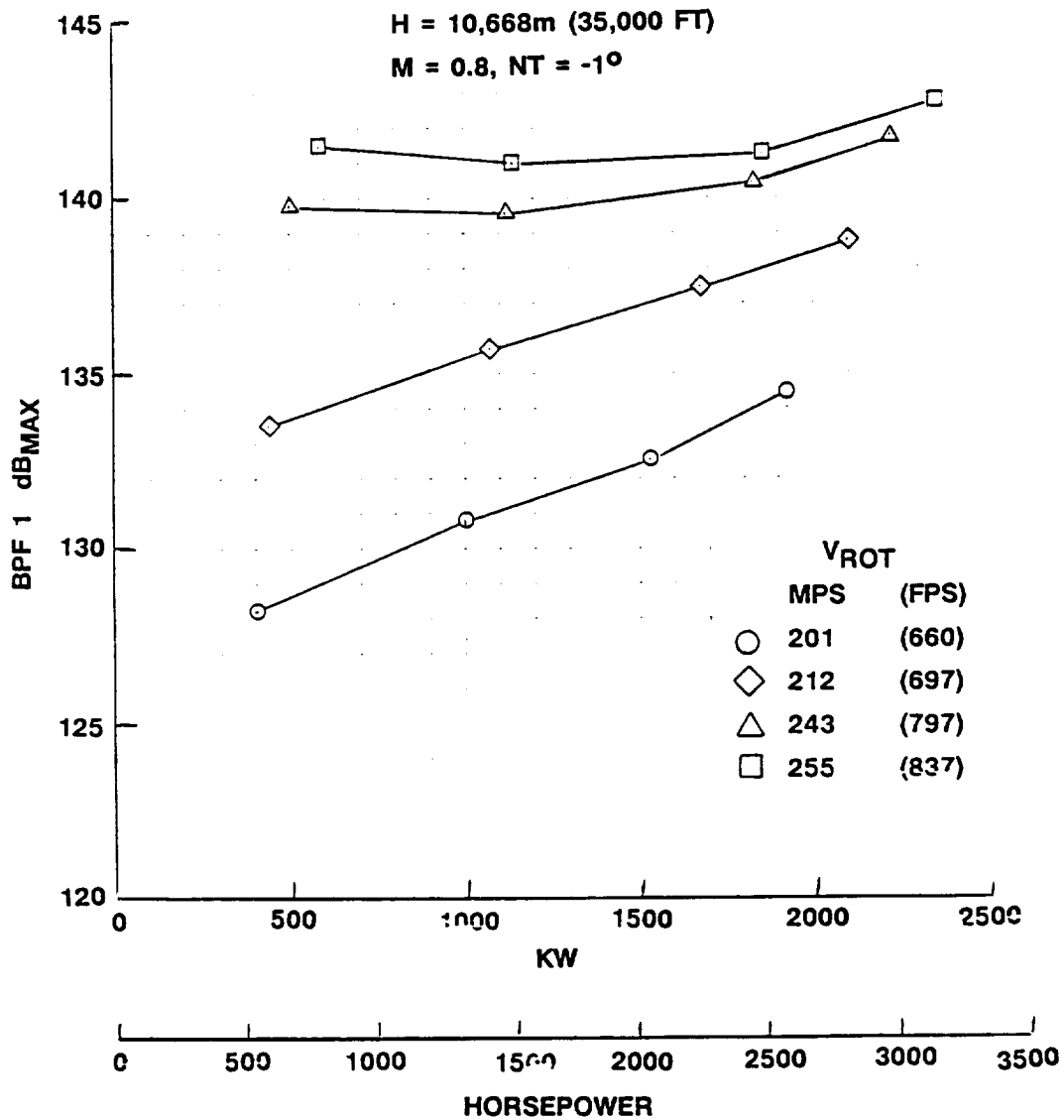
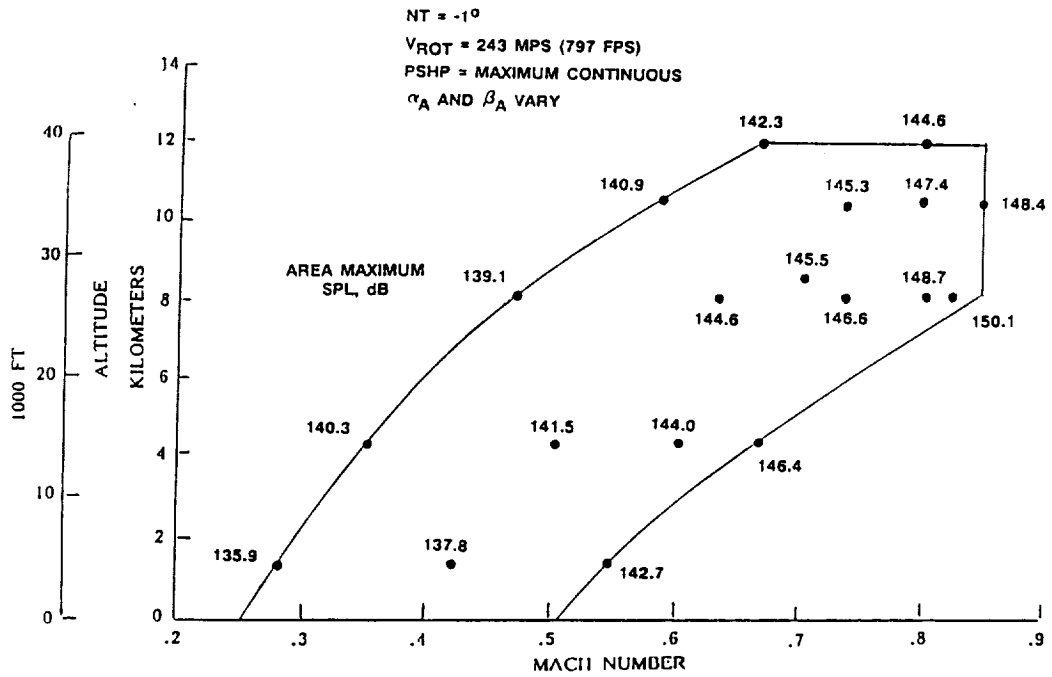
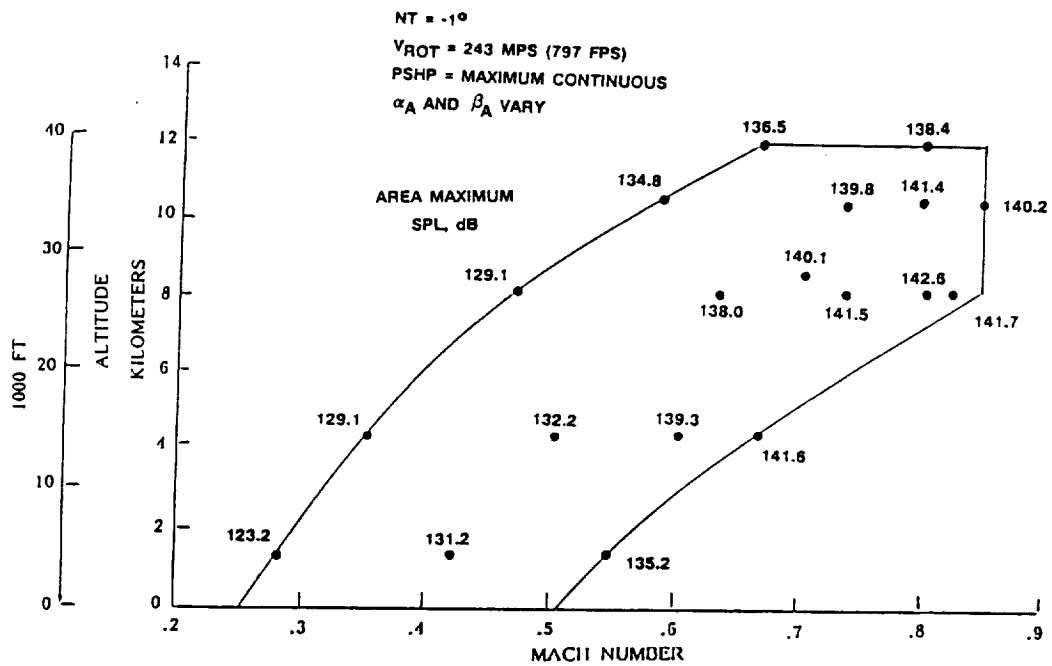


Figure 102. Wing Boom Measured SPL Dependence on Propfan Tip Speed and Power

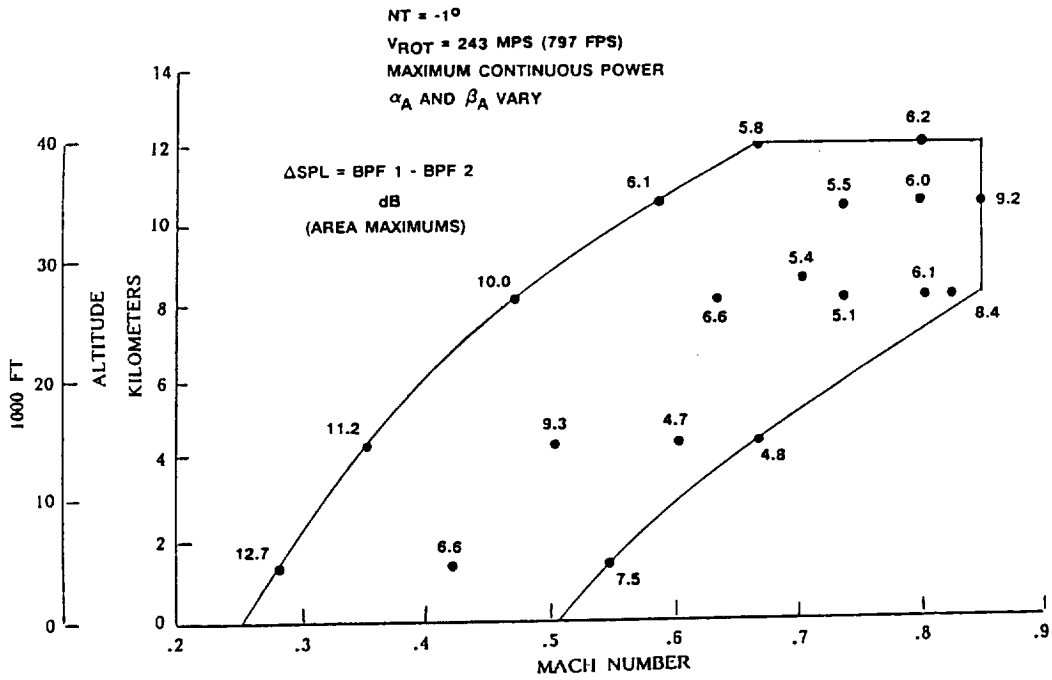


(a) BPF 1



(b) BPF 2

Figure 103. Fuselage Measured SPL Variation Over Flight Envelope



(c) Δ SPL FROM BPF 2 TO BPF 1

Figure 103. Fuselage Measured SPL Variation Over Flight Envelope (Continued)

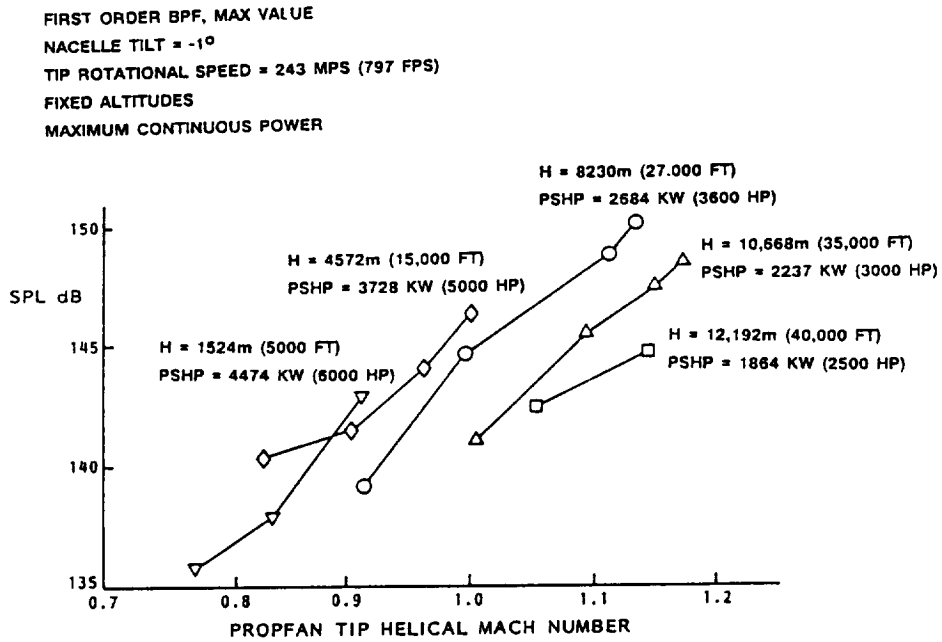


Figure 104. Effect of Propfan Helical Tip Mach Number on Fuselage SPL

SUPERSONIC PROP TIPS

H = 7620m (25,000 FT) AND 12,192m (40,000 FT)
M = 0.8

	CASE 1	CASE 2
M_{TH}	1.02	1.14
C_p	2.859	1.526
J	3.974	3.108
BPF 1 Δ dB	5.6	5.0
BPF 2 Δ dB	4.2	5.1

- Δ dB BASED ON FUSELAGE MAXIMUM SPLs
- Δ dB CORRECTED FOR $\Delta\alpha$

SUBSONIC PROP TIPS

H = 3048m (10,000 FT) AND 10,668m (35,000 FT)
M = 0.6

	CASE 3	CASE 4	CASE 5
M_{TH}	0.87	0.97	0.97
C_p	1.981	0.628	1.225
J	3.002	2.484	2.492
BPF 1 Δ dB	7.5	6.5	7.5
BPF 2 Δ dB	8.8	6.4	6.4

Figure 105. Test Conditions for Altitude Scaling Validation

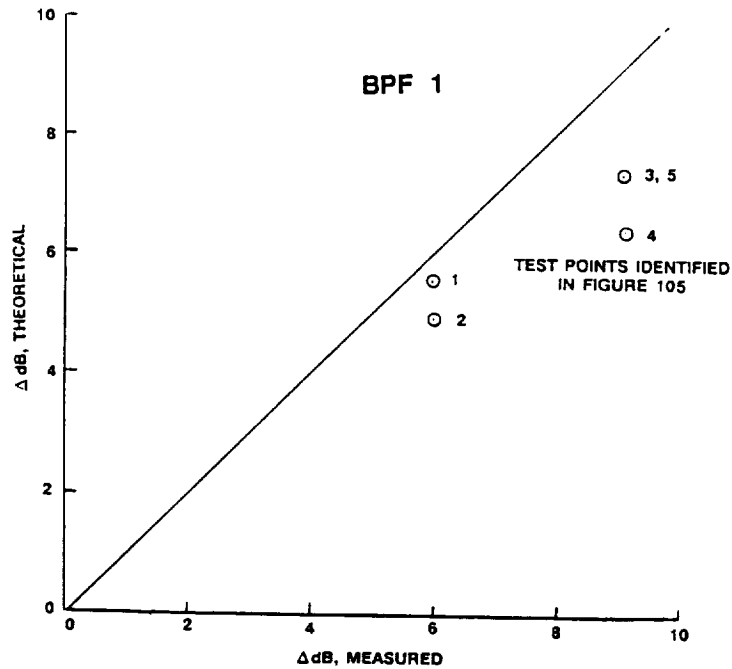


Figure 106. Results from Altitude Scaling Validation Tests

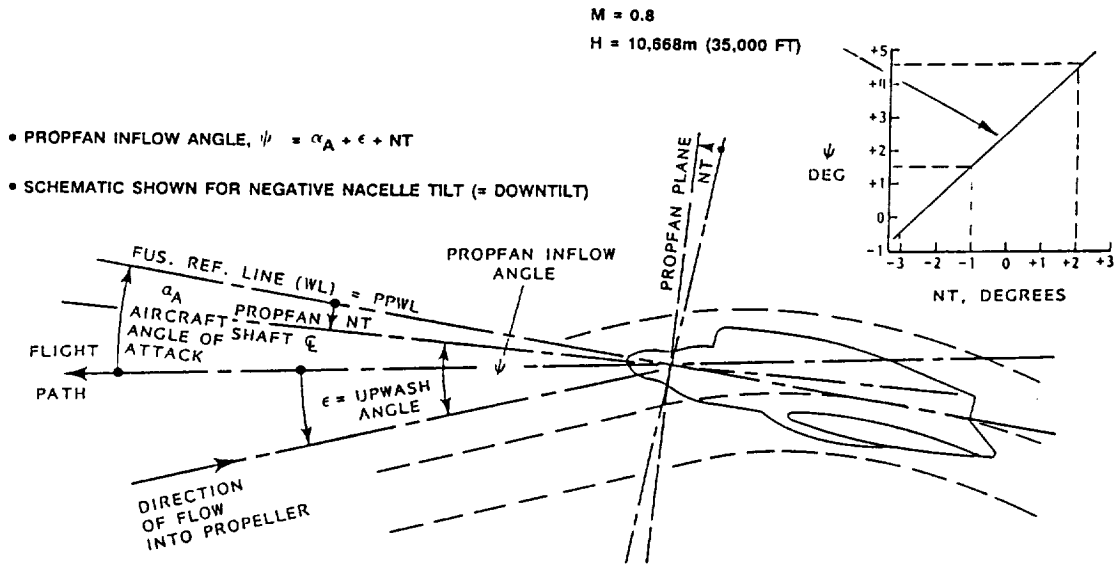


Figure 107. Effect of Nacelle Tilt on Propfan Inflow Angle

$$\alpha_{\text{BLADE LOCAL}} = \alpha_{\text{BLADE NOM}} \mp \psi ; \quad \begin{array}{l} - \text{ FOR UPGOING BLADE} \\ + \text{ FOR DOWNGOING BLADE} \end{array}$$

UPGOING BLADE - INCREASING NT:

- INCREASES ψ
- DECREASES BLADE ANGLE OF ATTACK
- DECREASES BLADE LOADING
- DECREASES LOADING NOISE

DOWNGOING BLADE - INCREASING NT:

- INCREASES ψ
- INCREASES BLADE ANGLE OF ATTACK
- INCREASES BLADE LOADING
- INCREASES LOADING NOISE

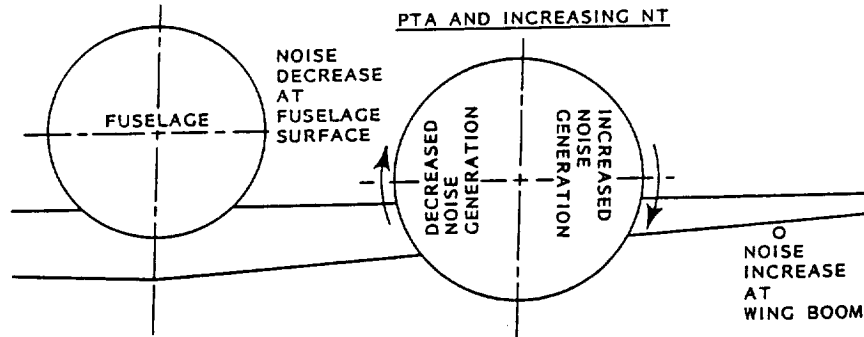


Figure 108. Expected Influence of Propfan Inflow Angle and Direction of Rotation on Near-Field Noise

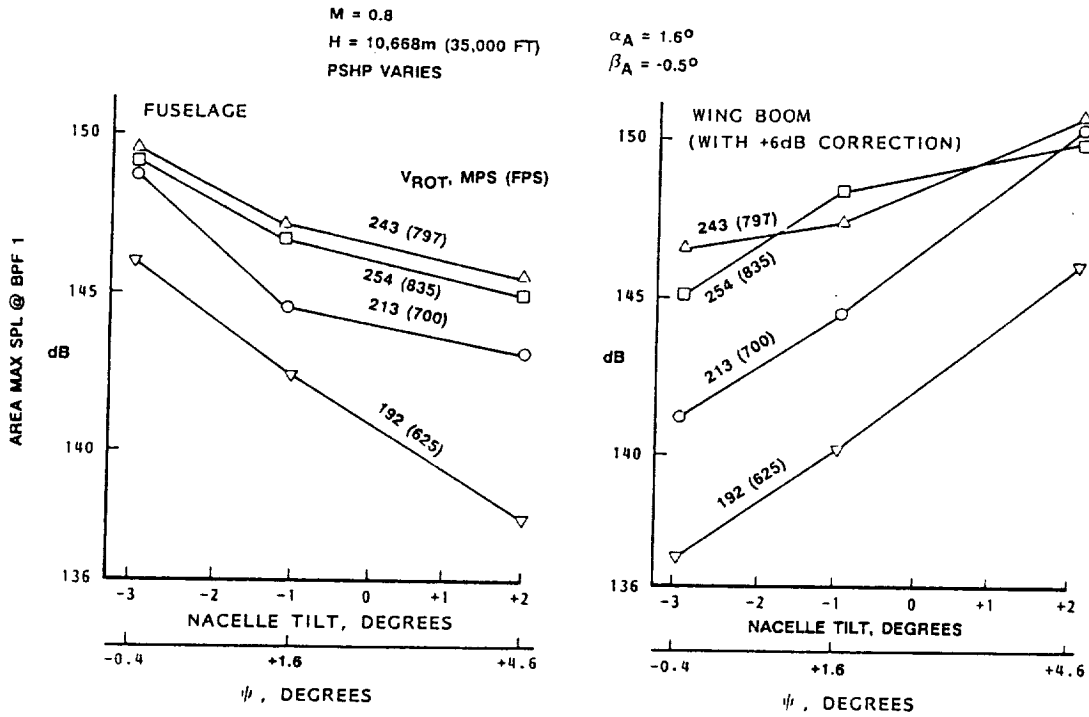


Figure 109. Effect of Nacelle Tilt on Fuselage and Wing Boom SPL

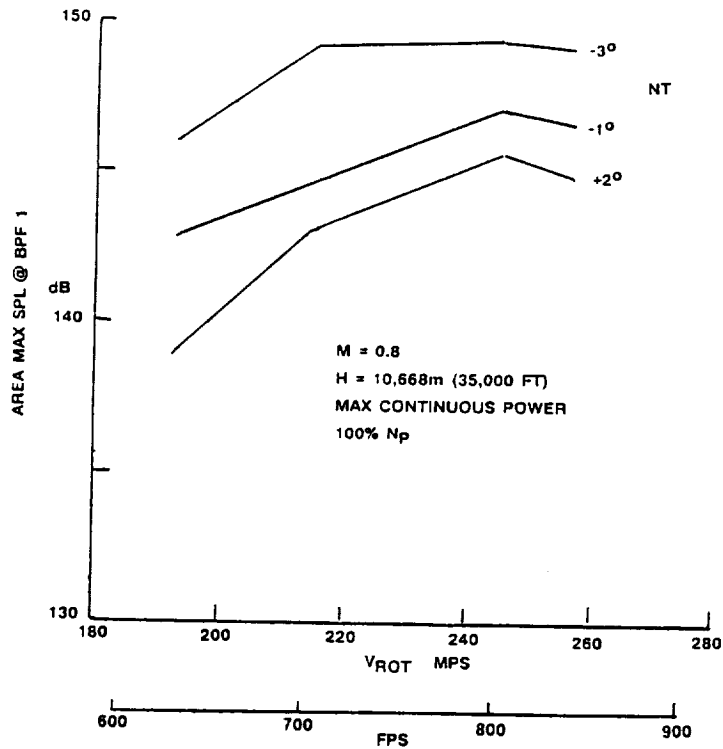


Figure 110. Effect of Nacelle Tilt on Fuselage SPL

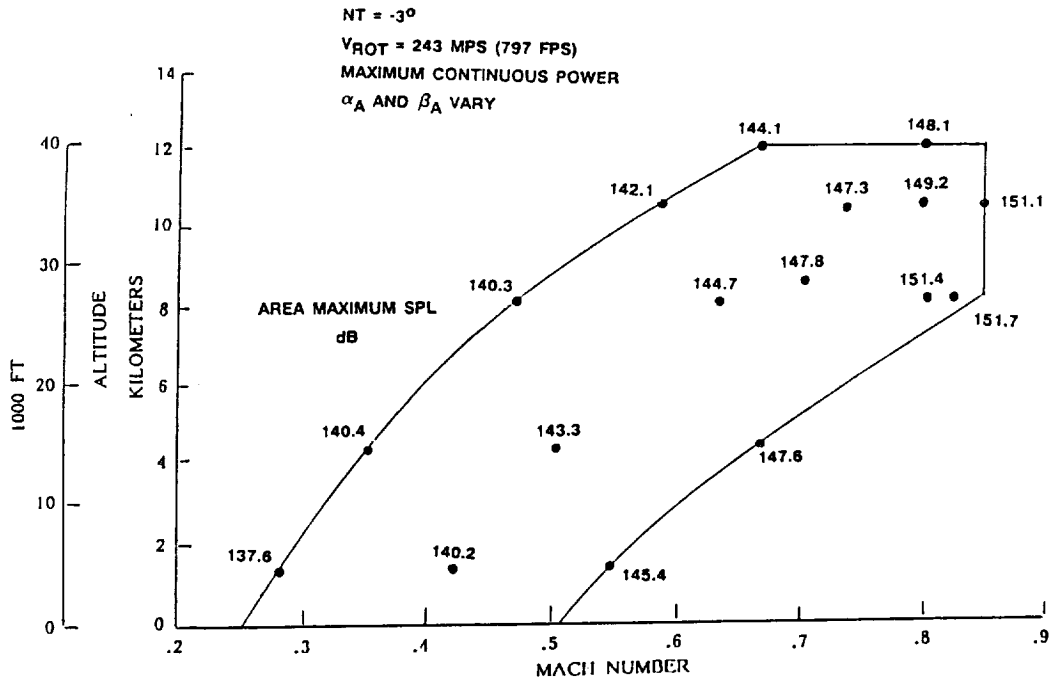


Figure 111. Fuselage SPL Variation Over Flight Envelope, NT = -3°

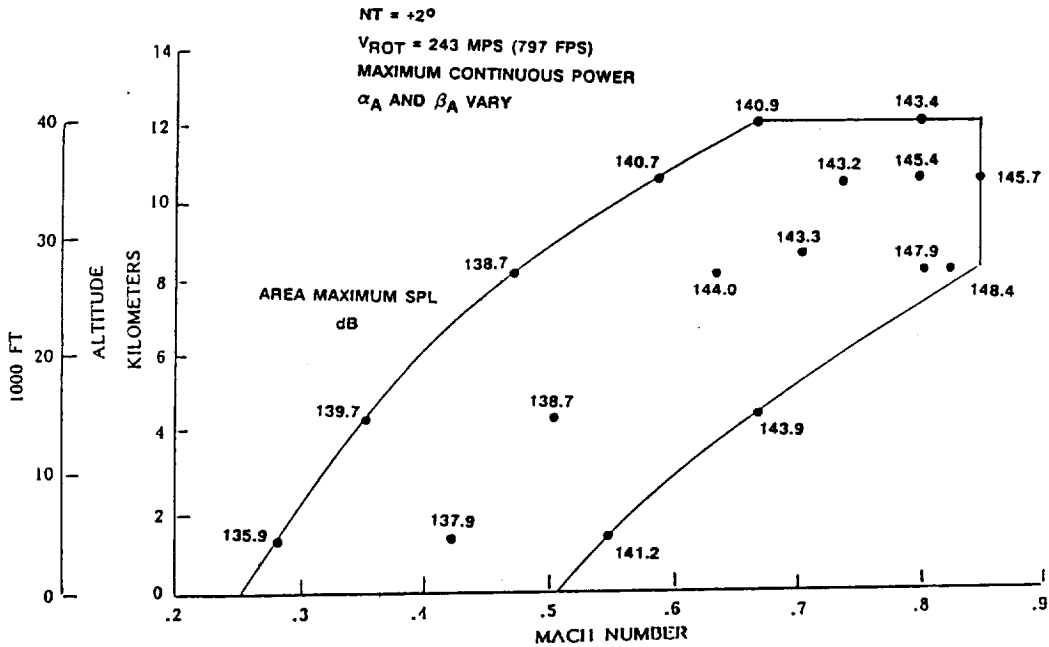


Figure 112. Fuselage SPL Variation Over Flight Envelope, NT = +2°

Use and/or disclosure is governed by the statement on the title page of this document.

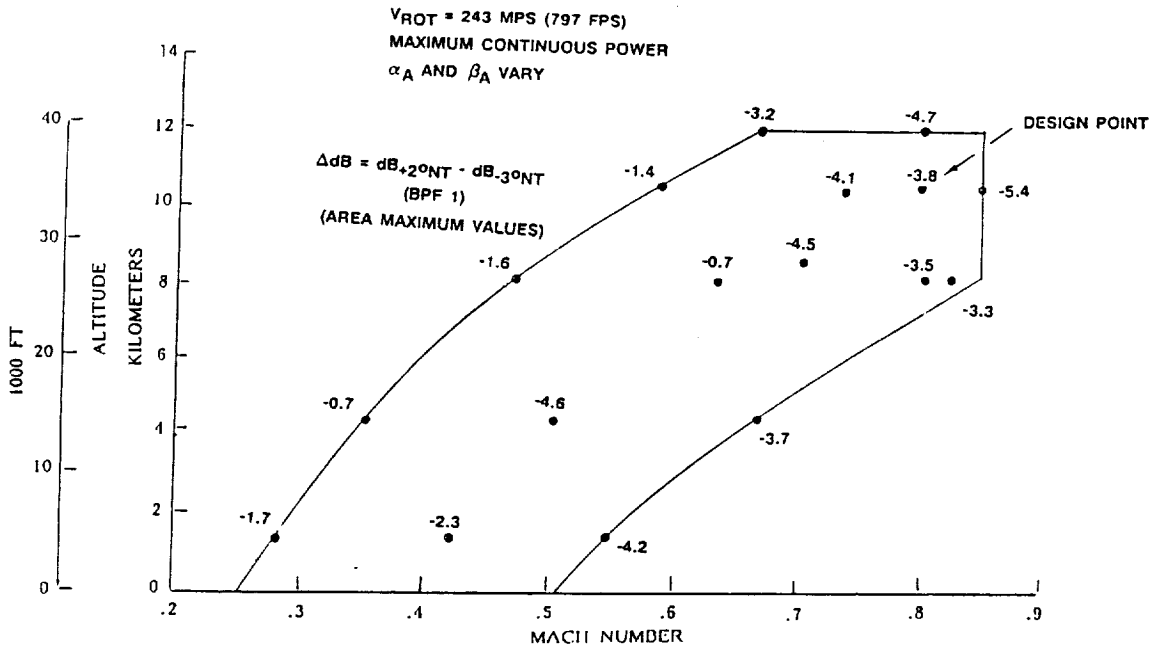


Figure 113. Effect of Nacelle Tilt on Fuselage SPL Over Flight Envelope

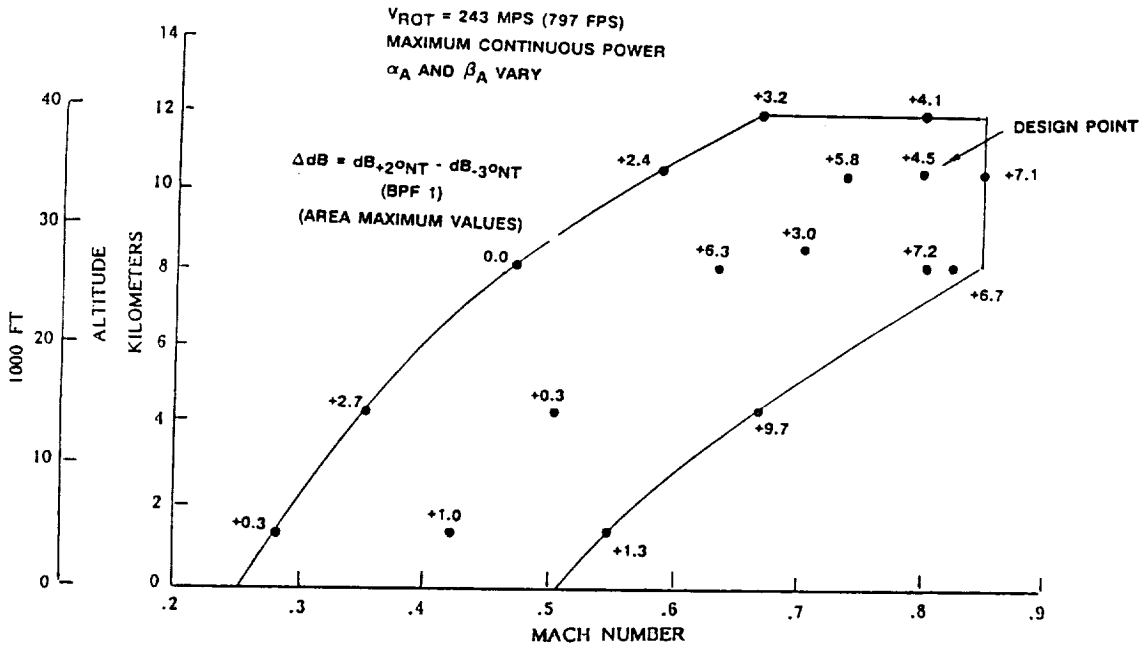


Figure 114. Effect of Nacelle Tilt on Boom SPL Over Flight Envelope

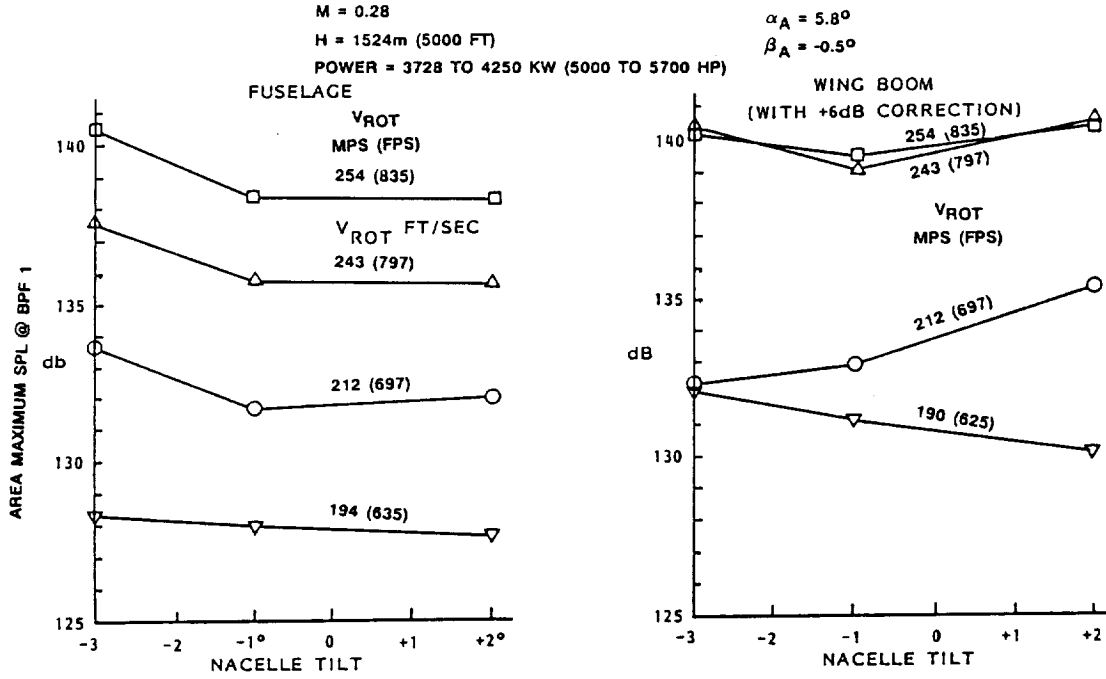


Figure 115. Effect of Nacelle Tilt on Fuselage and Boom SPLs

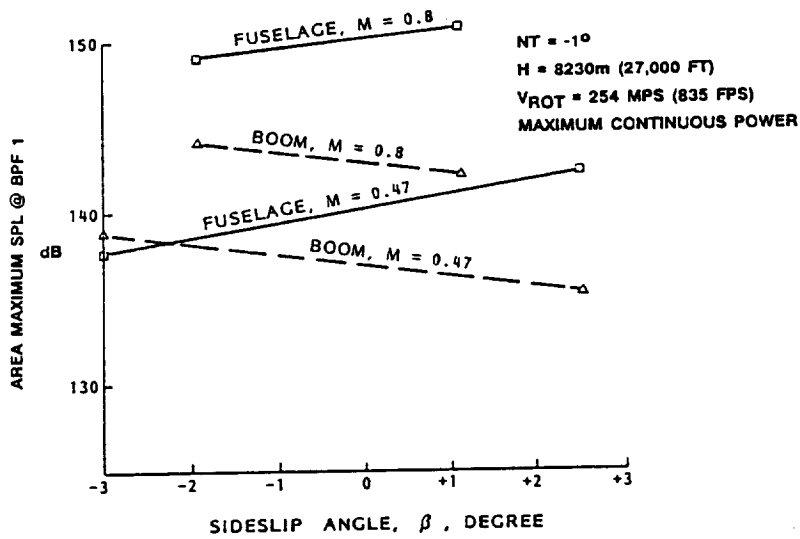


Figure 116. Effect of Sideslip on Fuselage and Boom SPLs

- o HAMILTON STANDARD (HANSON) FREQUENCY DOMAIN PROPELLER NOISE RADIATION THEORY
- o SOURCES
 - THICKNESS NOISE (MONOPOLE SOURCE)
 - BASED ON BLADE CHORD, THICKNESS, AIRFOIL SECTION, AND SWEEP DISTRIBUTIONS
 - STEADY LOADING NOISE (DIPOLE SOURCE)
 - BASED ON BLADE AERODYNAMIC LOADING DISTRIBUTION
 - SPANWISE PRESSURE DISTRIBUTION DERIVED FROM 2D LIFTING LINE METHODS
 - CHORDWISE PRESSURE DISTRIBUTION DERIVED FROM TRANSONIC AIRFOIL CODES
 - UNSTEADY LOADING NOISE (DIPOLE SOURCE)
 - BASED ON QUASI-STEADY AERODYNAMIC LOADING DISTRIBUTION
 - LASC SUPPLIED FLOW-FIELD INFORMATION
 - NON-LINEAR NOISE (QUADRUPOLE SOURCE)
 - BASED ON ACOUSTIC SHEAR TENSOR
- o PROPAGATION
 - FUSELAGE PREDICTIONS INCLUDE BOUNDARY LAYER REFRACTION AND FUSELAGE SCATTERING EFFECTS
 - WING BOOM PREDICTIONS ARE FREE-FIELD
- o PREDICTION
 - DISCRETE TONES AT BPF
 - AMPLITUDE AND RELATIVE PHASE OF PROPFAN TOTAL NOISE
- o PREDICTION METHODOLOGY DOES NOT INCLUDE:
 - EFFECT OF LEADING EDGE AND TIP EDGE VORTICES ON LOADING DISTRIBUTIONS (LIFTING SURFACE)
 - REFLECTIONS FROM FUSELAGE, WING, AND NACELLE
 - ANY EMPIRICAL ADJUSTMENTS

Figure 117. Propfan Near-Field Acoustic Prediction Methodology

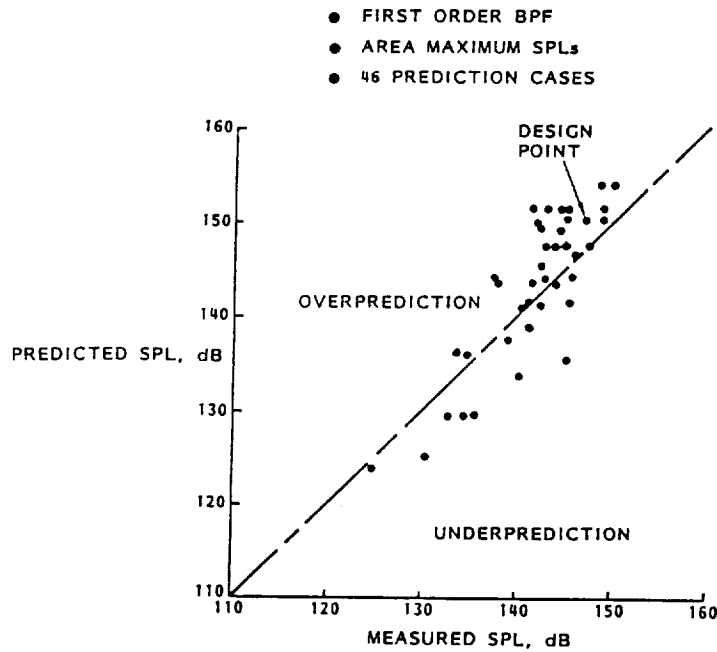


Figure 118. Summary of Fuselage Predicted and Measured SPLs

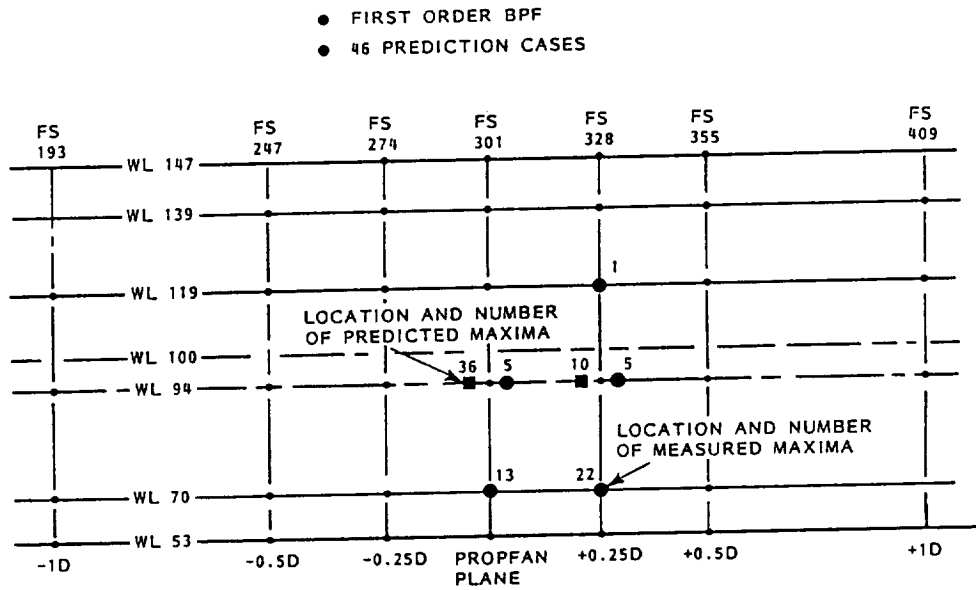


Figure 119. Summary of Predicted and Measured SPL Maxima Locations on Fuselage

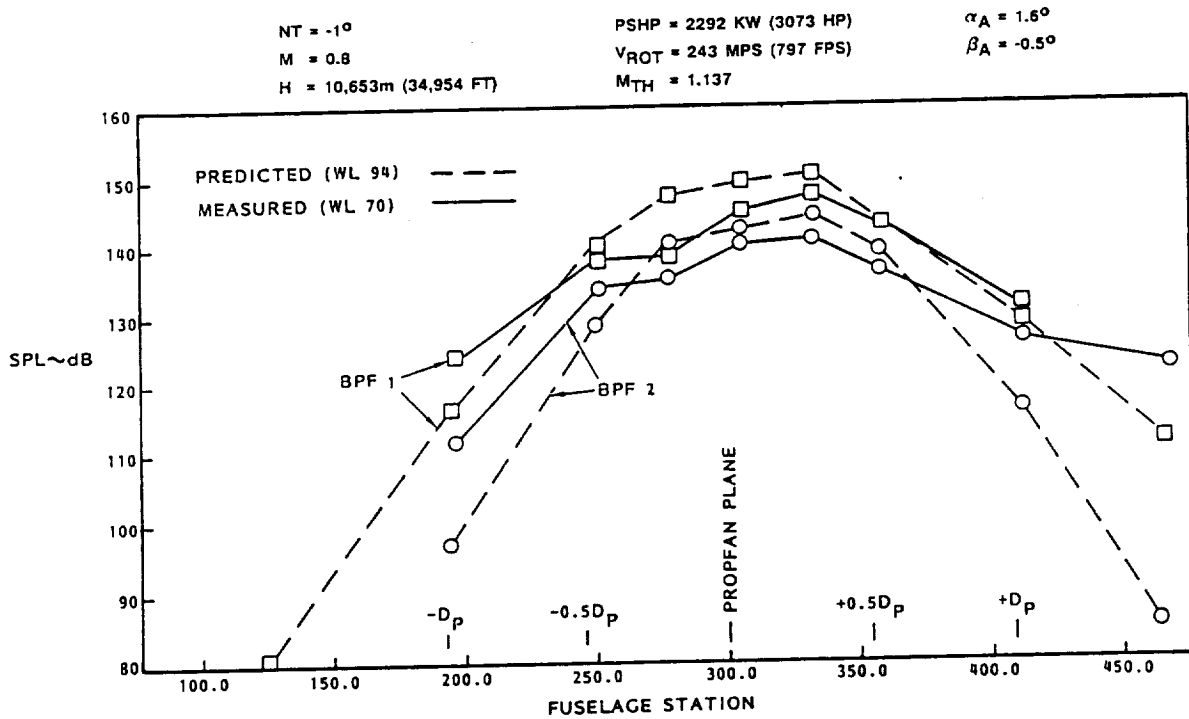


Figure 120. Fuselage Axial Distribution of Measured and Predicted SPL

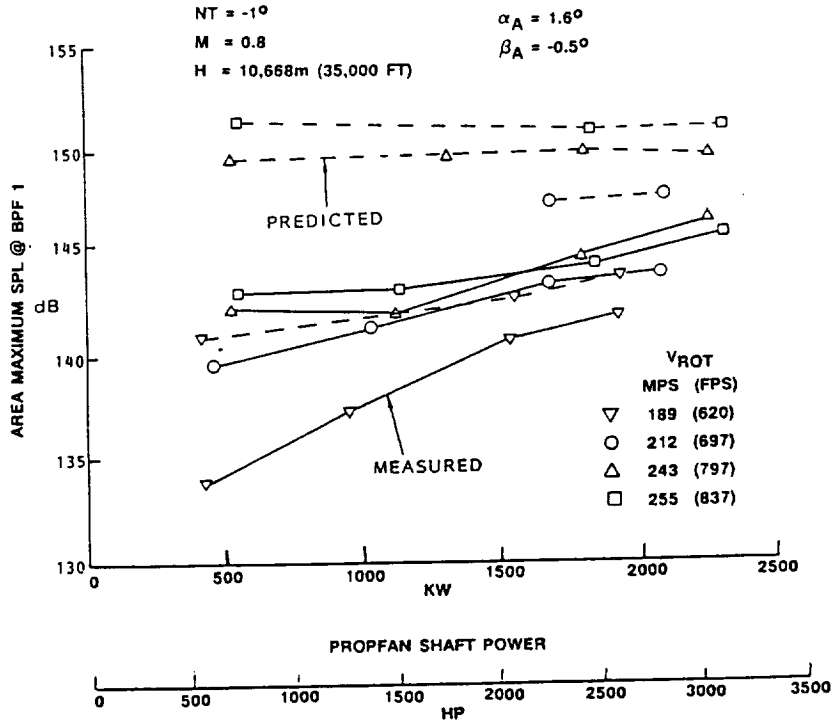


Figure 123. Predicted and Measured Fuselage SPL Dependence on Propfan Tip Speed and Power

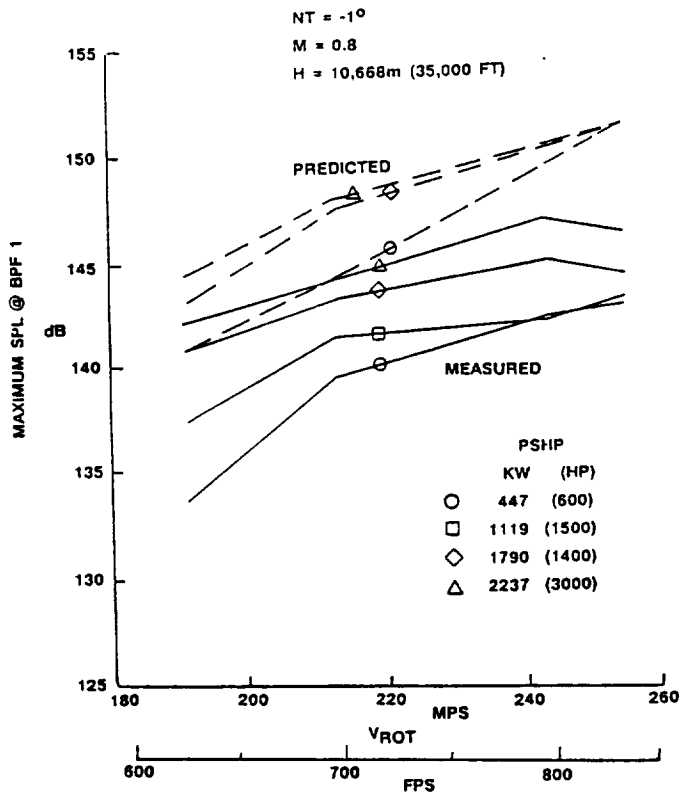


Figure 124. Variation of Predicted and Measured Fuselage SPL With Tip Speed

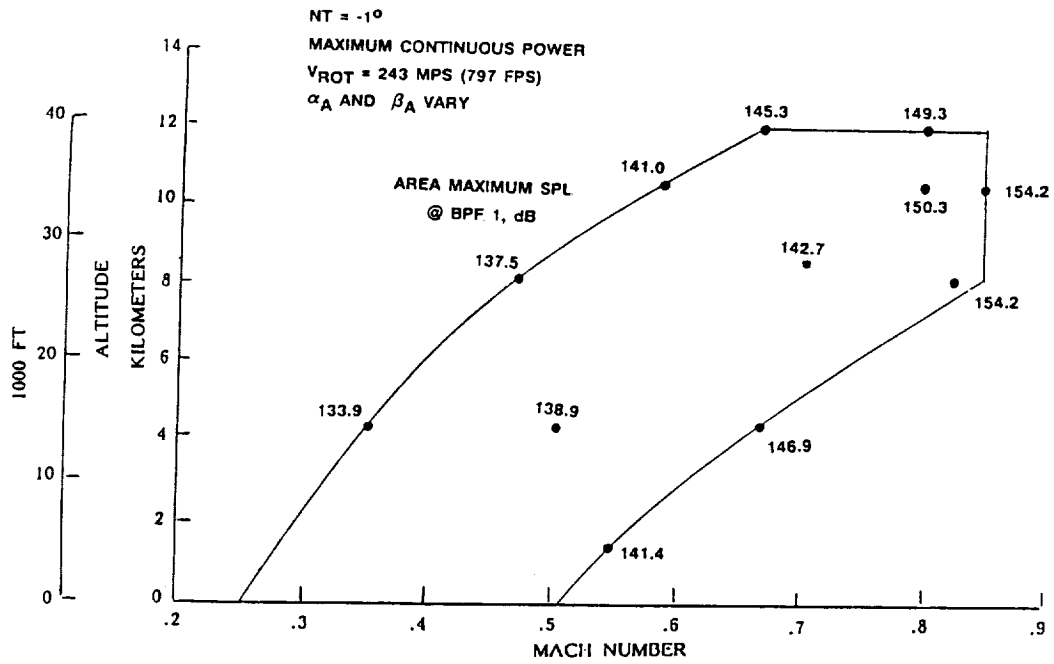


Figure 125. Fuselage Surface Predicted SPL Over Flight Envelope

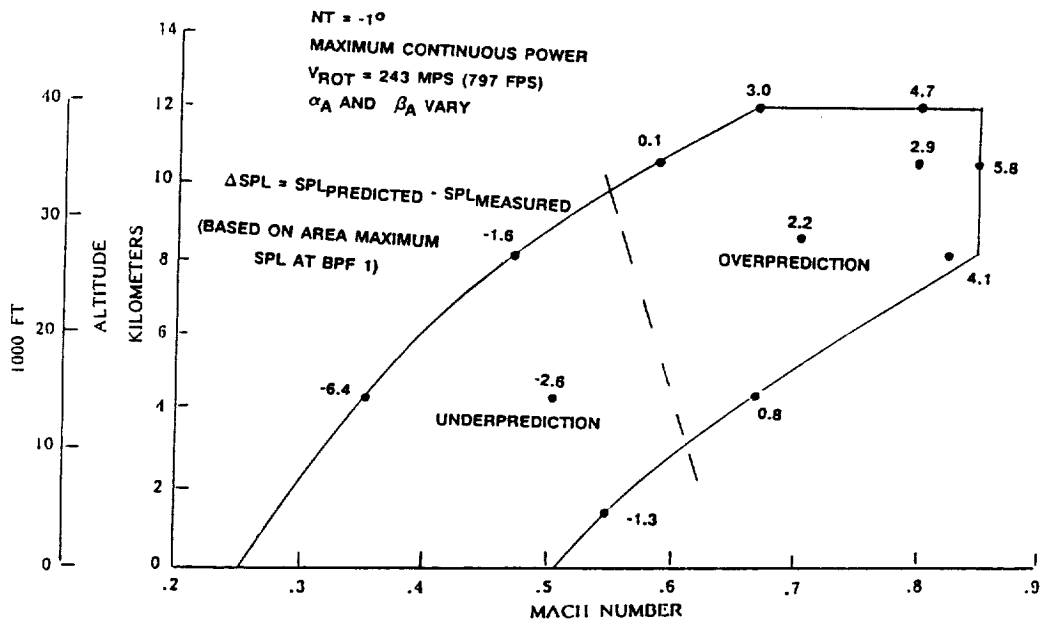


Figure 126. Fuselage Surface Predicted-Less-Measured SPL Over Flight Envelope

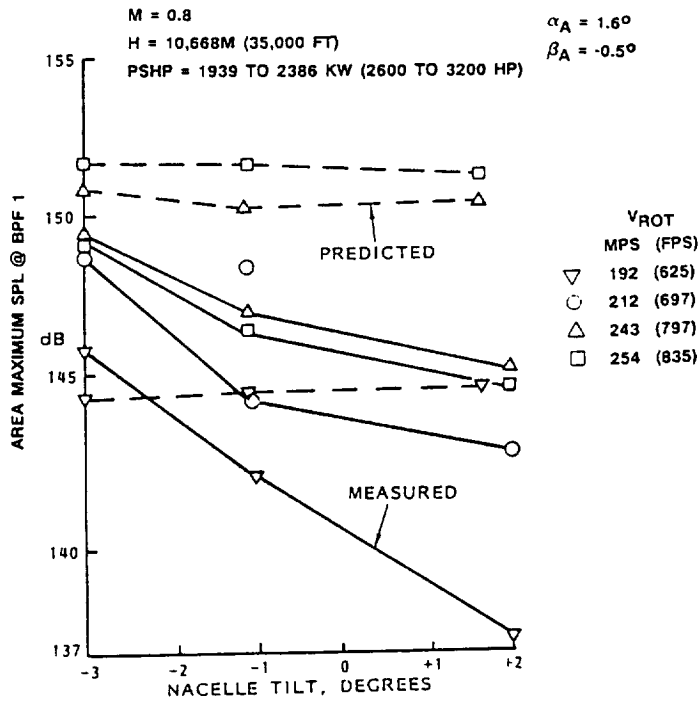


Figure 127. Predicted and Measured Effect of Nacelle Tilt on Fuselage SPL

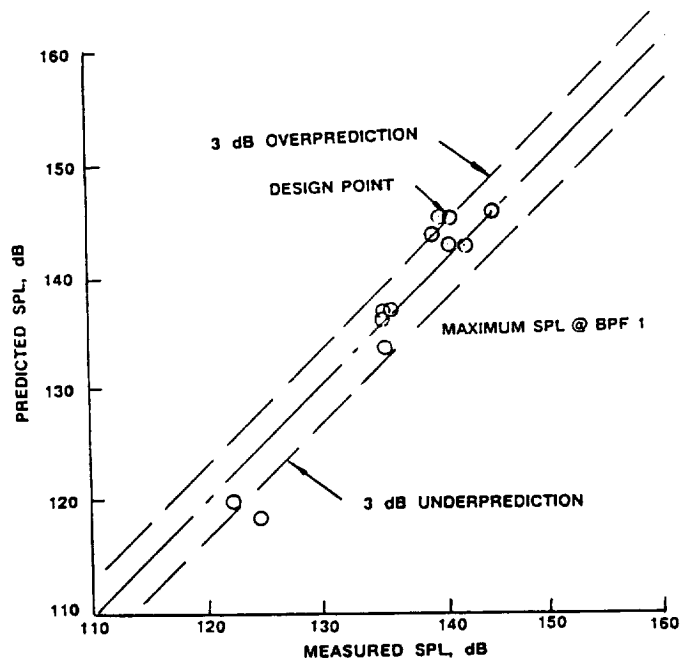


Figure 128. Summary of Predicted and Measured SPLs at the Wing Acoustic Boom

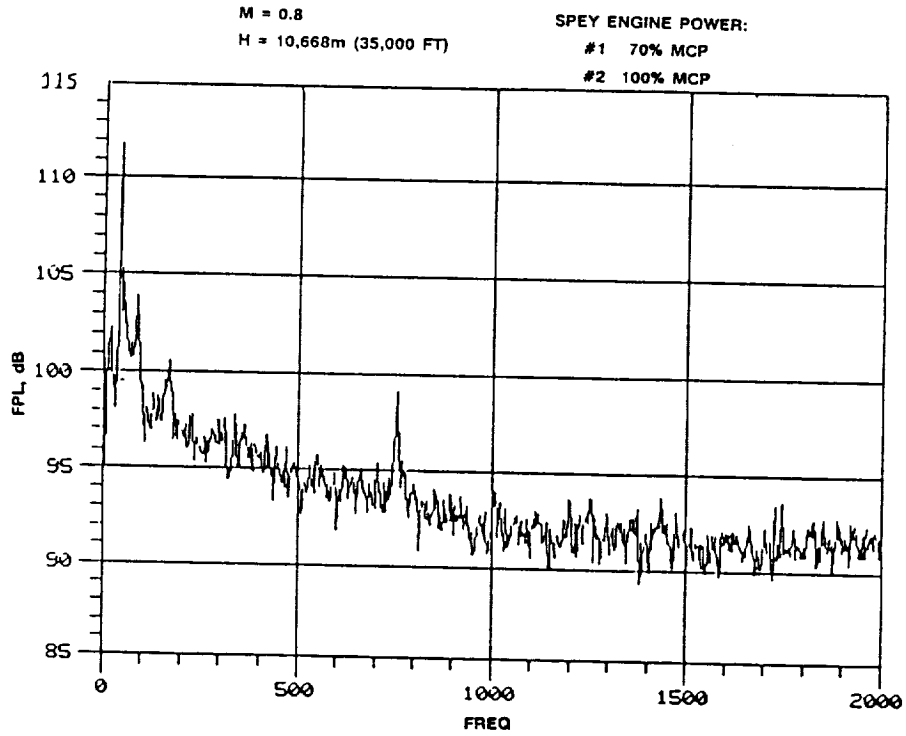


Figure 129. Wing Lower Surface Acoustic Data - Prop Off

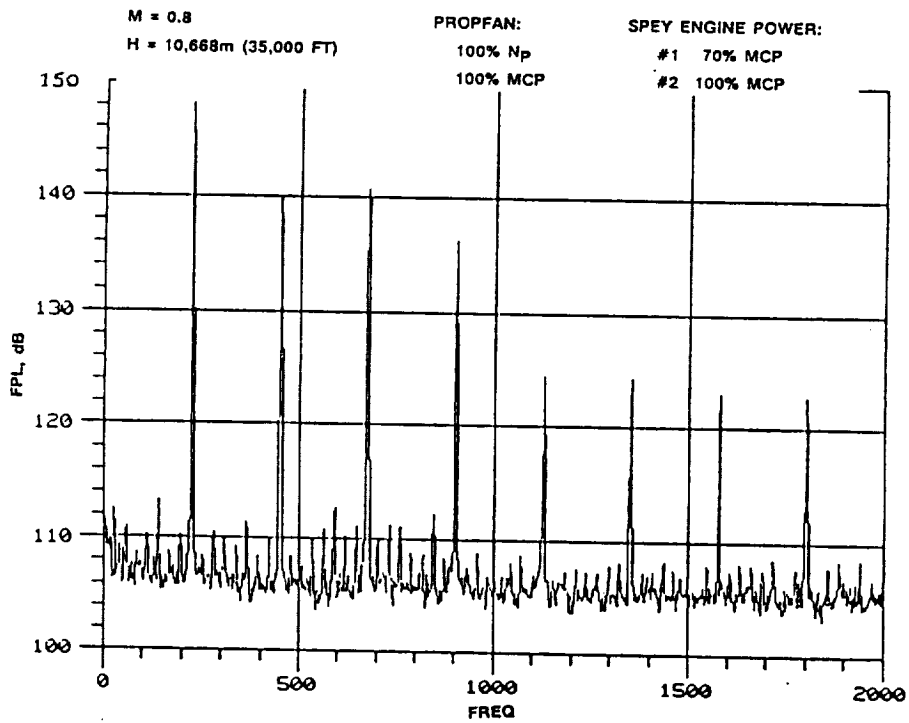


Figure 130. Wing Lower Surface Acoustic Data - Prop On



M = 0.8
H = 10,668m (35,000 FT)

SPEY ENGINE POWER:
#1 70% MCP
#2 100% MCP

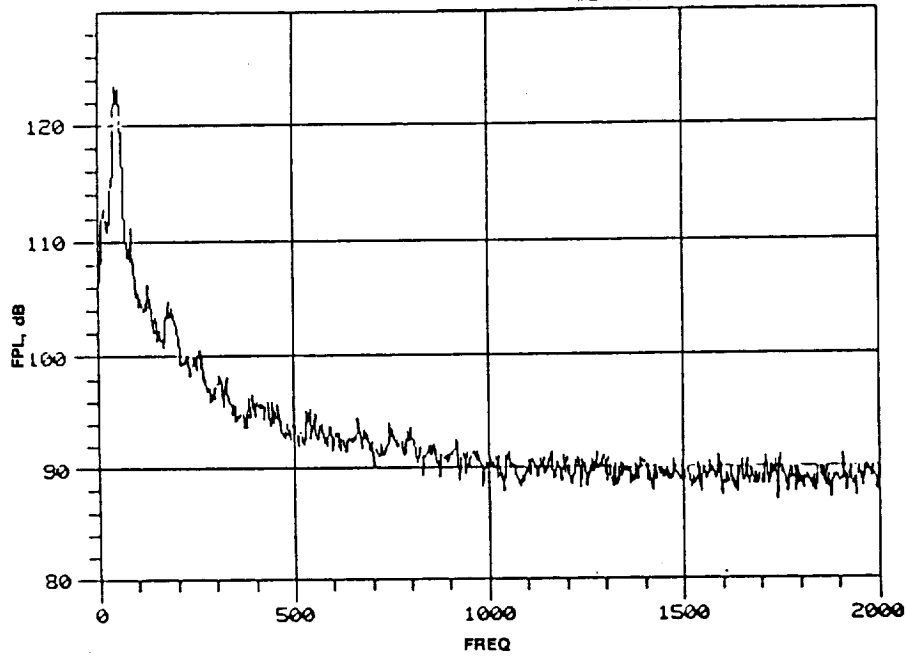


Figure 131. Wing Upper Surface Acoustic Data - Prop Off

M = 0.8
H = 10,668m (35,000 FT)

PROPFAN:
100% Np
100% MCP

SPEY ENGINE POWER:
#1 70% MCP
#2 100% MCP

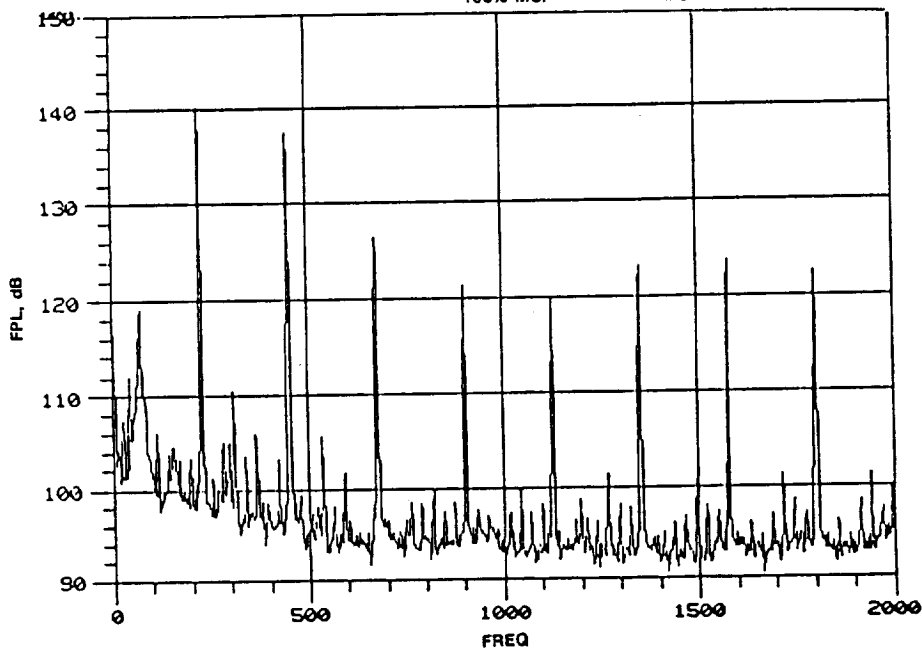


Figure 132. Wing Upper Surface Acoustic Data - Prop On

NT = -1°

M = 0.8

H = 10,653m (34,954 FT)

PSHP = 2292 KW (3073 HP)

MTH = 1.137

$\alpha_A = 1.6^\circ$, $\beta_A = -0.5^\circ$

DATA FROM WING LEADING EDGE TRANSDUCERS WHERE MAXIMUM FPL @ BPF 1 OCCURS

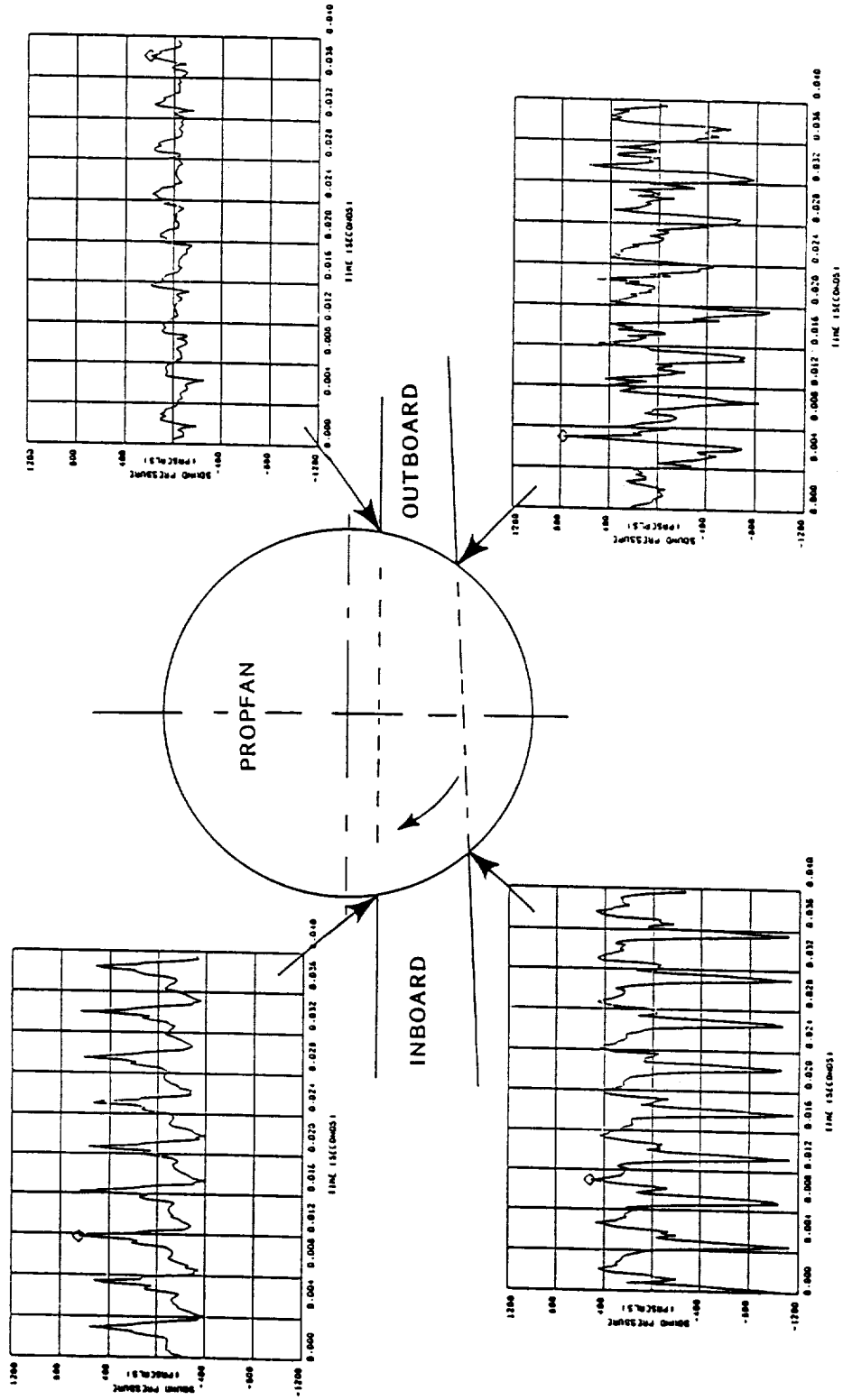


Figure 133. Slipstream/Wing Impingement; Fluctuating Pressure Time Histories

NT = -1° PSHP = 2292 KW (3073 HP) $\alpha_A = 1.6^{\circ}$, $\beta_A = -0.5^{\circ}$
 M = 0.8 VROT = 243 MPS (797 FPS) MTH = 1.137
 H = 10,653m (34,954 FT)

SPECTRA FROM WING LEADING EDGE TRANSDUCERS WHERE MAXIMUM FPL @ BPF1 OCCURS

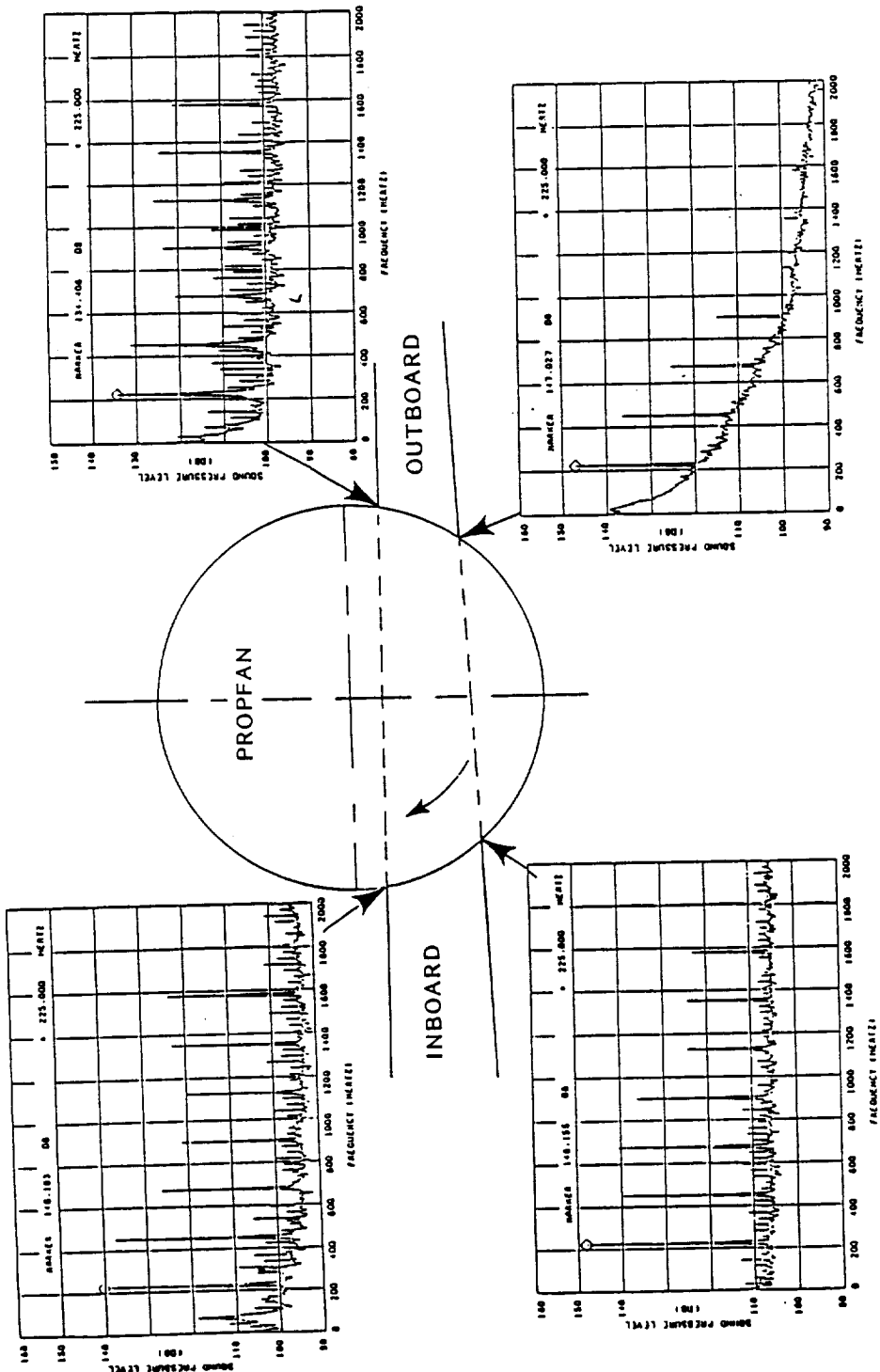


Figure 134. Slipstream/Wing Impingement; Narrow-Band Spectra of Fluctuating Pressures

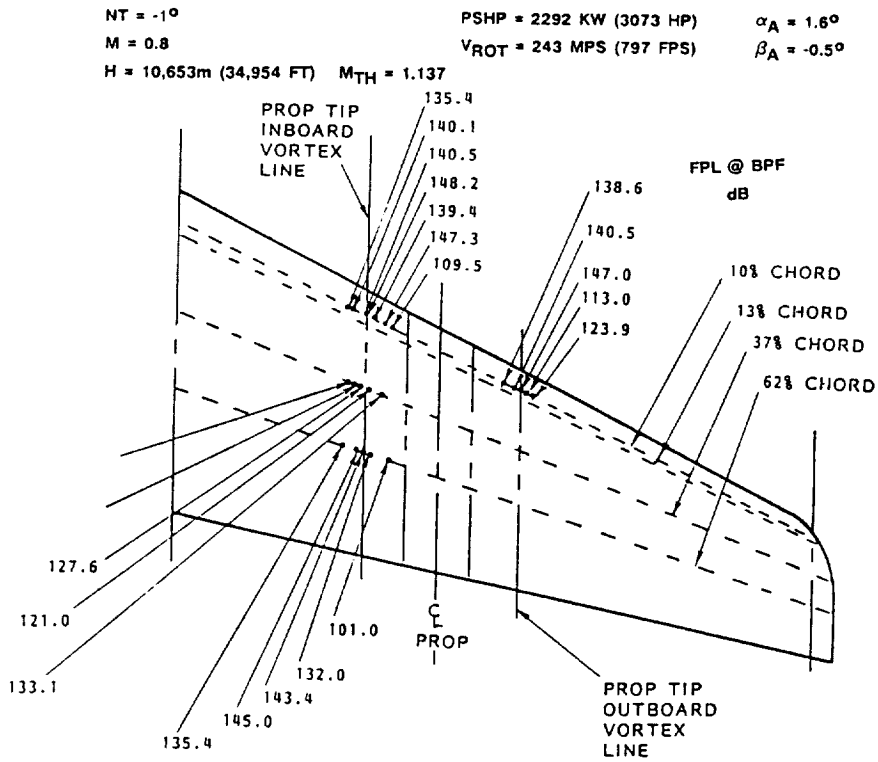


Figure 135. Wing Lower Surface Measured FPL Distribution

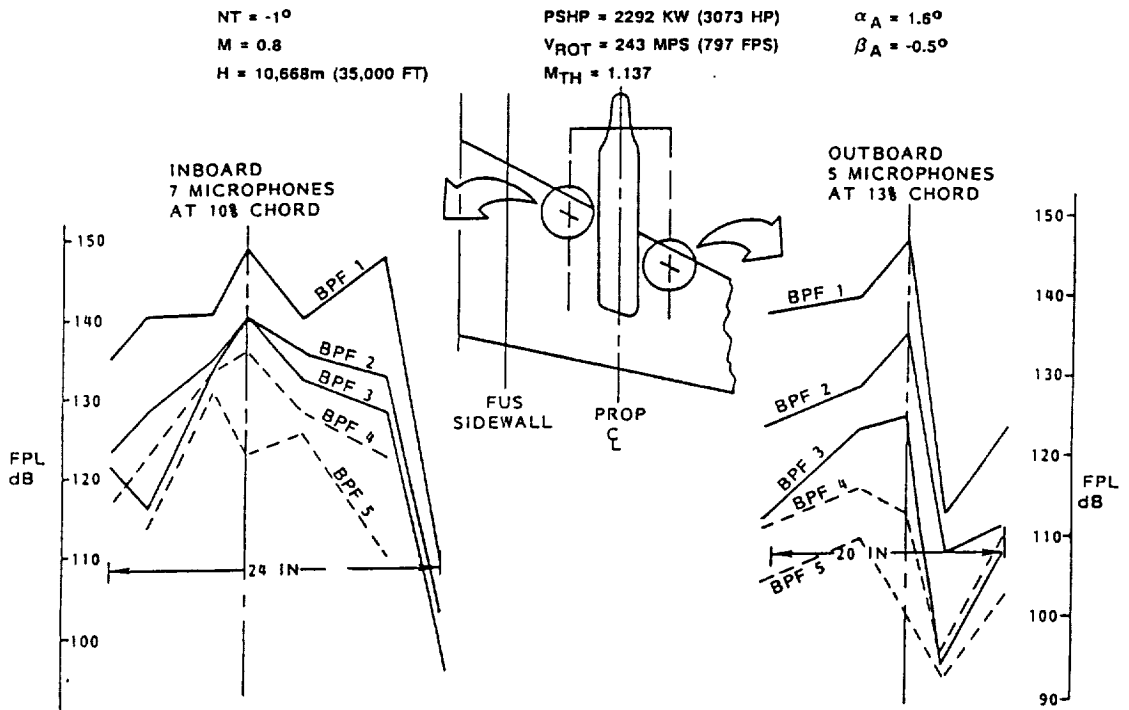


Figure 136. Wing Lower Surface Distribution of Measured FPLs Along Leading Edge

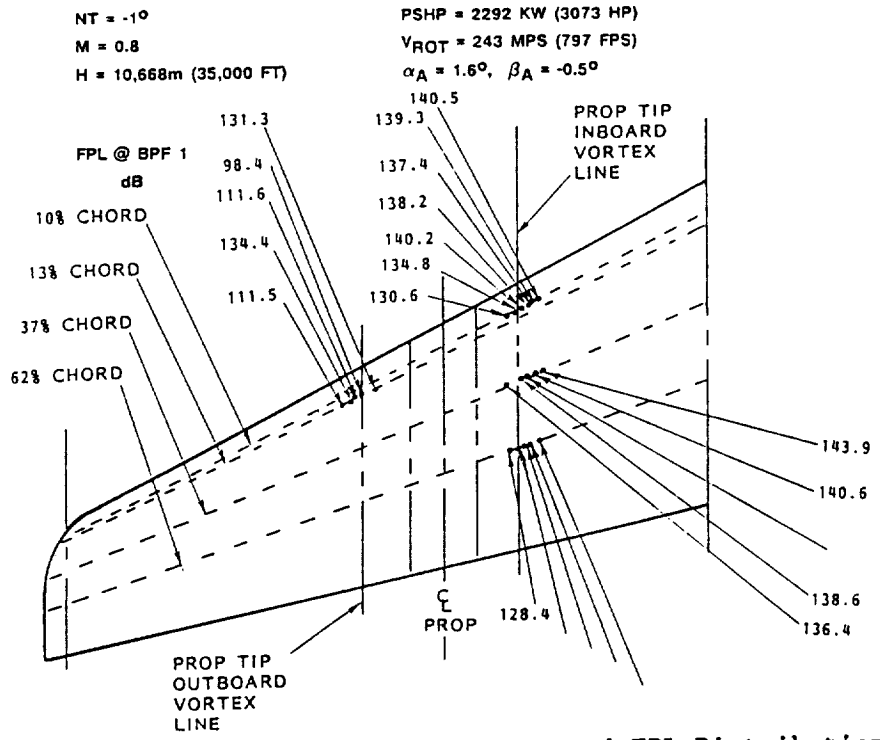


Figure 137. Wing Upper Surface Measured FPL Distribution

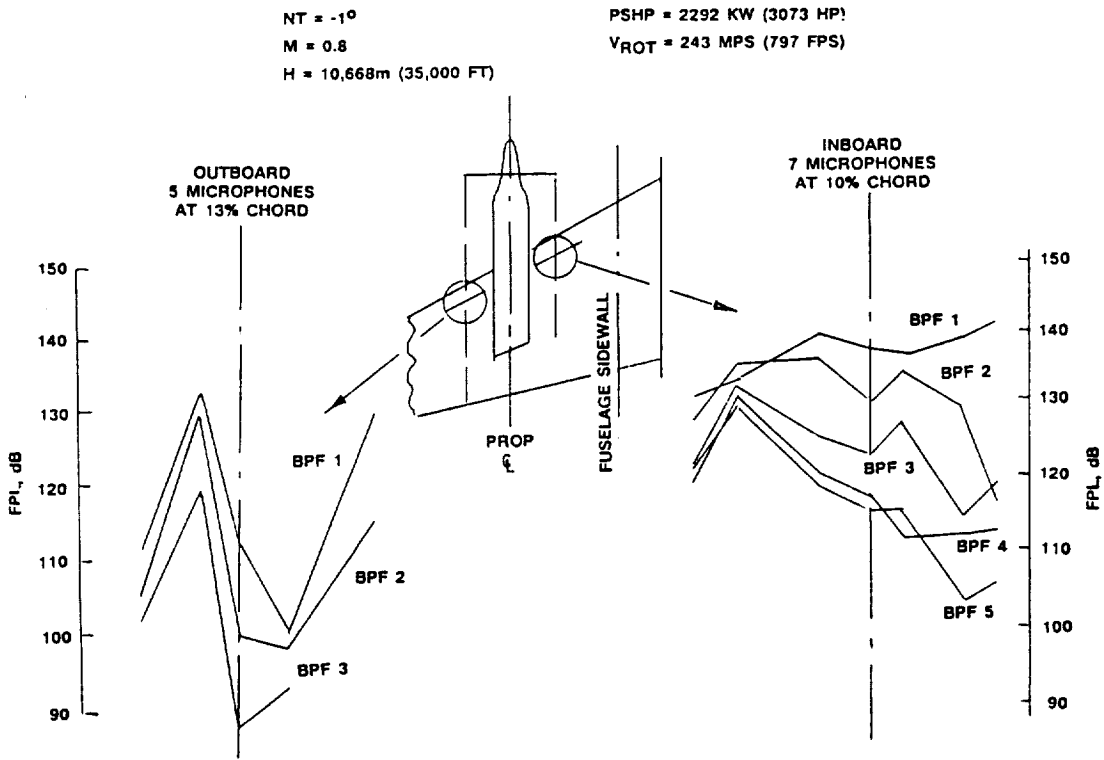


Figure 138. Wing Upper Surface Distribution of Measured FPLs Along Leading Edge

NT = -1°

M = 0.8

H = 10,668m (35,000 FT)

PSHP = 2292 KW (3073 HP)

V_{ROT} = 243 MPS (797 FPS)

M_{TH} = 1.137

α_A = 1.6°

β_A = -0.5°

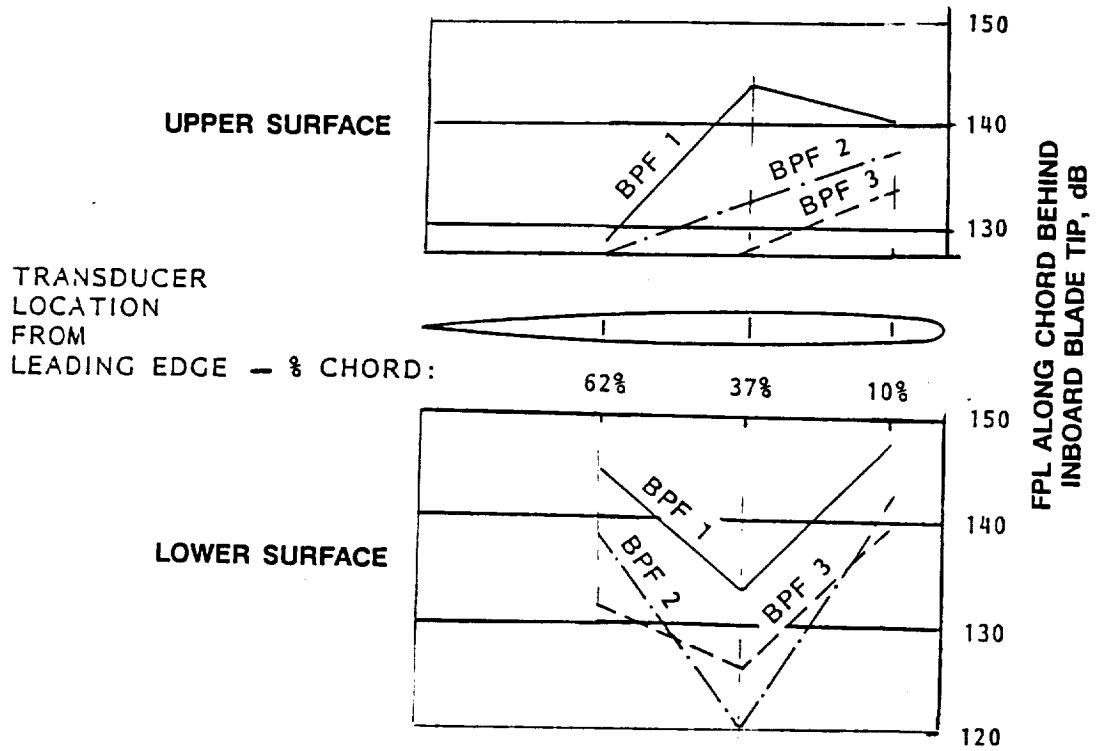


Figure 139. Chordwise Distribution of Measured FPL Over Wing Inboard Section

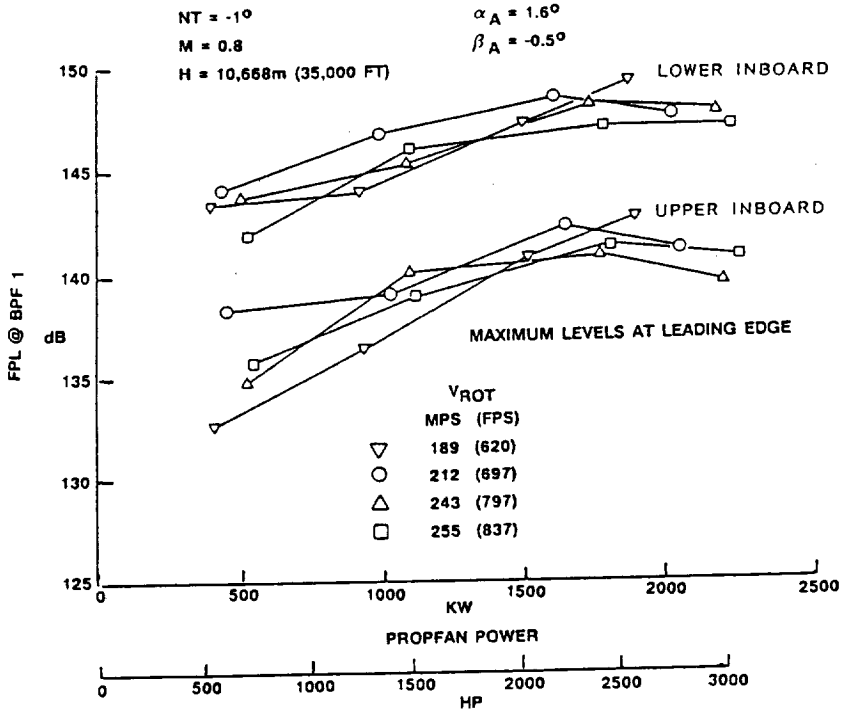


Figure 140. Wing Inboard Surface Measured FPL Dependence on Propfan Tip Speed and Power

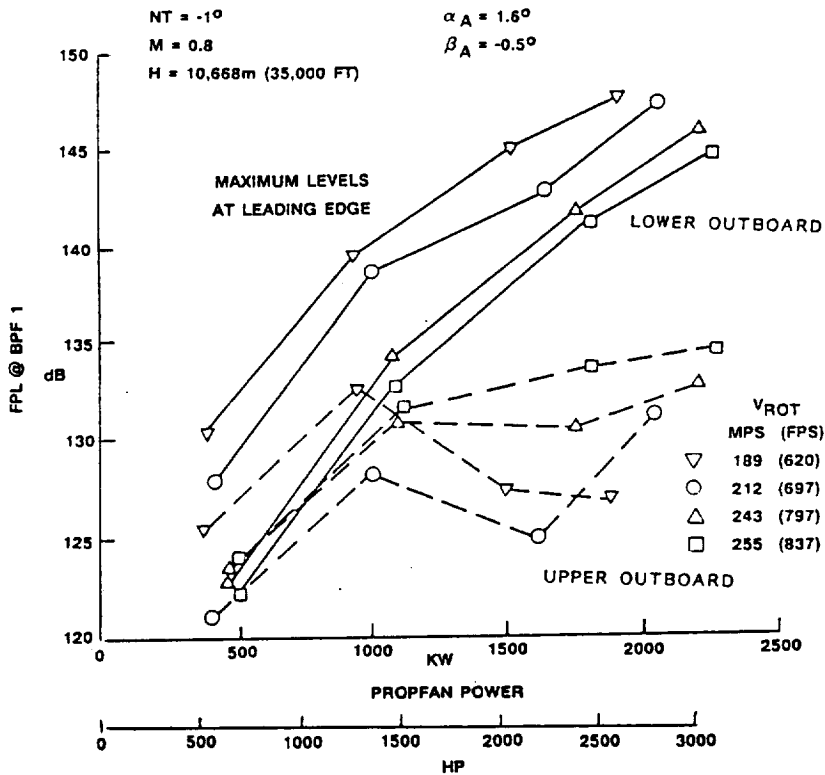


Figure 141. Wing Outboard Surface Measured FPL Dependence on Propfan Tip Speed and Power

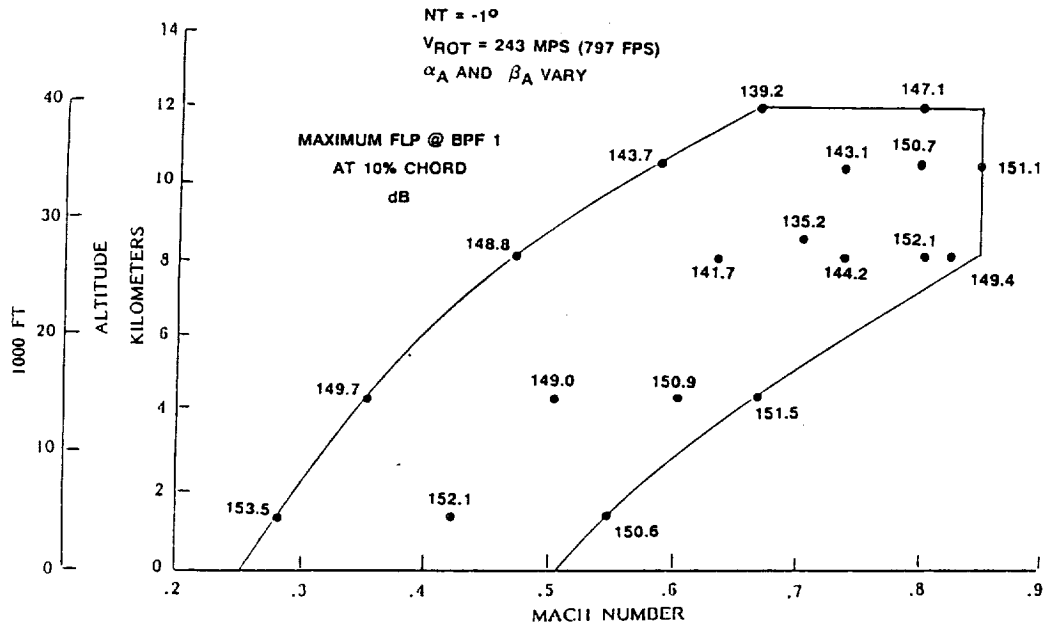


Figure 142. Wing Lower Inboard Measured FPLM Variation Over Flight Envelope

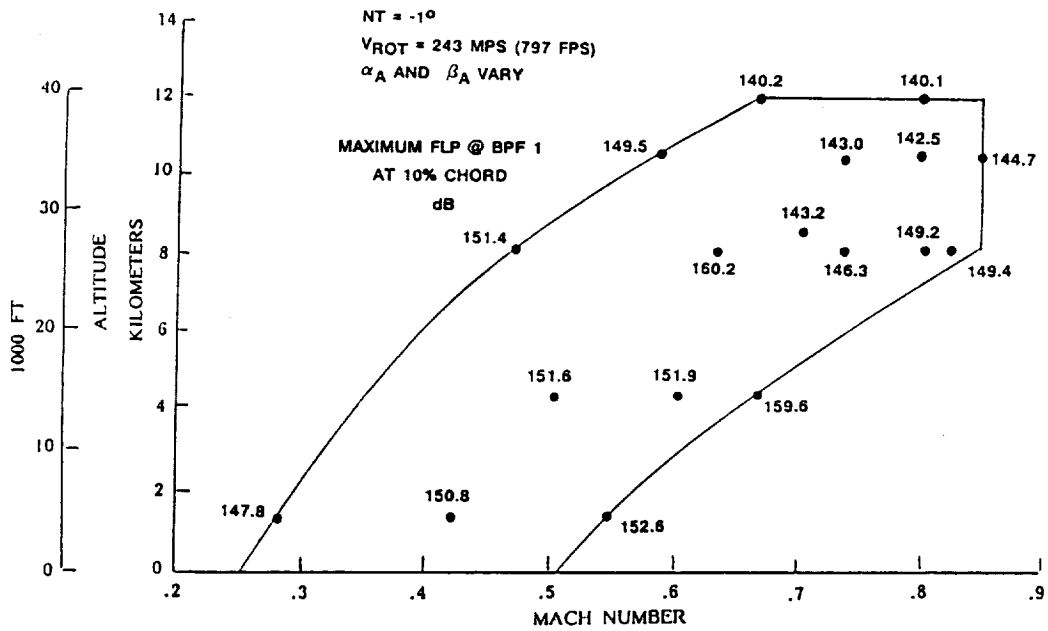


Figure 143. Wing Upper Inboard Measured FPLM Variation Over Flight Envelope

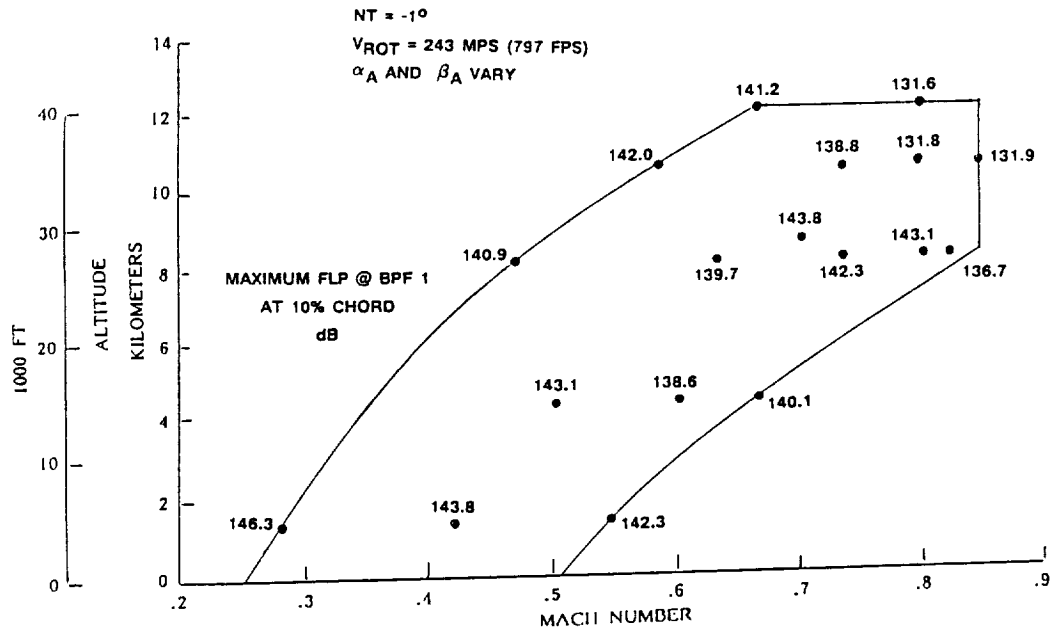


Figure 144. Wing Upper Outboard Measured FPLM Variation Over Flight Envelope

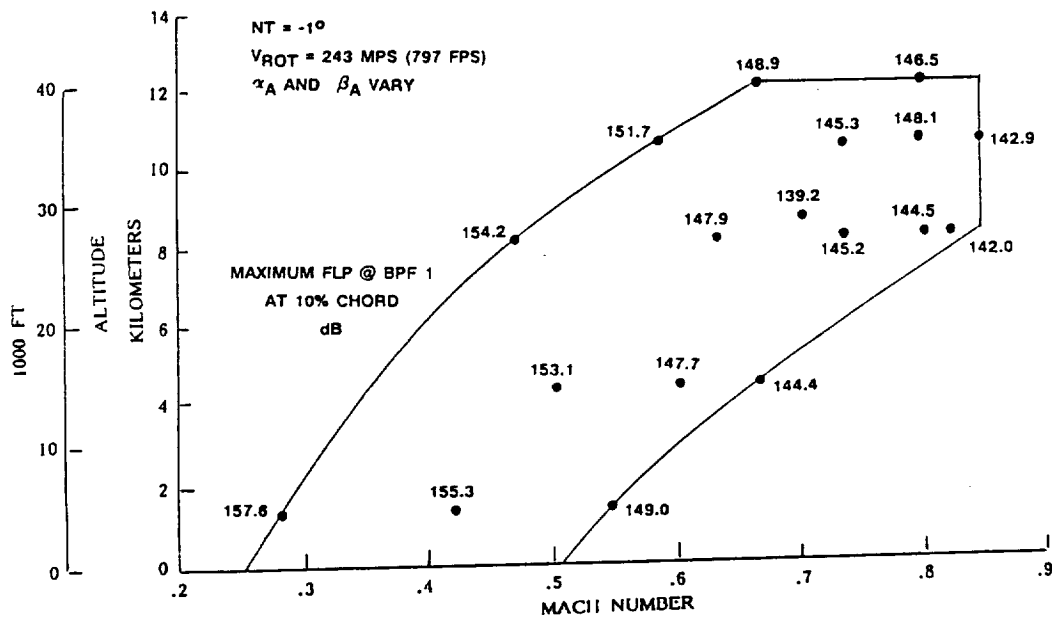


Figure 145. Wing Lower Outboard Measured FPLM Variation Over Flight Envelope

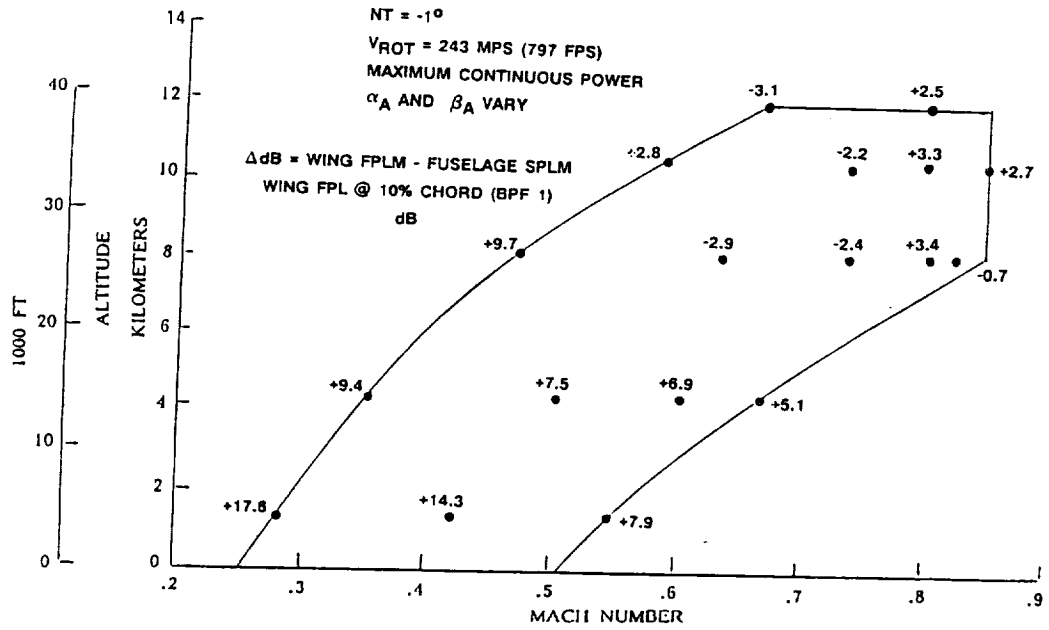


Figure 146. Relation Between Wing FPLM and Fuselage SPLM

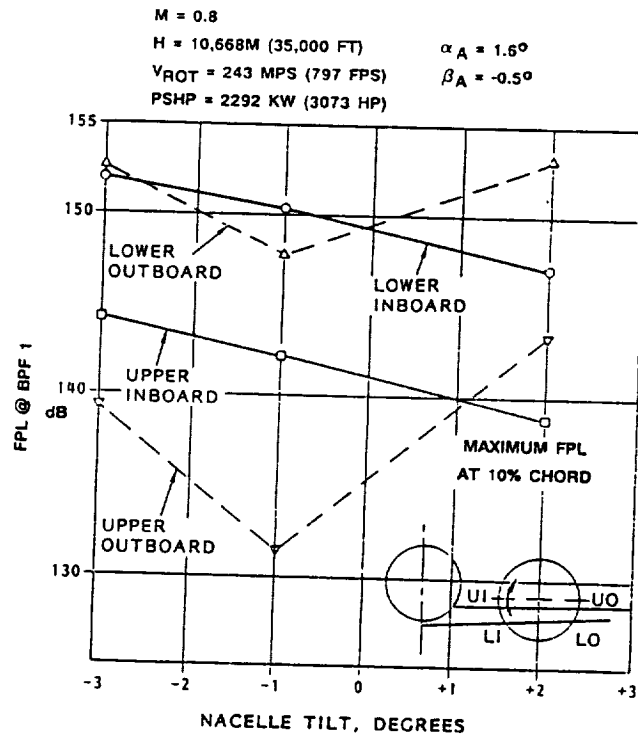


Figure 147. Effect of Nacelle Tilt on Wing Surface Measured FPLs by Quadrant

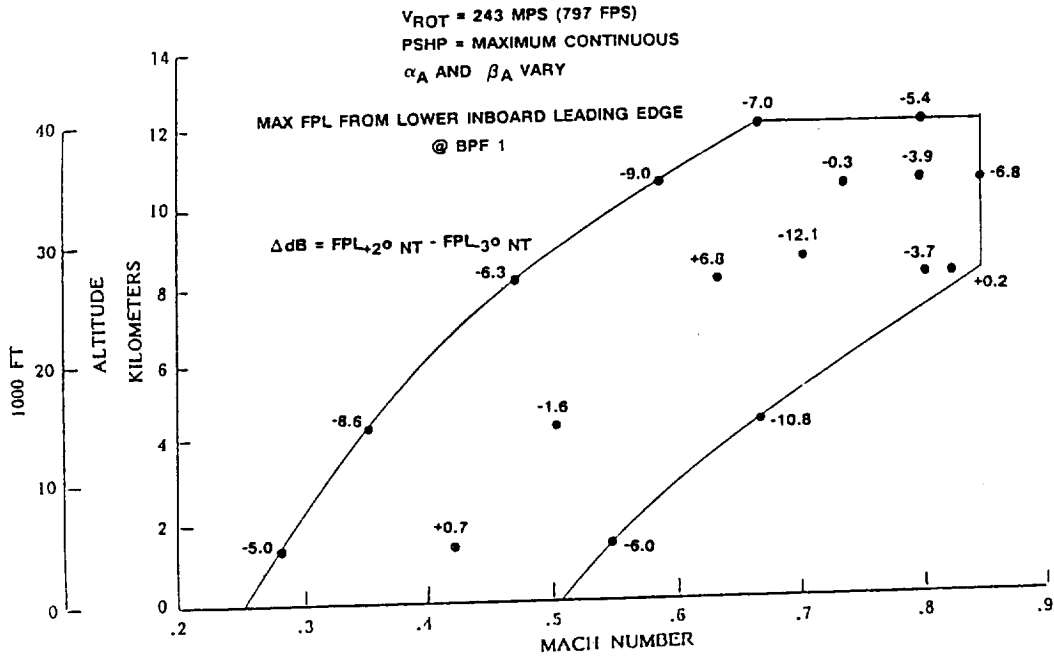


Figure 148. Effect of Nacelle Tilt on Wing Surface Measured FPLs Over Flight Envelope - Lower Inboard

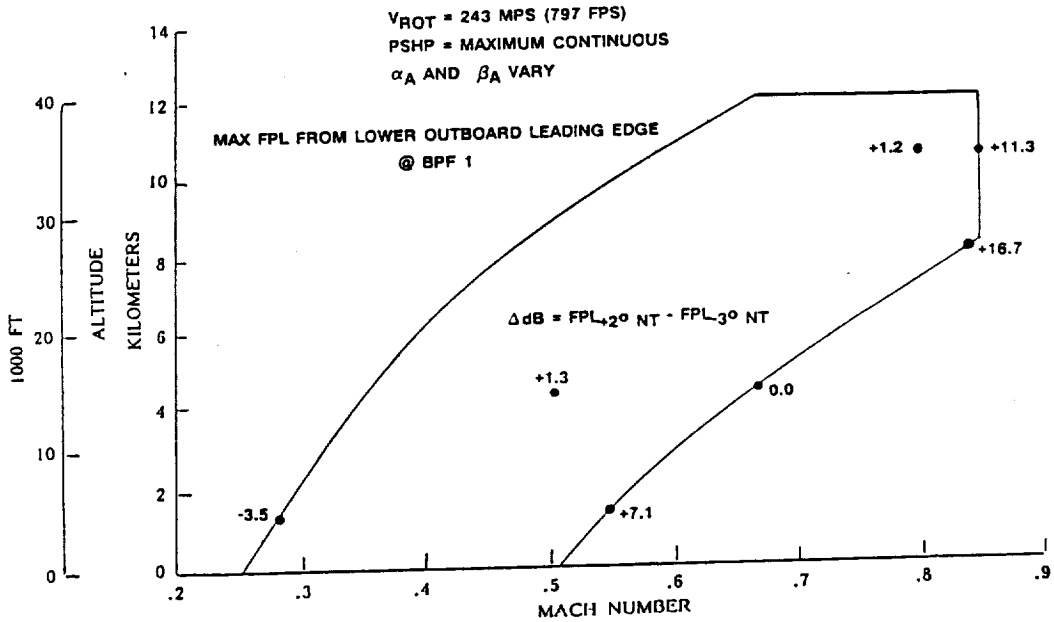
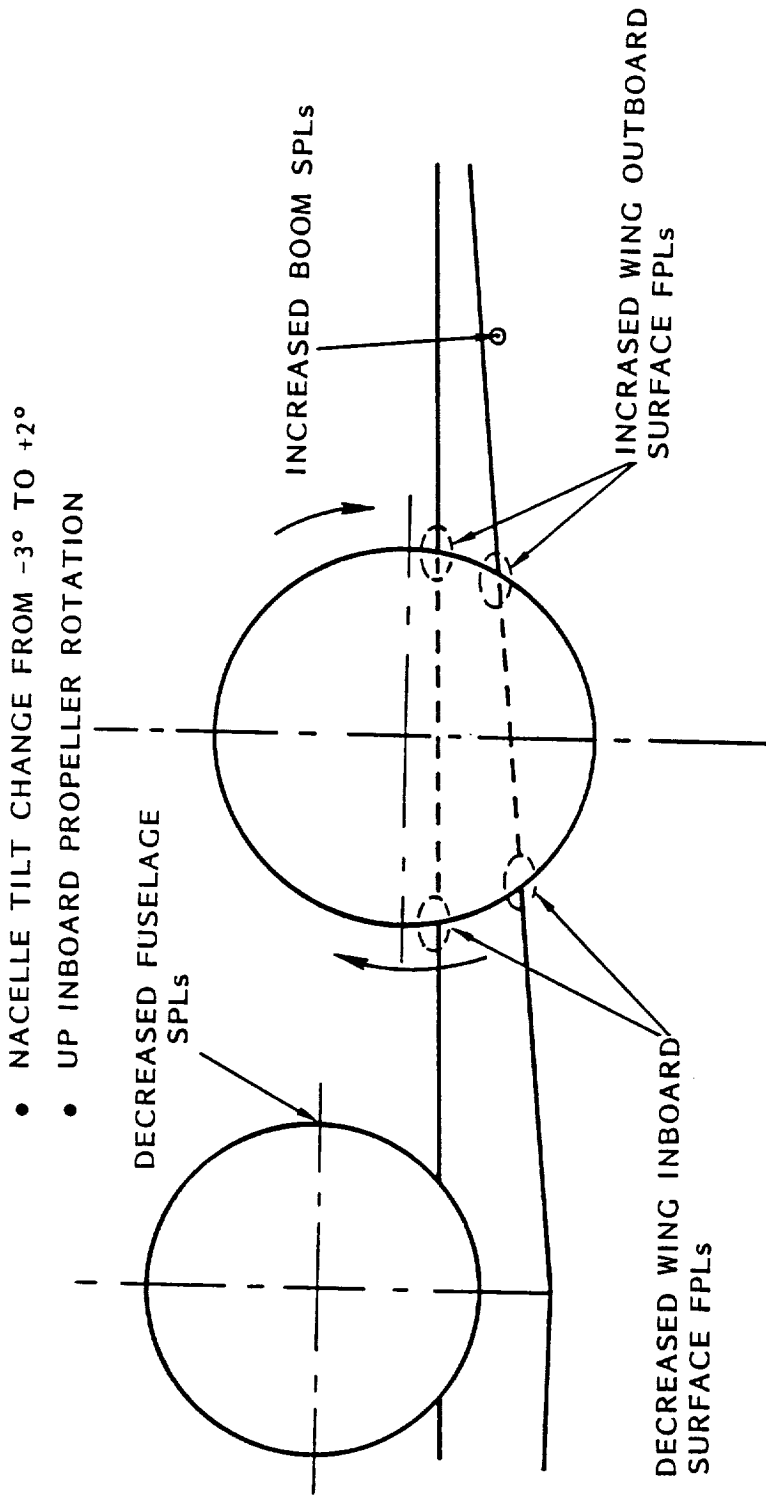


Figure 149. Effect of Nacelle Tilt on Wing Surface Measured FPLs Over Flight Envelope - Lower Outboard



- COMBINATION OF INCREASING NACELLE TILT (INCREASING INFLOW ANGLE) AND PROPFAN DIRECTION OF ROTATION PRODUCE SIMILAR EFFECTS FOR FPL's AND SPL's
- CREATED BY THE CYCLIC VARIATION OF THE PROPFAN LOADING AND TIP VORTEX STRENGTH DUE TO ROTATION IN A NON-AXIAL FLOW-FIELD

Figure 150. Correlation of Nacelle Tilt Effect on Wing FPLs and Fuselage SPLs

- o HAMILTON STANDARD PROCEDURE
- o CALCULATE PROPFAN WAKE CHARACTERISTICS
 - POTENTIAL WAKES (BASED ON LIFTING-LINE AERODYNAMICS FOR SPANWISE LOADING DISTRIBUTION)
 - VISCOUS WAKES (SILVERSTEIN WAKE MODEL BASED ON BLADE SECTION DRAG)
 - OBTAIN DISTURBANCE COMPONENT PERPENDICULAR TO THE WING SURFACES
- o DETERMINE DISTURBANCE MAGNITUDE AS A FUNCTION OF WAVE NUMBER
 - FOURIER TRANSFORM
- o DERIVE FPL ACROSS THE AIRFOIL SURFACE USING AIRFOIL LIFT RESPONSE METHOD
 - INFINITE SPAN, THIN, CONSTANT CHORD, SWEEPED WING
 - CALCULATES DIFFERENTIAL PRESSURE (PRESSURE TOP AND BOTTOM OF WING ASSUMED TO BE OF EQUAL AMPLITUDE AND OPPOSITE PHASE)
 - PROPFAN AXIS IS ASSUMED TO LIE IN THE PLANE OF THE WING SURFACE
- o PREDICTION
 - DISCRETE TONES AT BPF
 - AMPLITUDE AND RELATIVE PHASE OF FPL
- o PREDICTION METHODOLOGY DOES NOT INCLUDE
 - LEADING EDGE OR TIP EDGE VORTEX LIFT
 - UNSTEADY BLADE LOADS DUE TO INFLOW ANGLE-OF-ATTACK EFFECTS
 - ROLL-UP OF BLADE VORTEX SHEET IN TIP REGION
 - WING LOADING EFFECTS ON LIFT RESPONSE
 - ANY EMPIRICAL ADJUSTMENTS

Figure 151. Slipstream Impingement Fluctuating Pressure Prediction Methodology

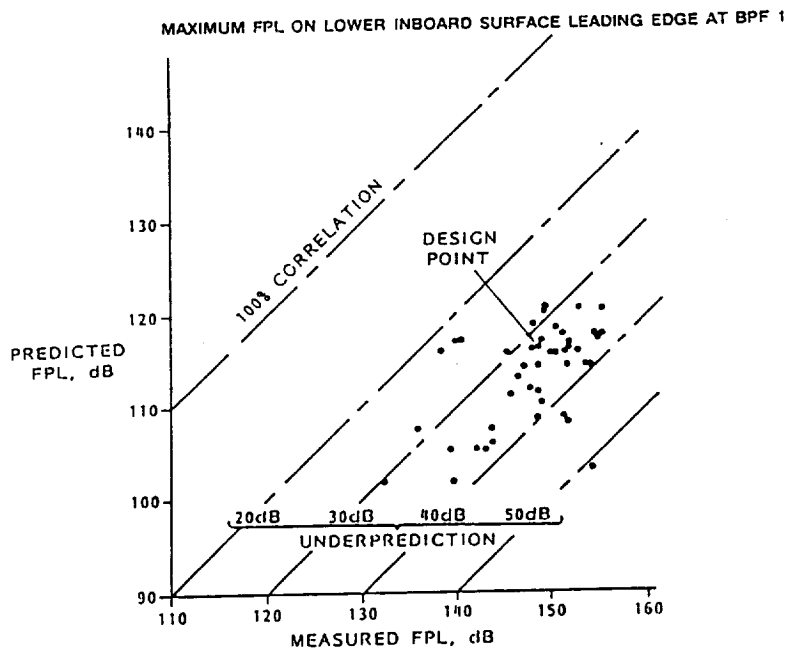


Figure 152. Summary of Wing Predicted and Measured FPLs

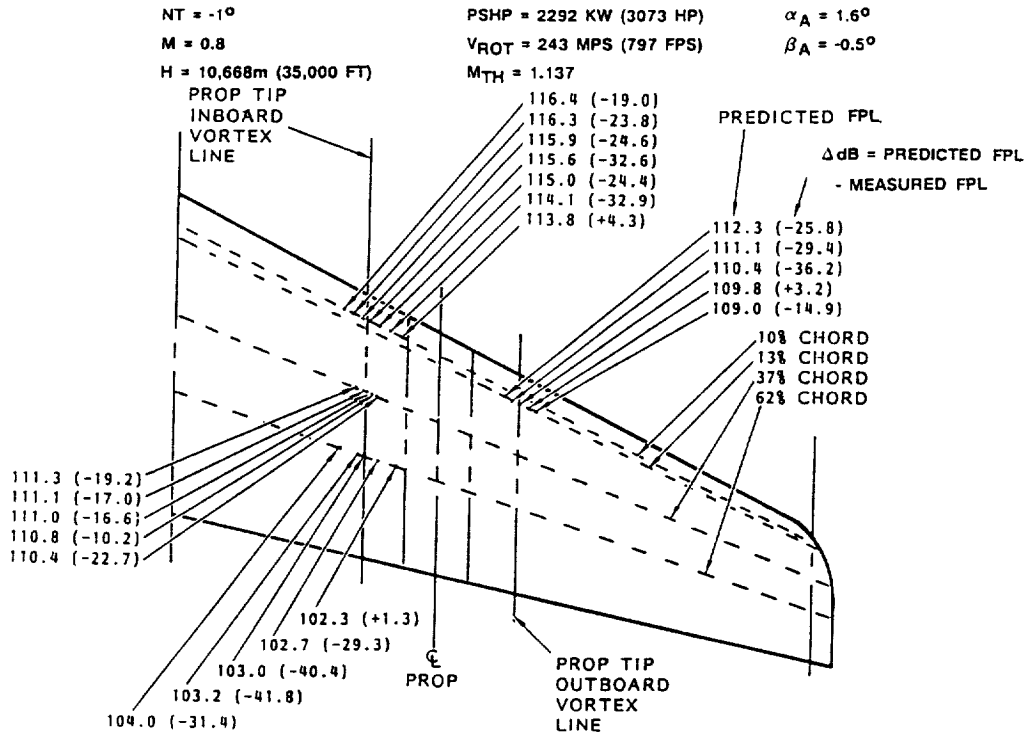


Figure 153. Wing Lower Surface Measured and Predicted FPLs

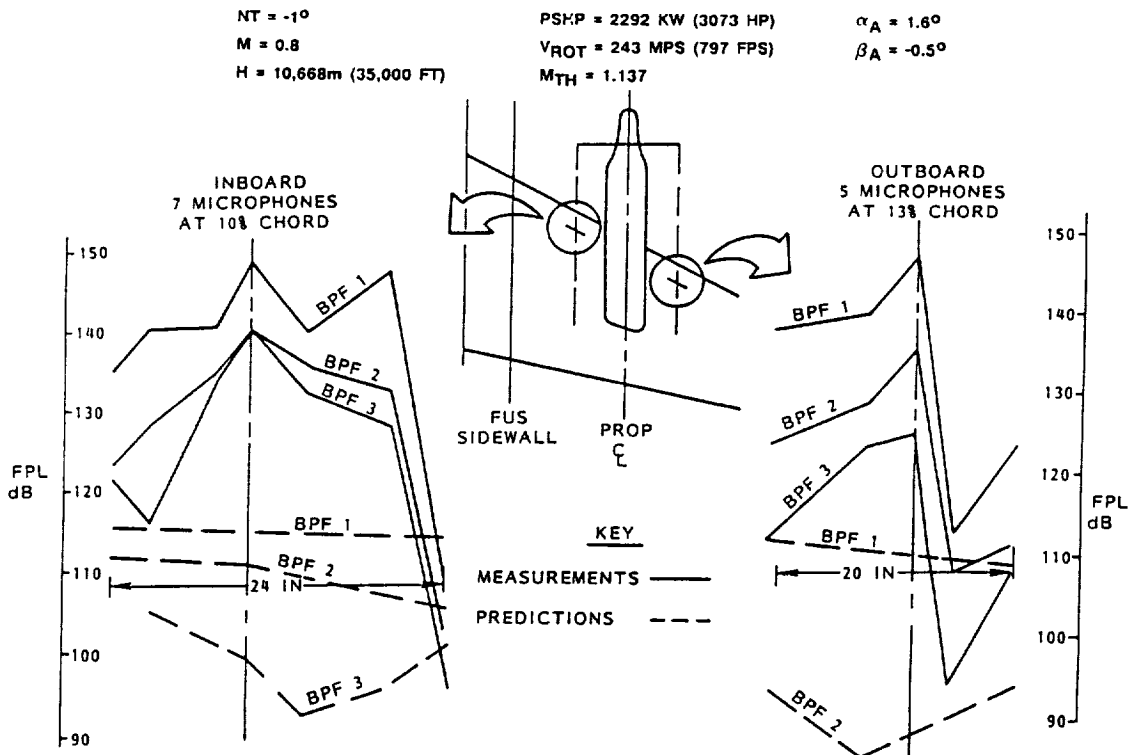


Figure 154. Wing Lower Surface Predicted and Measured FPL - Data from Leading Edge Microphones

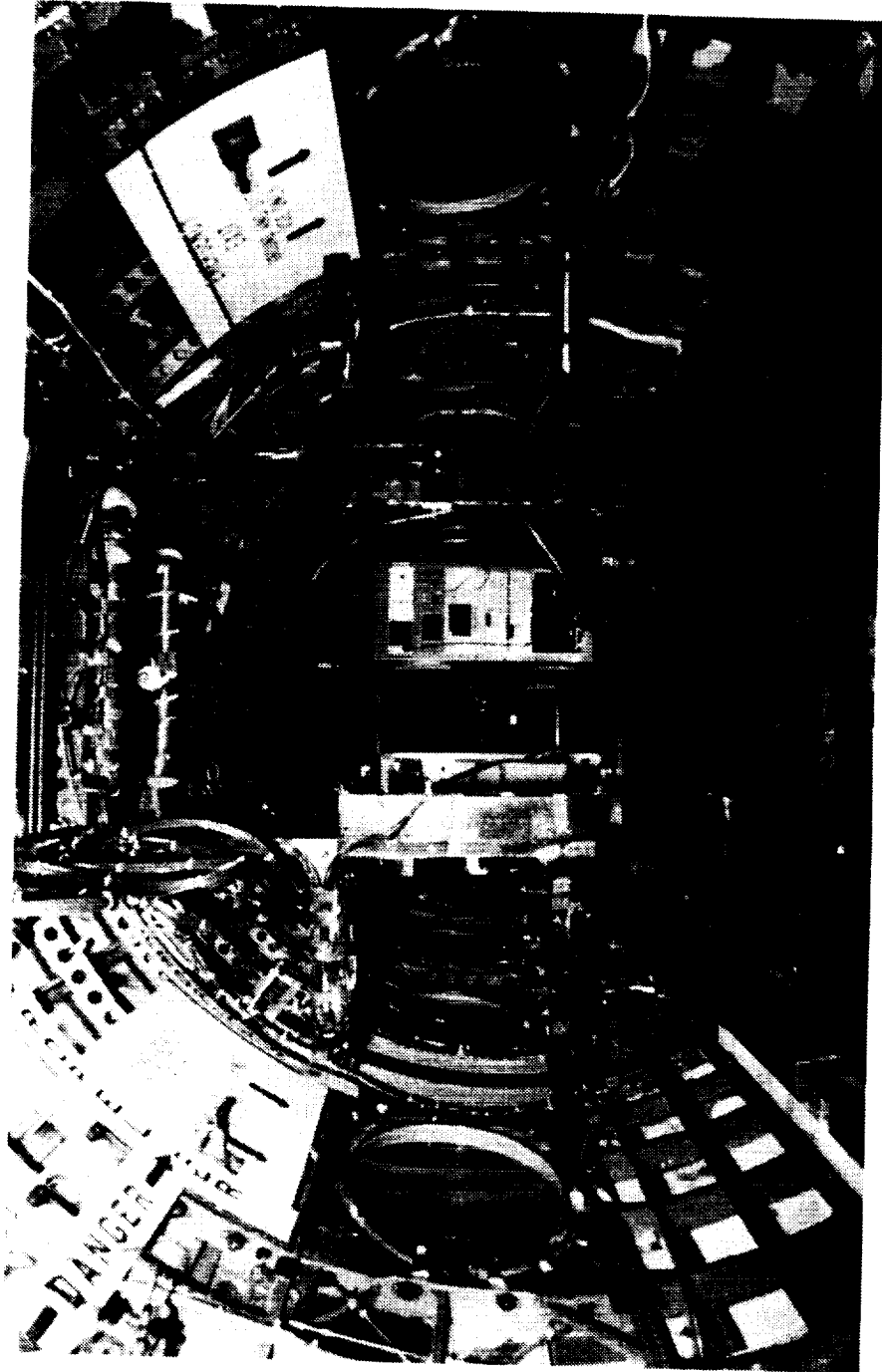


Figure 157. Cabin Interior Surface Conditions

ORIGINAL PAGE
BLACK AND WHITE PHOTOGRAPH

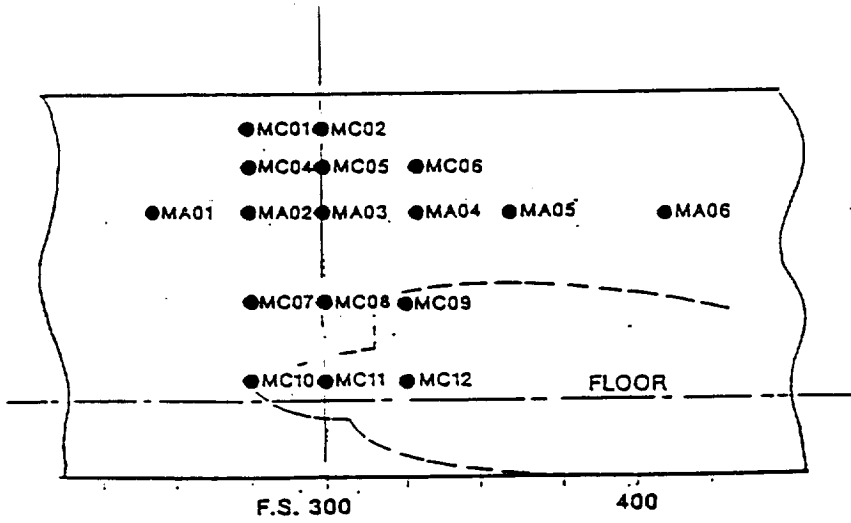
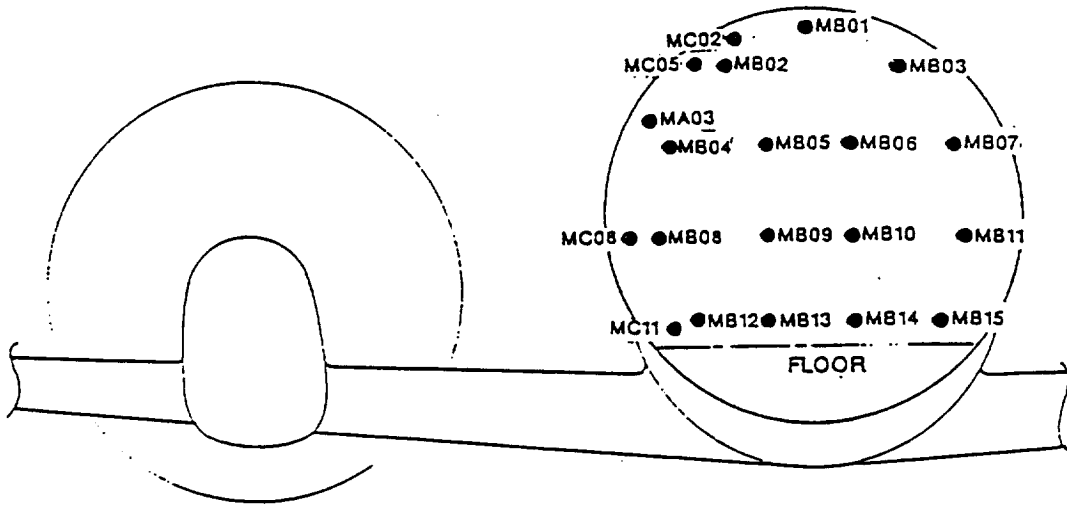


Figure 158. Identification and Positions of Cabin Microphones

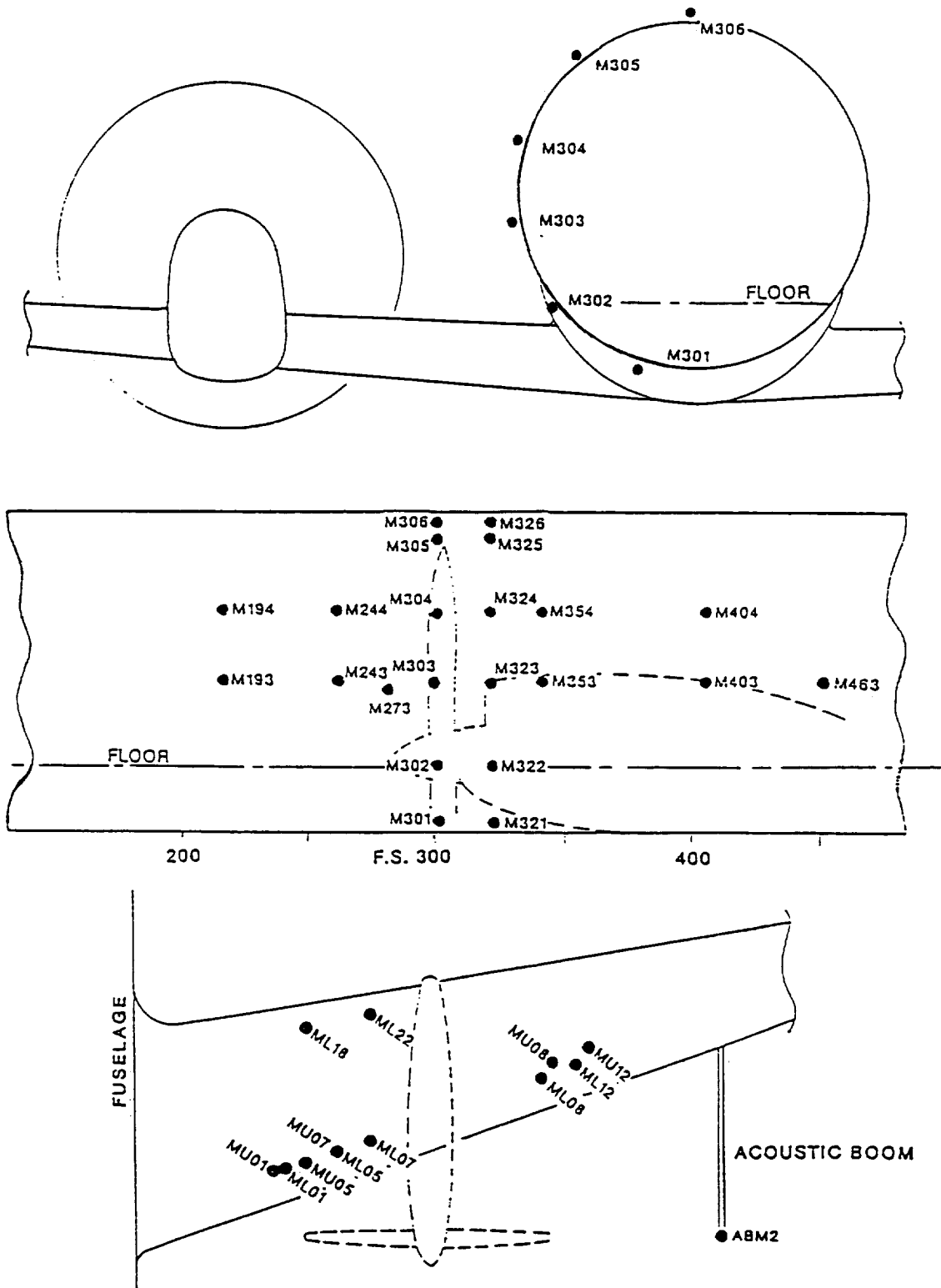


Figure 159. Identification and Positions of Selected Exterior Microphones

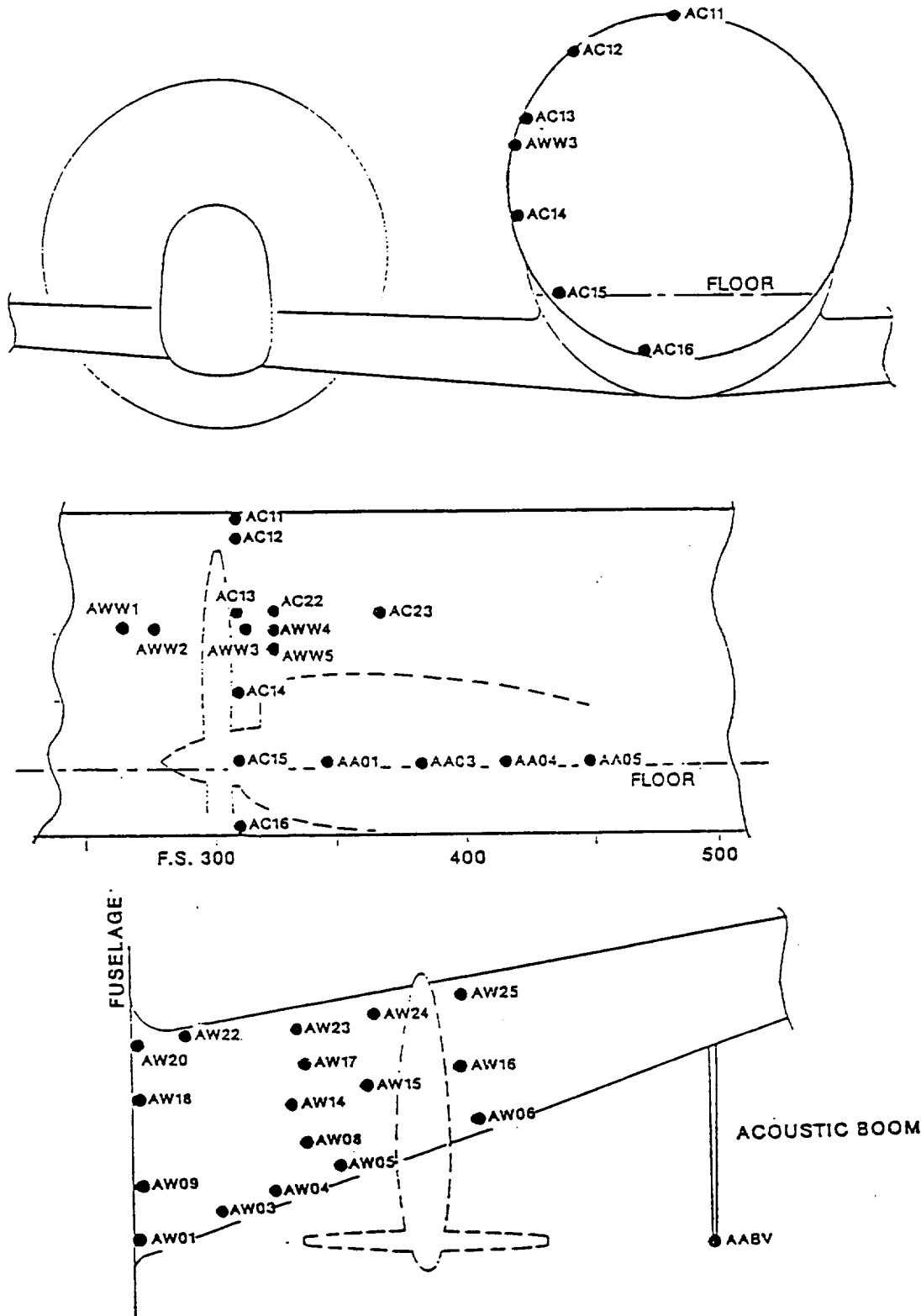


Figure 160. Identification and Positions of Selected Fuselage and Wing Accelerometers

VROT = 243 MPS (797 FPS)
 PSHP = 2259 KW (3029 HP)

NT = -1°
 M = 0.8
 H = 10,668m (35,000 FT)

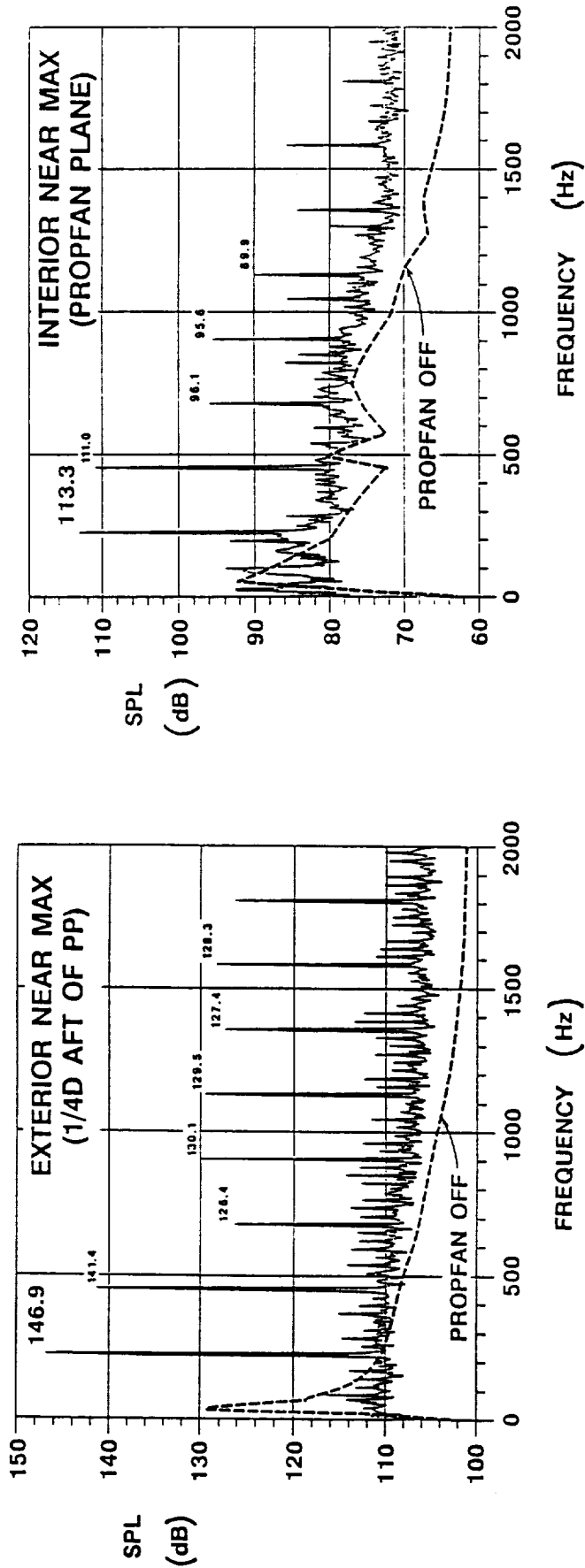


Figure 161. Cabin Noise Spectral Character and Comparison With External Noise

NT = -1°

M = 0.8

H = 10,668m (35,000 FT)

V_{ROT} = 243 MPS (797 FPS)

PSHP = 2259 KW (3029 HP)

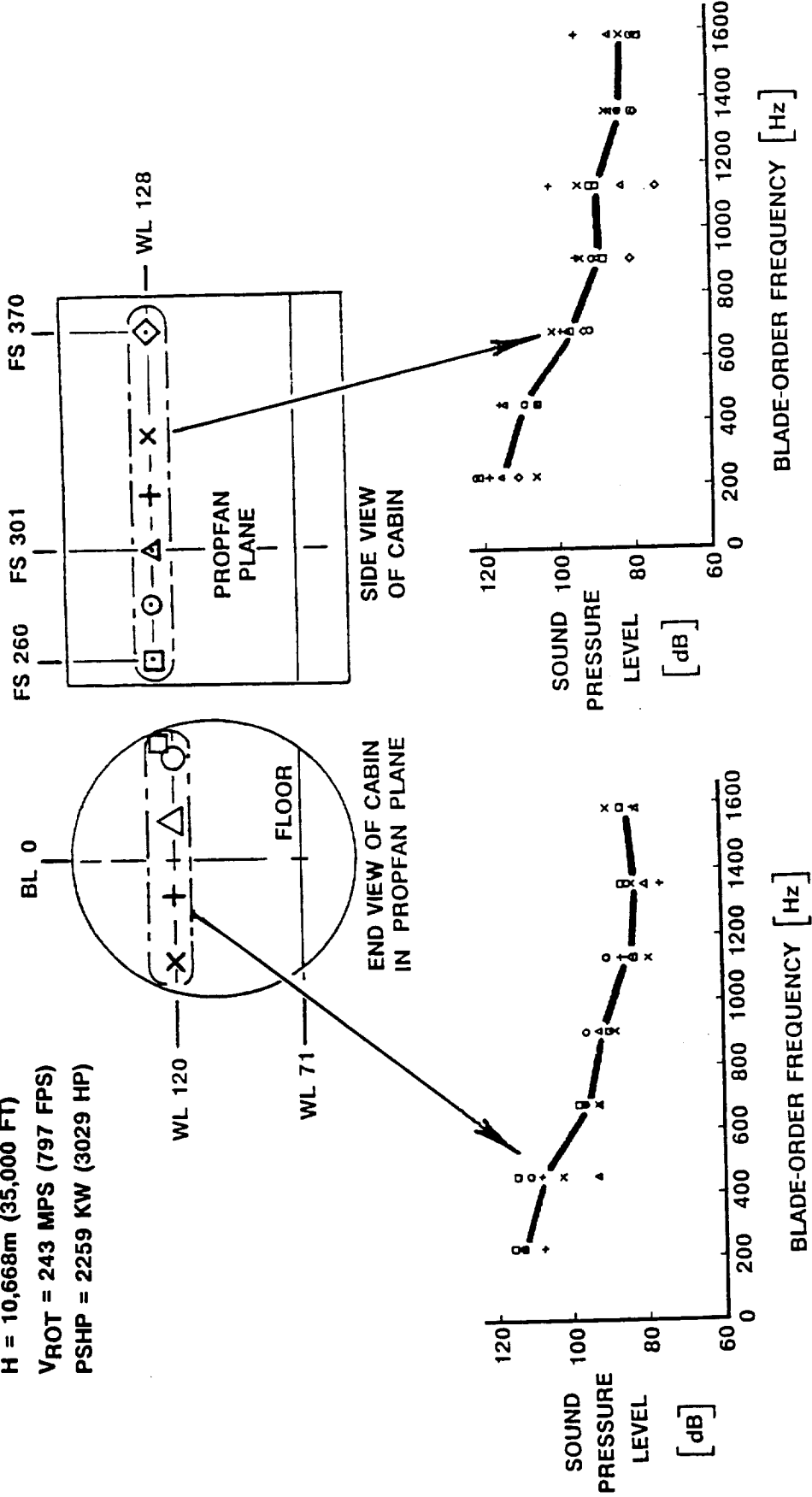


Figure 162. Lateral and Axial Variation of Cabin Noise

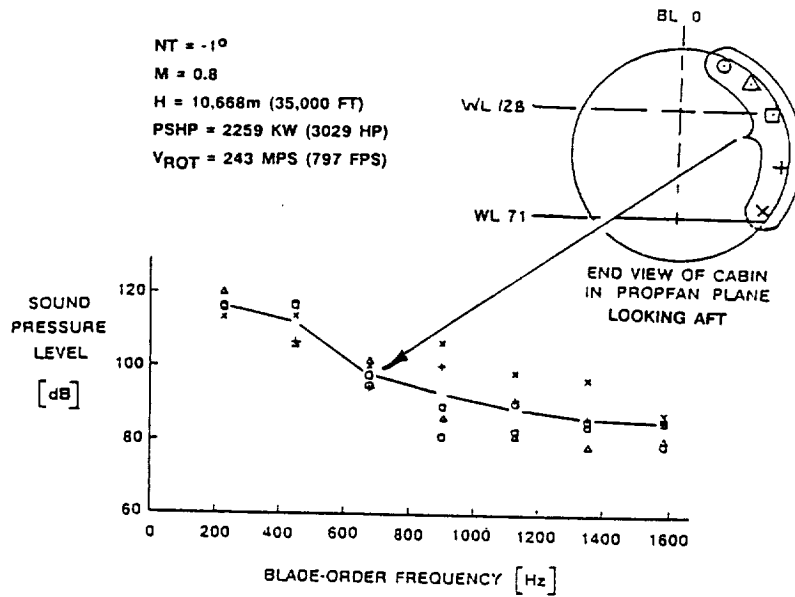


Figure 163. Circumferential Variation of Cabin Noise

NT = -1°
 M = 0.8
 H = 10,668m (35,000 FT)
 PSHP = 2259 KW (3029 HP)
 V_{ROT} = 243 MPS (797 FPS)

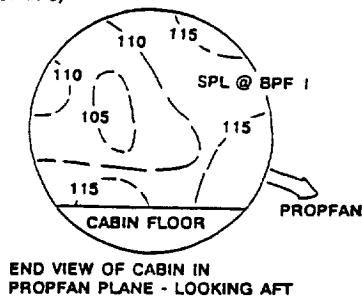


Figure 164. Spatial Variation of Cabin Noise in Propfan Plane, Blade Passage Frequency

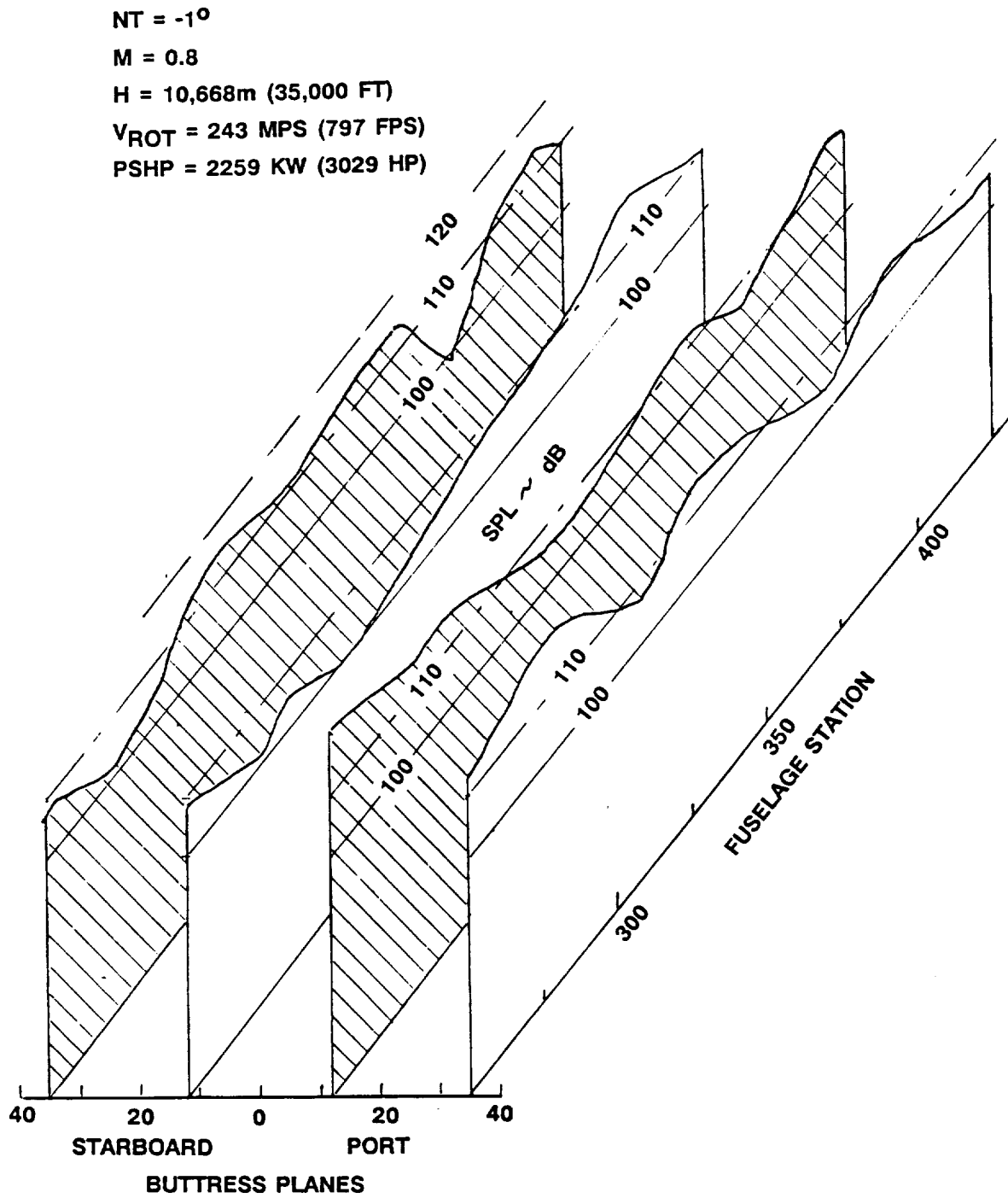


Figure 165. Cabin Noise Variation Fore and Aft in Four Buttress Planes

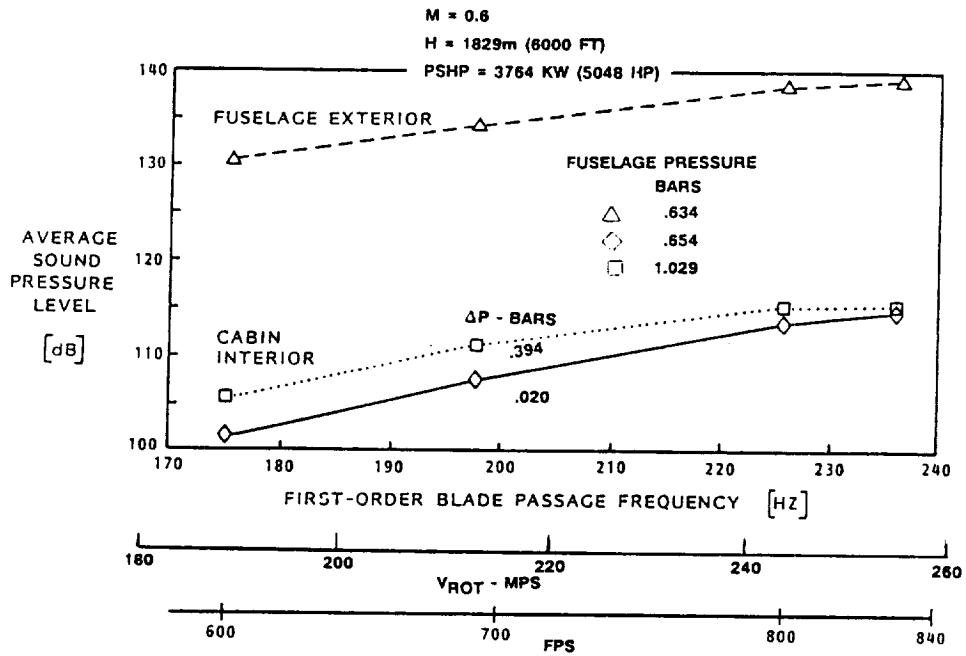


Figure 166. Effect of Fuselage Pressurization on Cabin Noise

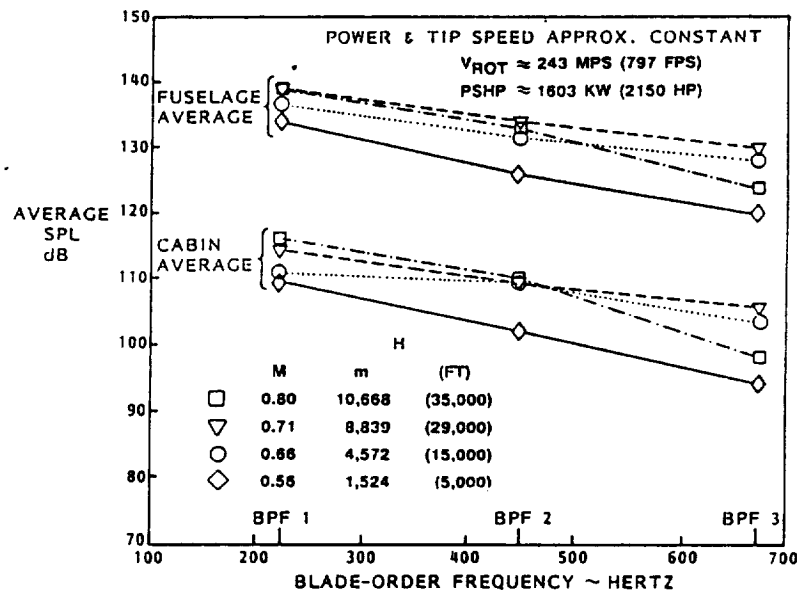


Figure 167. Effect of Cruise Flight Conditions on Cabin Noise

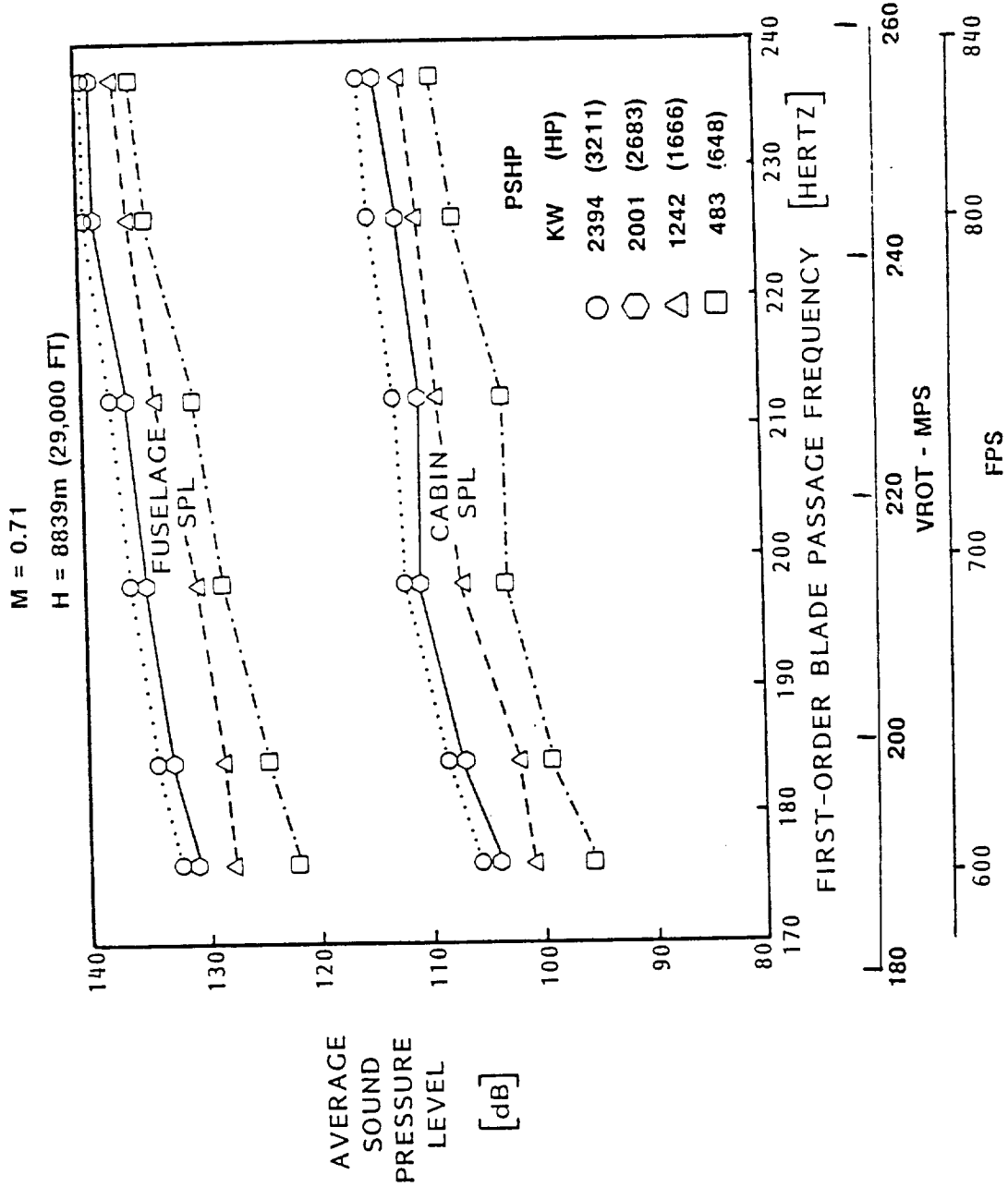


Figure 168. Effect of Propfan Power and Tip Speed on Cabin Noise

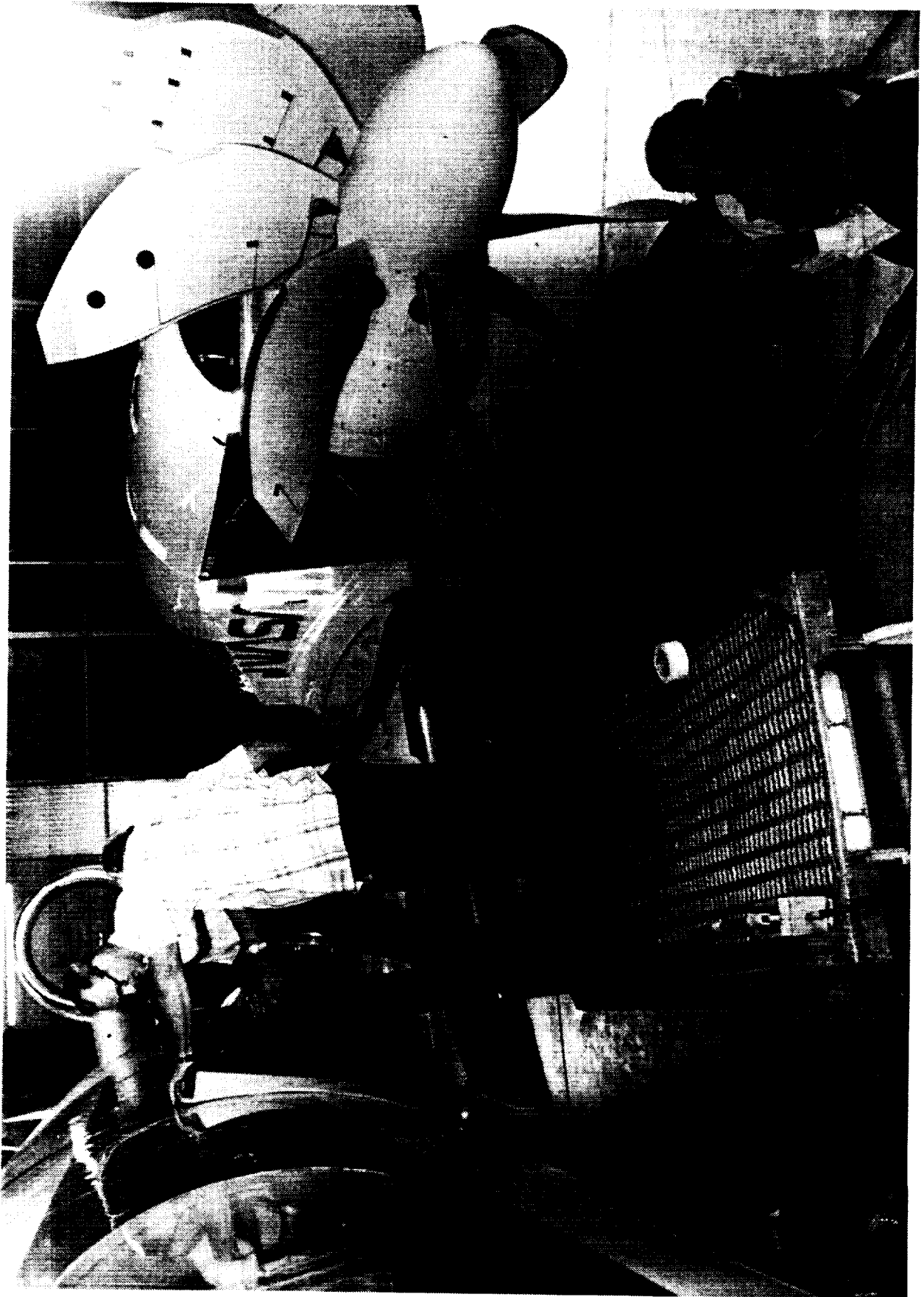


Figure 169. Acoustic Diagnostic Testing

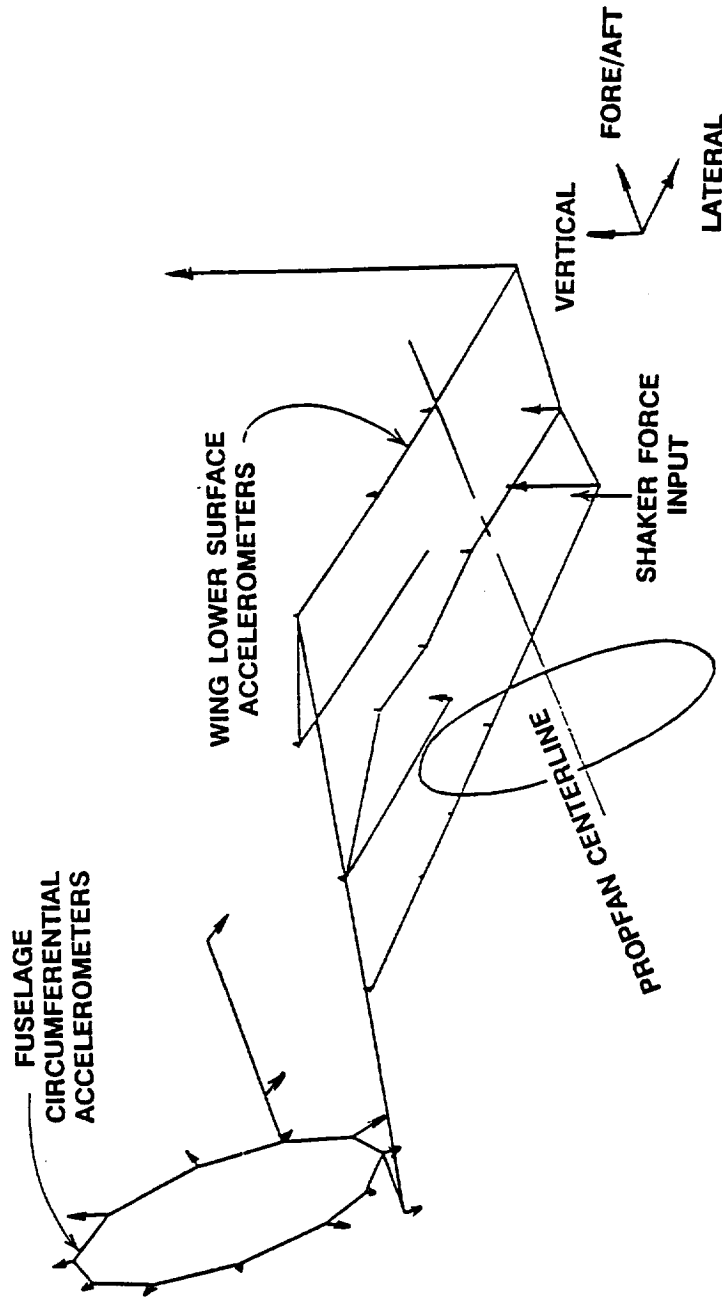


Figure 170. Comparative Response at 225 Hz for Wing and Fuselage Accelerometers with Shaker Force Applied at Front Spar Outboard of Drive Engine

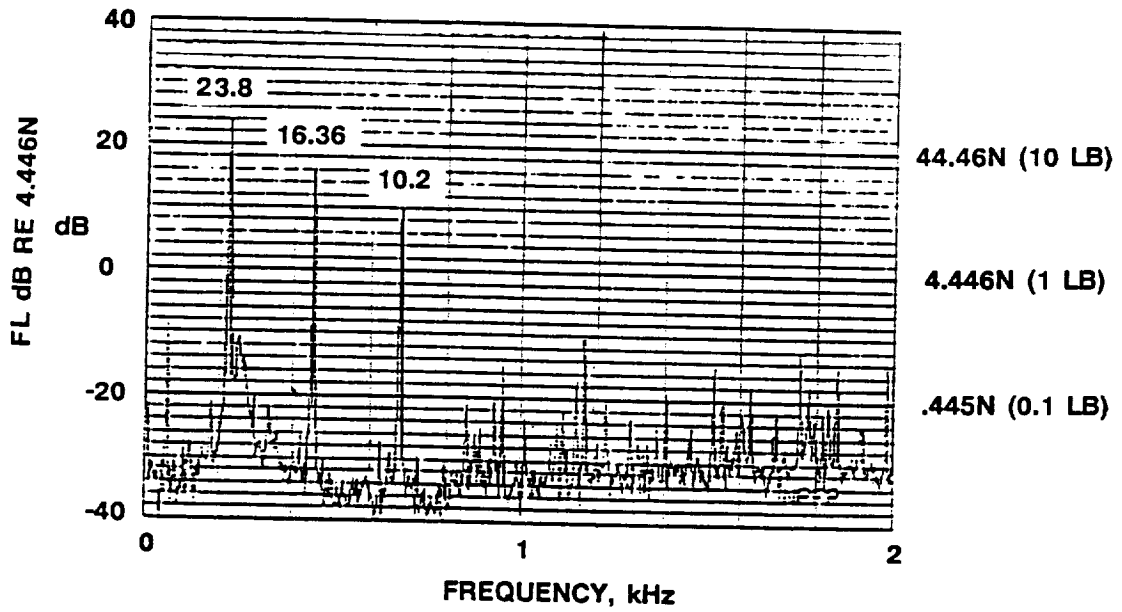


Figure 171. Typical Vibratory Force Spectrum Applied to Wing for Structureborne Noise Diagnosis

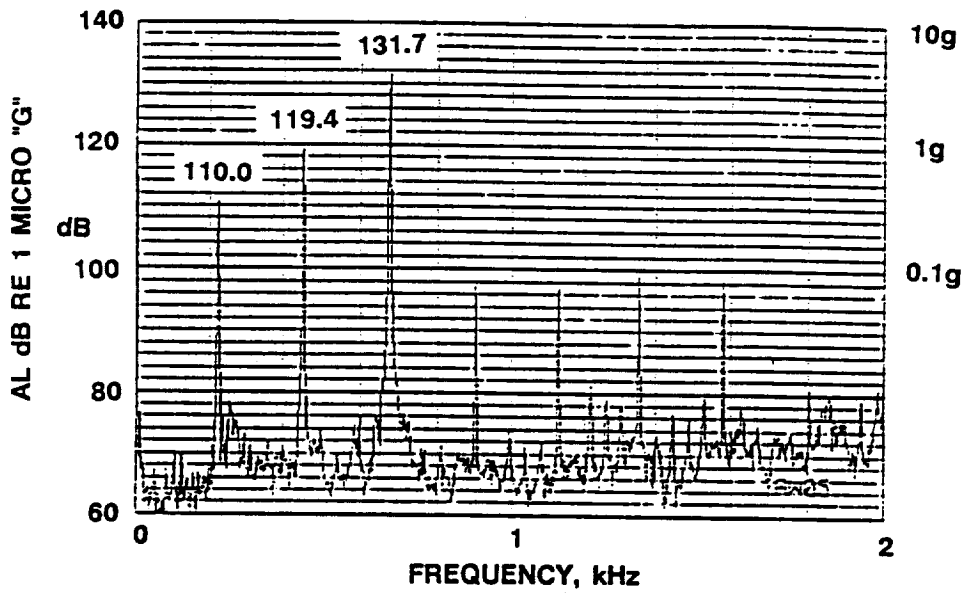


Figure 172. Vibratory Response at the Location of the Applied Force for the Force Spectrum of Figure 171

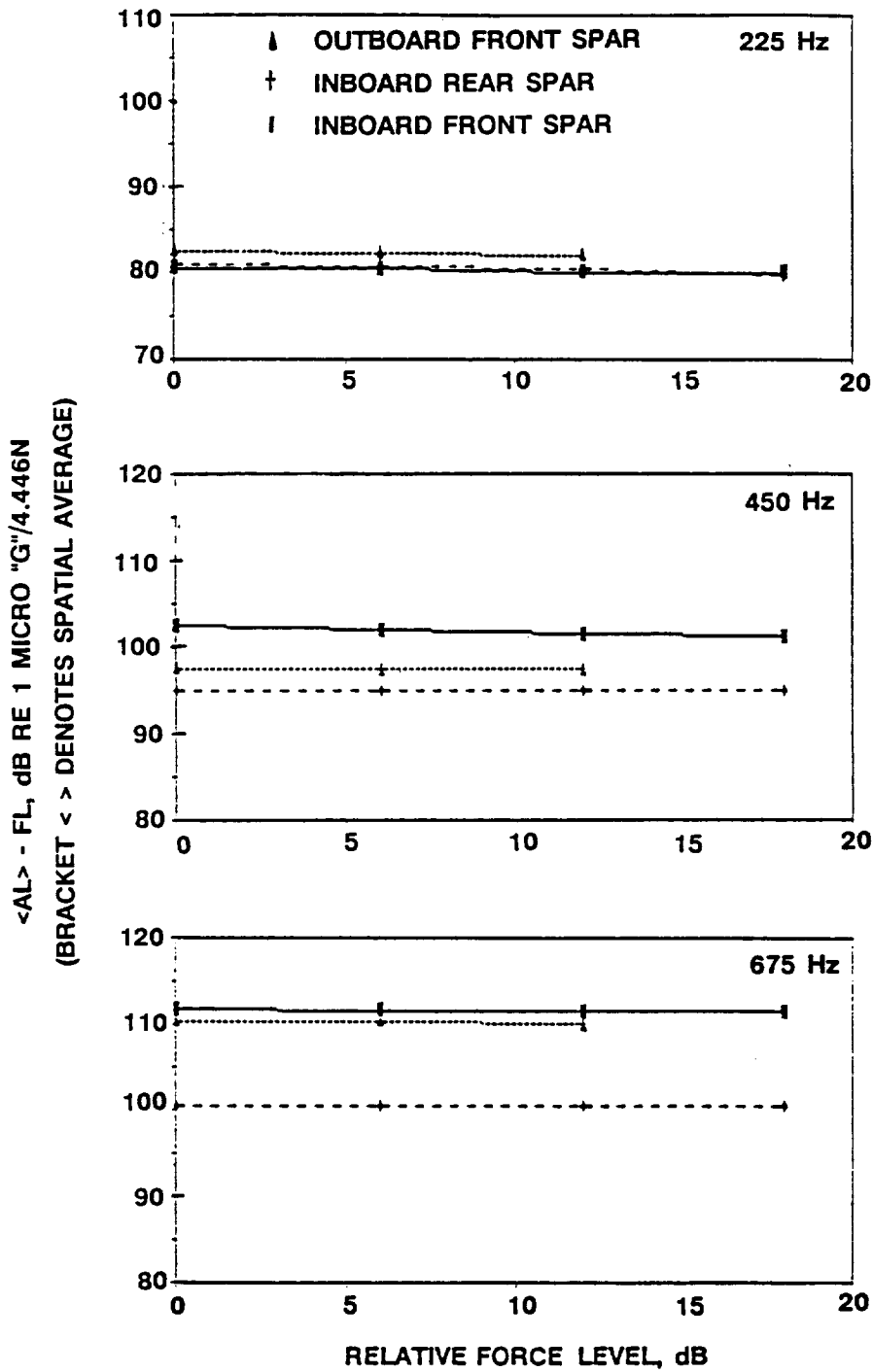


Figure 173. Relation Between Normalized Average Wing Tonal Vibration Level and Applied Force Level

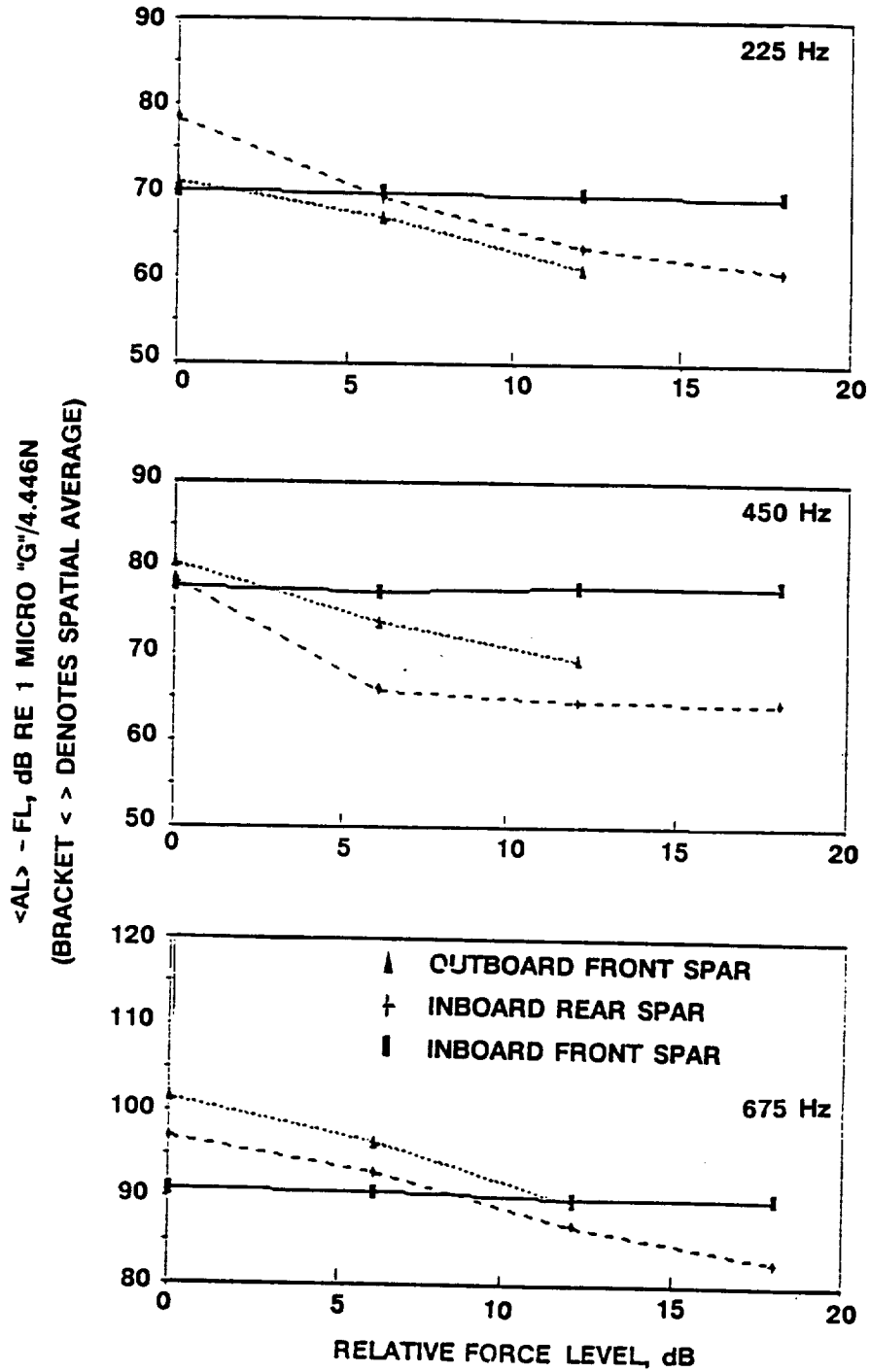


Figure 174. Relation Between Normalized Average Fuselage Tonal Vibration Level and Applied Force Level

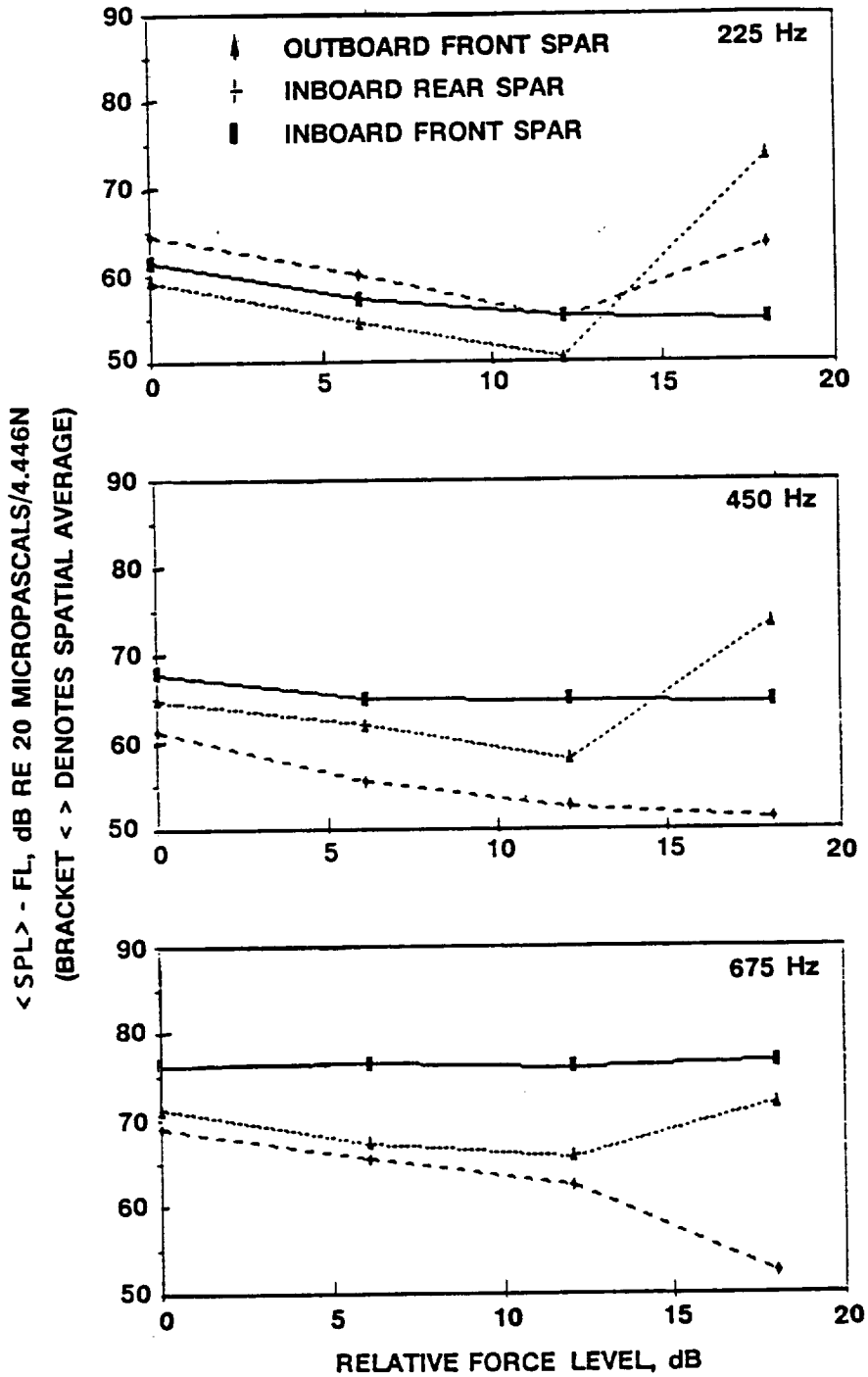
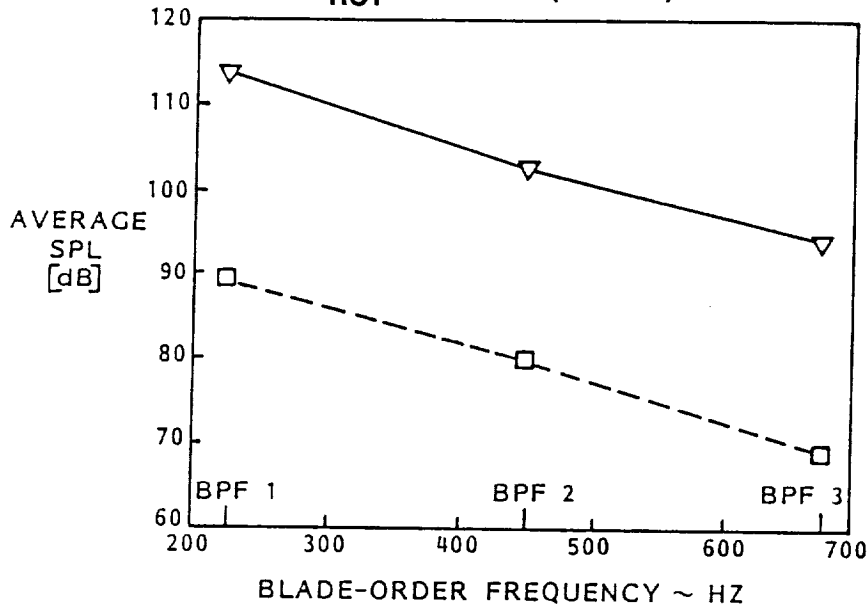


Figure 175. Relation Between Normalized Average Cabin Tonal Noise Level and Applied Force Level

M = 0.81
 H = 10,668m (35,000 FT)
 PSHP = 2259 KW (3030 HP)
 V_{ROT} = 243 MPS (797 FPS)



▽ MEASURED TOTAL CABIN SPL AT THE FRONT SPAR - PROPFAN PLANE
 □ PREDICTED CABIN SPL FROM WING VIBRATION/NOISE CORRELATION

M = 0.32
 H = 1524m (5000 FT)
 PSHP = 4176 KW (5600 HP)
 V_{ROT} = 243 MPS (797 FPS)

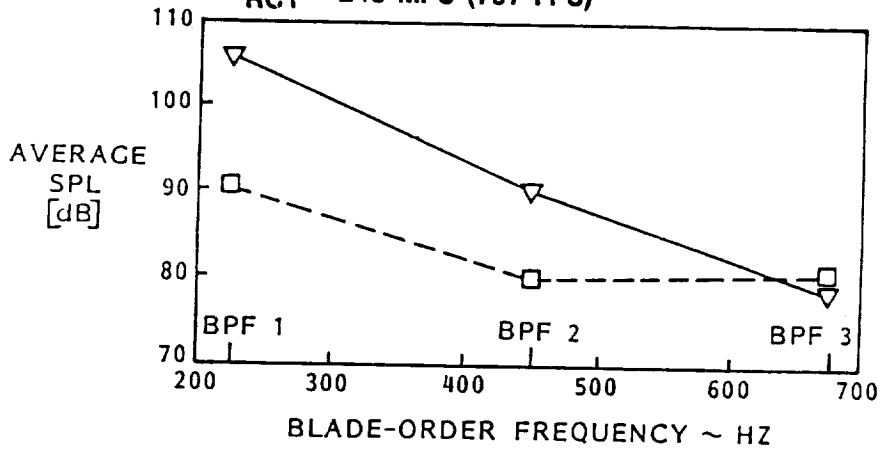


Figure 176. Comparison of Predicted Structureborne Noise and Measured Cabin Noise for High- and Low-Altitude Cruise

M = 0.8
H = 10,668m (35,000 FT)
PSHP = 2013 KW (2700 HP)

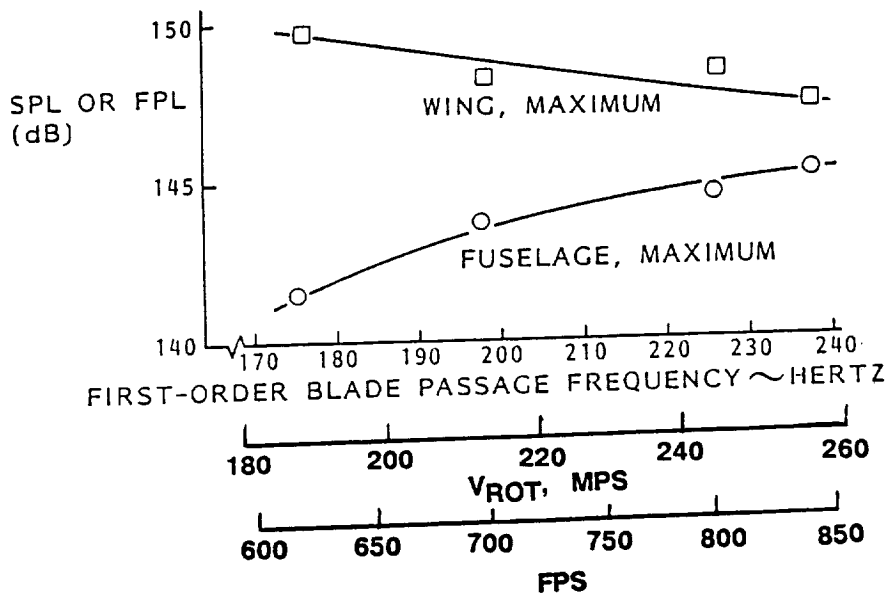


Figure 177. Comparison of Wing FPLs and Fuselage SPLs

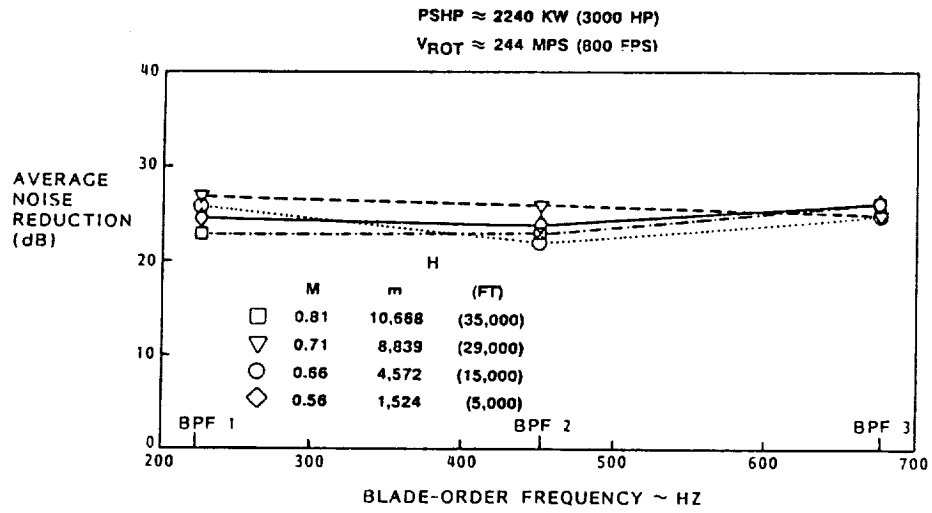


Figure 178. Noise Reduction at the First Three Orders of BPF

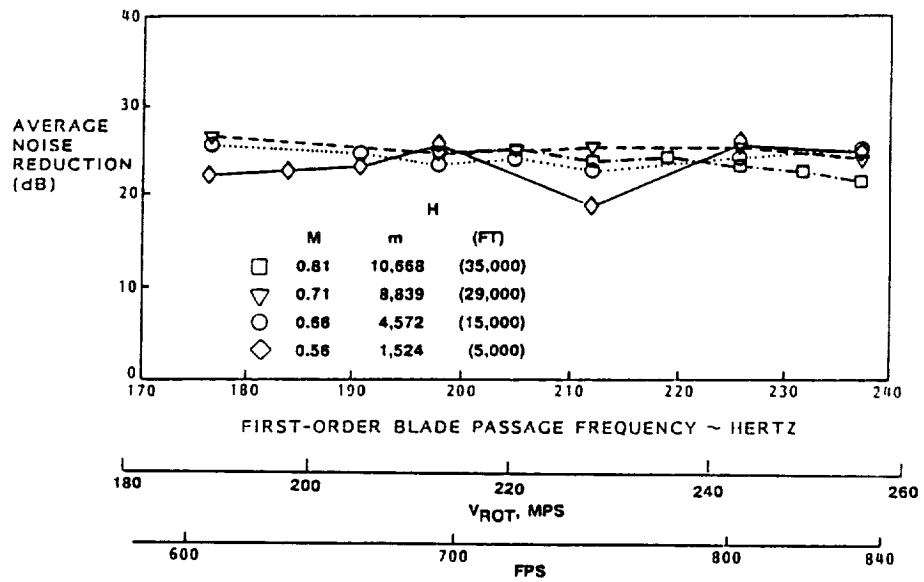


Figure 179. Noise Reduction for a Range of Tip Speeds/BPFs and Cruise Conditions

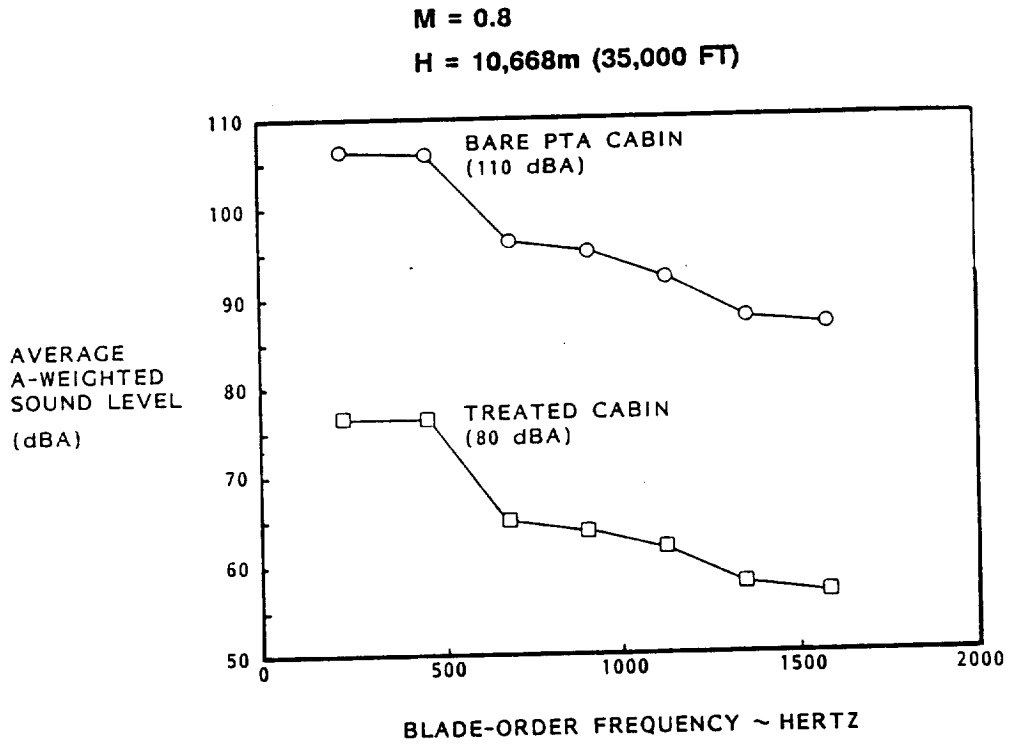


Figure 180. Noise Reduction Required to Achieve a Cabin Level of 80 dBA



Report Documentation Page

1. Report No. NASA CR-182278		2. Government Accession No.		3. Recipient's Catalog No.	
4. Title and Subtitle Propfan Test Assessment (PTA) Flight Test Report				5. Report Date April 1989	
				6. Performing Organization Code	
7. Author(s) B. H. Little, H.W.Bartel, N.N. Reddy, G. Swift, C.C. Withers, and J.E. Turnberg				8. Performing Organization Report No. LG89ER0026	
9. Performing Organization Name and Address Lockheed Aeronautical Systems Company 86 South Cobb Drive Marietta, GA 30063				10. Work Unit No. 535-03-01	
				11. Contract or Grant No. NAS3-24339	
12. Sponsoring Agency Name and Address NASA Lewis Research Center 21000 Brookpark Road Cleveland, OH 44135				13. Type of Report and Period Covered Contractor Report Final	
				14. Sponsoring Agency Code	
15. Supplementary Notes					
16. Abstract <p>The Propfan Test Assessment (PTA) aircraft was flown to obtain blade stress and noise data for a 2.74m (9 ft.) diameter single rotation propfan. Tests were performed at Mach numbers to 0.85 and altitudes to 12,192m (40,000 ft.). The propfan was well-behaved structurally over the entire flight envelope-- demonstrating that the blade design technology was completely adequate.</p> <p>Noise data were characterized by strong signals at blade passage frequency and up to 10 harmonics. Cabin noise was not so high as to preclude attainment of comfortable levels with suitable wall treatment. Community noise was not excessive.</p>					
17. Key Words (Suggested by Author(s)) Propfan, Advanced Turboprop, High-Speed Propeller, Flight Test			18. Distribution Statement Unclassified - Unlimited Subject Category 07		
19. Security Classif. (of this report) Unclassified		20. Security Classif. (of this page) Unclassified		21. No of pages	22. Price A10



2

